

# **A Thermoacoustic Characterization of a Rijke-type Tube Combustor**

Lars Nord

Thesis submitted to the Faculty of the  
Virginia Polytechnic Institute and State University  
in partial fulfillment of the requirements for the degree of

Master of Science  
in  
Mechanical Engineering

Dr. William R. Saunders, Chair  
Dr. Uri Vandsburger, Co-Chair  
Dr. Ricardo Burdisso

February, 2000  
Blacksburg, Virginia

Keywords: acoustics, chemiluminescence, combustion, flame instabilities

# **A Thermoacoustic Characterization of a Rijke-type Tube Combustor**

Lars Nord

Dr. William R. Saunders, Chair

Dr. Uri Vandsburger, Co-Chair

Department of Mechanical Engineering

## **(ABSTRACT)**

Pressure pulsations, or thermoacoustic instabilities, as they are called in the research community, can cause extensive damage in gas turbine combustion chambers. To understand the phenomena related to thermoacoustics, a simple Rijke-type tube combustor was built and studied. Extensive experimental results, as well as theoretical analyses related to the Rijke tube are presented in this thesis. The results, attributable to both the analyses and the experiments, help explain all the phenomena affecting the acoustic pressure in the combustor. The conclusion is that there are three separate yet related physical processes affecting the acoustic pressure in the tube. The three mechanisms are as follows: a main thermoacoustic instability in accordance to the Rayleigh Criterion; a vibrating flame instability where the flame sheet exhibits mode shapes; and a pulsating flame instability driven by heat losses to the flame stabilizer. All these instabilities affect the heat released to the gas in the combustor. The energy from the oscillating heat couples with the acoustics of the volume bounded by the tube structure. The experimental results in the study are important in order to obtain model parameters for prediction as well as for achieving control of the instabilities.

To Ragnhild

## Acknowledgements

I wish to thank the members of both the Virginia Active Combustion Control Group (VACCG) and the Reacting Flows Laboratory (RFL) for help during the progress of this thesis. A special thanks goes out to the three professors in my committee, Dr. Uri Vandsburger, Dr. William Saunders, and Dr. Ricardo Burdisso for all the help and support they provided during my time at Virginia Tech. I would also like to thank fellow students Ludwig Haber, who set up the optics system utilized in the experiments for this thesis; Chris Fannin, who set up a bench-top experiment for studying a vibrating flame phenomenon analyzed in the thesis; Bryan Eisenhower for general help with the tube combustor; John Richards for fabrication and calibration of pressure transducers; and Donald Grove for thermocouple fabrication and setup. A number of helpful discussions and general help in the laboratory have been provided from students Vivek Khanna and Steve Lepera. For assistance when collecting all the data presented in this thesis, Jesse Seymore has been very important and without Jesse the work would have taken much longer. For reviewing the thesis I thank Professor J. Lawrence McLaughlin and co-worker Helmer Andersen. Finally I would like to thank my parents Stig & Linnéa Nord, as well as Halley Orthmeyer for all the emotional support they have given me during the time I spent working on this thesis.

# Table of Contents

<b>Chapter 1</b>	<b>Introduction</b>	<b>1</b>
1.1	Background	1
1.2	Objectives and Scope	2
1.3	Technical Approach	3
<b>Chapter 2</b>	<b>Literature Review and Theoretical Background</b>	<b>4</b>
2.1	Literature Review	4
2.1.1	Thermoacoustics and Rijke-type Tube Combustors	4
2.1.2	Vibrating and Pulsating Flames	6
2.1.3	Review Articles	8
2.2	Theoretical Background	9
2.2.1	Solution of the Wave Equation for a Closed-Open Duct	9
2.2.2	The Rayleigh Criterion	13
2.2.3	Definition of Equivalence Ratio for Methane with Air as Oxidizer	14
<b>Chapter 3</b>	<b>Experimental Systems and Methods</b>	<b>16</b>
3.1	Overview of Experimental Components	16
3.2	Tube Combustor	17
3.3	Pressure Transducers	19
3.4	Thermocouples	20
3.5	Optical System for Chemiluminescence Measurements	21
3.6	Mass Flow Meters	23
3.7	Data Acquisition Equipment	24
<b>Chapter 4</b>	<b>Rijke-tube Thermoacoustic Characterization</b>	<b>26</b>
4.1	Acoustic Pressure	26
4.1.1	Limit Cycle and Harmonics	28
4.1.2	Subharmonic Response	29
4.1.3	Subsonic Instability	37

4.2 Chemiluminescence Measurements	42
4.3 Comparison of Pressure and Chemiluminescence Spectra	43
4.4 Axial Temperature Profiles	44
4.5 The Operational Characteristics of the Tube Combustor	45
4.6 Extensive Mapping of the Operating Region	46
4.7 Database on the World Wide Web	53
4.8 Resonance Frequencies	53
<b>Chapter 5 Conclusions and Future Work</b>	<b>58</b>
5.1 Conclusions	58
5.2 Future Work	59
<b>References</b>	<b>61</b>
<b>Appendix A Pressure Power Spectra for Constant Equivalence Ratio</b>	<b>66</b>
<b>Appendix B Pressure Power Spectra for Constant Flow Rate</b>	<b>87</b>
<b>Appendix C OH* Power Spectra for Constant Equivalence Ratio</b>	<b>108</b>
<b>Appendix D OH* Power Spectra for Constant Flow Rate</b>	<b>129</b>
<b>Appendix E Axial Temperature Distributions for Constant Equivalence Ratio</b>	<b>150</b>
<b>Appendix F Axial Temperature Distributions for Constant Flow Rate</b>	<b>171</b>
<b>Vita</b>	<b>192</b>

# Chapter 1 Introduction

## 1.1 Background

In a dry low  $\text{NO}_x$ -emission gas turbine, problems with pressure pulsations can occur in the combustion chamber. The pressure pulsations can couple with the structure and cause violent vibrations to the extent that the whole gas turbine fails. In the past, this was not a major problem because of the use of diffusion flames in addition to the secondary air supplied through holes in the combustor walls. Modern gas turbines with a dry low  $\text{NO}_x$ -system use premixed air-fuel so that it is no longer necessary to add secondary air. The cooling schemes have also changed; convective cooling is now often used instead of film cooling. This process made almost all the holes in the combustor walls vanish and thus the chamber essentially became a resonator with very little attenuation. To limit the production of  $\text{NO}_x$ , the flame is kept as lean as possible. However, this leads to a more unstable flame, with oscillating heat release that couples with the acoustics of the chamber. Therefore, in the past several years there has been a keen interest in the study of thermoacoustic (TA) instabilities, which is defined as the coupling between the heat release rate and the acoustic pressure. This problem has been studied for over a century. It began in 1877 when Lord Rayleigh described how the balance between acoustic dissipation and acoustic excitation, due to unsteady heat transfer, can lead to a self-excited, unstable acoustic response. The criterion, called the Rayleigh Criterion, have been studied by several researchers including Blackshear (1953), Putnam (1971), and Joos and Vortmeyer (1986). This fundamental perspective of energy balance is very useful in many ways, but it does not provide sufficient detail to explain all of the characteristics that may be observed during unstable TA response of a combustor.

A Rijke-type tube, named after an experimental setup presented by Rijke (1859), is a fundamental setup for the study of thermoacoustic instabilities. Rijke tubes and related devices have been studied by Putnam (1971), Bailey (1957), and a review of the field was presented by Raun, Beckstead, Finlinson, and Brooks (1993). The geometry of a Rijke tube, typically with a large length-to-diameter ratio, is much simpler than the

geometry of a full-scale combustor used in gas turbines. The large length-to-diameter ratio basically makes the problem one-dimensional which makes the acoustics easier to analyze, and, since there are no sudden area changes, the shedding of vortices is limited compared to a dump combustor. It is therefore possible to isolate specific phenomena related to thermoacoustics more effectively than in a full-scale combustor. The flame shape is typically a flat flame compared to the much more complex flames in gas turbine combustion chambers which means the flame-acoustic interaction also is less involved.

In the past, researchers have studied specific phenomena related to this area. Many researchers have studied the thermoacoustic instability in terms of amplitude and frequency. They have also studied how different parameters affect the TA instability. Others have concentrated on flame-acoustic interaction in terms of pulsating flame instabilities and vibrating flames. In this thesis, an effort is made to qualitatively understand all the phenomena that have some visual effect on the pressure power spectrum in a Rijke-type tube with a burner-stabilized premixed flame.

## 1.2 Objectives and Scope

The overall objective of the research conducted by Virginia Active Combustion Control Group [VACCG] was to increase the understanding of thermoacoustic instabilities to be able to predict and provide active control of the instabilities in a full-scale combustor. To achieve that, models for the TA instabilities, including flame dynamics, fluid dynamics, and acoustic-flame interactions, have to be developed.

The part of the project presented in this thesis involves the study of a simple tube combustor. VACCG members have investigated a number of theories associated with the phenomena occurring in the combustor. The research presented in this document will, with the help of extensive experimental data, strengthen the suggested theories. The experiments conducted will also serve as a database for the VACCG and the research community within this field. In addition the collected data can be helpful in the development of reduced-order modeling schemes that provide adequate prediction capabilities for the occurrence of thermoacoustic instabilities. The experimental

investigation included a mapping of the tube combustor in terms of acoustic pressure, temperature distribution, and chemiluminescence for the whole operating region.

### 1.3 Technical Approach

A very simple combustion process was selected to facilitate initial studies of thermoacoustic instabilities at Virginia Tech. The tube combustor is similar to a Rijke tube except that the boundary conditions are closed-open versus open-open. According to the Rayleigh Criterion this leads to a TA instability of the 2<sup>nd</sup> acoustic mode when the flame is placed at the middle of the tube. There are some important limitations associated with the study of TA instabilities in Rijke tubes versus real, full-scale combustors. Primarily, the fluid dynamic coupling is not important, as there are no vortical structures in the tube flow that can cause periodic heat release. This leads to easier studies of the features that were the focus of this test device. Specifically, the tube combustor was intentionally selected to eliminate coupling between TA instabilities and flow-instabilities. This thesis will, using frequency-domain formats, examine the observed acoustic and thermal-proportional response characteristics with interpretations based on the measurements viewed. There is a large amount of information that resides in the spectral representations of any dynamic system response measurements for linear or nonlinear systems. The information supports descriptions of physical phenomena responsible for unique spectral features. Therefore, it can be helpful to discern the details of the thermoacoustic pressure signatures for both dynamic modeling and system monitoring in any combustor system.

## Chapter 2 Literature Review and Theoretical Background

### 2.1 Literature Review

This literature review is not intended to be complete as far as all the literature that has been produced in the area of dynamics in Rijke tube combustors. The purpose of the review is to give a background to this thesis and to give some insight into the work that has been conducted in the research areas presented in the following sections.

#### 2.1.1 Thermoacoustics and Rijke-type Tube Combustors

The first published experiments regarding Rijke tubes were conducted by Rijke (1859) after whom the type of tube is named. He used an open-open tube and had a wire-gauze to locally heat up the air in the tube. By doing this, the tube produced a sound close to the fundamental tone of the tube. An explanation of the phenomena was published by Rayleigh (1877), (1878), where he states *“If heat be given to the air at the moment of greatest condensation, or taken from it at the moment of greatest rarefaction, the vibration is encouraged.”* This statement is now known as the Rayleigh Criterion. Putnam and Dennis (1953) studied three combustion systems exhibiting acoustical oscillations: 1) an open-open tube with a premixed flame, 2) a closed-open tube with a premixed flame, and 3) a closed-open tube with a diffusion flame. They concluded from tests and from the analysis that oscillations were amplified when two requirements were fulfilled simultaneously: First, an oscillating component of the heat release was in phase with the pressure variation, and second, the point of heat release was close to a point of maximum pressure amplitude in the combustor. By studying different configurations, they added knowledge to the field by describing the amount and type of change in apparatus configuration necessary either to eliminate or encourage oscillations. In the appendix of Putnam and Dennis’s paper, a thermodynamic treatment of the phase requirement between rate of heat release and pressure (the Rayleigh Criterion) was presented. Putnam and Dennis (1954) made an investigation regarding a combustion chamber with a mesh-screen flame holder. The exhaust gases passed out through a converging nozzle and a stack. The depth of the flame holder and the length of the stack

could be varied. A theory for the gauze tones produced was also presented. Putnam presents these investigations, and much more information, in his book “*Combustion Driven Oscillations in Industry*” (1971), where he states the Rayleigh Criterion in an integral form. He also concluded that the condition required for combustion driven oscillations to occur is determined by the integral  $\oint p h d(\omega t)$ . Here  $p$  is the acoustic pressure,  $h$  the unsteady part of the heat release, and  $\omega$  the angular frequency. Blackshear (1953) explained in detail the mechanism whereby the heat addition can drive or damp an oscillation. In the experimental work he examined the effect of a flame on a standing wave system by measuring the ability of the flame to damp an imposed standing wave rather than to examine spontaneous excitation. A system, which was either closed-closed or closed-open, was used, and the flame’s role was investigated by considering the following variables: fuel-air ratio, inlet temperature, flame holder position, sound amplitude, and inlet velocity. Bailey (1957) used an open-open tube to study flame-excited oscillations. His results were in agreement with the Rayleigh Criterion. Joos and Vortmeyer (1986) investigated how the Rayleigh Criterion is satisfied with superimposed oscillations in situations when more than one frequency is excited. To do this, they conducted simultaneous recordings of oscillations in the sound pressure, sound particle velocity, and energy. For measurements of the heat release rate oscillation, OH\* radiation was studied. OH\* is excited OH-radicals which, when going from their excited state to their ground state, emit light, and are assumed to be proportional to the heat released. “*The Spectroscopy of Flames*” by Gaydon (1974), a paper by Diederichsen and Gould (1965), and the thesis “*An Investigation Into the Origin, Measurement and Application of Chemiluminescent Light Emissions from Premixed Flames*” by Haber (2000) provide more insight into this area. In accordance to the Rayleigh Criterion, Joos and Vortmeyer found self-excited oscillations when the sound particle velocity preceded the sound pressure. This was the case when only one frequency was excited. However, when more than one frequency was excited the sound particle velocity phase, in relation to the sound pressure phase, changed with time. The sound particle velocity phase lagged behind the pressure at some stages; however, the oscillations were still sustained. Their conclusion was that it is sufficient for sustained oscillations to fulfill the Rayleigh Criterion temporarily.

An extensive theoretical investigation was conducted by Bloxside, Dowling, and Langhorne (1988) in conjunction with an experimental investigation by Langhorne (1988). Their objective was to predict the frequency and onset fuel-air ratio for oscillations to occur in practical geometries. They developed a model for the dynamic behavior of the flame in response to an unsteady velocity field. The theoretical predictions were then tested against experimental data. They found that the predicted and measured frequencies were within 6 Hz and that the theory was able to predict trends in variations in frequency as either equivalence ratio, inlet Mach number, or duct geometry were changed. The oscillation frequency shift, with equivalence ratio, showed a non-linear behavior both in the experiments and in the calculations. The frequency dependence on the inlet Mach number showed a linear effect. Cho, Kim, and Lee (1998) conducted a parametric study, with measurements of acoustic pressure and flame radiation in various conditions in order to understand the effect of physical parameters, such as Reynold's number and equivalence ratio, in a ducted premixed flame burner. They concluded that Reynold's number neither affects the maximum pressure peak nor the fundamental frequency of the system to any large extent. The equivalence ratio, however, was an important parameter in terms of the maximum pressure peak and the fundamental frequency.

In summary, it can be noted that the primary role of the studies of Rijke-type tubes throughout the literature have either been related to the Rayleigh Criterion, in terms of confirming it and/or extending it, or they have been related to parametric studies, where the effects of fuel-air ratio, fluid velocity, flame holder position, and duct geometry were examined.

### **2.1.2 Vibrating and Pulsating Flames**

Both vibrating and pulsating instabilities are seen in burner-stabilized premixed flames. Vibrating flames, also called wrinkled flames, are cellular instabilities and are typically seen at Lewis numbers below unity. Pulsating instabilities, however, occurs at Lewis numbers above unity and are one-dimensional instabilities in the axial direction of the combustor system.

Markstein (1964) published articles on non-steady flame propagation. Among the relative articles is Markstein's "Perturbation Analysis of Stability and Response," in which he discussed vibrating flames which is examined further in Chapter 4 of this thesis. Margolis (1980) also discussed pulsating instabilities. He showed, with a linear stability analysis, that steady burner-stabilized flames with conduction losses to the flame holder may be unstable to one-dimensional disturbances. His theory will also be further discussed in Chapter 4. Pelce and Clavin (1982) completed an analytical study to provide a rigorous description of the coupling between the hydrodynamic and diffusive effects occurring in premixed flame fronts. A paper by Clavin and Garcia (1983) was a continuation of their previous work, but here they dropped an assumption about temperature independent diffusivities. Searby and Clavin (1986) also analyzed wrinkled flames in weakly turbulent flows. Pulsating and cellular flame instabilities were examined by Buckmaster (1983). He investigated the linear stability of a premixed flame attached to a porous plug burner. His results confirmed Margolis's prediction that the flame holder can make an instability region, in the wave- and Lewis-number plane, accessible to real mixtures. The flame holder can displace the stability/instability boundaries to a region with parameters more realistic for real mixtures.

Van Harten, Kapila, and Matkowsky (1984) made an analysis of the interaction of a plane, steady flame with a normally incident acoustic wave. They found that the flow field divides into an outer acoustic region where linear equations can be used, and an inner flame zone in which diffusion and reaction takes place and the equations are non-linear. They conclude that the flame influences the acoustics through a density discontinuity and that the acoustic disturbance affects the flame primarily by changing the mass flux through the flame. This required an investigation of the flame structure. The flame structure problem is non-linear which generally means only numerical solutions can be obtained. They provided analytical solutions for two special cases though: 1) low-frequency acoustics, and 2) small heat release coupled with low amplitude acoustics. McIntosh has written a number of articles in the field of non-steady flames. McIntosh and Clarke (1984) made a mathematical analysis of burner-stabilized flames for arbitrary Lewis numbers, and in a follow-up McIntosh (1986) included acoustical interference in the analysis. McIntosh (1987) also made an analysis similar to the two

previous papers, but this time he used a finite tube length upstream and downstream of the burner and also included the impedance of the burner. An application of the theory from 1986/1987 was then made by McIntosh (1990). His theory was applied to predict where the flame should be located in a tube to cause most amplification of the fundamental tone. The results showed good correspondence with the Rayleigh Criterion. Searby and Rochwerger (1991) made an experimental and theoretical investigation of the coupling between a premixed laminar flame front and acoustic standing waves in tubes. They investigated a parametric acoustic instability of planar flames which was first recognized by Markstein. They concentrated on what they call a secondary instability which oscillates with double the period of the acoustic oscillation. Comparison between experiments and theory indicated that the mechanism responsible for the self-excited secondary instability was the parametric instability described by Markstein. Baillot, Durox, and Prud'homme (1992) conducted an experimental study of vibrating flames above a cylindrical burner. They examined fundamental characteristics of flow perturbations and combustion interaction by pumping the flow with a sinusoidal modulation caused by a speaker. Durox, Baillot, Searby, and Boyer (1997) investigated the mechanism leading to a change in the flame shape by using a Bunsen burner. They also examined the motion of the flame front and the modification of the upstream velocity field. It is concluded that strong acoustic forcing at high frequency (in the order of 1000 Hz) leads to a strong deformation of a conical flame which deforms to a flattened hemisphere above the burner exit. A year later Durox, Ducruix, and Baillot (1998) conducted a similar study to the 1997 study. They observed that beyond a given acoustic amplitude, cells appear and stay on the flame. The cells were found to oscillate at half the excitation frequency.

### 2.1.3 Review Articles

For the interested reader a number of review articles have been produced in the area of thermoacoustics and Rijke tubes. Putnam and Dennis (1956) conducted a survey about organ-pipe oscillations in combustion systems and Mawardi (1956) discussed the generation of sound by turbulence and by heat processes. Feldman (1968) made a short review of the literature on Rijke thermoacoustic phenomena and Culick (1989) discussed

combustion instabilities in propulsion systems. McManus, Poinso, and Candel (1993) discussed active control, as well as other aspects, of combustion instabilities. An extensive review of Rijke tubes, Rijke burners, and related devices was produced by Raun, Beckstead, Finlison, and Brooks (1993).

## 2.2 Theoretical Background

In this section a theoretical explanation of a number of terms used throughout this document will be given. The acoustics of a closed-open Rijke-type tube, an integral form of the Rayleigh Criterion, as well as the equivalence ratio for methane burning in air will be discussed.

### 2.2.1 Solution of the Wave Equation for a Closed-Open Duct

For a closed-open duct, as in Figure 2.1, the pressure will take the following form, assuming plane waves:

$$p(x, t) = Ae^{i\omega t - ikx} + Be^{i\omega t + ikx} \quad (1)$$

where  $A$  and  $B$  are constants,  $\omega$  the angular frequency and  $k$  the wave number.

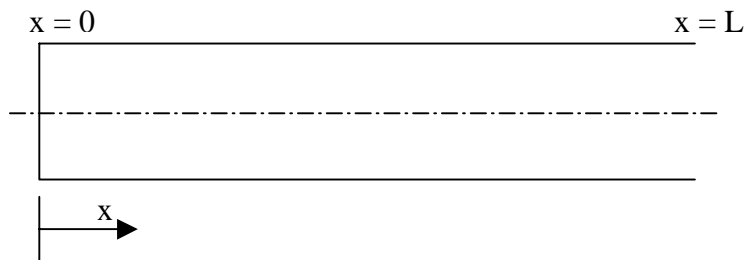


Figure 2.1 Closed-open duct

Euler's Equation for plane waves:

$$\frac{\partial p}{\partial x} = -i\omega\rho u(x, t) \quad (2)$$

Here  $\rho$  is the density of the fluid and  $u(x, t)$  the particle velocity.

Take the derivative of  $p$  in Equation 1 with respect to  $x$ :

$$\frac{\partial p}{\partial x} = -ikAe^{i\omega t - ikx} + ikBe^{i\omega t + ikx} \quad (3)$$

and substitute into Euler's Equation:

$$u(x, t) = \frac{ikAe^{i\omega t - ikx}}{i\omega\rho} + \frac{ikBe^{i\omega t + ikx}}{-i\omega\rho} \quad (4)$$

Since  $k = \frac{\omega}{c}$ , where  $c$  is the speed of sound in the fluid, the expression can be simplified:

$$u(x, t) = \frac{Ae^{i\omega t - ikx} - Be^{i\omega t + ikx}}{\rho c} \quad (5)$$

Boundary condition at  $x = 0$ :

$$u(0, t) = 0 \quad (6)$$

This gives:

$$\frac{Ae^{i\omega t} - Be^{i\omega t}}{\rho c} = 0 \quad (7)$$

Which gives:

$$A - B = 0 \quad (8)$$

Or:

$$A = B \quad (9)$$

The boundary condition at  $x = L$  is a bit more complicated. The wave impedance there must equal the radiation impedance of the opening as defined in the equation:

$$\frac{p(L, t)}{u(L, t)} = z_{rad} \quad (10)$$

For plane waves the opening radiates sound as an un baffled piston (Kinsler, et. al. (1982)):

$$z_{rad} = \rho c \left( \frac{1}{4} (ka)^2 + i0.6ka \right) \quad (11)$$

where  $a$  is the radius of the duct.

Here the real part is the resistance and the imaginary part the reactance.

Using Equations (1), (5), and (9), the left-hand side of Equation (10) can be written as:

$$\frac{p(L,t)}{u(L,t)} = \frac{Ae^{i\omega t - ikL} + Ae^{i\omega t + ikL}}{\left( \frac{Ae^{i\omega t - ikL} - Ae^{i\omega t + ikL}}{\rho c} \right)} \quad (12)$$

Or simplified:

$$\frac{p(L,t)}{u(L,t)} = \rho c \frac{e^{-ikL} + e^{ikL}}{e^{-ikL} - e^{ikL}} \quad (13)$$

Since

$$e^{i\theta} = \cos(\theta) + i \sin(\theta) \quad (14)$$

Equation (13) can be written as:

$$\frac{p(L,t)}{u(L,t)} = \rho c \frac{\cos(-kL) + i \sin(-kL) + \cos(kL) + i \sin(kL)}{\cos(-kL) + i \sin(-kL) - \cos(kL) - i \sin(kL)} \quad (15)$$

Since  $\cos(-kL) = \cos(kL)$ , and  $\sin(-kL) = -\sin(kL)$  Equation (15) can be written as:

$$\frac{p(L,t)}{u(L,t)} = \rho c \frac{2 \cos(kL)}{-2i \sin(kL)} \quad (16)$$

Or:

$$\frac{p(L,t)}{u(L,t)} = i \rho c \cot(kL) \quad (17)$$

For resonance, the resistive part of the radiation impedance goes to zero which gives the following expression:

$$z_{rad, resonance} = i \rho c 0.6 ka \quad (18)$$

Equate Equations (17) and (18):

$$\rho c \cot(kL) = \rho c 0.6 ka \quad (19)$$

Or:

$$\cot(kL) = 0.6 ka \quad (20)$$

This equation can be solved numerically, or one can use the fact that for  $ka \ll 1$

$$0.6 ka \approx \tan(0.6 ka) \quad (21)$$

Equation (20) can now be rewritten as:

$$\cot(kL) \approx \tan(0.6 ka) \quad (22)$$

Or:

$$\frac{\cos(kL)}{\sin(kL)} = \frac{\sin(0.6ka)}{\cos(0.6ka)} \quad (23)$$

Therefore:

$$\cos(kL)\cos(0.6ka) - \sin(kL)\sin(0.6ka) = 0 \quad (24)$$

This can be written as:

$$\cos(kL + 0.6ka) = 0 \quad (25)$$

The solution of this equation is:

$$k_n L + 0.6k_n a = \left(\frac{2n-1}{2}\right)\pi \quad n = 1, 2, 3, \dots \quad (26)$$

Or since  $k = \frac{\omega}{c} = \frac{2\pi f}{c}$ :

$$\frac{2\pi f_n}{c} L + \frac{2\pi f_n}{c} 0.6a = \left(\frac{2n-1}{2}\right)\pi \quad (27)$$

Solving for  $f_n$  gives:

$$f_n = \frac{c}{2} \frac{\left(\frac{2n-1}{2}\right)}{L + 0.6a} \quad (28)$$

Or:

$$f_n = \frac{c \left(\frac{2n-1}{4}\right)}{L + 0.6a} \quad (29)$$

The denominator is sometimes referred to as the effective length of the duct.

$$L_{eff} = L + 0.6a \quad (30)$$

$f_n$  are the eigenfrequencies of the system, where  $n$  is the mode number.

In Table 2.1 the frequencies of the first seven modes of a closed-open system at room temperature, with  $c = 343$  m/s,  $L = 60$  inches and  $a = 2.85/2$  inches. The conversion factor 1 inch = 0.0254 m has been used

Table 2.1 The 7 first eigenfrequencies of the system

Mode Number $n$	Eigenfrequency $f_n$ [Hz]
1	55
2	166
3	277
4	388
5	499
6	610
7	721

### 2.2.2 The Rayleigh Criterion

Thermoacoustic instabilities are the result of the coupling between the unsteady heat release and the acoustic pressure, and they are well described by the Rayleigh Integral:

$$R = \int_t^{t+T} p'(t)Q'(t)dt$$

, where  $R$  is the Rayleigh Index,  $p'(t)$  the acoustic pressure and  $Q'(t)$  the unsteady part of the heat release rate.

The unsteady heat release is proportional to the acoustic particle velocity  $\bar{u}'(t - \tau)$ , where  $\tau$  is the time lag between a change in flow rate and a change in heat release rate:

$$Q'(t) \sim \bar{u}'(t - \tau)$$

This leads to the following integral:

$$R \cong \int_t^{t+T} p'(t)\bar{u}'(t - \tau)dt$$

Adding heat where the Rayleigh Index is negative would add damping to the system, whereas adding heat where the Rayleigh Index is positive could lead to thermoacoustic instability if the amount of heat added is large enough to overcome the damping of the system. In Figure 2.1 are the spatial distribution of the acoustic pressure, particle

velocity, and the Rayleigh Index shown for a closed-open tube. Note that adding heat where the Rayleigh Index is maximum would be “ideal” to cause an instability. For the closed-open system the Rayleigh Index turns out to be maximum at mid-span in the tube.

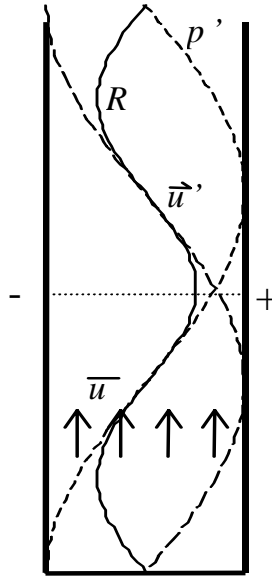
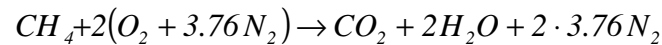


Figure 2.1 The Rayleigh Index for a closed-open system. The solid line shows the spatial distribution of the Rayleigh Index.

### 2.2.3 Definition of Equivalence Ratio for Methane with Air as Oxidizer

The stoichiometric equation for methane-air combustion is (neglecting minor species):



The fuel/air-ratio on volume basis for stoichiometric combustion:

$$\left(\frac{F}{A}\right)_{stoich} = \frac{\sum \text{Fuel molecules}}{\sum \text{Air molecules}} = \frac{1}{2 \cdot 4.76} = \frac{1}{9.52}$$

The equivalence ratio  $\phi$  is defined as:

$$\phi = \frac{\left(\frac{F}{A}\right)_{actual}}{\left(\frac{F}{A}\right)_{stoic}} = 9.52 \left(\frac{F}{A}\right)_{actual} = 9.52 \frac{Q_{fuel}}{Q_{air}}$$

where  $Q_{fuel}$  is the volumetric flow of fuel and  $Q_{air}$  is the volumetric flow of air.

The fuel-air ratio on mass basis:

$$\begin{aligned} \left(\frac{F}{A}\right)_{stoic} &= \frac{n_{fuel} MW_{fuel}}{\sum_i n_i MW_i} = \frac{1 \cdot MW_{CH_4}}{2 \cdot MW_{O_2} + 2 \cdot 3.76 \cdot MW_{N_2}} = \\ &= \frac{16.04}{2 \cdot 31.999 + 2 \cdot 3.76 \cdot 28.014} = \frac{1}{17.12} \end{aligned}$$

where  $n_i$  is the number of moles of species  $i$  and  $MW_i$  the molecular weight of species  $i$ .

$$\phi = \frac{\left(\frac{F}{A}\right)_{actual}}{\left(\frac{F}{A}\right)_{stoic}} = 17.12 \left(\frac{F}{A}\right)_{actual} = 17.12 \frac{\dot{m}_{fuel}}{\dot{m}_{air}}$$

Here  $\dot{m}_{fuel}$  is the mass flow of fuel and  $\dot{m}_{air}$  is the mass flow of air.

## Chapter 3 Experimental Systems and Methods

### 3.1 Overview of Experimental Components

A closed-open Rijke-type tube combustor was used for the work of this study as shown schematically in Figure 3.1.

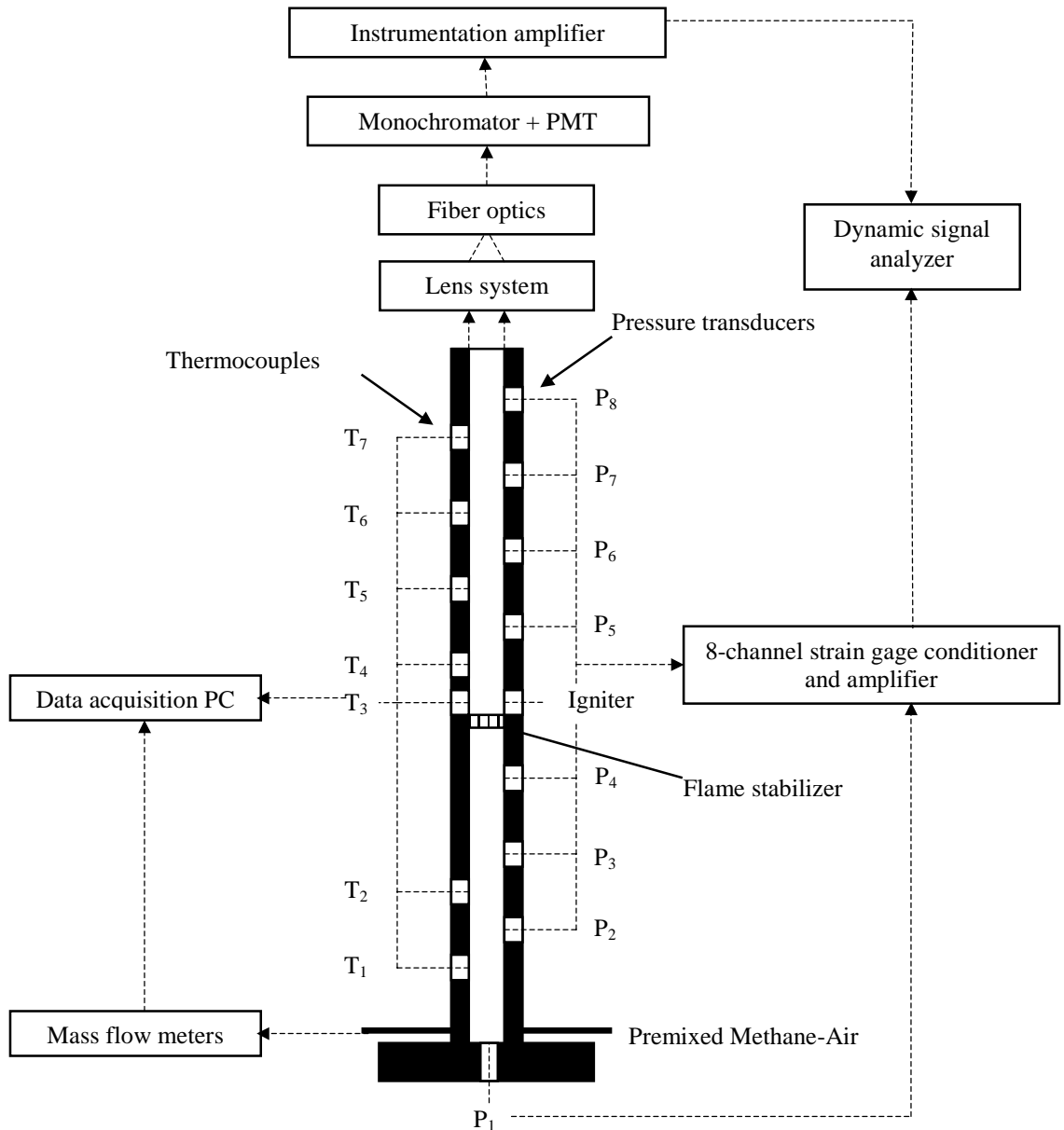


Figure 3.1 Overall experimental setup of the tube combustor

Premixed methane-air coming from a gas mixer was fed into the bottom part of the combustor through copper tubes with small holes drilled in the cylindrical shaped tubes. The flame was stabilized by a ceramic honeycomb, located mid-span, where the Rayleigh Index is maximum for the 2<sup>nd</sup> acoustic mode, as mentioned in Chapter 2. For temperature measurements seven type K thermocouples were inserted through the combustor wall with the bead located on the centerline of the combustor. The data was processed in a data acquisition PC. For pressure measurements, pressure transducers were mounted on the opposite side as well as one in the bottom of the tube and were connected to a strain gage amplifier and conditioner. The data was processed in a dynamic signal analyzer. For chemiluminescence measurements of the flame, an optical system was utilized, which consisted of lenses, a fiber optic cable, a monochromator, and a photomultiplier tube (PMT). The signal from the PMT was amplified and analyzed with a dynamic signal analyzer.

### **3.2 Tube Combustor**

The tube combustor itself consisted of a 60" long steel tube with an inner diameter of 2.85", as seen in Figures 3.2 and 3.3. Seven holes, to be used for insertion of two thermocouples below and five above the flame holder, were drilled and tapped on one side of the combustor. On the opposite side seven holes for pressure transducers were drilled and tapped. In addition, an igniter for ignition of the pre-mixed methane-air was inserted one inch above the flame holder. A hole for a pressure transducer was also located in the bottom of the tube for use as a reference for the acoustic pressure since a pressure maximum will always be located at the closed end regardless of the frequency of the fluctuation. The flame is viewable through two view windows on each side of the tube. A mount for the optical system was located on top of the combustor.

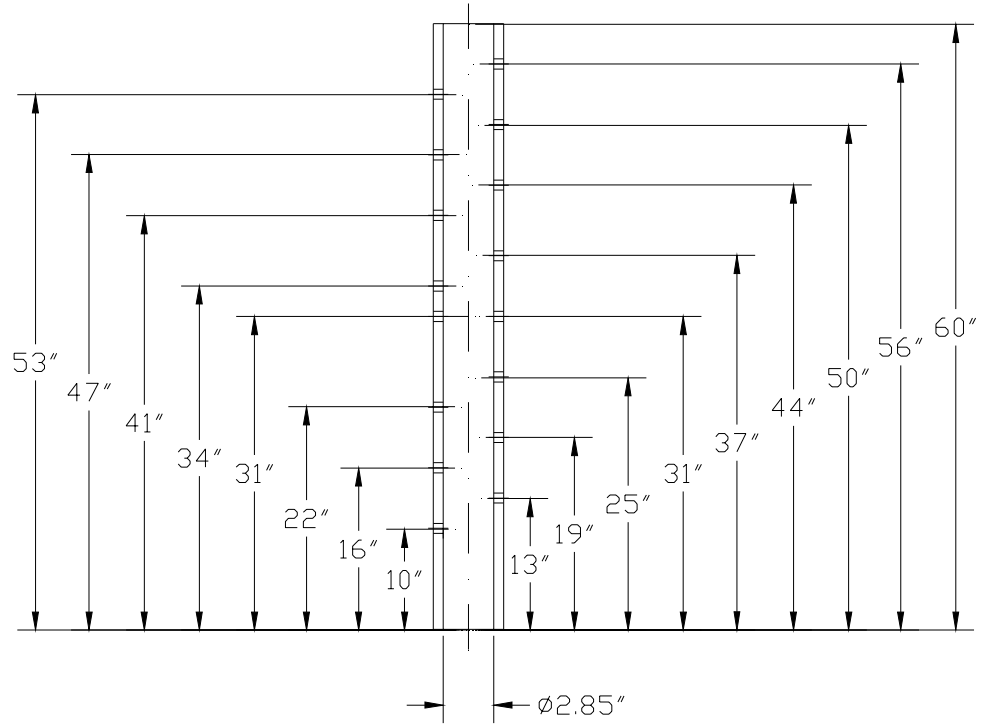


Figure 3.2 Tube combustor dimensions

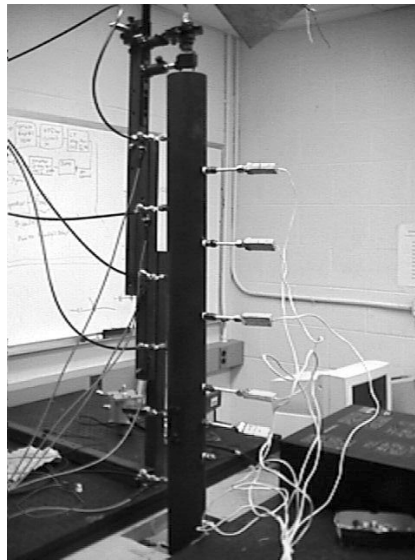
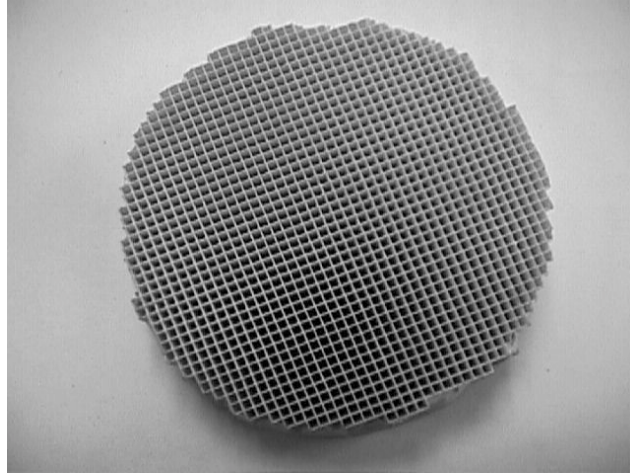


Figure 3.3 Tube combustor equipped with thermocouples, pressure transducers, and optics system

The ceramic honeycomb [Al<sub>2</sub>O<sub>3</sub>] used for the stabilization of the laminar flame in the combustor is shown in Figure 3.4. The flame stabilizer was mounted 30" from the bottom of the tube combustor for excitation of the 2<sup>nd</sup> acoustic mode.



*Figure 3.4 Ceramic honeycomb used as a flame holder in the tube combustor. The area restriction was approximately 50%.*

### 3.3 Pressure Transducers

The pressure transducers, Sensym low-pressure transducers, were mounted in T-connections as shown in Figure 3.5. One of the connections in the T was connected to the tube combustor via a teflon connector. The opposite connection was connected to an “infinite tube”, a five meters long plastic tube, to limit the reflective pressure waves travelling back up the line and affecting the pressure at the transducer. The third connection was used for calibration of the transducers. The calibration procedure is described in a technical brief by Richards, et. al. (1999). The signals from the eight pressure transducers were amplified in a strain gage conditioner and amplifier, model 2100, made by Measurements Group Incorporated.

In the pressure measurements, the effects of errors in the strain gage conditioner and amplifier as well as in the Hewlett Packard dynamic signal analyzer were negligible compared to the error in the transducer itself. The error for the Sensym pressure transducers were within  $\pm 0.2\%$ .



Figure 3.5 Sensym pressure transducer mounted in a T-connection

### 3.4 Thermocouples

The temperature measurements were conducted with thermocouples of type K, as seen in Figure 3.6. The wire used was 0.01" diameter type K thermocouple wire. The bead diameter ranged from 0.029" to 0.04" for the thermocouples. The measured surface temperature of the thermocouple may be considerable different from the desired gas temperature. With the bead diameter being approximately three to four times larger than the lead wire, the convective behavior of the bead is close to that of a cylinder [Hibshman (1999)]. The analysis described by Hibshman was initially used to correct the temperatures; however, findings by one of the VACCG members, Vivek Khanna, suggested that due to interaction between the walls, the honeycomb, and the thermocouple beads, a different approach was necessary. The findings arose at the end of the author's research at Virginia Tech and will not be discussed in this thesis; consequently, the collected temperature data was left uncorrected.

The fabrication procedure of the thermocouples and the data acquisition system for collection of the temperature data are described in a technical brief by Grove, et. al. (1999).

The error in the temperature measurements mainly came from the thermocouples. ASTM standards specify that the initial calibration tolerances for type K thermocouples be  $\pm 2.2^{\circ}\text{C}$  or  $\pm 0.75\%$ , whichever is greater, for the temperature range  $0^{\circ}\text{C}$  to  $1250^{\circ}\text{C}$ .

The maximum error in the 8<sup>th</sup>-order polynomials describing the temperature as a function of voltage is  $\pm 0.7^\circ\text{C}$  for the temperature range  $0^\circ\text{C}$  to  $1370^\circ\text{C}$ .

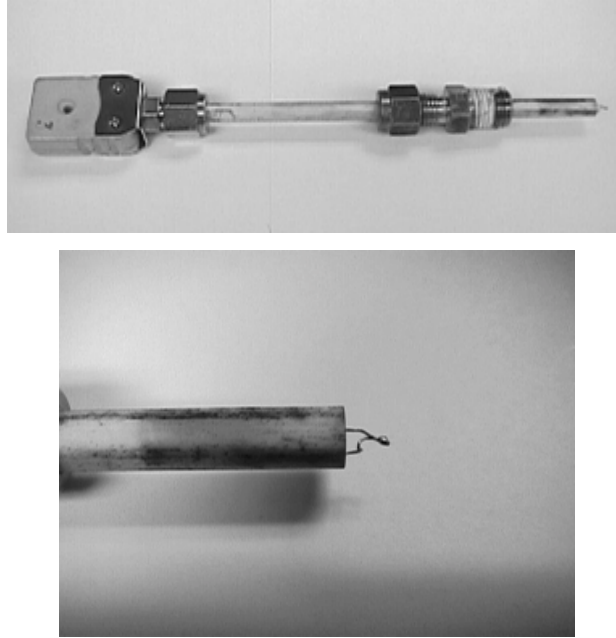


Figure 3.6 Type K thermocouple

### 3.5 Optical System for Chemiluminescence Measurements

To measure the heat release oscillation of the flame in the tube combustor an optical system was utilized. Excited OH-radicals, which when going from their excited state to their ground state emit light, are assumed to be proportional to the heat release rate from the flame. The optical system used for these chemiluminescence measurements consisted of the following:

- A system of two short focal length lenses: Two, 25.4 mm fused silica lenses.
- Optical Fiber: 200  $\mu\text{m}$ , silica core fiber.
- Monochromator: 0.5 m Jarrell-Ash monochromator.
- Photomultiplier: R955 Hamamatsu ten stages photomultiplier tube.

The setup, constructed by VACCG member Ludwig Haber, is shown in Figure 3.7.

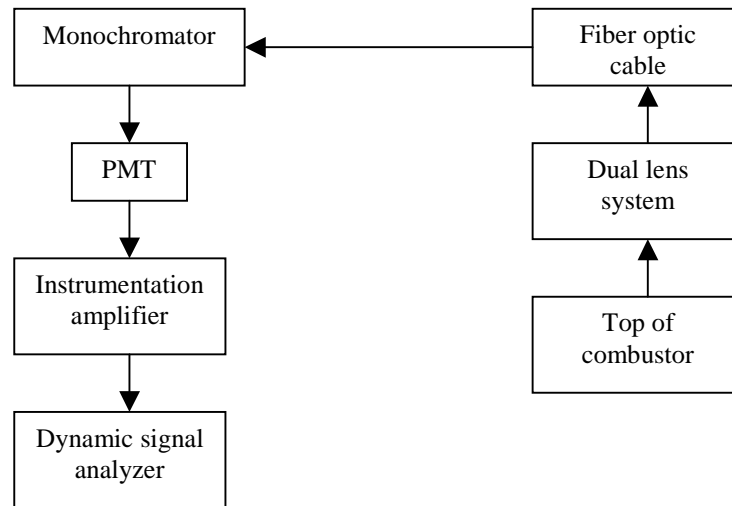


*Figure 3.7 Optical system setup for chemiluminescence measurements of light emitted from the flame in the tube combustor*

The two lenses were mounted in a lens holder held up by a structure on top of the tube combustor. They can be seen in Figure 3.8. The image of the light traveling through the lenses was minified onto a fiber optic cable which transmitted the light into a monochromator. The monochromator separated out a wavelength of 309.5 nm which is in the vicinity of one of the OH-radical wavelength peaks in the light emitted from the flame. The light was channeled into the photomultiplier tube which created a current proportional to the light intensity. The PMT signal was amplified in an instrumentation amplifier and analyzed in a dynamic signal analyzer.

The purpose of the chemiluminescence measurements was not to give an absolute measurement of the heat release rate. Therefore, the error is limited to how accurate the monochromator was in terms of wavelengths since a specific wavelength was examined. The monochromator has an accuracy in wavelength of  $\pm 1 \text{ \AA}$  for the centerline of the outlet slit.



Figure 3.8 Lenses and fiber optics setup on top of the tube combustor

### 3.6 Mass Flow Meters

Two Hastings Instruments HFM-200 mass flow meters, one for the air and the other for the methane, were utilized for measuring the incoming mass flows to the fuel-air mixer upstream of the tube combustor.

Air mass flow meter range: 0-25.000 Standard liters/minute.

Methane mass flow meter range: 0-1.5000 Standard liters/minute.

The accuracy specifications for the two mass flow meters were 1 % of full scale. With full scales as mentioned above, the accuracy would be  $\pm 0.25$  Standard liters/minute and  $\pm 0.015$  Standard liters/minute respectively. A drift in the zero setting of the air mass flow meter also occurred where the maximum drift caused an error of +0.25 Standard liters/minute. The standard state is defined as 0°C, and 760 torr.

### 3.7 Data Acquisition Equipment

Two data acquisition boards mounted in a PC Pentium 200 were used to acquire the fuel and air mass flows as well as the temperature data. The software utilized was LabView version 4 by National Instruments. Screen shots of the virtual instruments used in LabView are shown in Figures 3.9 and 3.10. The data acquisition boards used were DT2801-A for flow measurements and DT2805 for temperature measurements. Pressure measurement as well as chemiluminescence measurements were analyzed with a Hewlett Packard dynamic signal analyzer 35665A .

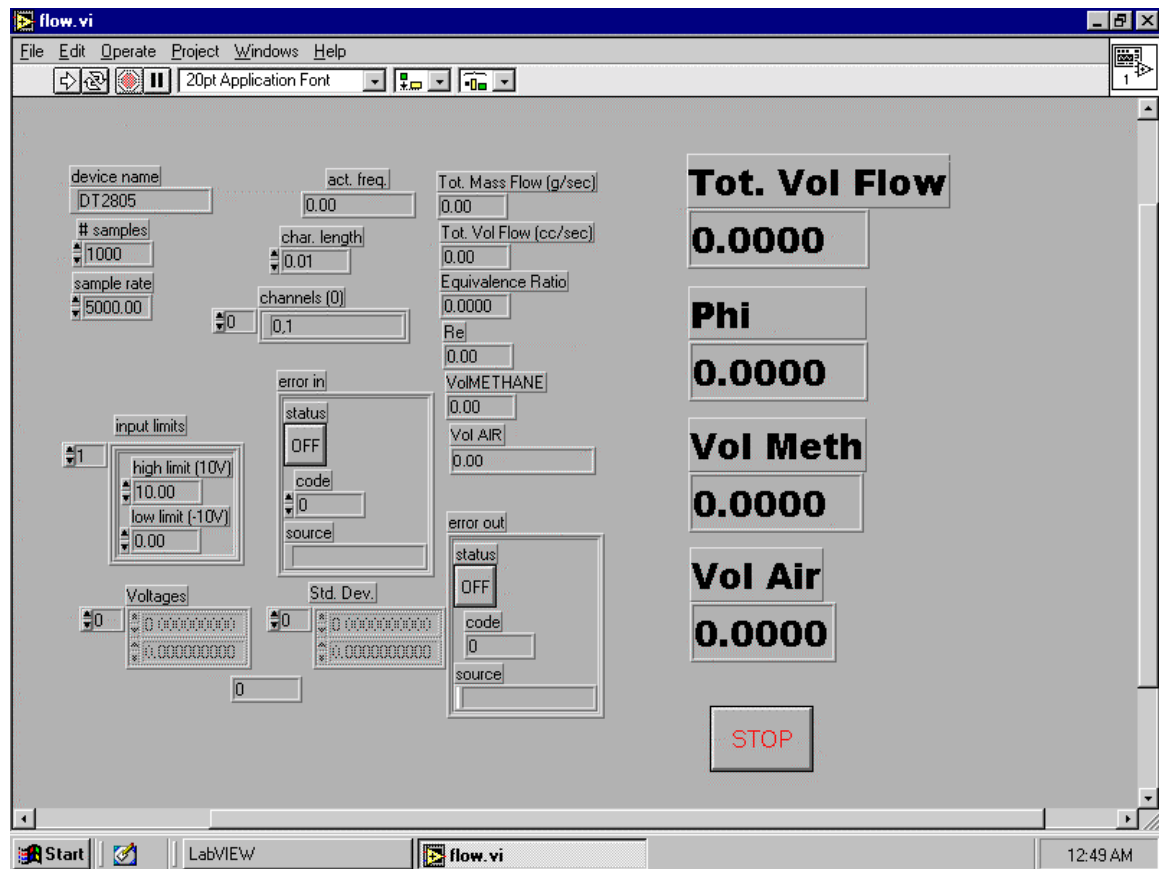


Figure 3.9 Front panel of the virtual instrument in LabView used for the flow data acquisition

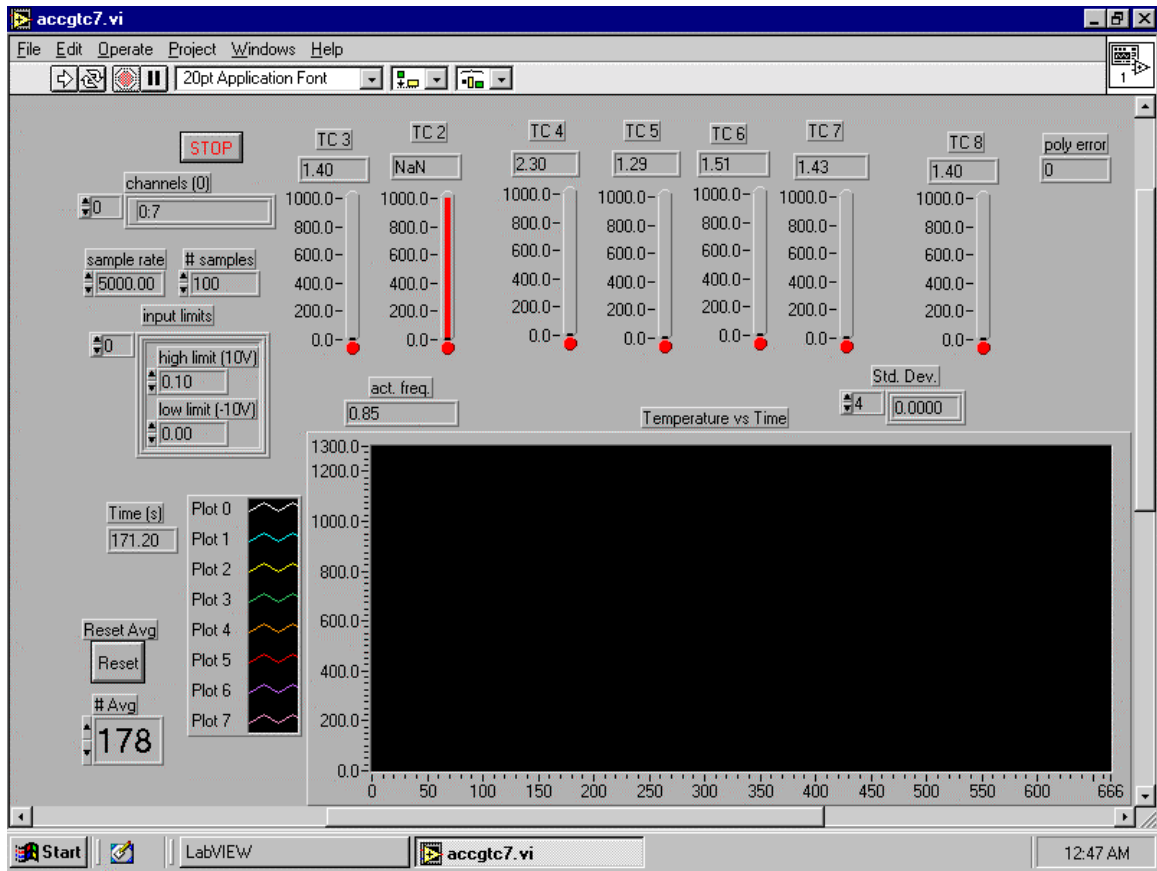


Figure 3.10 Front panel of the virtual instrument in LabView used for the temperature data acquisition

## **Chapter 4      Rijke-tube Thermoacoustic Characterization**

VACCG members have investigated a number of theories associated with the phenomena occurring in the tube combustor. The research presented in this chapter will, with the help of extensive experimental data, strengthen the suggested theories. The experiments conducted also serves as a database for the VACCG and the research community within this field. In addition the collected data can be helpful in the development of reduced-order modeling schemes that provide adequate prediction capabilities for the occurrence of thermoacoustic instabilities. The experimental investigation included a mapping of the tube combustor in terms of acoustic pressure, temperature distribution, and chemiluminescence for the whole operating range. Different regions in the pressure power spectrum and in the OH\*-spectrum (OH-radicals assumed proportional to the unsteady heat release rate) are analyzed, and the analysis includes a discussion of two different types of flame instabilities, namely pulsating and vibrating flames. In addition, temperature profiles and tube resonances are presented.

### **4.1    Acoustic Pressure**

The signature of the acoustic pressure exhibits useful information of the system and it can help to identify reduced-order schemes that provide adequate prediction capabilities for the occurrence and control of thermoacoustic instabilities. A typical pressure spectrum of the tube combustor can be seen in Figure 4.1, where the pressure is measured with the pressure transducer located at the closed end of the combustor.

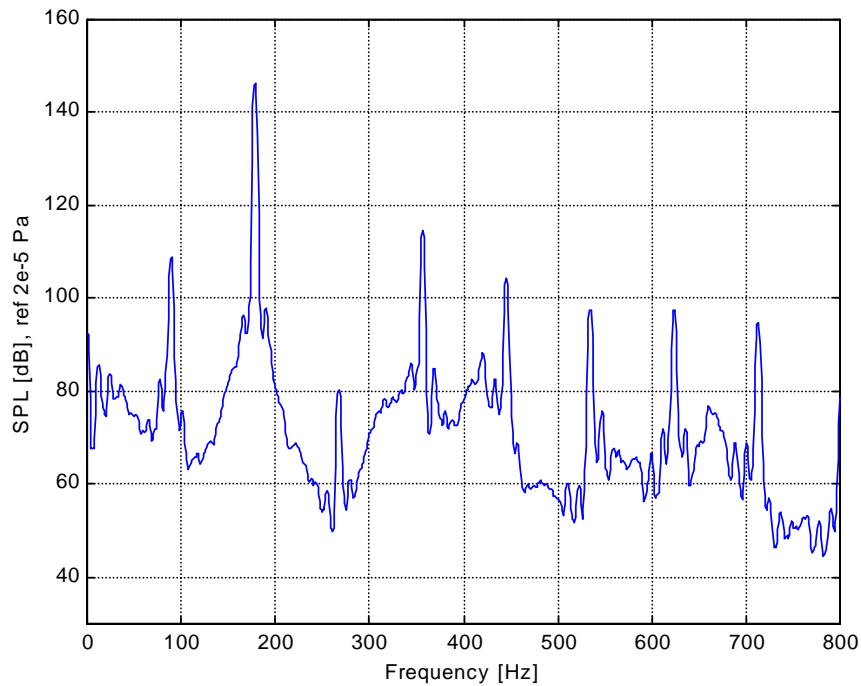


Figure 4.1 Power spectrum of pressure for  $\phi = 0.60$ ,  $Q_{tot} = 120$  cc/s

In the pressure spectrum several different regions can be distinguished:

1. At around 180 Hz a limit cycle oscillation can be seen. In this case the 2<sup>nd</sup> mode of the combustor goes unstable in agreement with the Rayleigh Criterion described in Chapter 2. Also, the harmonics of the limit cycle are visible in the spectrum.
2. A strong signal can be seen at half the limit cycle. The hypothesis is that an oscillation of the flame sheet occurs with double the period of the forcing function which in this case is a pulsation of the acceleration of the gas column surrounding the flame. This is caused by the limit cycle. The harmonics of this subharmonic frequency are also visible in the spectrum.
3. A low frequency peak, typically at 10-20 Hz, is visible in Figure 4.1. The hypothesis is that it is caused by a pulsating flame instability. This subsonic response also modulates the other peaks in the spectrum.

In the following text these different features will either be explained, or at least a hypothesis presented for the origin of these characteristics.

#### 4.1.1 Limit Cycle and Harmonics

In certain non-linear systems a self-excited oscillation, or a limit cycle occurs. Consider, for example, the following mass-spring-damper system:

$$m\ddot{x} - c(1 - x^2)\dot{x} + kx = 0$$

where  $m$  is the mass,  $c(1-x^2)$  the damping term, and  $k$  the stiffness term of the system. For small values of  $x$  the damping will be negative and will put energy in to the system, but for large values of  $x$  the damping will be positive and remove energy from the system. At some displacement amplitude  $|x|$  of the system, the system will reach a limit cycle due to this damping term.

For the tube combustor, the 2<sup>nd</sup> acoustic mode is excited and exhibits a limit cycle. That is in agreement with the Rayleigh Criterion. The second mode turns out to have a frequency around 180 Hz. In the power spectra, harmonics of the limit cycle are also visible. In the pressure power spectrum depicted in Figure 4.2, the limit cycle is marked out.

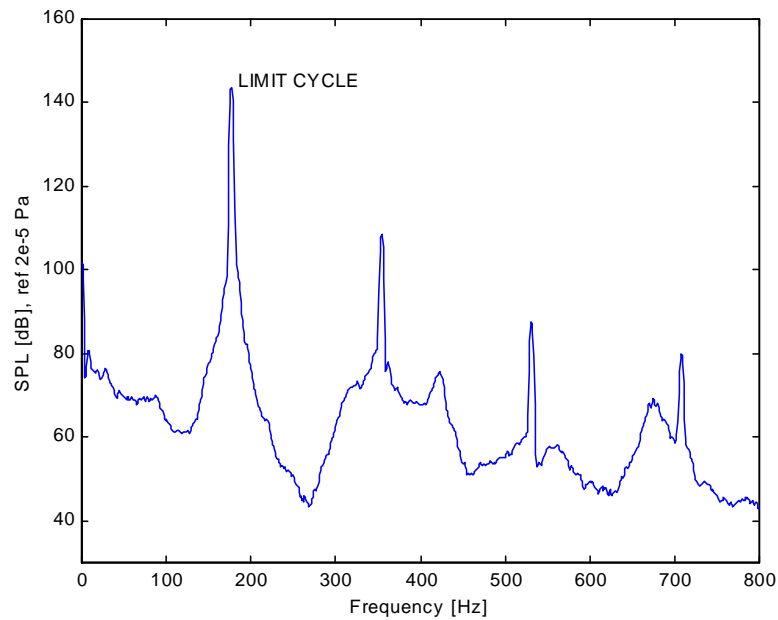


Figure 4.2 Pressure power spectrum of limit cycle for  $\phi = 0.50$ ,  $Q_{tot} = 160$  cc/s

### 4.1.2 Subharmonic Response

The hypothesis, described by Markstein (1964), assumes that the flame can be approximated as a membrane which exhibits oscillations. Markstein treated the flame as a membrane, and forced it with an oscillation of the acceleration of the gas column surrounding the flame. The differential equation that describes this situation is based on non-linear second-order dynamics:

$$(\varepsilon - 1)F_4'' + 2(1 + \kappa)F_4' + [2\kappa + (1 - \varepsilon^{-1})(\gamma\kappa^{-1} - 1)]F_4 = 0 \quad (31)$$

with  $F_4$  being the amplitude of the flame distortion,  $\varepsilon = \frac{\rho_{unburned}}{\rho_{burned}}$ ,  $\kappa$  a dimensionless wave number  $\kappa = KL$ , where  $K$  is the wave number and  $L$  a characteristic length.  $\gamma$  is a dimensionless acceleration  $\gamma(\tau) = \frac{L}{\varepsilon S_u} a(t)$ . Here  $S_u$  is the laminar flame speed and  $a(t)$  the variable acceleration.

When the following substitutions are made in Equation 31:

$$z = \frac{1}{2} \omega t = \frac{\omega \tau}{2K\varepsilon S_u}$$

$$e^{-\beta z} Y(z) = F_4'$$

where  $\beta = \frac{\kappa}{\Omega}(\kappa + 1)$ , with  $\Omega = \frac{1}{2}(1 + \varepsilon^{-1})\frac{\omega L}{S_u}$

the standard form of the Mathieu's equation results:

$$Y'' + (a - 2q \cos 2z)Y = 0 \quad (32)$$

where  $a = (\frac{\kappa}{\Omega})^2(2\varepsilon\kappa - \kappa^2 + \varepsilon^{-1} - \varepsilon - 1)$  and  $q = \kappa D$ . Here  $D = 2\frac{\varepsilon - 1}{\varepsilon + 1} \frac{d}{L}$ .

The solution of the Mathieu's equation can be written as:

$$Y(z) = C_1 e^{\mu z} \Phi(z) + C_2 e^{-\mu z} \Phi(-z) \quad (33)$$

where  $C_1$  and  $C_2$  are arbitrary constants and  $\Phi(z)$  is either of double the period of the forcing function or of the same period as the forcing function. Here  $\mu = \frac{L}{L_{th}}$ , where  $L_{th}$

is the thermal width of the flame front  $L_{th} = \frac{k}{c_p \rho_u S_u}$ , with  $k$  being the thermal conductivity and  $c_p$  the specific heat at constant pressure.

The solution dependence on the values of  $\mu$  and  $\Phi(z)$  leads to either a stable or unstable solution. If unstable, the function  $\Phi(z)$  will have either the same period as the forcing or double the period. In the case of the flame in the tube combustor, the solution ends up unstable in the region where the period has twice the period of the forcing. The forcing in this case is, as mentioned before, the pulsation of the acceleration of the gas column determined by the thermoacoustic limit cycle response. Double the period corresponds to half the frequency, which means the flame sheet would oscillate with a frequency half of the limit cycle frequency. When the flame sheet oscillates, the flame surface area changes, and since the heat release is proportional to the flame surface area the heat release rate will oscillate. In addition, as the flame oscillates, the heat loss to the flame stabilizer and the combustor walls changes which leads to a change in the net heat put into the gas. The change in heat release couples with the acoustic particle velocity and one can expect to see a subharmonic peak at half the limit cycle frequency in the pressure spectra as well as in the chemiluminescence spectra at a frequency around 90 Hz. A zoom around the subharmonic response can be seen in Figure 4.3.

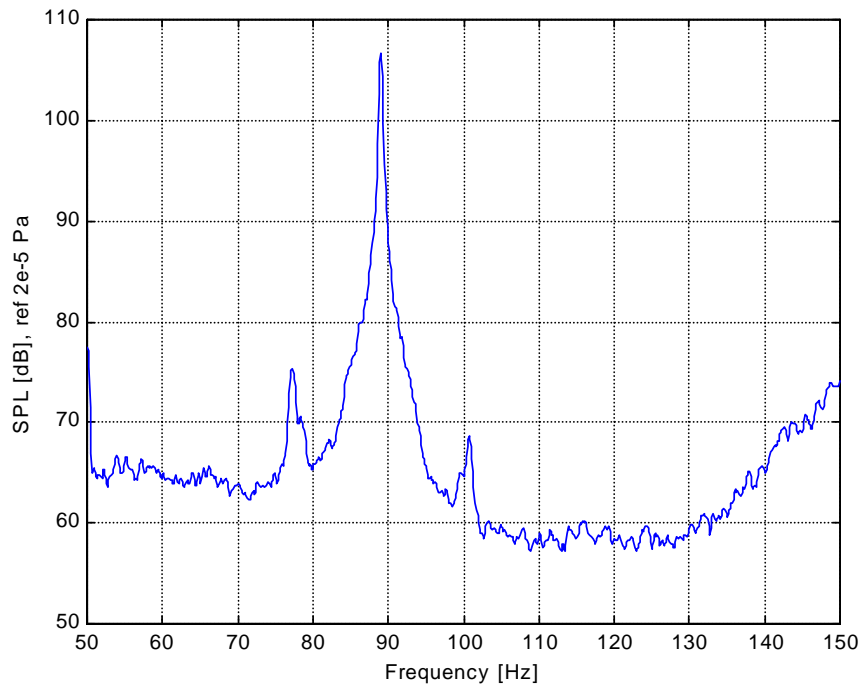


Figure 4.3 Zoom of pressure power spectrum of subharmonic response for  $\phi = 0.60$ ,  $Q_{tot} = 120$  cc/s

To determine if this feature in the tube combustor is the same as Markstein described, experiments were conducted to dampen the thermoacoustic instability of the 2<sup>nd</sup> acoustic mode or/and shift the TA instability in frequency and therefore also affect the subharmonic response in level or in frequency. All the pressure gages with the infinite lines were taken out except for the very bottom one (P1), where the pressure was measured. The thermocouples and the igniter were also removed and holes plugged up. To dampen out the second acoustic mode, refer to the pressure and velocity mode shapes, as seen in Figures 4.4 and 4.5. The locations of all the taps are marked out in the figures.

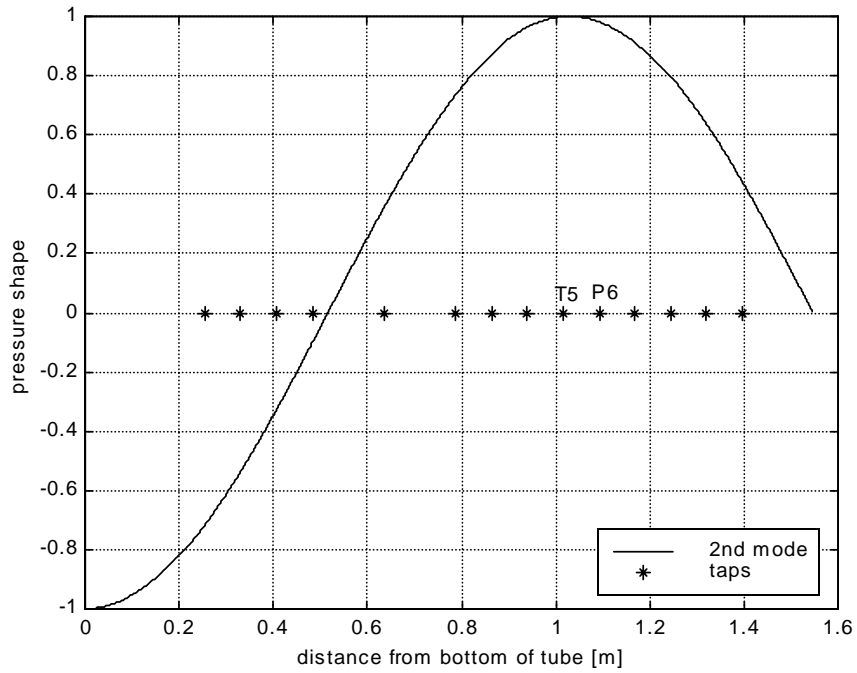


Figure 4.4 Pressure mode shape for 2<sup>nd</sup> mode with tap locations marked

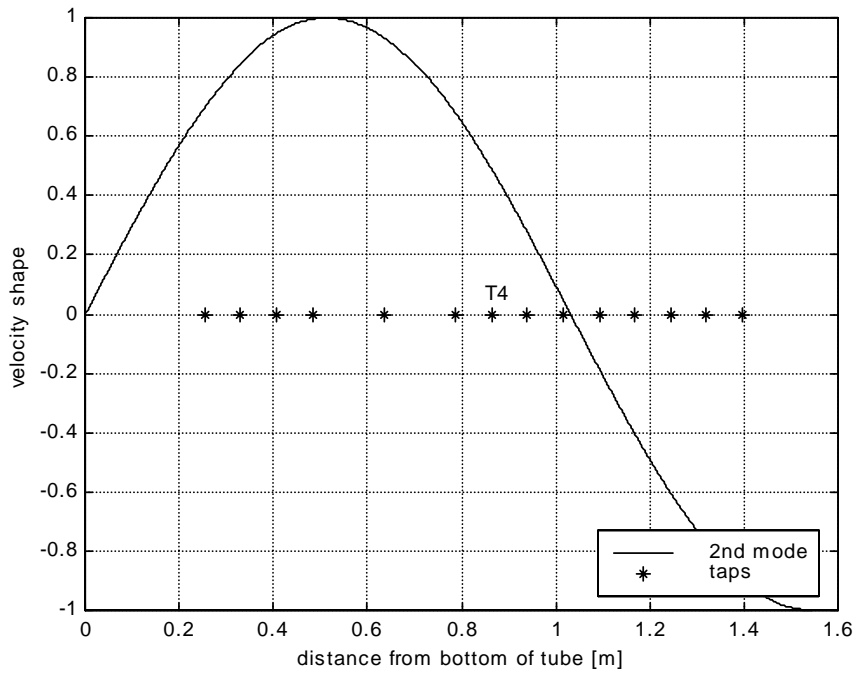


Figure 4.5 Velocity mode shape for 2<sup>nd</sup> mode with tap locations marked

At first all the holes, except for the very bottom one where the pressure was measured, were plugged up. As seen in Figure 4.6 the TA instability was then around 180 Hz and the subharmonic instability was clearly visible in the spectrum at 90 Hz (111dB).

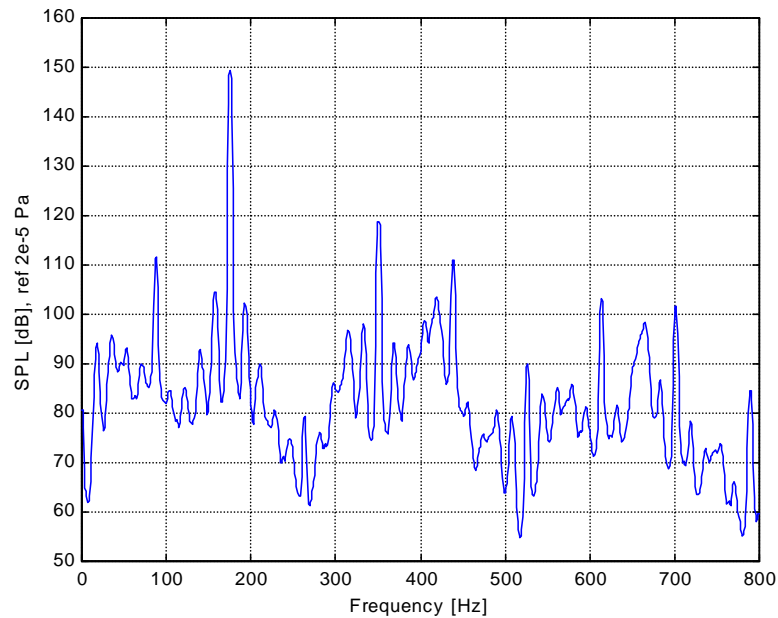


Figure 4.6 Pressure power spectrum with all holes, in tube combustor, plugged up

To affect the pressure shape and thereby dampen the second acoustic mode the tap at location P6 was taken out (refer to Figure 4.7 and Figure 3.1). The level of the limit cycle clearly went down about 10 dB, and the frequency shifted upwards to around 195 Hz. However, the subharmonic was still visible in the spectrum though. The increase in frequency implies that the hole acted as a spring to provide additional stiffness.

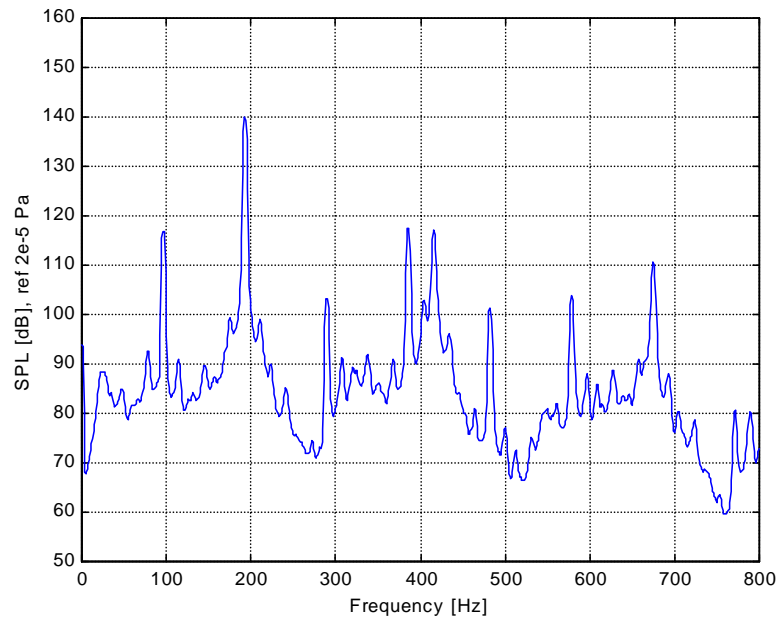


Figure 4.7 Pressure power spectrum with tap at location P6 taken out

To further dampen the mode, the tap at location T5 was taken out as well. With both the taps at P6 and T5 removed, the limit cycle level dropped an additional 10 dB and the frequency shifted to around 205 Hz. As can be seen in Figure 4.8 the subharmonic instability was no longer present in the pressure spectrum.

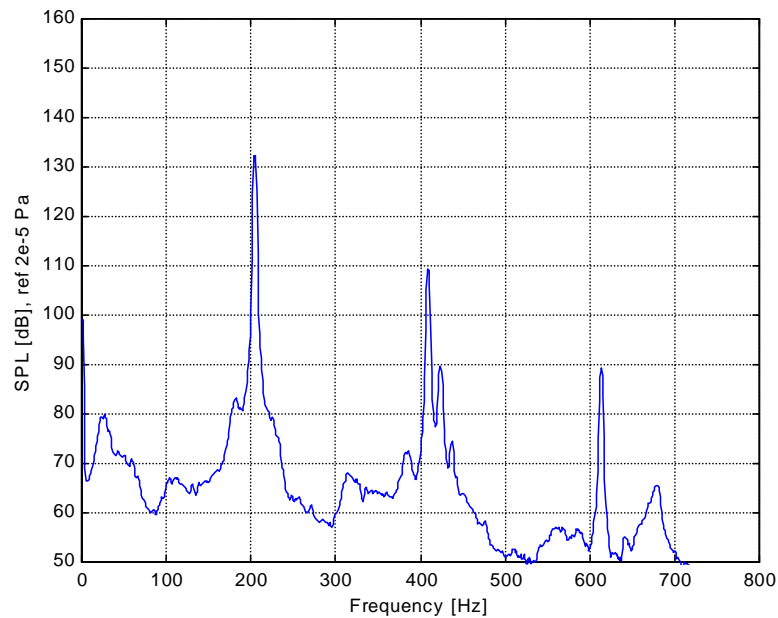
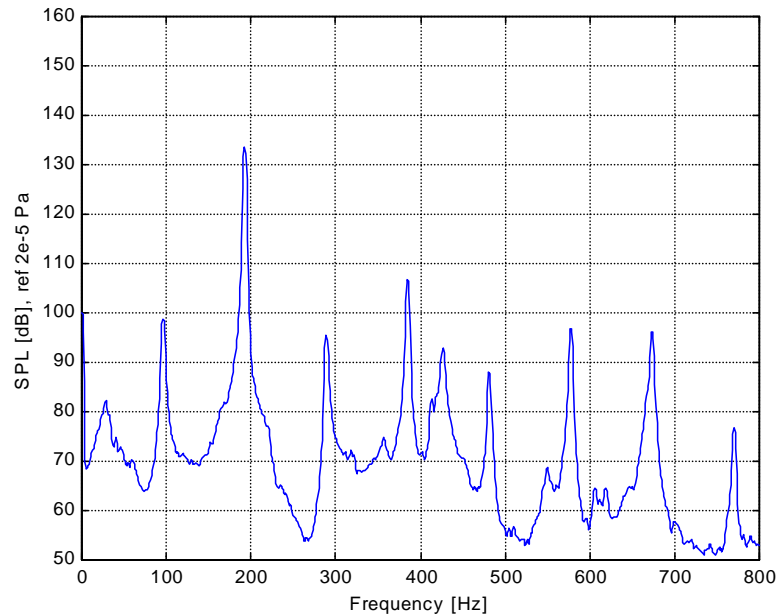


Figure 4.8 Pressure power spectrum with taps at location P6 and T5 taken out

The question is whether the subharmonic instability is mostly dependent on the limit cycle amplitude or the limit cycle frequency. If the instability is sensitive to the limit cycle frequency which affects the subharmonic frequency it would support the hypothesis that the flame sheet does exhibit mode shapes and has some preferred “resonance frequencies.” To get more information regarding that aspect, the tap at location T4 seen in Figures 4.9 and 3.1 was removed, while the taps at P6 and T5 were reinstalled. As seen in Figure 4.9 the level of the limit cycle is just about at the same level as in Figure 4.8, but the limit cycle frequency is lower. The subharmonic instability is not visible in Figure 4.8; however, it is clearly visible in Figure 4.9. This suggests that the flame sheet has in fact some preferred frequencies which then can be seen as resonances of the flame.



*Figure 4.9 Pressure power spectrum with tap at location T4 taken out*

The above discussion strengthens the hypothesis about flame sheet vibrations. Please note that all the above measurements were taken under the same conditions, namely at an equivalence ratio of 0.78 and a total flow of 118 cc/s.

It should also be noted that the level of the TA instability plays an important for the subharmonic instability. For a certain frequency of the limit cycle, there is a

‘threshold’ amplitude that the limit cycle must have to drive the subharmonic instability. The threshold amplitude changes in level depending on the frequency of the limit cycle, as discussed previously, where it was stated that the flame sheet seems to have some preferred frequencies.

Still, further proof of the existence of a vibrating flame is necessary. For this purpose, a bench-top burner was constructed to study the possibility of a flame sheet exhibiting mode shapes. The experimental setup, constructed by VACCG member Chris A. Fannin, is shown schematically in Figure 4.10. A speaker connected to a plenum with an injection port for reactants, in this case premixed methane-air, and a port for pressure measurements, was used. On the top of the plenum, a ceramic honeycomb was placed to stabilize the flame. Phase locked photographs with a CCD camera were taken of the flame sheet.

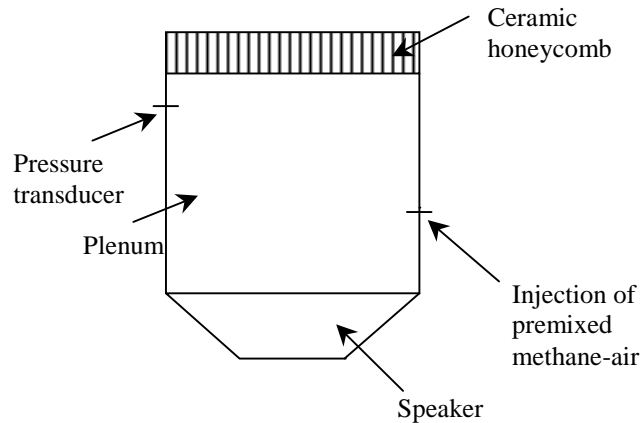


Figure 4.10 Bench-top burner for the study of flame sheet mode shapes

CCD camera images of two flame modes are shown in Figures 4.11 and 4.12. The lighter areas indicate higher flame intensity. The axisymmetric mode in Figure 4.11 shifted between being dark in the center and light in the center. The non-axisymmetric mode in Figure 4.12 shifted between one half lit up/one half dark and then reversed.

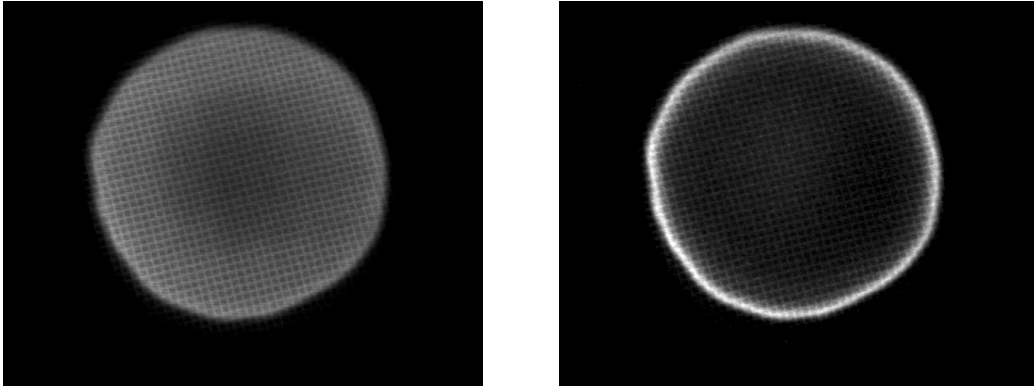


Figure 4.11 Axisymmetric flame mode

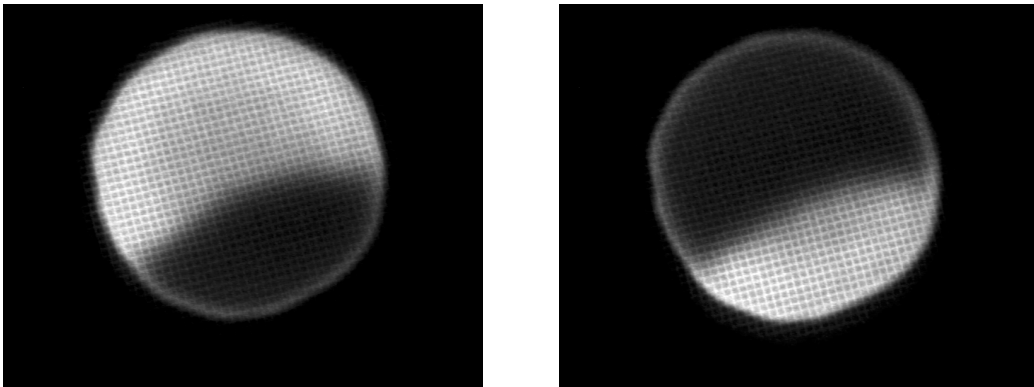


Figure 4.12 Non-axisymmetric flame mode

Even though the boundary conditions of the bench top burner were different from the tube combustor, the experiments further strengthen the hypothesis of flame sheet mode shapes and resonances for a burner-stabilized flame.

### 4.1.3 Subsonic Instability

The instability seen at a low frequency, 10-20 Hz, is likely to be a pulsating flame phenomenon which has been investigated by several researchers including Margolis (1980) and Buckmaster (1983).

The presentation below will follow an analysis described by Margolis (1980). When the flame sheet is close to the flame stabilizing ceramic honeycomb, heat losses to the honeycomb decrease the temperature of the flame and therefore the flame speed goes

down. The forced convection, which is the unburned mixture flowing downstream, pushes up the flame sheet further away from the flame holder. The heat loss to the stabilizer then decreases thereby causing the flame temperature to rise and thus the flame speed will increase. The flame speed will then overcome the forced convection, and the flame moves down towards the honeycomb again. With the flame moving down, the heat losses to the ceramic material will increase again, and the flame sheet will oscillate, typically at low frequencies in the subsonic region. This will cause the overall rate of heat release to the fluid to be oscillatory which will couple with the acoustic pressure field.

The problem formulation is as follows:

Assumptions:

- The flow is assumed isobaric for the mean pressure, one-dimensional, and free of body forces and radiative heat losses.
- A multi-component Fick's law describes species diffusion.
- The only hydrodynamic effect is assumed to be the thermal expansion of the fluid.
- $\rho\lambda$ ,  $\rho^2 D_k$ , and  $c_{p,k}=c_p$  are all constants, where  $\rho$  is the incoming density of the fluid,  $\lambda$  the thermal conductivity,  $D_k$  the diffusion coefficient and  $c_{p,k}$  the specific heat of species  $k$ .

Conservation of mass of species  $k$ :

$$\frac{\partial Y_k}{\partial t} + m_0 \frac{\partial Y_k}{\partial \psi} = \rho^2 D_k \frac{\partial^2 Y_k}{\partial \psi^2} - \rho^{-1} R_k M_k \quad k = 1, 2, 3, \dots, N-1$$

Here  $Y_k$  is the mass fraction of species  $k$ ,  $m_0$  the incoming mass flux per unit area,  $\rho$  the incoming density of the fluid,  $D_k$  the diffusion coefficient,  $R_k$  the rate of chemical production, and  $M_k$  the molecular weight. The spatial coordinate is transferred to a mass coordinate:

$$\psi(x, t) = \int_0^x \rho(\bar{x}, t) d\bar{x}$$

Energy equation in terms of the temperature:

$$\frac{\partial T}{\partial t} + m_0 \frac{\partial T}{\partial \psi} = \frac{\rho \lambda}{c_p} \frac{\partial^2 T}{\partial \psi^2} + (\rho c_p)^{-1} \sum_{k=1}^{N-1} R_k M_k (h_k^0 - h_n^0)$$

Here  $T$  is the temperature of the fluid and  $h_k^0$  the enthalpy of formation for species  $k$ . With the appropriate initial conditions and the boundary conditions stated below for the two differential equations, the problem is specified.

$$T(\psi = 0, t) = T_u$$

$$Y_k - \frac{\rho^2 D_k}{m_0} \frac{\partial Y_k}{\partial \psi} \Big|_{\psi=0} = \varepsilon_k \quad k = 1, 2, 3, \dots, N-1$$

$$T, Y_1, \dots, Y_{N-1} \text{ bounded at } \psi = \infty$$

Here  $\varepsilon_k$  is the mass fraction of species  $k$  before combustion. For an analysis of the above stated problem, refer to Margolis (1980). His results show that a steady-state adiabatic flame is likely to be stable for typical parameter values. However, for incoming flow velocities sufficiently less than the adiabatic flame speed, the unstable region in his solution becomes feasible for many flames.

In the tube combustor the frequencies for this pulsating flame instability typically ranges from 10 to 20 Hz. A tendency of an increase in amplitude and frequency is visible for an increase in equivalence ratio. Shown in Figure 4.13 is a “zoom” on the frequency range around the pulsating instability and the tendency of the pulsating frequency to increase with equivalence ratio can be seen.

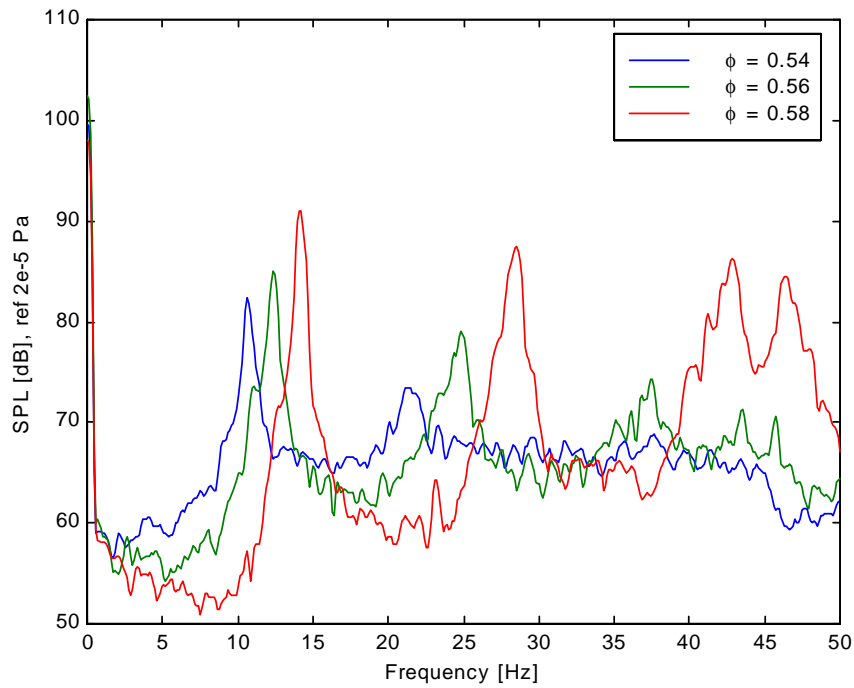


Figure 4.13 Pressure power spectrum of pulsating flame instability

The subsonic response of the flame was also observed to cause an amplitude modulation of the limit cycle, the subharmonic response, and the harmonics of them as is visualized in Figure 4.14 where three amplitude modulations (AM) are marked. The data was taken at an equivalence ratio of 0.70 and a total flow of 100 cc/s.

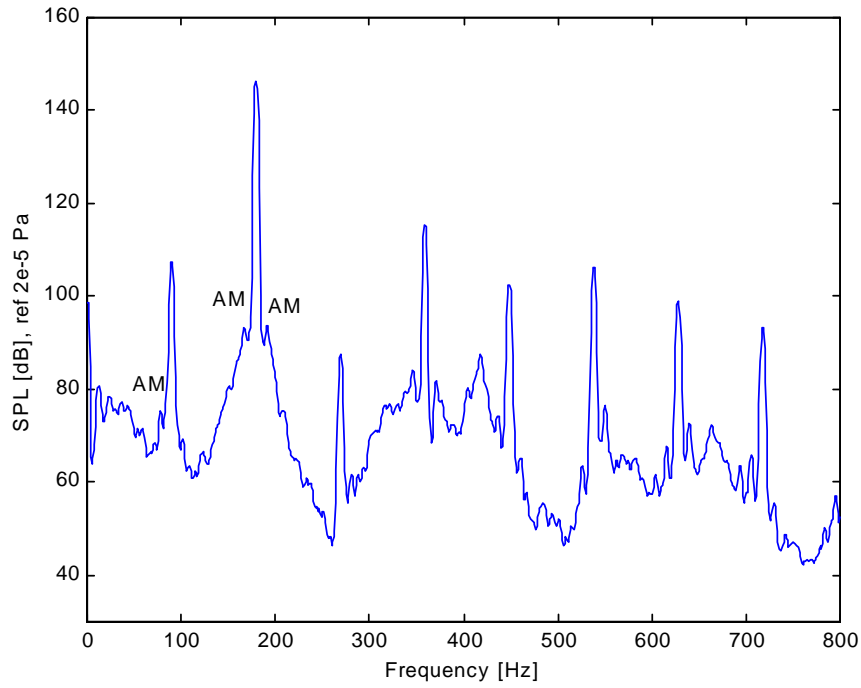


Figure 4.14 Pressure power spectrum with amplitude modulation

The mathematical description of the modulation is the multiplication of a time function  $f(t)$  by a periodic function  $\cos(\omega_0 t)$ . This causes a translation in the frequency domain according to the convolution:

$$\mathfrak{F}\{f(t)\cos(\omega_0 t)\} = \int_{-\infty}^{\infty} f(t) \frac{e^{i\omega_0 t} + e^{-i\omega_0 t}}{2} e^{-i\omega t} dt$$

or

$$f(t)\cos(\omega_0 t) \Leftrightarrow \frac{1}{2}F(\omega - \omega_0) + \frac{1}{2}F(\omega + \omega_0)$$

or

$$f(t)\cos(\omega_0 t) \Leftrightarrow \frac{1}{2}F(f - f_0) + \frac{1}{2}F(f + f_0)$$

For the tube combustor, the modulation signal is the pulsating instability and the modulated signals are the limit cycle, the subharmonic response, and their harmonics.

The data strengthens the pulsating instability theory for several reasons:

- The frequency range observed in the tube combustor is in the same range as described in the theory.
- The increase in equivalence ratio increases the frequency of the instability in the tube combustor. This is also suggested in Margolis theory since an increase in the equivalence ratio increases the flame temperature which, in turn, means higher flame speed. The higher flame speed would overcome the forced convection quicker and thus the frequency would increase.

## 4.2 Chemiluminescence Measurements

The optical system, described in Chapter 3, detects light emitted from the flame. Radicals that get excited by the chemical reaction emit light when moving from their excited energy state to their ground state. In the present study, light at a wavelength of 309.5 nm, which is in the vicinity of one of the peaks for the light emitted from excited OH-molecules, was acquired. The lens system minified the flame image onto the optical fiber which then channeled the light into the monochromator. The monochromator separated the wavelengths onto a photomultiplier which yielded a current proportional to the light intensity and was transferred to an instrumentation amplifier.

However, there were some difficulties related to these measurements. The noise level sometimes buried some of the peaks in the spectra. The noise was due to the randomness in the chemical reaction, the dark noise of the PMT, obstruction of the lens view (thermocouples blocking the light emitted from the flame), and other possible effects. The signal to noise ratio was improved with the removal of the thermocouples that blocked some of the light emitted from the flame and with the increase in aperture of the fiber optic cable. A typical spectrum is shown in Figure 4.15.

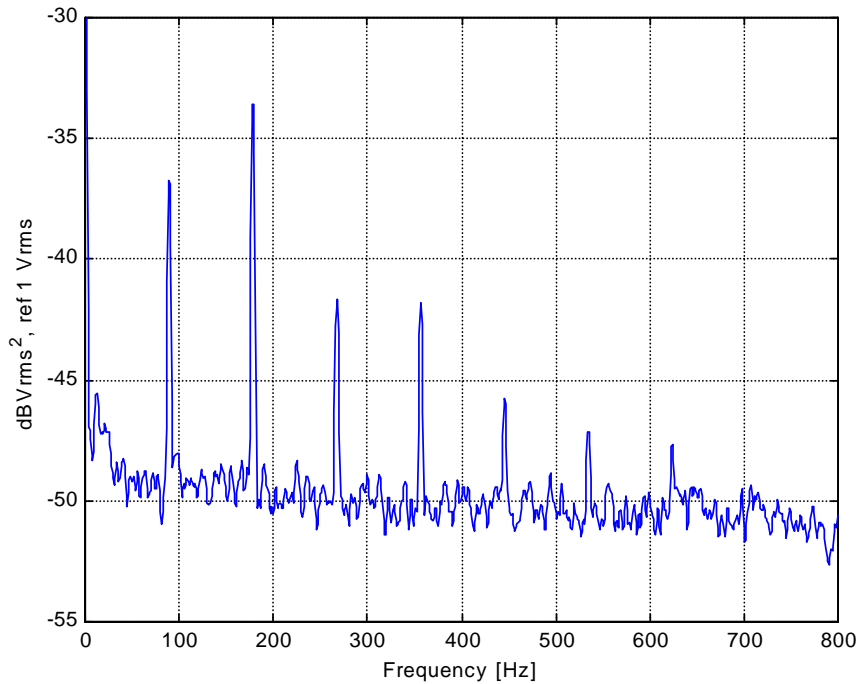


Figure 4.15 Power spectrum of the PMT signal for  $\phi = 0.60$ ,  $Q = 120$  cc/s

Refer to Section 4.6 for further analysis of the chemiluminescence data.

### 4.3 Comparison of Pressure and Chemiluminescence Spectra

To compare the  $\text{OH}^*$  spectrum with the pressure spectrum, the two spectra are shown in the same graph in Figure 4.16. The pressure power spectrum and the chemiluminescence power spectrum are very similar. The peaks of the spectra are virtually at the same frequencies with the exception that some peaks of the  $\text{OH}^*$  spectrum get buried in the noise, as mentioned in Section 4.2. The pulsating instability and oscillating flame sheet phenomena are generally more visible in the chemiluminescence spectrum. This makes sense since both these phenomena directly affect the heat release rate from the flame sheet.

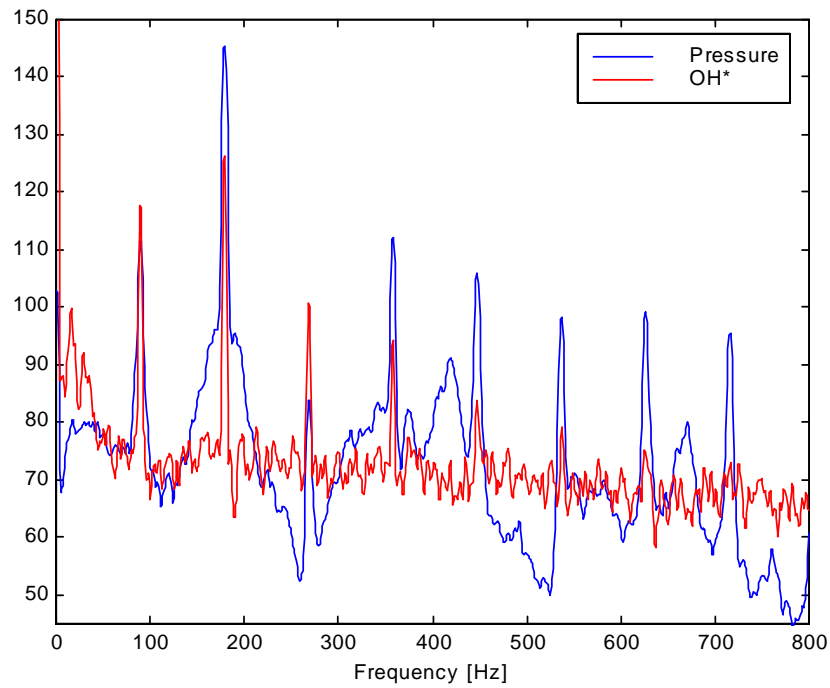


Figure 4.16 Overlapped pressure and  $OH^*$  power spectra

#### 4.4 Axial Temperature Profiles

To investigate how the axial temperature profile affects the thermoacoustic instabilities and to get the temperature distribution for the Finite Element Analysis, the axial temperatures were measured at seven different locations, as seen in Figure 3.1 in Chapter 3. As expected there is a big jump in temperature at the flame location. The temperatures upstream of the flame holder were marginally affected by changes in settings such as changes in equivalence ratio and/or flow rate, whereas the temperatures downstream of the flame holder were affected significantly more. A typical axial temperature profile is shown in Figure 4.17.

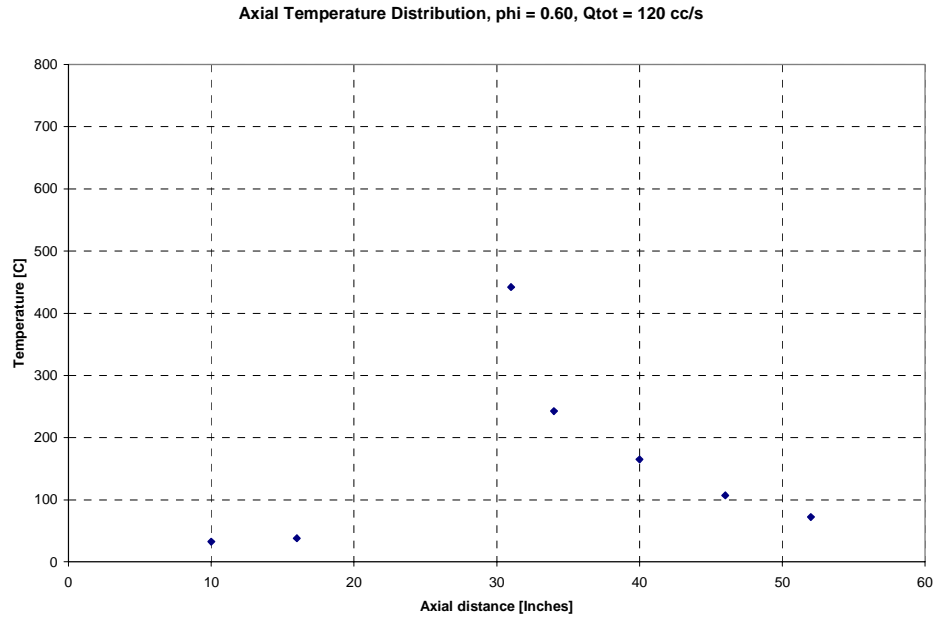
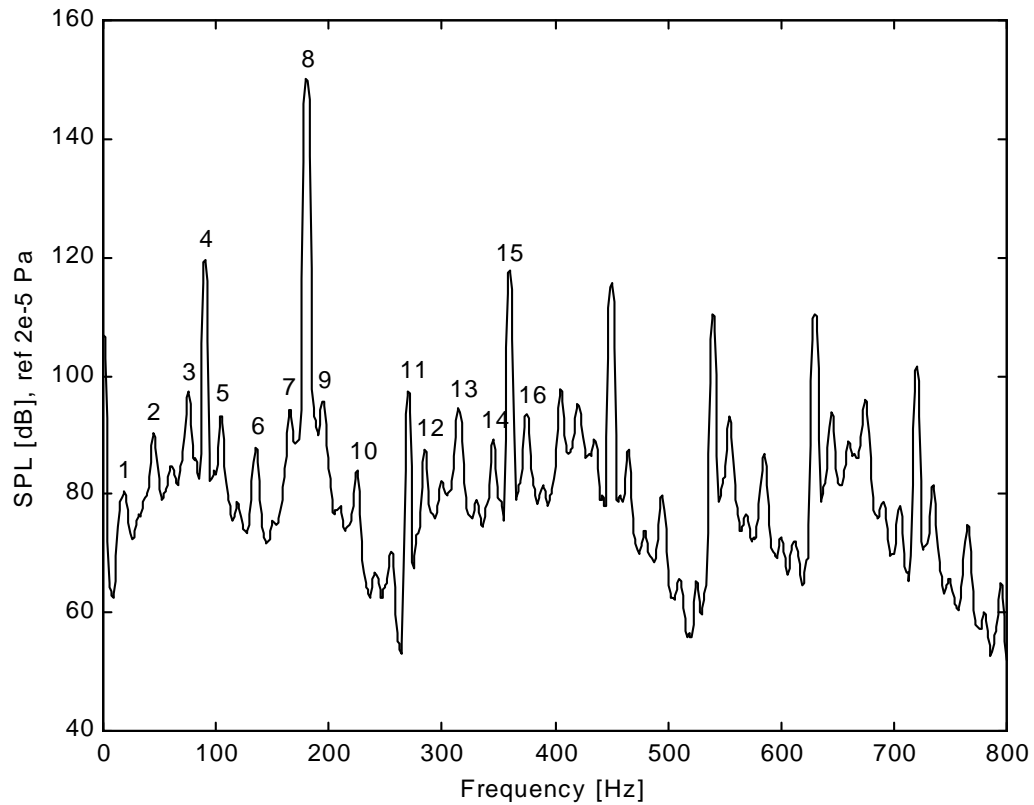


Figure 4.17 Axial temperature profile for  $\phi = 0.60$ ,  $Q = 120$  cc/s

Refer to Section 4.6 for further analysis of the temperature data.

## 4.5 The Operational Characteristics of the Tube Combustor

As concluded in the previous sections there are three important phenomena that affect the acoustic pressure in the tube combustor: the thermoacoustic instability that causes the 2<sup>nd</sup> mode to go unstable; the oscillating flame sheet which appears as a subharmonic; and a pulsating flame instability at around 10-20 Hz. Figure 4.18 is a description of the total picture including a table with descriptions of the different peaks in the spectrum. The data were taken at an equivalence ratio of 0.65 and a total flow of 120 cc/s.



Peak - Description	Peak - Description	Peak - Description
1 - pulsating instability	7 - lower AM	13 - $7f_{LC}/4$
2 - $f_{LC}/4$	8 - $f_{LC}$ , TA instability	14 - lower AM
3 - lower AM	9 - upper AM	15 - $2f_{LC}$ , $4f_{LC}/2$ , $8f_{LC}/4$
4 - subharmonic, $f_{LC}/2$ , $2f_{LC}/4$	10 - $5f_{LC}/4$	16 - upper AM
5 - upper AM	11 - $3f_{LC}/2$ , $6f_{LC}/4$	
6 - $3f_{LC}/4$	12 - upper AM	

\* $f_{LC}$  is the limit cycle frequency. AM stands for amplitude modulation. TA stands for thermoacoustic.

Figure 4.18 The total picture including peak description

## 4.6 Extensive Mapping of the Operating Region

The fluctuating pressure, chemiluminescence, and temperatures were measured for a number of settings, in terms of equivalence ratio and total flow rate. The mapping was made to provide information about how changes in settings affect the pressure and OH\* power spectra. In addition, an extensive mapping like this can provide helpful information for anyone who would like to model a closed-open duct with, for example, CFD. In Figure 4.19, a graph of all the settings used is shown.

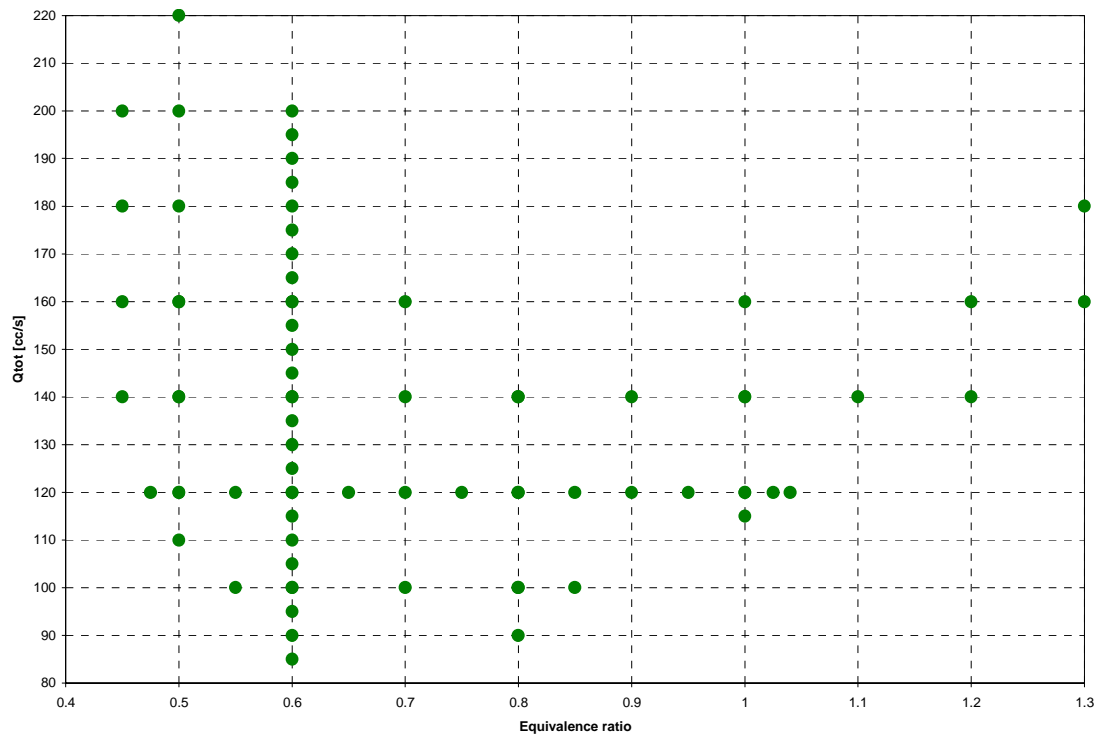


Figure 4.19 Tube combustor test settings

The mapping was made with one parameter held constant while varying the other, i.e., holding equivalence ratio constant and varying the total flow rate or vice versa. Typical tendencies, when increasing either equivalence ratio or flow rate (and thereby increasing the total heat released), can be seen in Figures 4.20, 4.21, and 4.22.

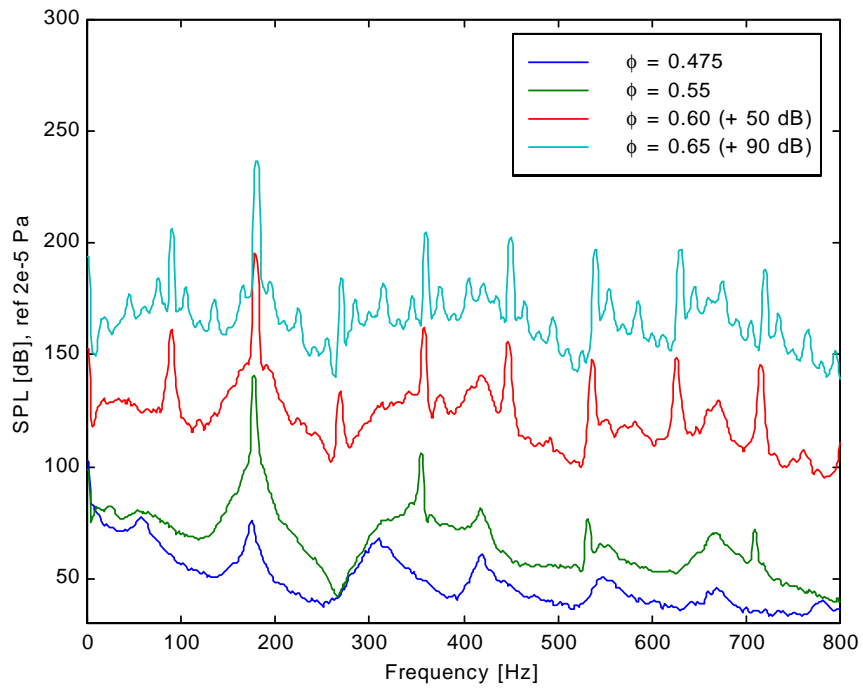


Figure 4.20 Effect of an increase in equivalence ratio on the pressure

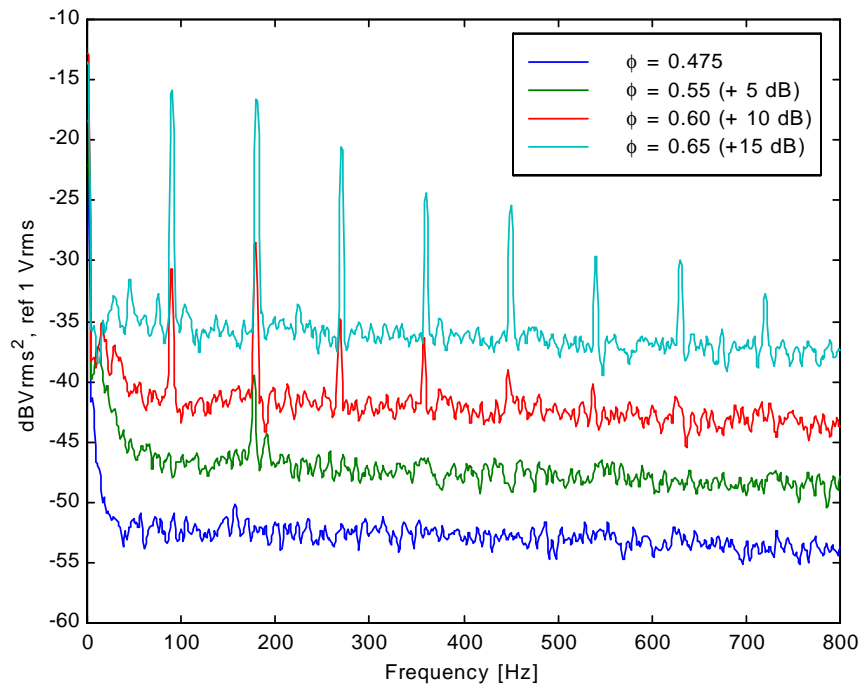


Figure 4.21 Effect of an increase in equivalence ratio on the  $\text{OH}^*$ -measurements

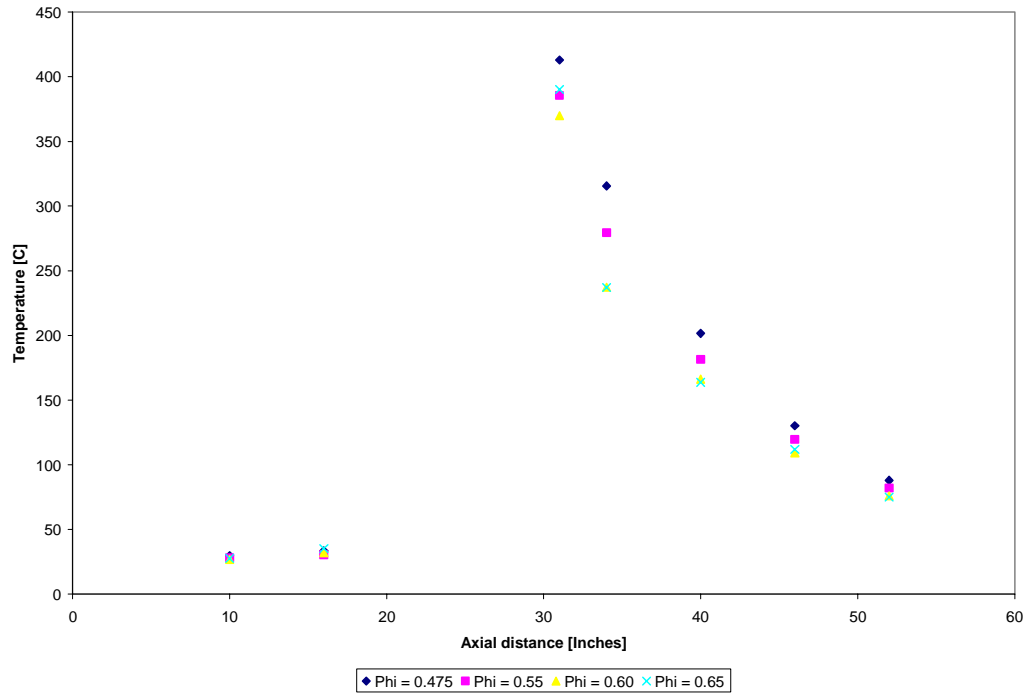


Figure 4.22 Effect of an increase in equivalence ratio on the axial temperature profile

Note that the some of the spectra in Figures 4.20 and 4.21 have been shifted vertically for display purposes. As can be seen in Figure 4.20, for the lowest setting the heat release is not quite enough to overcome the damping in the tube and to cause a thermoacoustic instability. Instead we are seeing the tube resonances with the 1<sup>st</sup> mode around 55 Hz, the 2<sup>nd</sup> around 175 Hz, and higher modes at higher frequencies. With a slight increase in equivalence ratio, and therefore an increase in the heat released, the instability appears, reaches a limit cycle, and as mentioned before it is the 2<sup>nd</sup> acoustic mode that goes unstable. Also visible are the harmonics of the limit cycle. At yet a higher equivalence ratio, the subharmonic response appears in the spectrum, as well as harmonics of it. At an even higher equivalence ratio, the pulsating instability is somewhat visible, and one can see that it modulates the other peaks. The tendency is the same in Figure 4.21. At the lowest setting there are no peaks visible because the thermoacoustic instability is not present. With an increase in the equivalence ratio, the TA instability appears, and is followed by the subharmonic response, the pulsating instability, and their harmonics for yet higher settings. It is hard to draw any conclusions from the temperature profiles shown in Figure 4.22. The variations are very small and do

not show any consistency. A better trend of the temperature variations can be seen in Figure 4.23 and are described in the next paragraph.

The temperature at the T3 location, which can be seen in Figure 4.23, goes up because of the higher heat release rate and because the flame sheet is thicker at higher flow rates. The T3 thermocouple would therefore be closer to the top of the flame sheet. As seen in Figures 4.24 and 4.25, the pressure and OH\* limit cycle amplitudes goes up with a higher flow rate, and this is expected since a higher flow rate means more fuel is burned in the flame thus more heat being released. The higher heat release rate means more energy is available to be fed into the acoustics. At low flow rates the subharmonic response is not visible in the spectrum. This can be seen in the amplitude plots in Figures 4.26 and 4.27 where the levels are very low at flow rates below 120 cc/s. The amplitude of the subharmonic response reaches a maximum at a flow rate of approximately 160 cc/s. This is further evidence of a vibrating flame phenomenon with preferred flame sheet frequencies. The frequency of the main instability (around 180 Hz) varies with heat release rate which then leads to a variation of the subharmonic frequency. If the flame sheet had some preferred frequencies, a behavior as seen in Figures 4.26 and 4.27 would be expected.

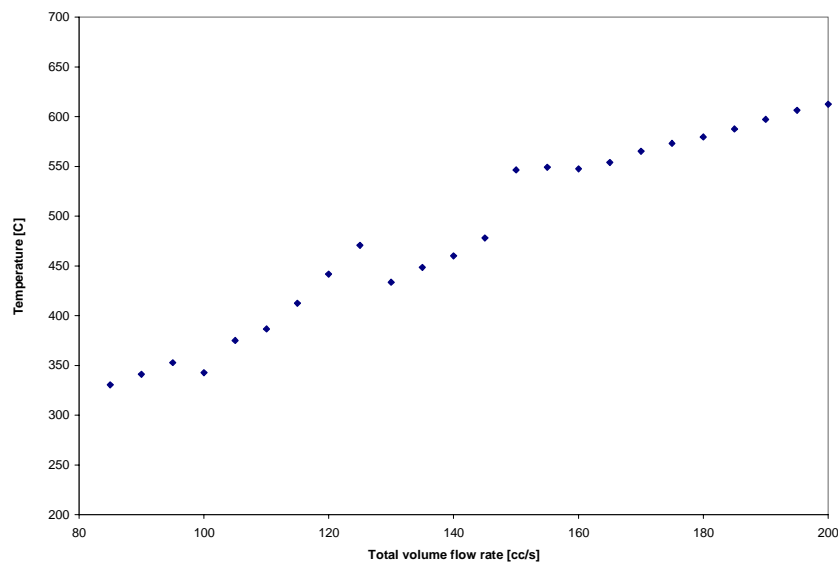


Figure 4.23 Variation of temperature T3 with flow rate

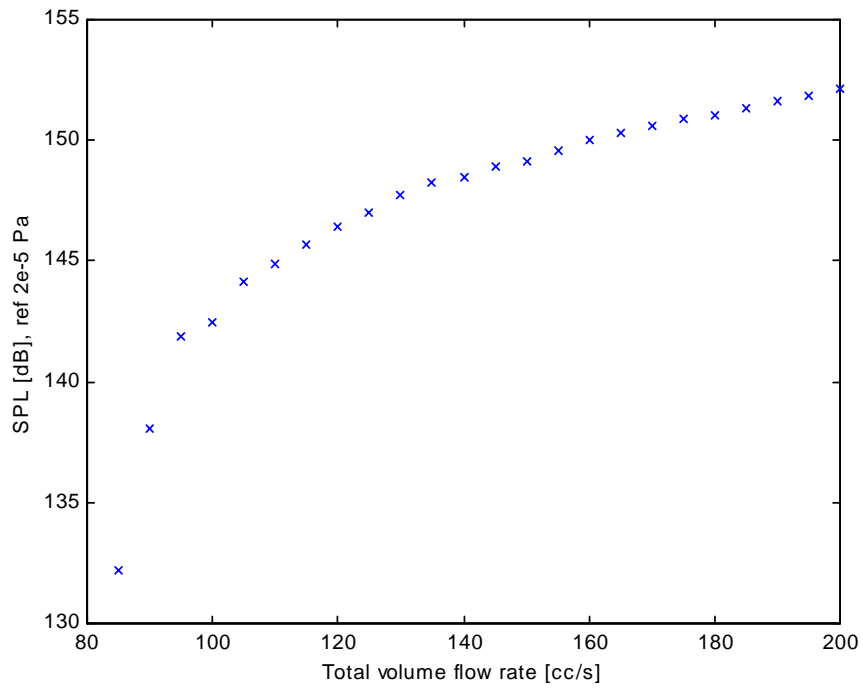


Figure 4.24 Variation of pressure limit cycle amplitude with flow rate

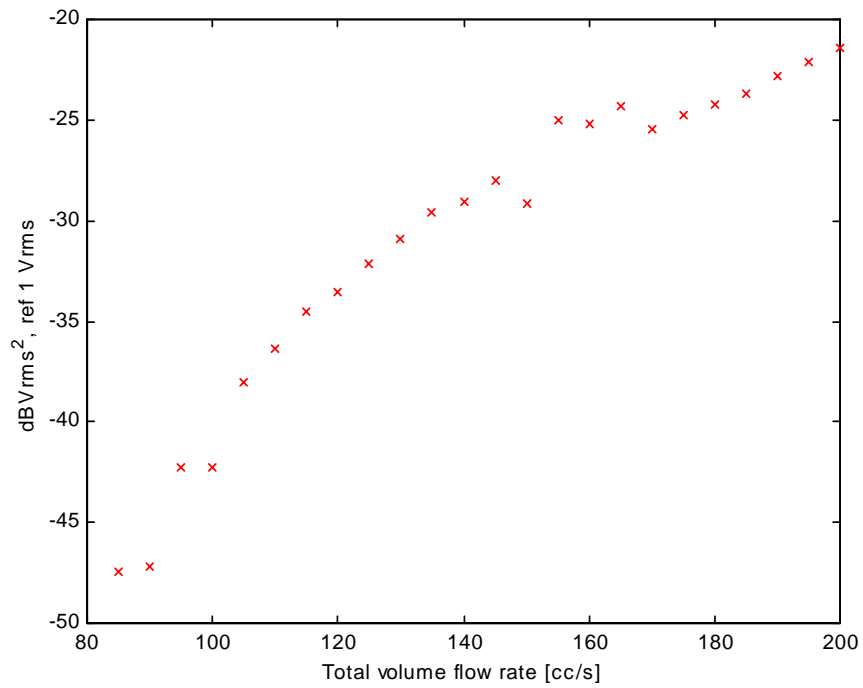


Figure 4.25 Variation of OH\* limit cycle amplitude with flow rate

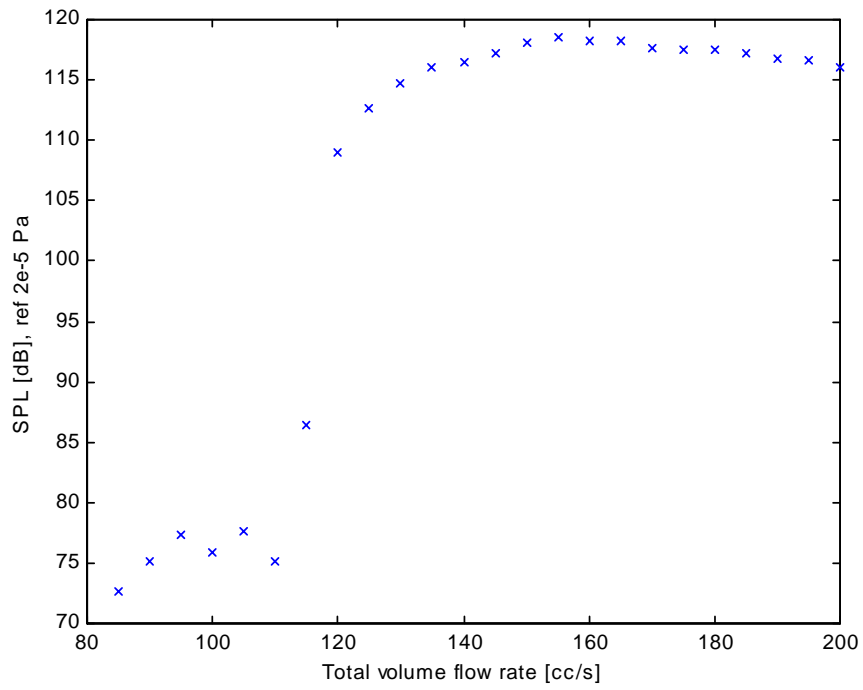


Figure 4.26 Variation of pressure subharmonic amplitude with flow rate

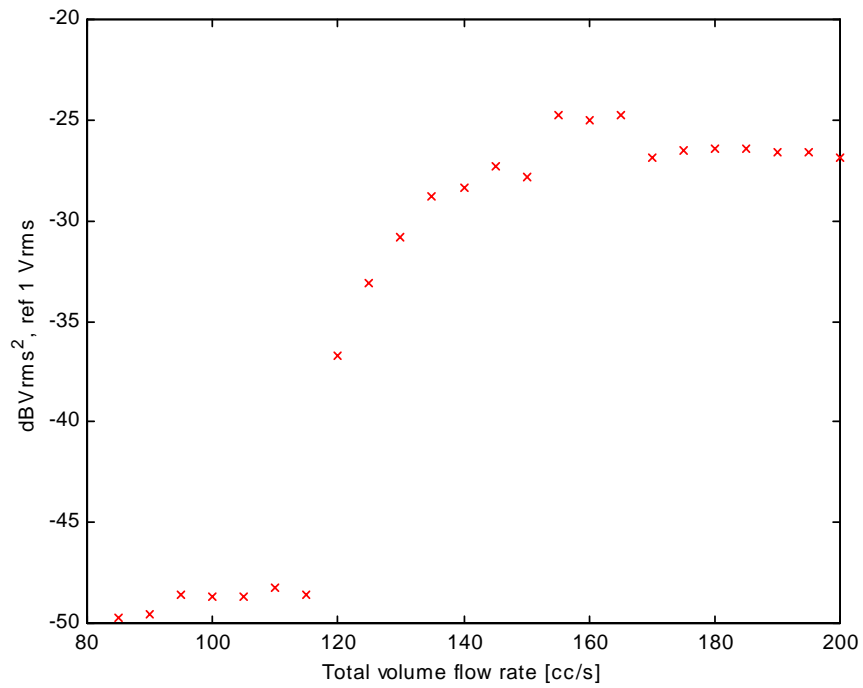


Figure 4.27 Variation of  $OH^*$  subharmonic amplitude with flow rate

## 4.7 Database on the World Wide Web

To provide an accessible database for researchers interested in either comparing data, in terms of pressure power spectra, OH\* power spectra, and axial temperature distribution, or to compare analysis results such as CFD analysis, to data from a Rijke-type tube combustor, the data has been made available on the WWW. It is possible to download the data at:

<http://www.combustion.me.vt.edu>

## 4.8 Resonance Frequencies

The acoustic resonances of the tube combustor have been measured and calculated. The calculations were made with the wave equation (cold case, i.e., at room temperature, as described in Chapter 2) and with a first generation finite element method (FEM) code which sees the tube as a beam (cold case and hot, i.e., at elevated temperature when combustion is taken place, case). The cold case measurements were performed by exciting the tube with random noise through a speaker and measuring the pressure. The hot case measurements were at a low enough setting, in terms of equivalence ratio and total flow rate, before the thermoacoustic instability had appeared as seen in Figure 4.28.

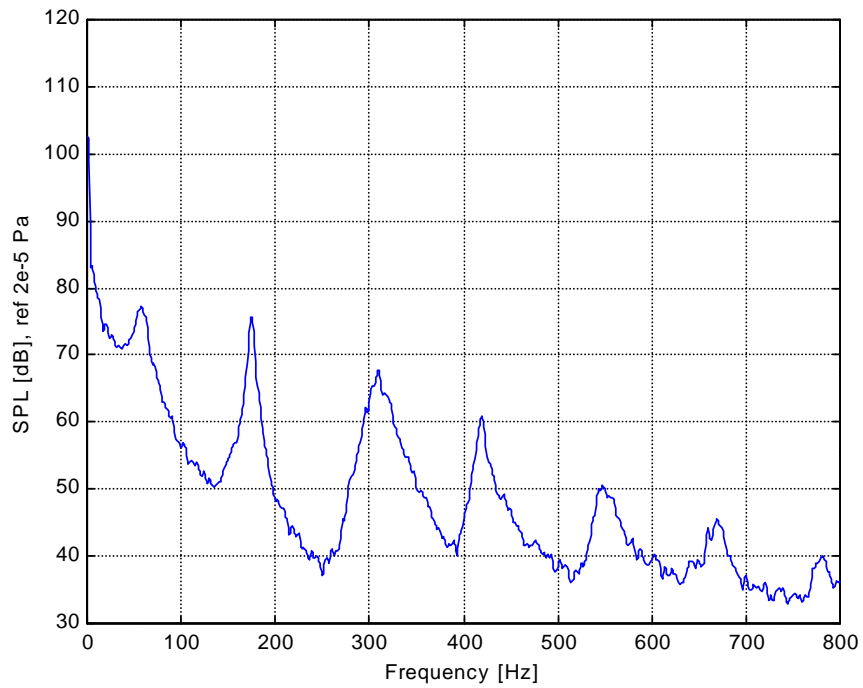


Figure 4.28 Tube combustor resonances,  $\phi = 0.475$ ,  $Q_{tot} = 120$  cc/s

A listing of all the cases examined is given in Table 4.1.

Table 4.1 Resonance frequencies of tube combustor

Mode	Cold tube measurements [Hz]	Cold tube FEM [Hz]	Cold tube wave equation [Hz]	Hot tube measurements [Hz]	Hot tube FEM [Hz]
1	55	55	55	58	64
2	159	166	166	175	179
3	272	277	277	310	319
4	380	388	388	419	428
5	494	499	499	548	568
6	594	610	610	670	677
7	713	722	721	780	816

As can be seen in Table 4.1, the cold and hot case calculations generally show a higher frequency for each mode than the measurements do (note that for the hot case

calculations uncorrected temperatures were used, as discussed in Chapter 3). An investigation of the cause of the differences was initiated. All the pressure gages were removed, except for one located in the very bottom of the combustor at location P1, as seen in Figure 3.1 in Chapter 3. Also, all the thermocouples were removed as well as the optics system on top of the tube. The speaker, which excited the tube with fixed sine waves at chosen frequencies, was mounted at locations P4, T6, and P2 respectively in the tube combustor (refer to Figure 3.1 in Chapter 3). The results are shown in Table 4.2.

*Table 4.2 Resonance frequencies of tube combustor without pressure transducers, thermocouples and optics system*

<b>Mode</b>	<b>Speaker at P4 location Frequency [Hz]</b>	<b>Speaker at T6 location Frequency [Hz]</b>	<b>Speaker at P2 location Frequency [Hz]</b>
1	*	54	*
2	161	165	163
3	277	276	273
4	380	378	378
5	495	494	496
6	595	595	595
7	714	713	715

\* A single frequency was hard to determine. The resonance was spanned over a range of frequencies.

From a comparison of the data in Table 4.1, it can be seen that the results are slightly closer to the calculated values, but still there is a relatively big difference between measurements and calculations in forms of the wave equation and the FEM code. Also worth noting is that the speaker clearly interacts with the tube combustor which can be because the frequencies shift depending on where the speaker is mounted.

The flame holder in the tube combustor was present in all the above measurements. To investigate the role of the flame holder it was taken out of the combustor. The speaker was, as in the previous measurements, mounted at different locations and the tube was excited with frequency fixed sine waves. The results of these measurements are presented in Table 4.3.

Table 4.3 Resonance frequencies of tube combustor without pressure transducers, thermocouples, optics system and flame holder

Mode	Speaker at P4 location Frequency [Hz]	Speaker at T6 location Frequency [Hz]	Speaker at P2 location Frequency [Hz]
1	*	55	*
2	165	168	166
3	278	277	275
4	386	385	386
5	497	496	497
6	607	606	606
7	714	*	720

\* A single frequency was hard to determine. The resonance was spanned over a range of frequencies.

The frequencies are closer to the calculated frequencies than before. The calculations are now within  $\pm 1\%$  of the measurements.

A frequency response of the speaker with plenum was also taken to get further knowledge about the tube combustor – speaker interaction. The amplitude and the phase of the frequency response is shown in Figure 4.29.

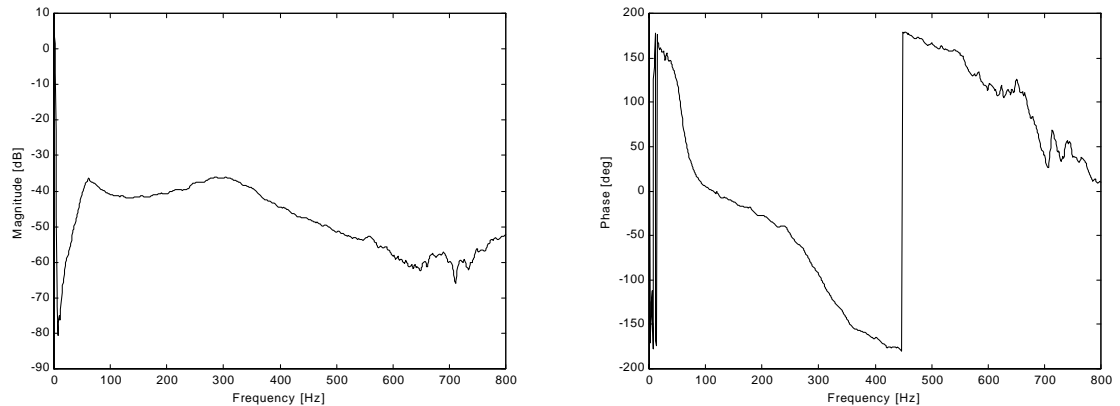


Figure 4.29 Frequency response of speaker including plenum

The speaker plenum exhibited resonances at around 60 Hz and 300 Hz as demonstrated by the magnitude plot as a peak and in the phase plot as a 180 degrees phase shift. There is also a resonance at a higher frequency, although not well-defined.

The plenum resonances do have an effect on the tube resonances, and are especially obvious around the 60 Hz area. When the speaker is mounted in locations P2 and P4, the 1<sup>st</sup> tube resonance gets blurred out. This is possibly due to the speaker plenum's resonance in the vicinity of 60 Hz.

## Chapter 5      Conclusions and Future Work

### 5.1 Conclusions

All the phenomena that affect the acoustic pressure in a Rijke-type tube combustor have been experimentally examined in this thesis. In correspondence with previous research in this area, the Rayleigh Criterion could be verified and proved valid for the tube combustor in the study. As predicted by theory, the 2<sup>nd</sup> acoustic mode became excited with a flame mid-span in a closed-open tube. In addition to thermoacoustic instabilities caused in accordance with the Rayleigh Criterion, several other phenomena were observed. With the aid of extensive experimental results, a vibrating flame and a pulsating flame occurrence have been identified.

All the experimental data collected during this work support the suggested theories for a vibrating flame as well as a pulsating flame instability. The vibrating flame occurrence is an oscillating behavior of the flame sheet anchored on the flame-stabilizing honeycomb in the tube combustor. The flame exhibits mode shapes, as proven by a bench-top experiment and supported by a variety of experiments with the tube combustor itself. The flame sheet has preferred frequencies for the mentioned oscillation. In the Rijke-type tube, the flame sheet is unstable at a frequency of half the forcing function. The forcing function was, in the case of the tube combustor, the main thermoacoustic instability in accordance with the Rayleigh Criterion.

The pulsating instability is based on heat losses to the flame stabilizer in conjunction with changes in flame speed caused by the heat losses. When the flame sheet is close to the ceramic honeycomb, the heat losses to the honeycomb decrease the flame temperature which in turn causes a decrease in the flame speed. The forced convection, which is the unburned mixture flowing downstream, forces the flame sheet upwards in the tube which then leads to a change in the heat released to the gas from the flame. When the heat losses to the honeycomb decrease, due to the increased distance, the flame temperature and therefore the flame speed increases and overcomes the forced convection. The flame sheet will then move back towards the honeycomb and the scenario will repeat. The changes in the heat release to the fluid will couple with the

acoustics and a peak will show up in the acoustic pressure spectrum. The pulsating instability of the tube combustor is at a low frequency in the subsonic region. The above mentioned phenomena were also visible in the chemiluminescence spectrum of the tube combustor.

To summarize, there are three phenomena evident from the acoustic pressure and the chemiluminescence measurements of the tube combustor:

- The main thermoacoustic instability, in accordance with the Rayleigh Criterion, causing the 2<sup>nd</sup> acoustic mode of the tube to become unstable.
- The vibrating flame instability with flame mode shapes oscillating with a frequency of half the thermoacoustic instability.
- The pulsating flame instability with an, in the axial direction of the tube combustor, oscillation caused by the heat losses to the flame stabilizing honeycomb, typically in the subsonic frequency region.

Extensive data was taken of the whole operating region of the tube combustor in order to analyze the above described phenomena and to provide a database accessible over the Internet for researchers interested in comparing experimental data to theoretical calculations.

## 5.2 Future Work

While this work was in progress, several researchers in the VACCG conducted experiments and analyses related to the tube combustor. Much work was focused upon control issues and analytical models of the combustor and its phenomena. The compilation of data and analyses presented in this thesis should be attempted for a 3-D combustor where the acoustics is more complicated and fluid dynamics plays a more vital part. The instabilities described may also occur in 3-D systems and the understanding of them would be important in attempting to control the instabilities and in predicting instability frequencies and amplitude levels. The last step would be to investigate a full-scale gas turbine combustor used in power plants all over the world. By understanding the phenomena occurring in a simple tube combustor the likelihood of understanding them in a full-scale gas turbine combustor is much greater. In order to be able to

successfully control the instabilities occurring in a combustor, an understanding of the physical occurrences is very important.

Typically, gas turbines are dual fuel machines which means they run both on gaseous fuel (usually natural gas) and liquid fuel (usually fuel oil). It is therefore important to investigate the thermoacoustic problem also for liquid fuel. This document only investigated the gas fuel problem which is different from the liquid fuel problem where such things as fuel atomization, fuel vaporization, and related phenomena occur.

According to Vivek Khanna, member of the VACCG, the correction procedure of temperatures collected by thermocouples in Rijke-type combustors should be investigated. The initial correction procedure for the temperature data collected for this thesis work is not sufficient for these types of combustors. This investigation would be important for future temperature corrections in Rijke-type combustors and related devices.

It would also be beneficial to create a CFD model of the tube combustor system to compare the experimental results with the calculated results.

## References

- Bailey, J. J., "A Type of Flame-Excited Oscillation in a Tube," *Journal of Applied Mechanics*, vol. 24 (1957), pp. 333-339.
- Baillet, F., D. Durox, and R. Prud'homme, "Experimental and Theoretical Study of a Premixed Vibrating Flame," *Combustion and Flame*, vol. 88 (1992), pp. 149-168.
- Blackshear, P. L., Jr., "Driving Standing Waves by Heat Addition," *Fourth Symposium (International) on Combustion*, pp. 553-566 (1953).
- Bloxside, G. J., A. P. Dowling, and P. J. Langhorne, "Reheat Buzz: An Acoustically Coupled Combustion Instability. Part 2. Theory," *The Journal of Fluid Mechanics*, vol. 193 (1988), pp. 445-473.
- Buckmaster, J., "Stability of the Porous Plug Burner Flame," *SIAM Journal of Applied Mathematics*, vol. 43 (1983), pp. 1335-1349.
- Cho, S., J. Kim, and S. Lee, "Characteristics of Thermoacoustic Oscillation in a Ducted Flame Burner," *AIAA paper 98-0473* (1998).
- Clavin, P., and P. Garcia, "The Influence of the Temperature Dependence of Diffusivities on the Dynamics of Flame Fronts," *Journal de Mécanique Théorique et Appliquée*, vol. 2 (1983), pp. 245-263.
- Culick, F. E. C., "Combustion Instabilities in Propulsion Systems," *Combustion Instabilities Driven by Thermoacoustic Sources, NCA* vol. 4 (1989) pp. 33-52.
- Diederichsen, J., and R. D. Gould, "Combustion Instability: Radiation from Premixed Flames of Variable Burning Velocity," *Combustion and Flame*, vol. 9 (1965), pp. 25-31.

Durox, D., F. Baillot, G. Searby, and L. Boyer, "On the Shape of Flames Under Strong Acoustic Forcing: A Mean Flow Controlled by an Oscillating Flow," *Journal of Fluid Mechanics*, vol. 350 (1997), pp. 295-310.

Durox, D., S. Ducruix, and F. Baillot, "Strong Acoustic Forcing on Conical Premixed Flames," *Twenty-Seventh Symposium (International) on Combustion* (1998), pp. 883-889.

Feldman, K. T., Jr., "Review of the Literature on Rijke Thermoacoustic Phenomena," *Journal of Sound and Vibration*, vol. 7 (1968), pp. 83-89.

Gaydon, A. G., *The Spectroscopy of Flames*, 2<sup>nd</sup> edition (London: Chapman and Hall, 1974).

Grove, D. E., L. Nord, W. R. Saunders, L. Haber, U. Vandsburger, and C. A. Fannin, "Tube Combustor Temperature Acquisition System," *VACCG Technical Brief* (1998).

Haber, L. C., "An Investigation Into the Origin, Measurement and Application of Chemiluminescent Light Emissions from Premixed Flames," *Master's Thesis, Virginia Polytechnic Institute and State University* (2000).

Hibshman, J. R., "An Experimental Study of Soot Formation in Dual Mode Laminar Wolfhard-Parker Flames," *Master's Thesis, Virginia Polytechnic Institute and State University* (1999).

Joos, F., and D. Vortmeyer, "Self-Excited Oscillations in Combustion Chambers with Premixed Flames and Several Frequencies," *Combustion and Flame*, vol. 65 (1986), pp. 253-262.

Kinsler, L. E., A. R. Frey, A. B. Coppens, and J. V. Sanders, *Fundamentals of Acoustics*, 3<sup>rd</sup> edition (New York: John Wiley & Sons, 1982).

Langhorne, P. J., "Reheat Buzz: An Acoustically Coupled Combustion Instability. Part 1. Experiment," *The Journal of Fluid Mechanics*, vol. 193 (1988), pp. 417-443.

Margolis, S. B., "Bifurcation Phenomena in Burner-Stabilized Premixed Flames," *Combustion Science and Technology*, vol. 22 (1980), pp. 143-169.

Markstein, G. H., *Nonsteady Flame Propagation* (New York: Macmillan, 1964).

Mawardi, O. K., "Aero-Thermoacoustics, the Generation of Sound by Turbulence and by Heat Processes," *Reports of Progress in Physics*, vol. 19 (1956), pp. 156-187.

McIntosh, A. C., and J. F. Clarke, "Second Order Theory of Unsteady Burner-Anchored Flames With Arbitrary Lewis Number," *Combustion Science and Technology*, vol. 38 (1984), pp. 161-196.

McIntosh, A. C., "The Effect of Upstream Acoustic Forcing and Feedback on the Stability and Resonance Behaviour of Anchored Flames," *Combustion Science and Technology*, vol. 49 (1986), pp. 143-167.

McIntosh, A. C., "Combustion-Acoustic Interaction of a Flat Flame Burner System Enclosed Within an Open Tube," *Combustion Science and Technology*, vol. 54 (1987), pp. 217-236.

McIntosh, A. C., "Short Communication On Flame Resonances in Tubes," *Combustion Science and Technology*, vol. 69 (1990), pp. 147-152.

McManus, K. R., T Poinsot, and S. M. Candel, "A Review of Active Control of Combustion Instabilities," *Progress in Energy and Combustion Science*, vol. 19 (1993), pp. 1-29.

Pelce, P., and P. Clavin, "Influence of Hydrodynamics and Diffusion upon the Stability Limits of Laminar Premixed Flames," *Journal of Fluid Mechanics*, vol. 124 (1982), pp. 219-237.

Putnam, A. A., and W. R. Dennis, "Study of Burner Oscillations of the Organ-Pipe Type," *Transactions of the ASME*, vol. 75 (1953), pp. 15-28.

Putnam, A. A., and W. R. Dennis, "Burner Oscillations of the Gauze-Tone Type," *The Journal of the Acoustical Society of America*, vol. 26 (1954), pp. 716-725.

Putnam, A. A., and W. R. Dennis, "Survey of Organ-Pipe Oscillations in Combustion Systems," *The Journal of the Acoustical Society of America*, vol. 28 (1956), pp. 246-259.

Putnam, A. A., *Combustion-Driven Oscillations in Industry* (New York: American Elsevier Publishing Company, 1971).

Raun, R. L., M. W. Beckstead, J. C. Finlinson, and K. P. Brooks, "A Review of Rijke Tubes, Rijke Burners and Related Devices," *Progress in Energy and Combustion Science*, vol. 19 (1993), pp. 313-364.

Rayleigh, Lord, "The Explanation of Certain Acoustical Phenomena," *Nature*, vol. 18 (1878), pp. 319-321.

Rayleigh, Lord, *The Theory of Sound*, vol. II, 2<sup>nd</sup> edition (London: Macmillan, 1926).

Richards, J. S., W. R. Saunders, C. A. Fannin, and L. Nord, "Calibration of the SLP004D Pressure Transducer for Use in the Tube Combustor," *VACCG Technical Brief* (1998).

Rijke, P. L., "Notice of a New Method of Causing a Vibration of the Air Contained in a Tube Open at Both Ends," *Philosophical Magazine*, vol. 17 (1859), pp. 419-422.

Searby, G., and P. Clavin, "Weakly Turbulent, Wrinkled Flames in Premixed Gases," *Combustion Science and Technology*, vol. 46 (1986), pp. 167-193.

Searby, G., and D. Rochwerger, "A Parametric Acoustic Instability in Premixed Flames," *Journal of Fluid Mechanics*, vol. 231 (1991), pp. 529-543.

Van Harten, A., A. K. Kapila, and B. J. Matkowsky, "Acoustic Coupling of Flames," *SIAM Journal of Applied Mathematics*, vol. 43, no. 5 (October 1984), pp. 982-995.

## **Appendix A      Pressure Power Spectra for Constant Equivalence Ratio**

In Appendix A, power spectra of the pressure measurements from the extensive mapping experiments will be presented. The equivalence ratio was held constant with varying flow rate for each data series. First the 0.50-equivalence ratio series will be presented, followed by  $\phi = 0.60$ , 0.80 and 1.00 respectively. All sound pressure levels have a reference pressure of  $2e-5$  Pa.

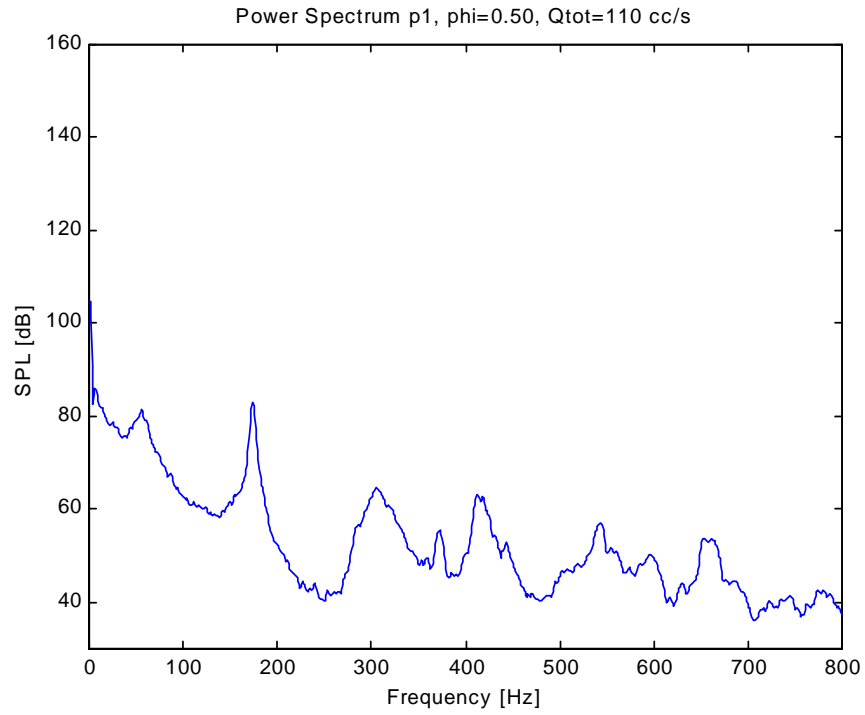


Figure A.1 Pressure power spectrum for  $\phi = 0.50$ ,  $Q_{tot}=110$  cc/s

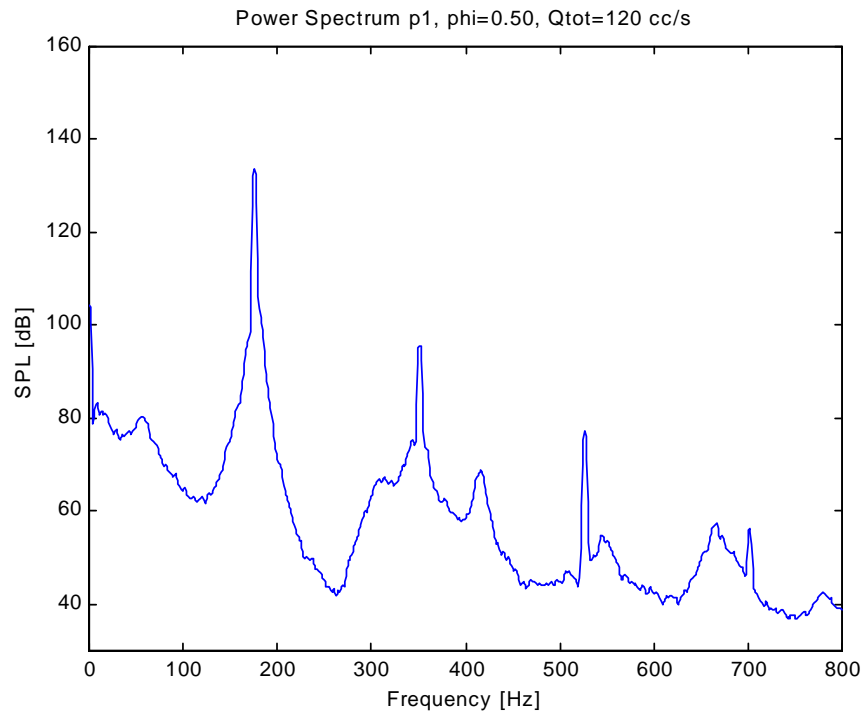


Figure A.2 Pressure power spectrum for  $\phi = 0.50$ ,  $Q_{tot}=120$  cc/s

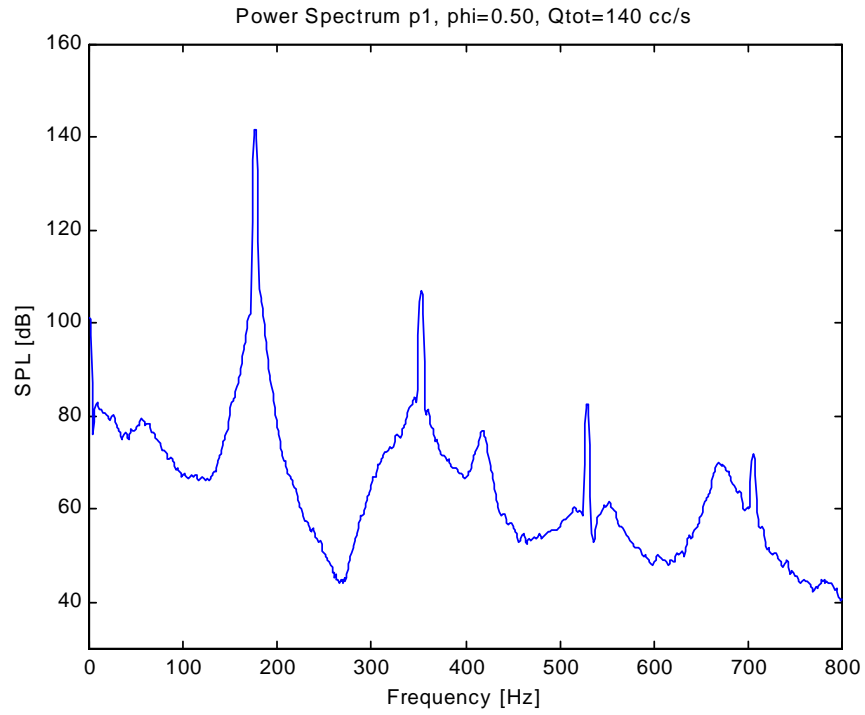


Figure A.3 Pressure power spectrum for  $\phi = 0.50$ ,  $Q_{tot}=140$  cc/s

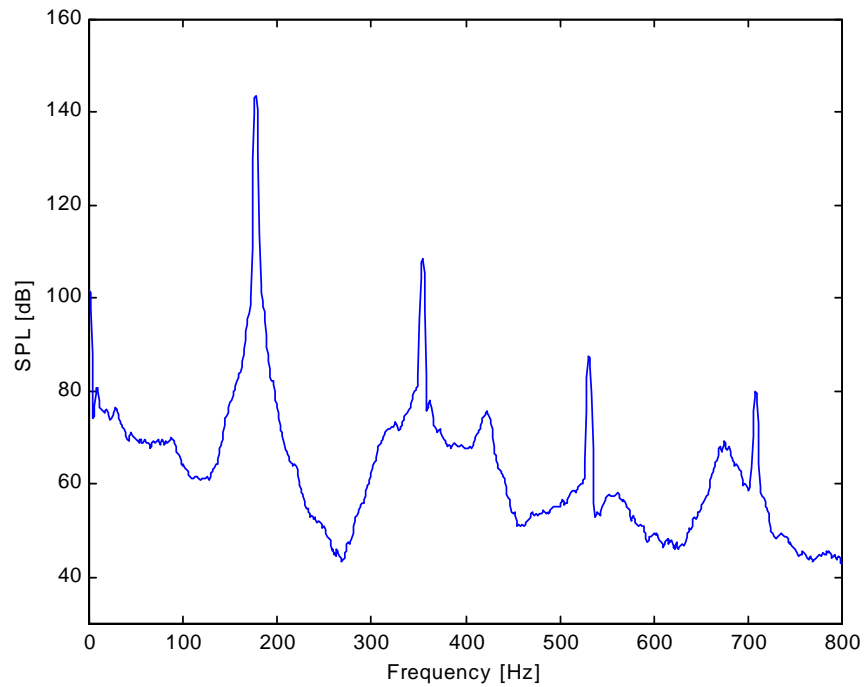


Figure A.4 Pressure power spectrum for  $\phi = 0.50$ ,  $Q_{tot}=160$  cc/s

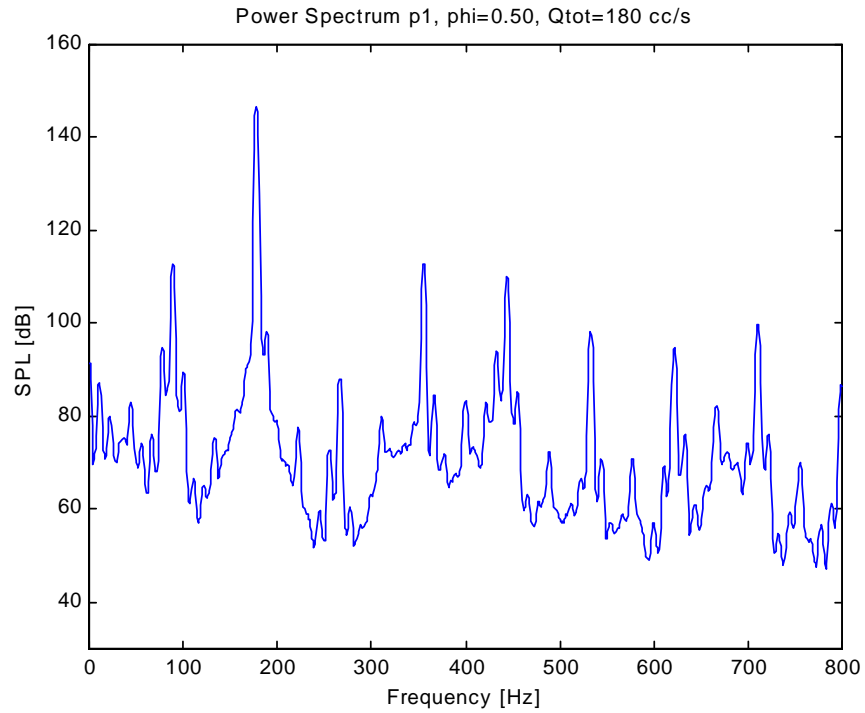


Figure A.5 Pressure power spectrum for  $\phi = 0.50$ ,  $Q_{tot}=180$  cc/s

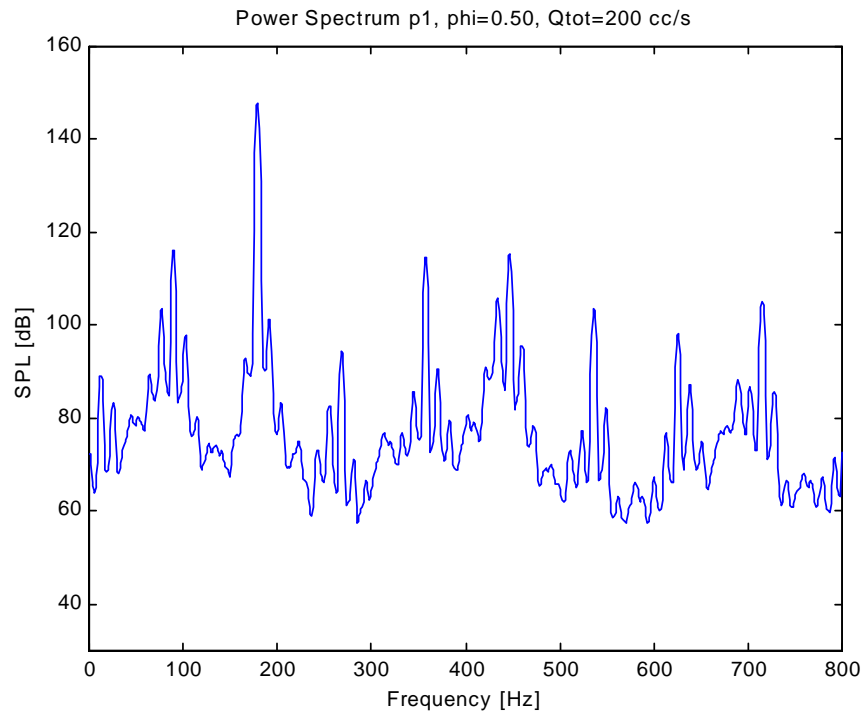


Figure A.6 Pressure power spectrum for  $\phi = 0.50$ ,  $Q_{tot}=200$  cc/s

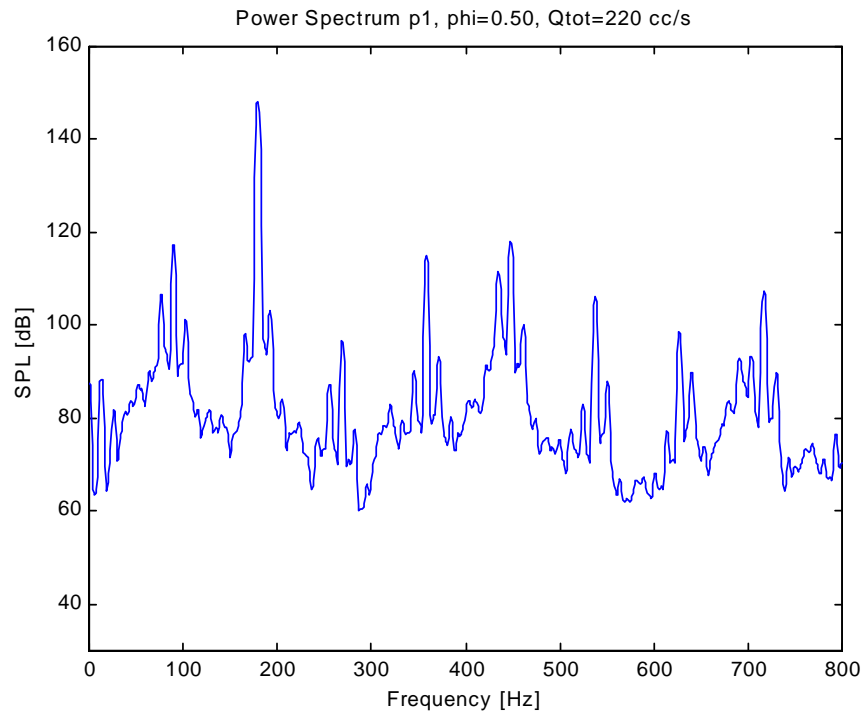


Figure A.7 Pressure power spectrum for  $\phi = 0.50$ ,  $Q_{tot}=220$  cc/s

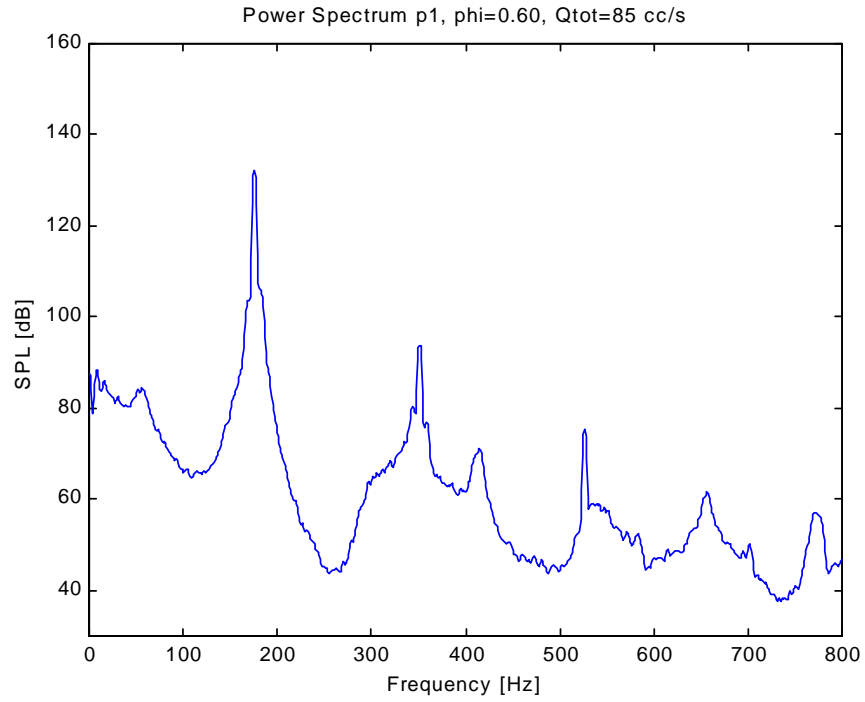


Figure A.8 Pressure power spectrum for  $\phi = 0.60$ ,  $Q_{tot}=85$  cc/s

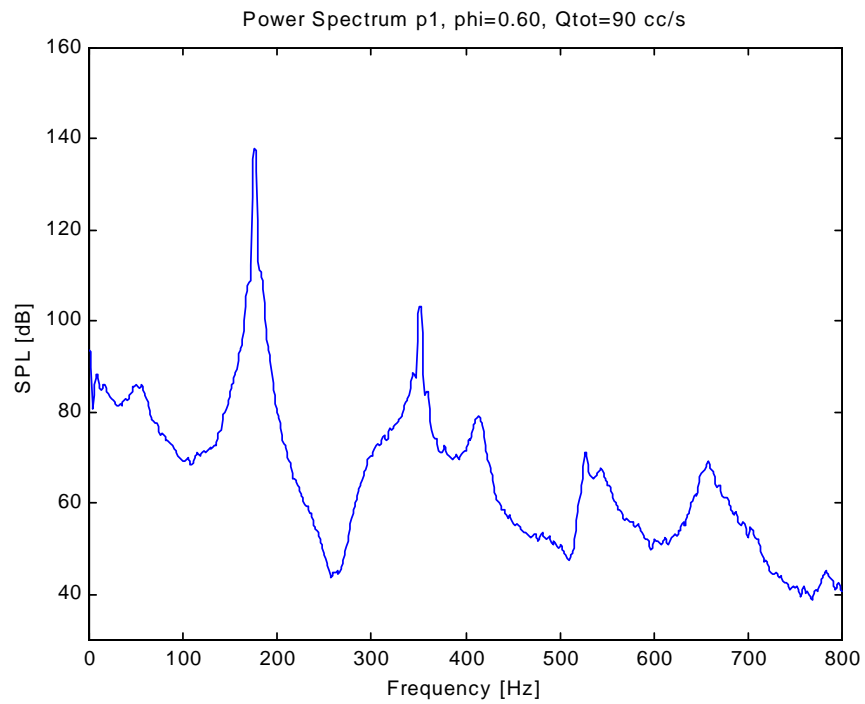


Figure A.9 Pressure power spectrum for  $\phi = 0.60$ ,  $Q_{tot}=90$  cc/s

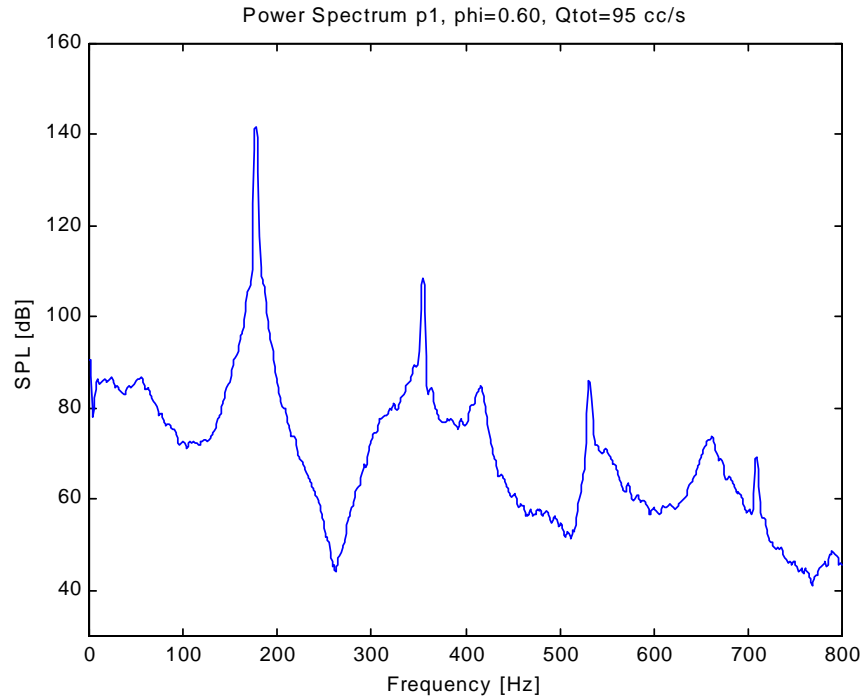


Figure A.10 Pressure power spectrum for  $\phi = 0.60$ ,  $Q_{tot}=95$  cc/s

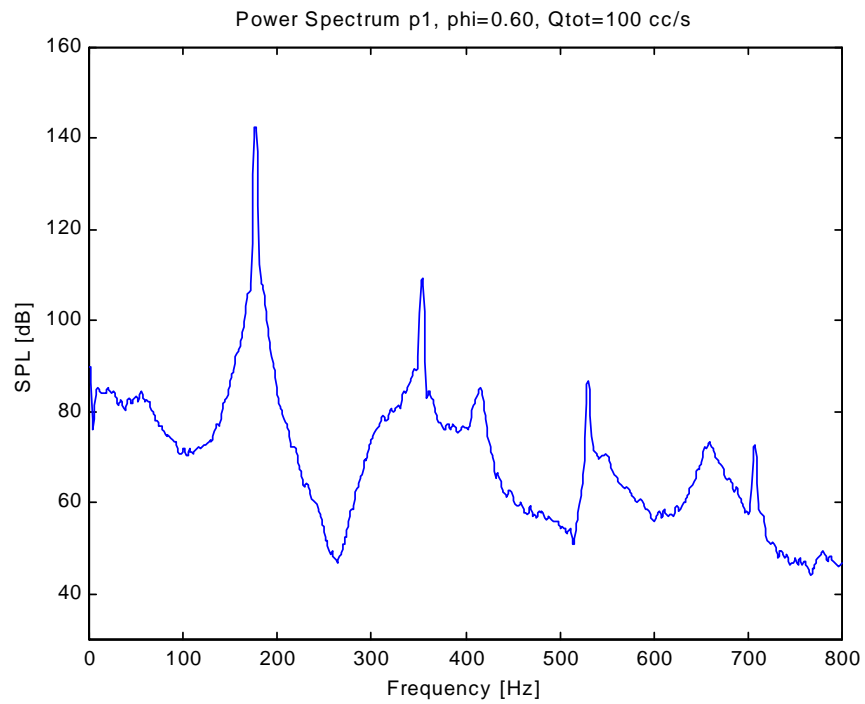


Figure A.11 Pressure power spectrum for  $\phi = 0.60$ ,  $Q_{tot}=100$  cc/s

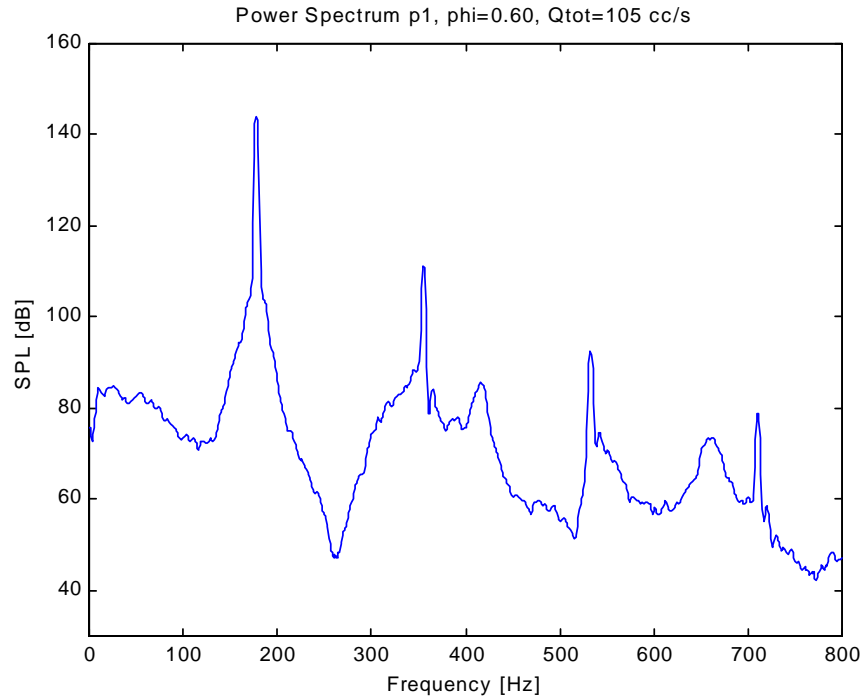


Figure A.12 Pressure power spectrum for  $\phi = 0.60$ ,  $Q_{tot}=105$  cc/s

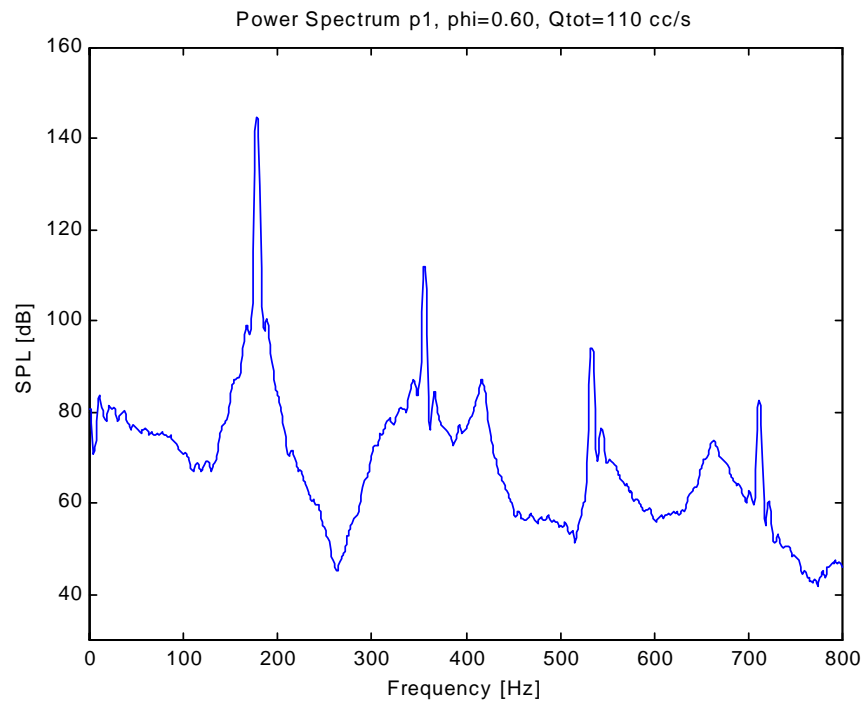


Figure A.13 Pressure power spectrum for  $\phi = 0.60$ ,  $Q_{tot}=110$  cc/s

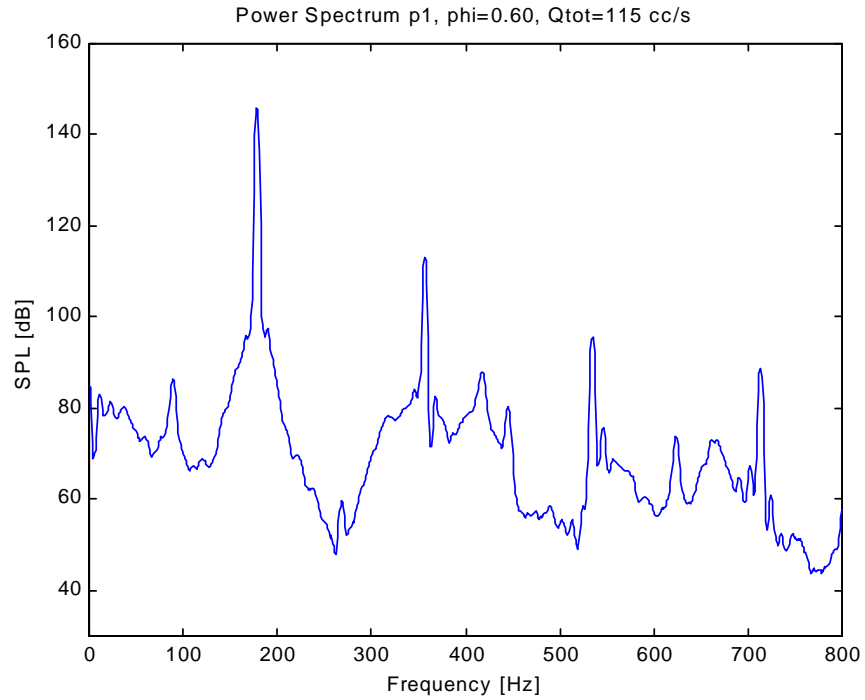


Figure A.14 Pressure power spectrum for  $\phi = 0.60$ ,  $Q_{tot}=115$  cc/s

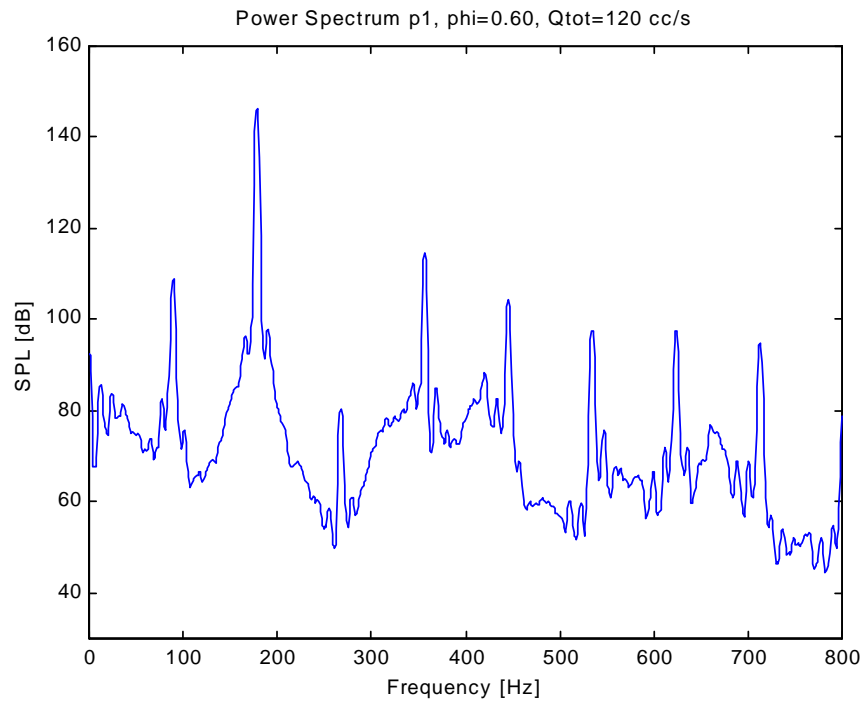


Figure A.15 Pressure power spectrum for  $\phi = 0.60$ ,  $Q_{tot}=120$  cc/s

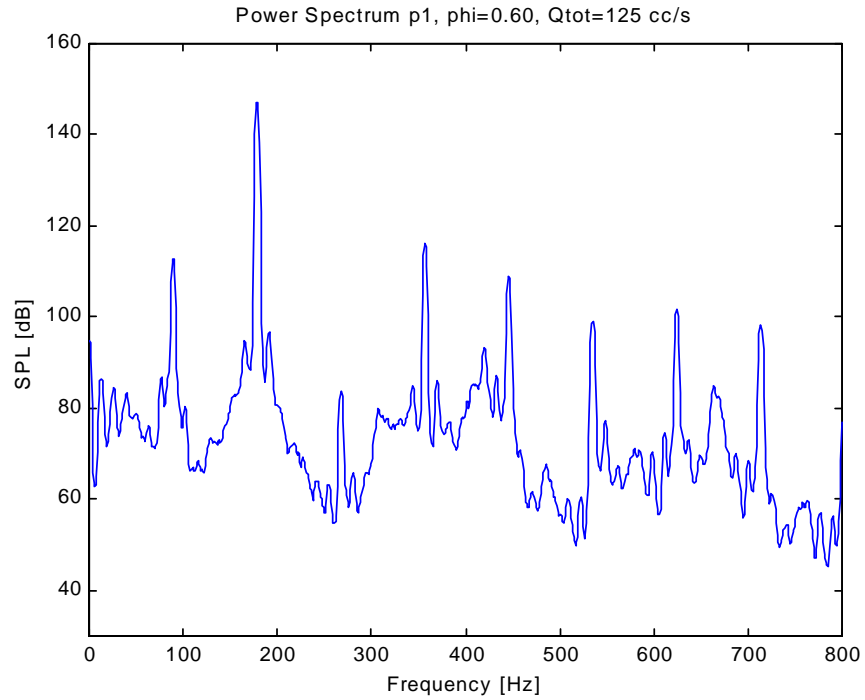


Figure A.16 Pressure power spectrum for  $\phi = 0.60$ ,  $Q_{tot}=125$  cc/s

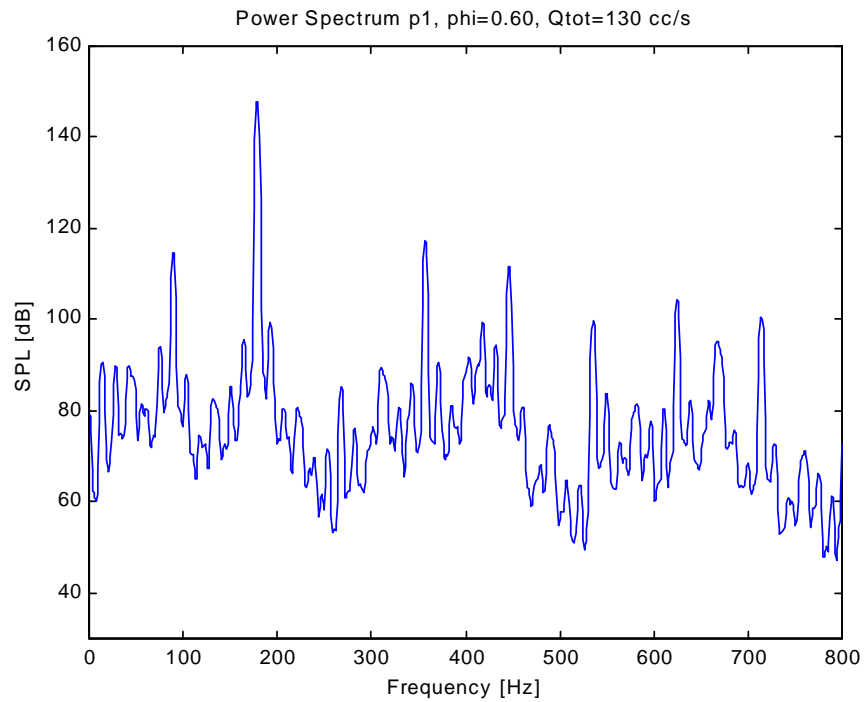


Figure A.17 Pressure power spectrum for  $\phi = 0.60$ ,  $Q_{tot}=130$  cc/s

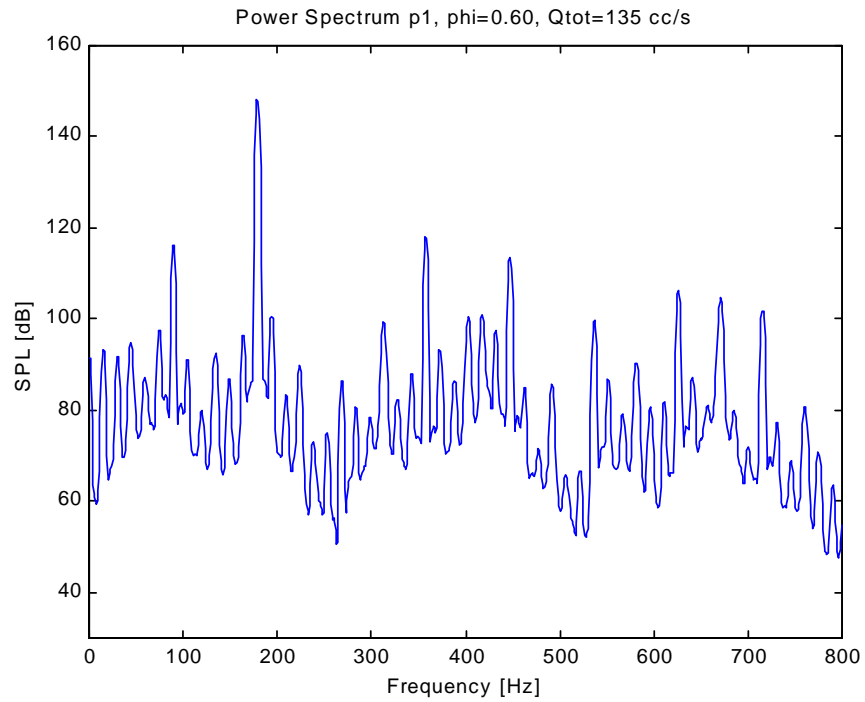


Figure A.18 Pressure power spectrum for  $\phi = 0.60$ ,  $Q_{tot}=135$  cc/s

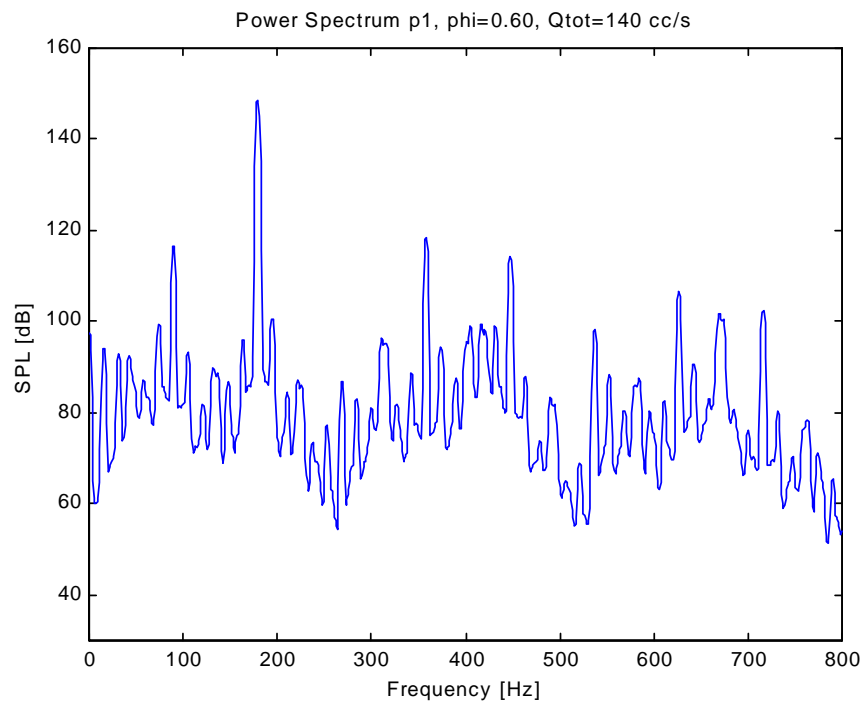


Figure A.19 Pressure power spectrum for  $\phi = 0.60$ ,  $Q_{tot}=140$  cc/s

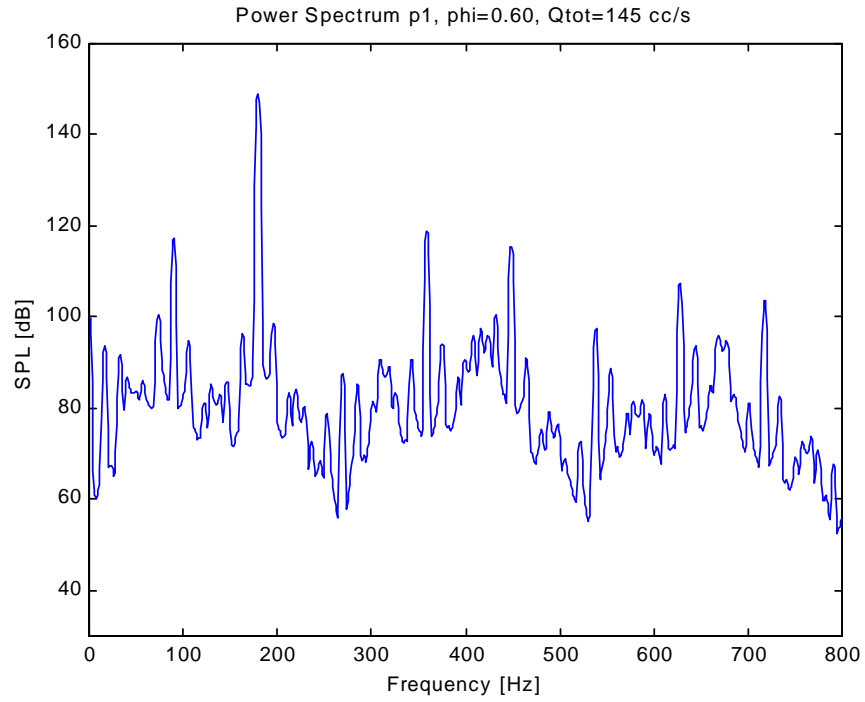


Figure A.20 Pressure power spectrum for  $\phi = 0.60$ ,  $Q_{tot}=145$  cc/s

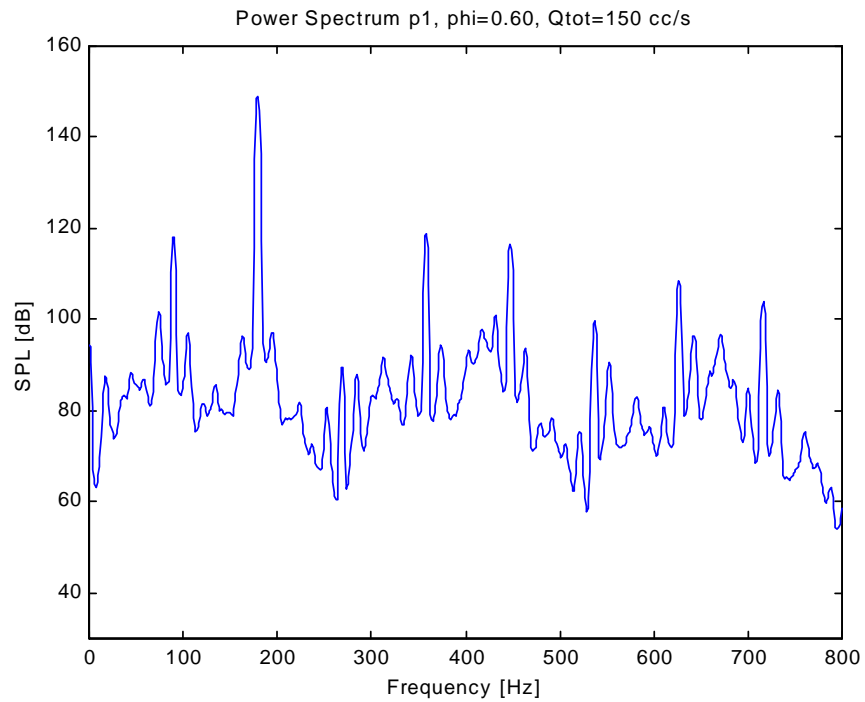


Figure A.21 Pressure power spectrum for  $\phi = 0.60$ ,  $Q_{tot}=150$  cc/s

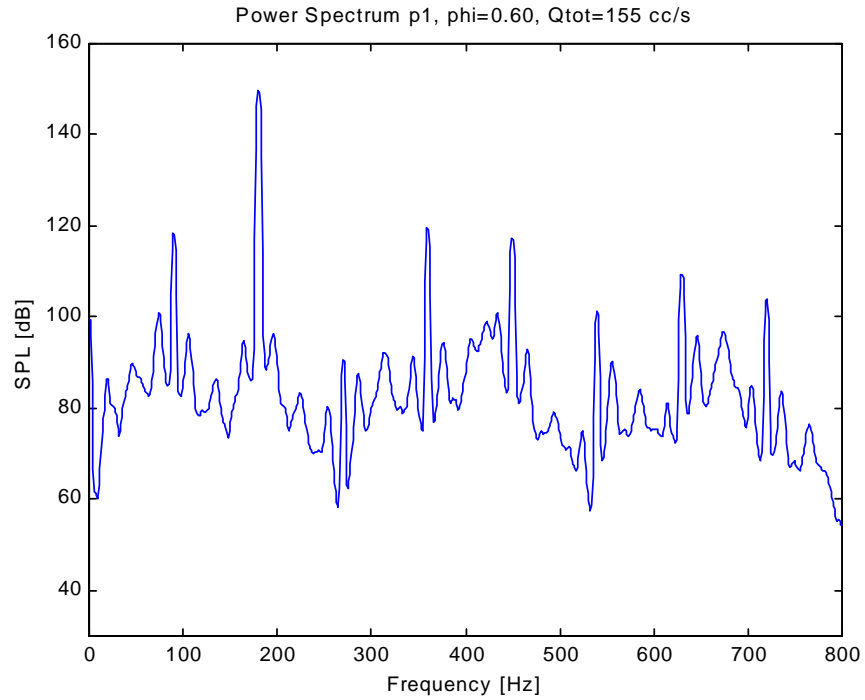


Figure A.22 Pressure power spectrum for  $\phi = 0.60$ ,  $Q_{tot}=155$  cc/s

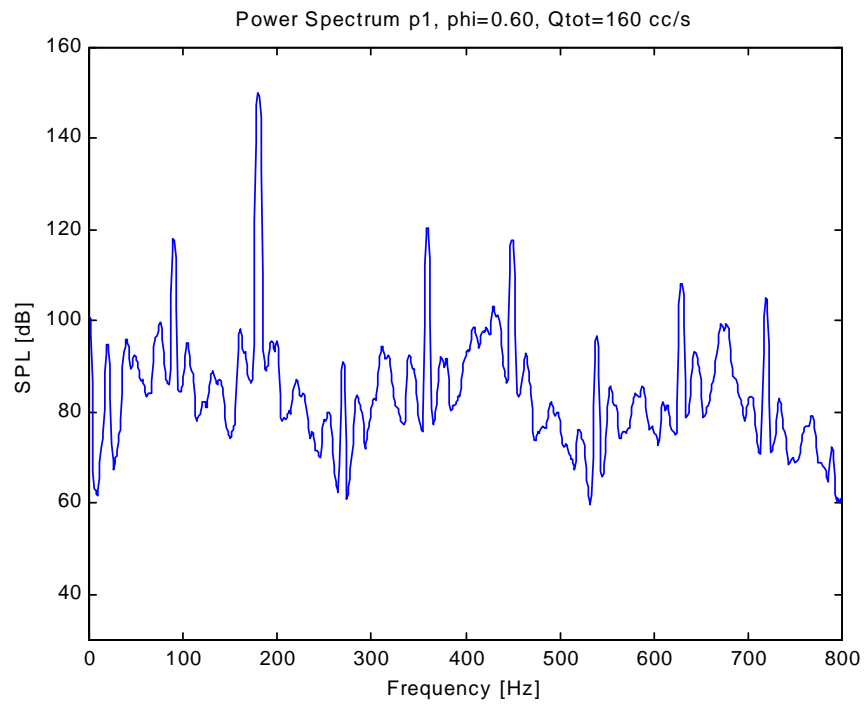


Figure A.23 Pressure power spectrum for  $\phi = 0.60$ ,  $Q_{tot}=160$  cc/s

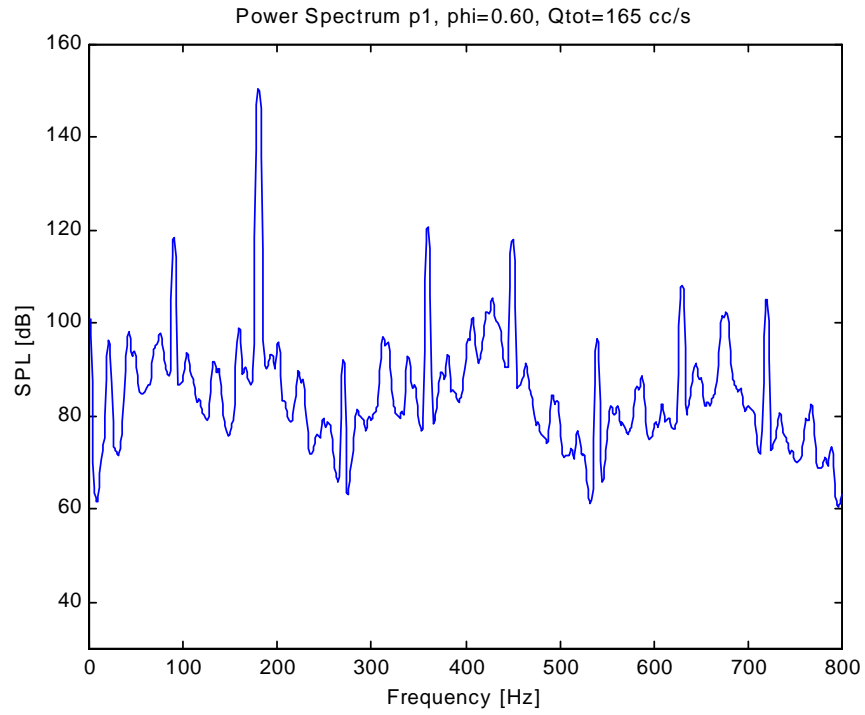


Figure A.24 Pressure power spectrum for  $\phi = 0.60$ ,  $Q_{tot}=165$  cc/s

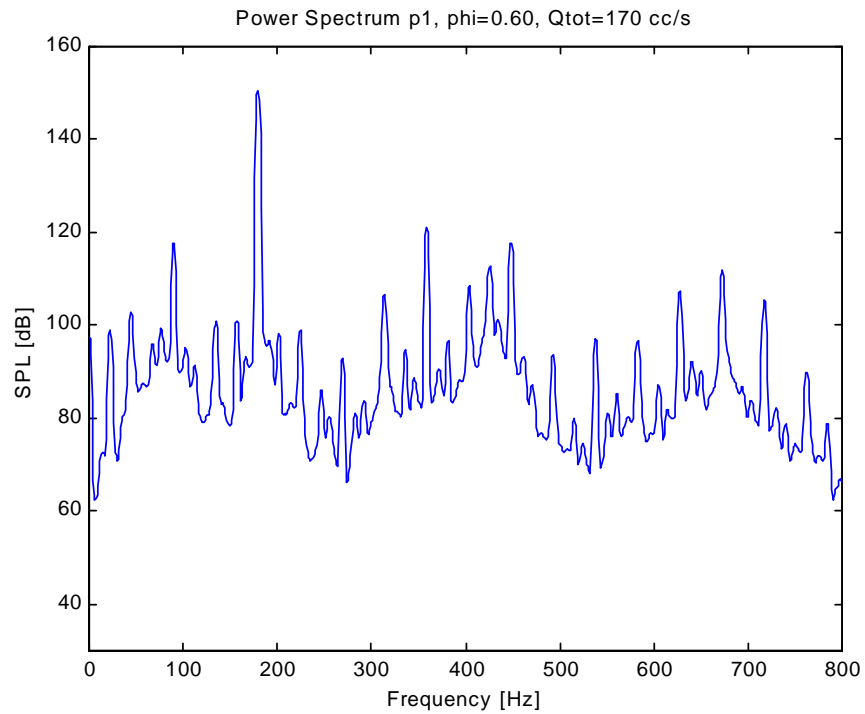


Figure A.25 Pressure power spectrum for  $\phi = 0.60$ ,  $Q_{tot}=170$  cc/s

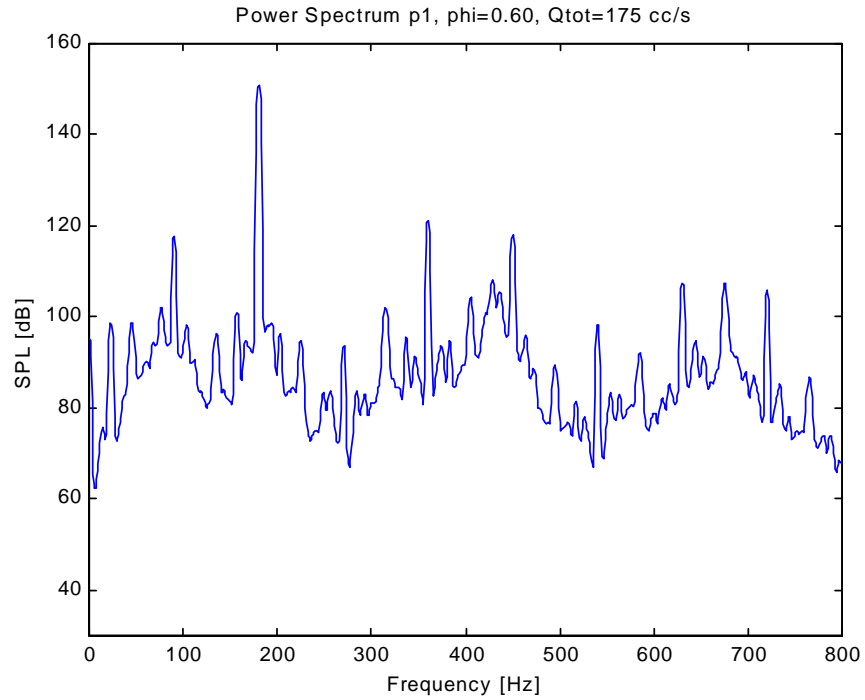


Figure A.26 Pressure power spectrum for  $\phi = 0.60$ ,  $Q_{tot}=175$  cc/s

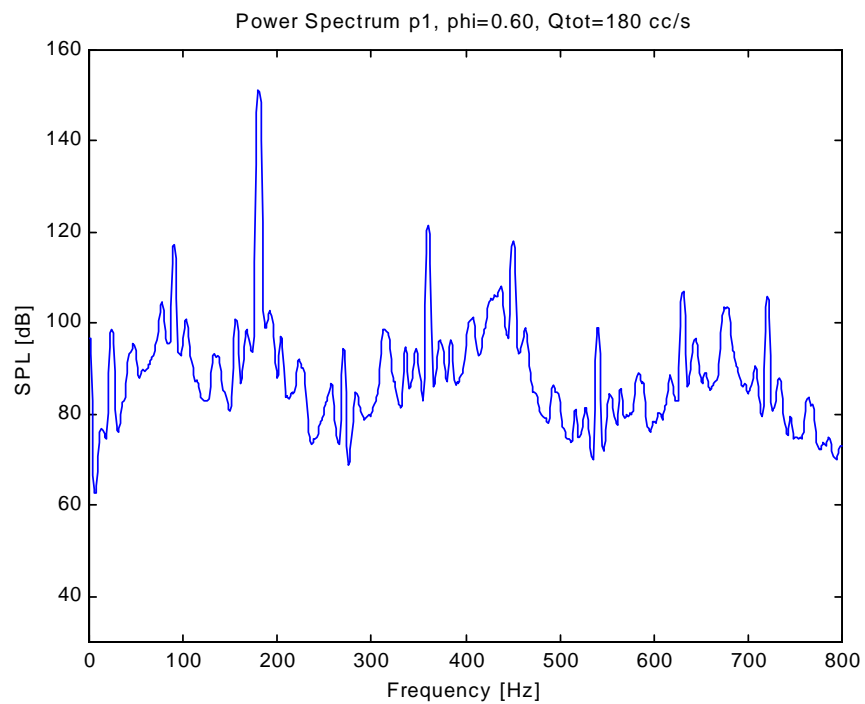


Figure A.27 Pressure power spectrum for  $\phi = 0.60$ ,  $Q_{tot}=180$  cc/s

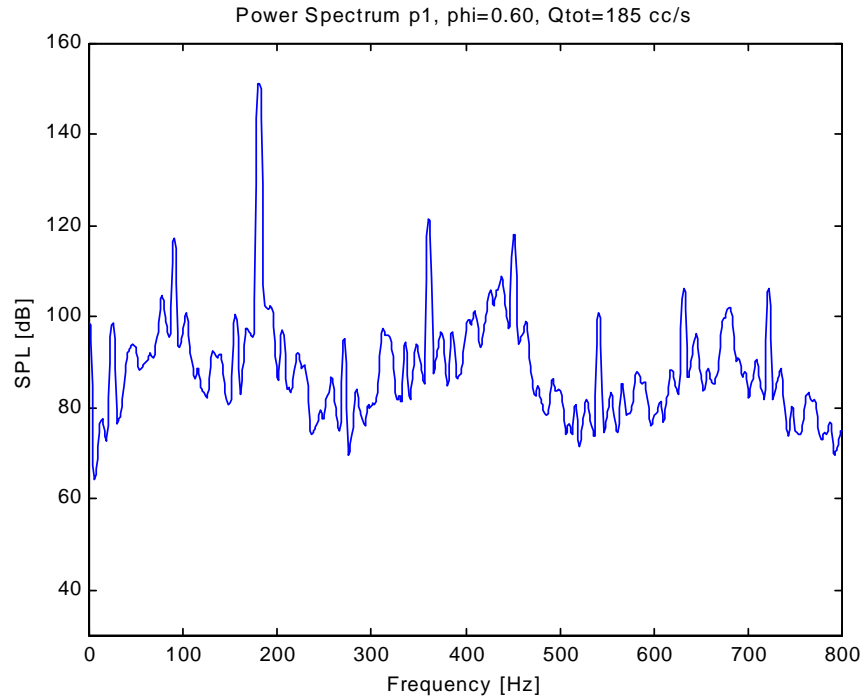


Figure A.28 Pressure power spectrum for  $\phi = 0.60$ ,  $Q_{tot}=185$  cc/s

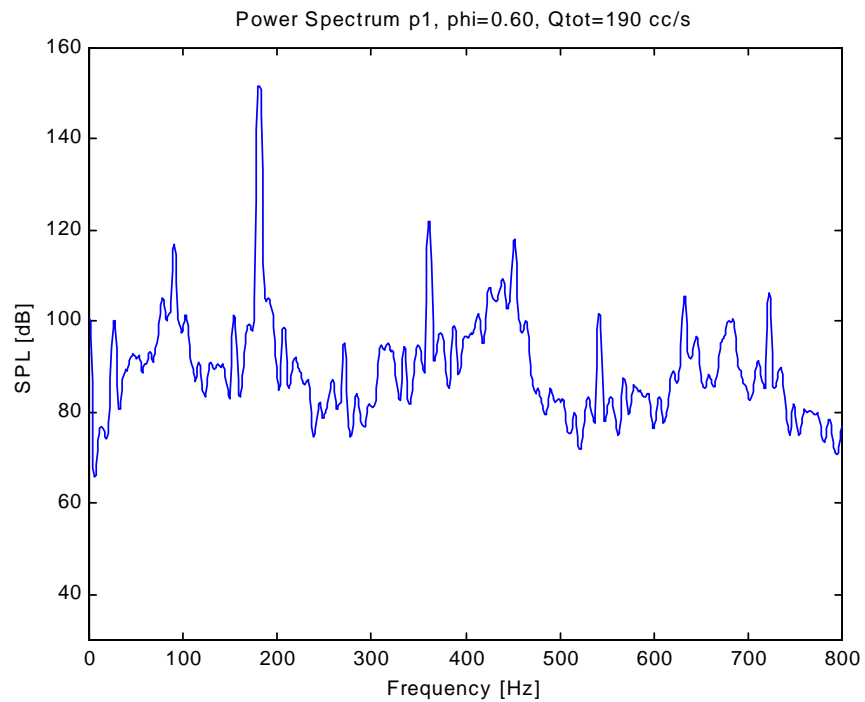


Figure A.29 Pressure power spectrum for  $\phi = 0.60$ ,  $Q_{tot}=190$  cc/s

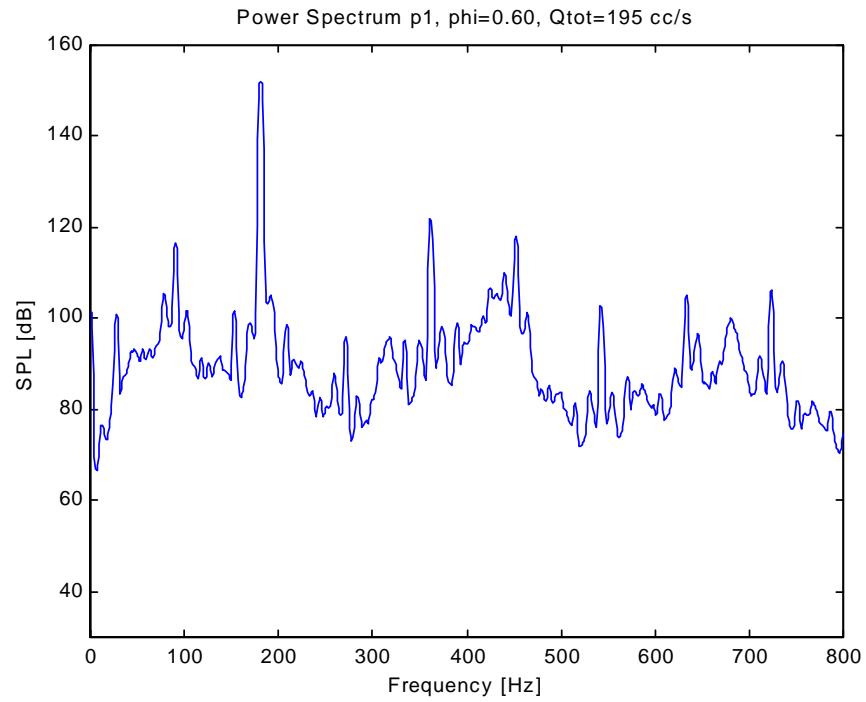


Figure A.30 Pressure power spectrum for  $\phi = 0.60$ ,  $Q_{tot}=195$  cc/s

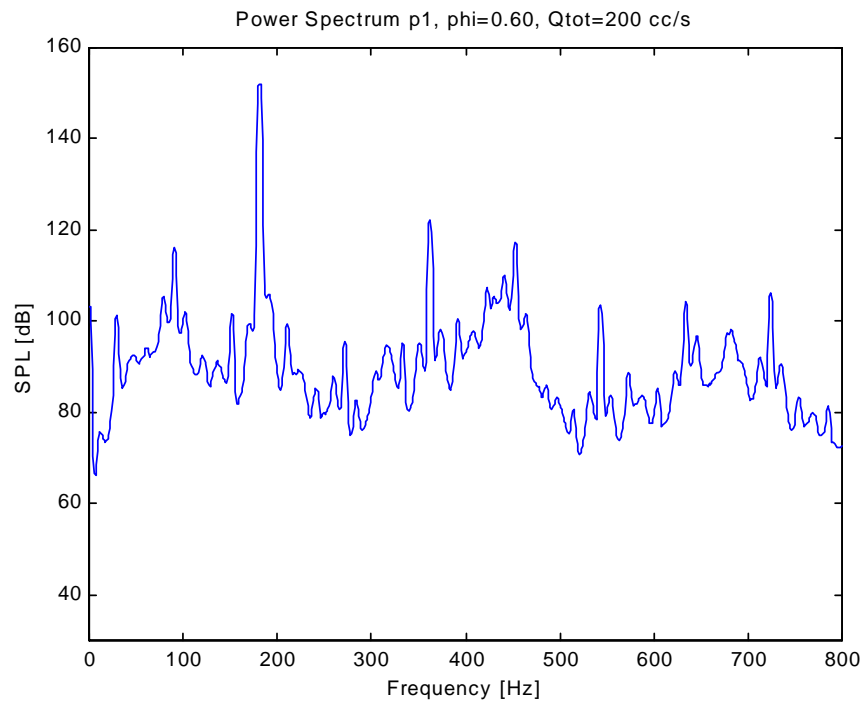


Figure A.31 Pressure power spectrum for  $\phi = 0.60$ ,  $Q_{tot}=200$  cc/s

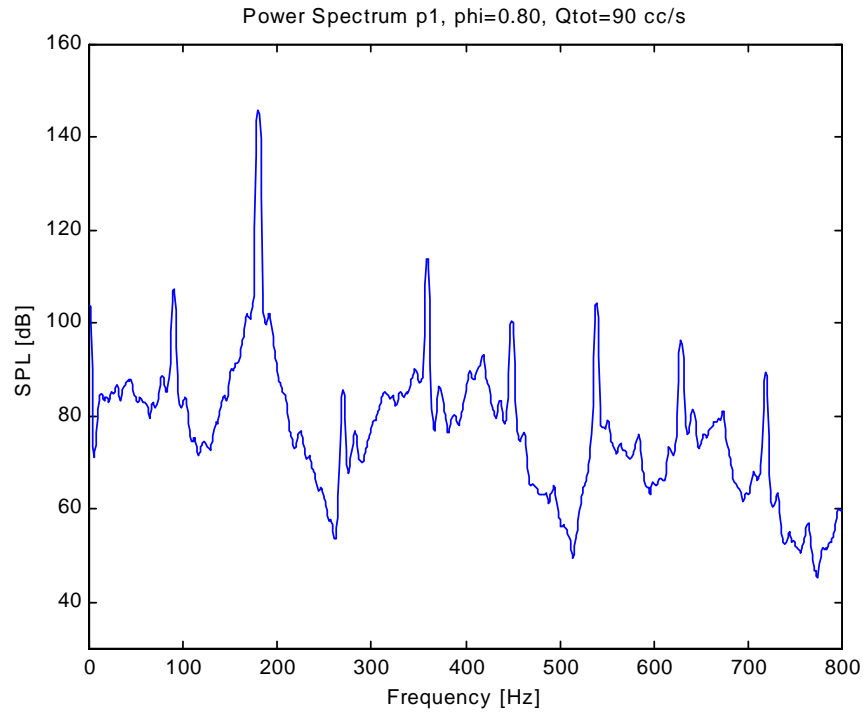


Figure A.32 Pressure power spectrum for  $\phi = 0.80$ ,  $Q_{tot}=90$  cc/s

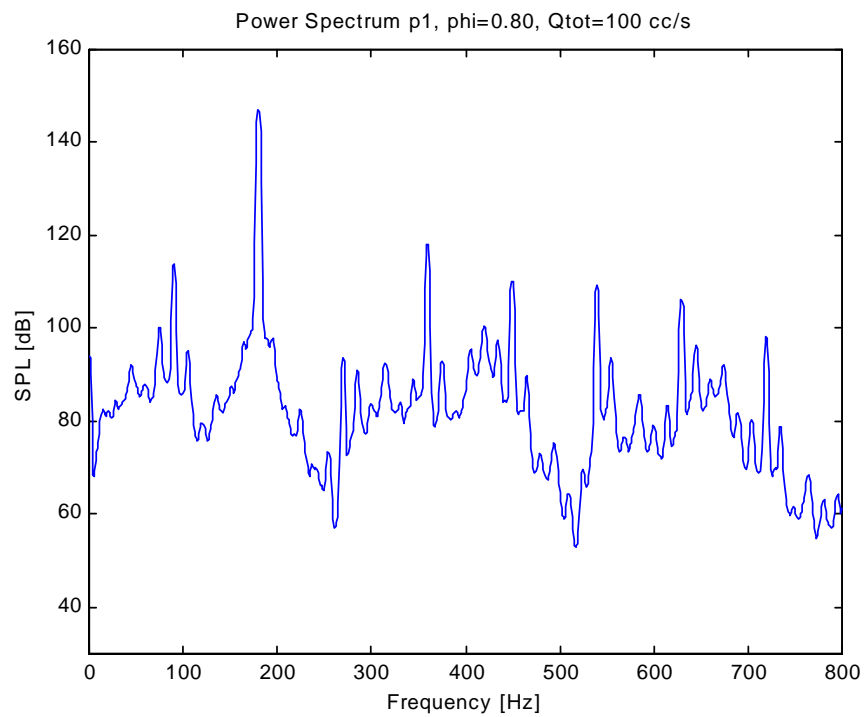


Figure A.33 Pressure power spectrum for  $\phi = 0.80$ ,  $Q_{tot}=100$  cc/s

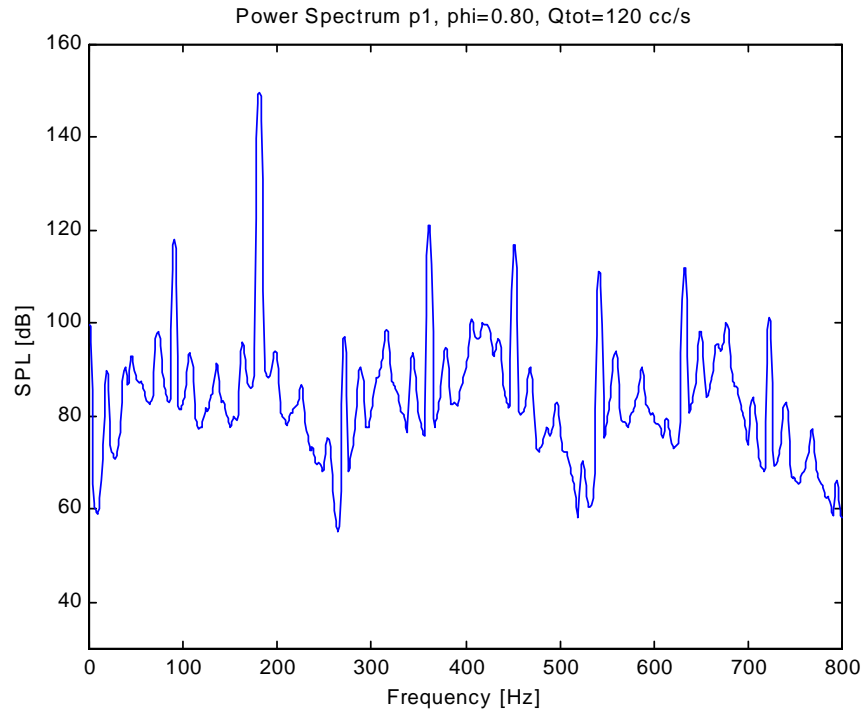


Figure A.34 Pressure power spectrum for  $\phi = 0.80$ ,  $Q_{tot}=120$  cc/s

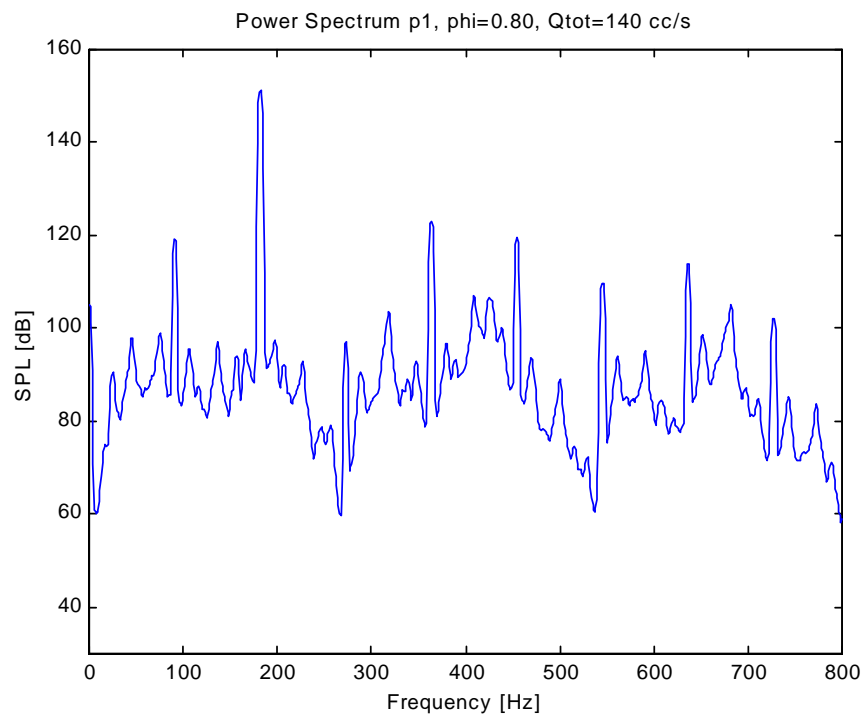


Figure A.35 Pressure power spectrum for  $\phi = 0.80$ ,  $Q_{tot}=140$  cc/s

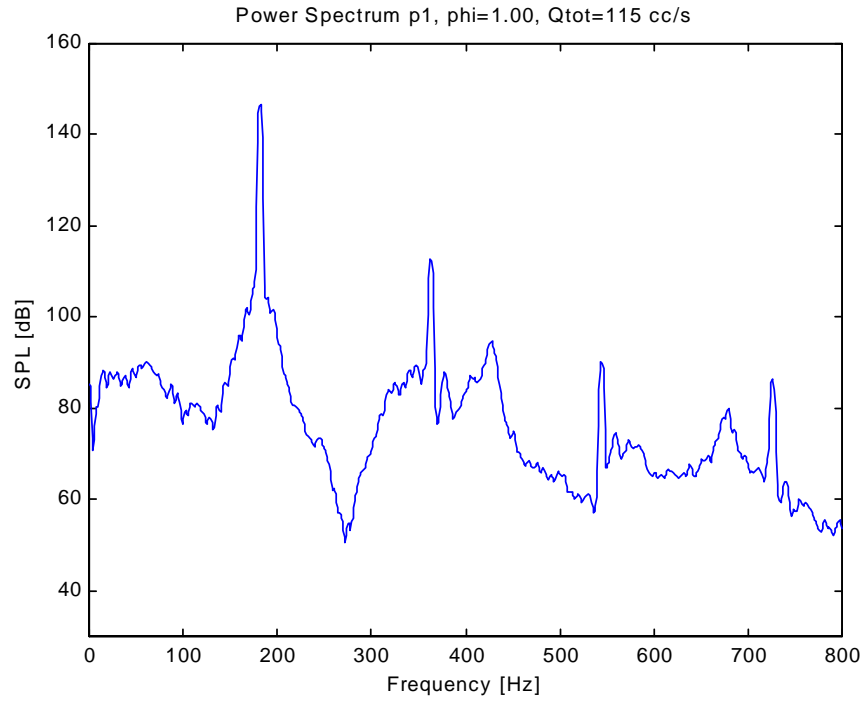


Figure A.36 Pressure power spectrum for  $\phi = 1.00$ ,  $Q_{tot} = 115$  cc/s

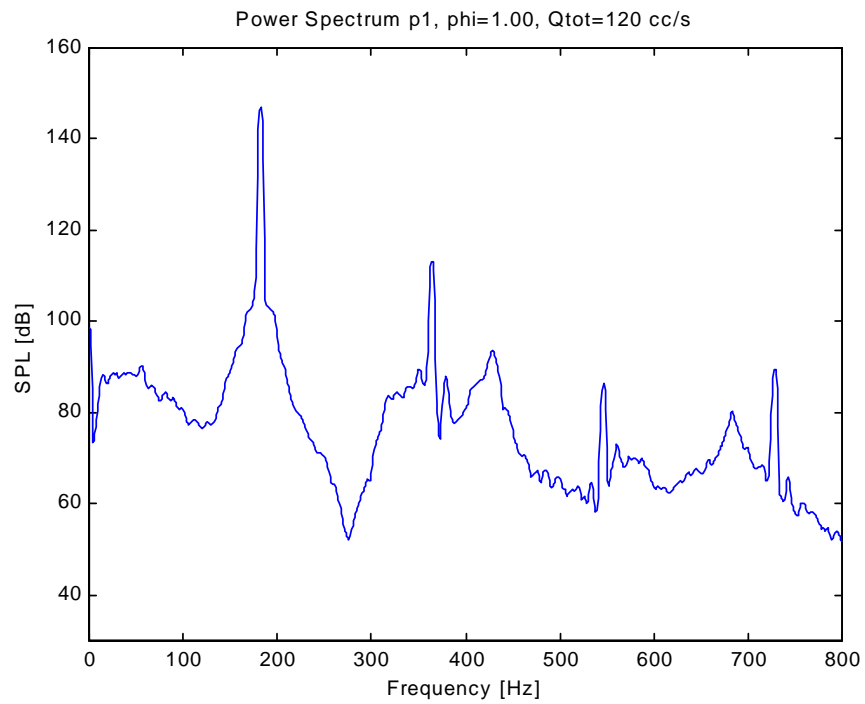


Figure A.37 Pressure power spectrum for  $\phi = 1.00$ ,  $Q_{tot} = 120$  cc/s

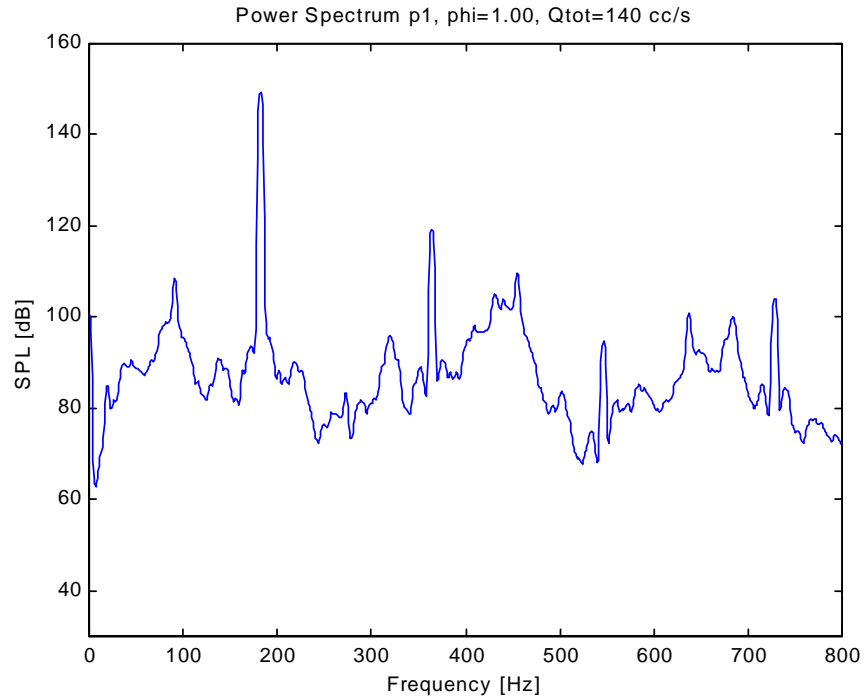


Figure A.38 Pressure power spectrum for  $\phi = 1.00$ ,  $Q_{tot}=140$  cc/s

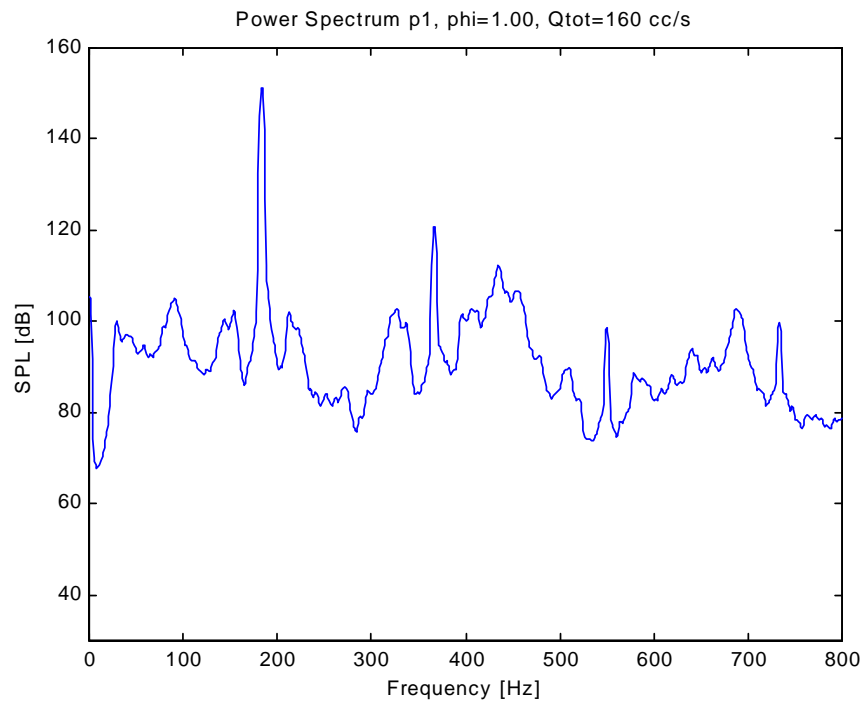


Figure A.39 Pressure power spectrum for  $\phi = 1.00$ ,  $Q_{tot}=160$  cc/s

## **Appendix B      Pressure Power Spectra for Constant Flow Rate**

In Appendix B, power spectra of the pressure measurements from the extensive mapping experiments will be presented. The flow rate was held constant with varying equivalence ratio for each data series. First the 100 cc/s flow rate series will be presented, followed by  $Q = 120, 140, 160, 180,$  and 200 cc/s series. All sound pressure levels have a reference pressure of  $2e-5$  Pa.

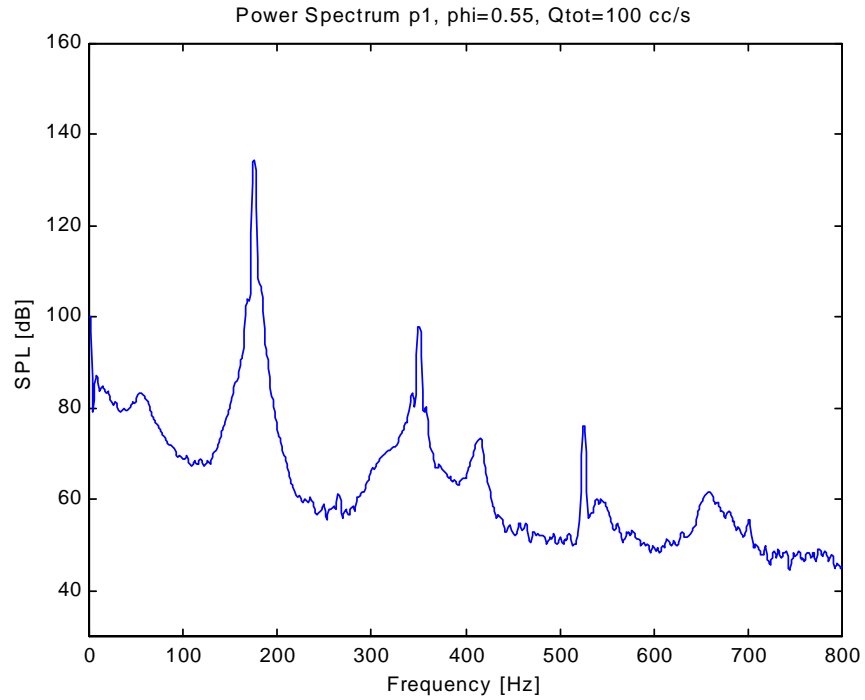


Figure B.1 Pressure power spectrum for  $\phi = 0.55$ ,  $Q_{tot} = 100$  cc/s

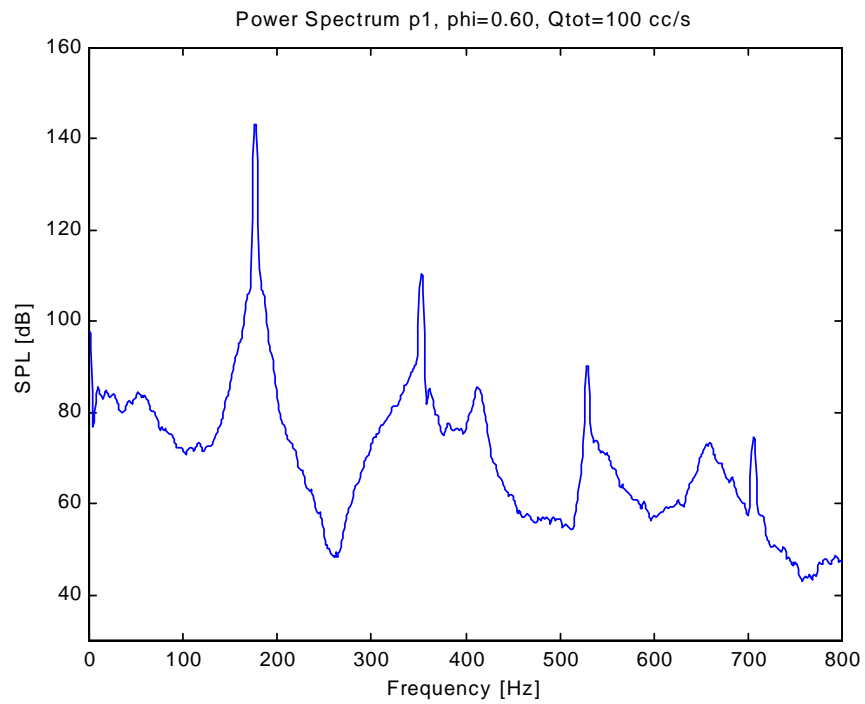


Figure B.2 Pressure power spectrum for  $\phi = 0.60$ ,  $Q_{tot} = 100$  cc/s

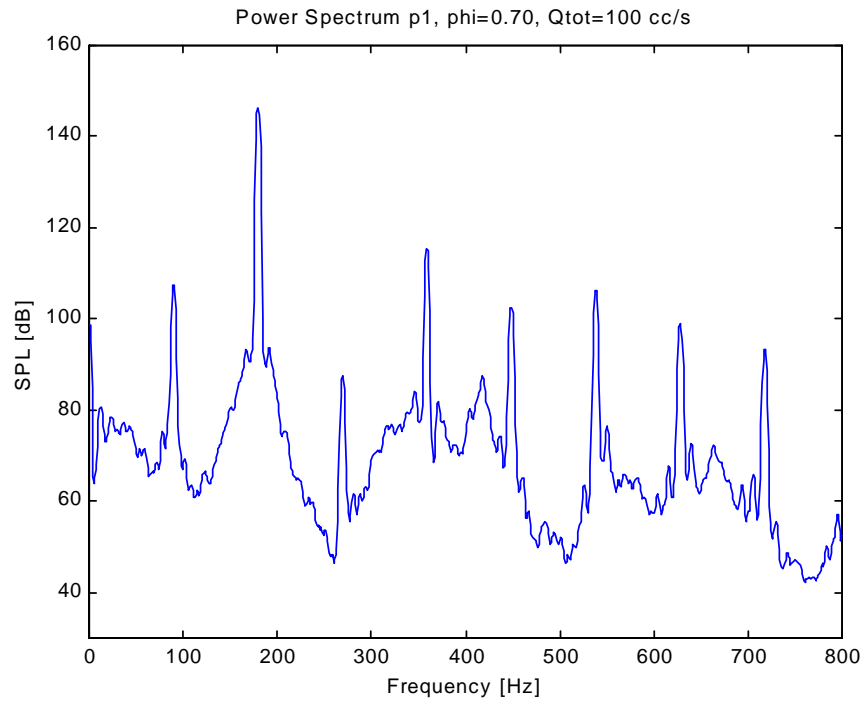


Figure B.3 Pressure power spectrum for  $\phi = 0.70$ ,  $Q_{tot}=100$  cc/s

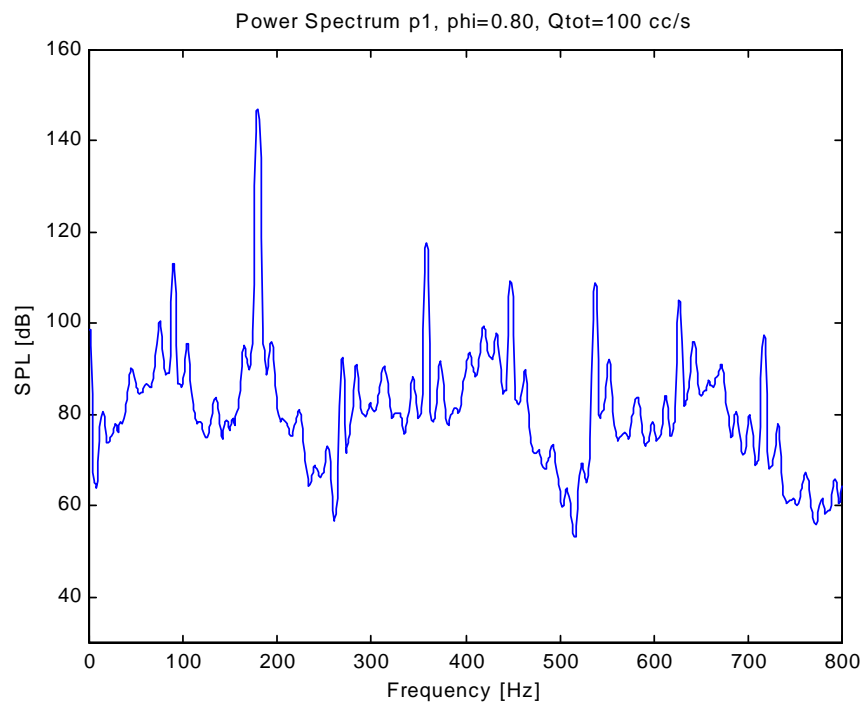


Figure B.4 Pressure power spectrum for  $\phi = 0.80$ ,  $Q_{tot}=100$  cc/s

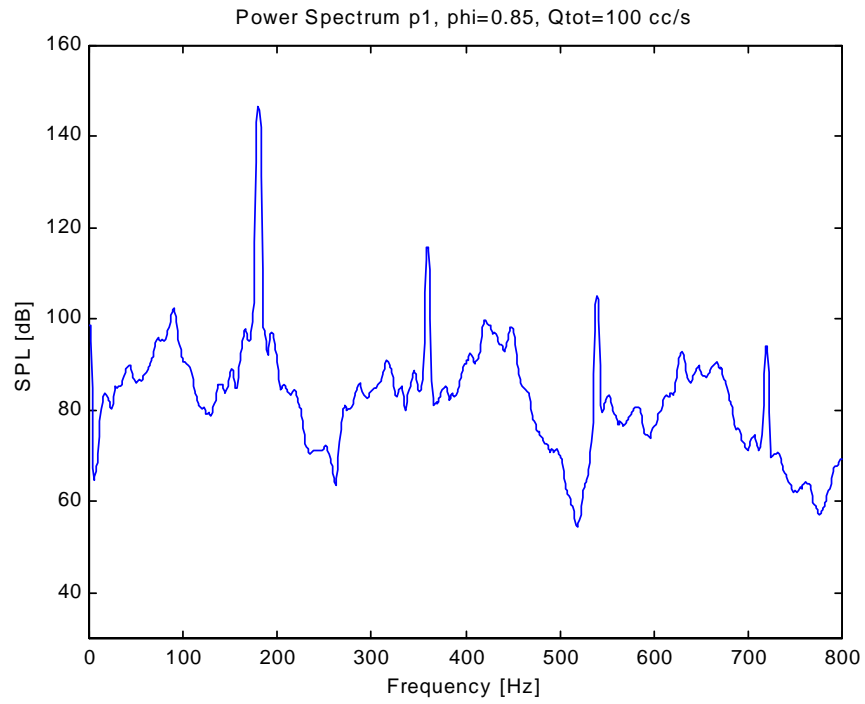


Figure B.5 Pressure power spectrum for  $\phi = 0.85$ ,  $Q_{tot}=100$  cc/s

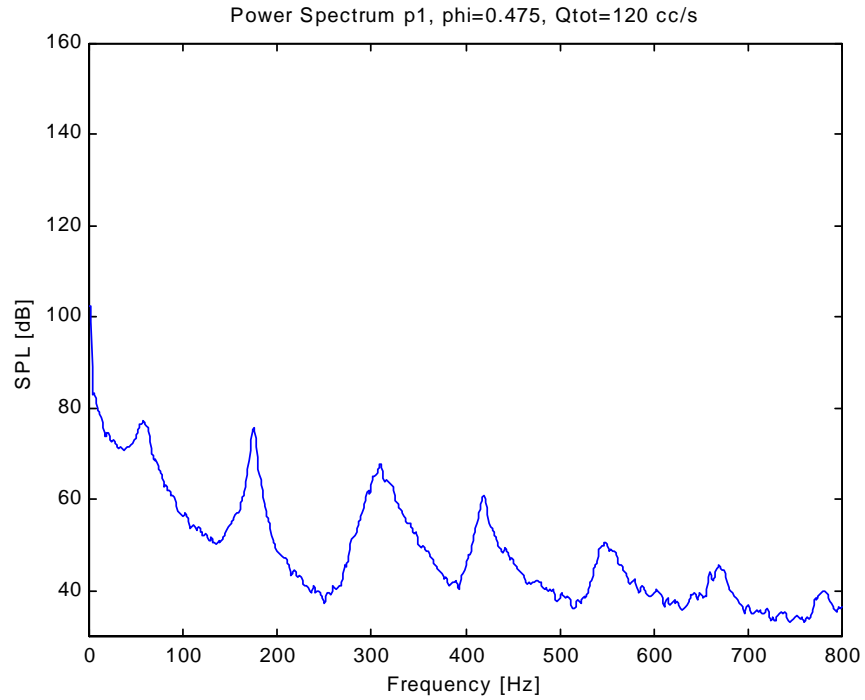


Figure B.6 Pressure power spectrum for  $\phi = 0.475$ ,  $Q_{tot}=120$  cc/s

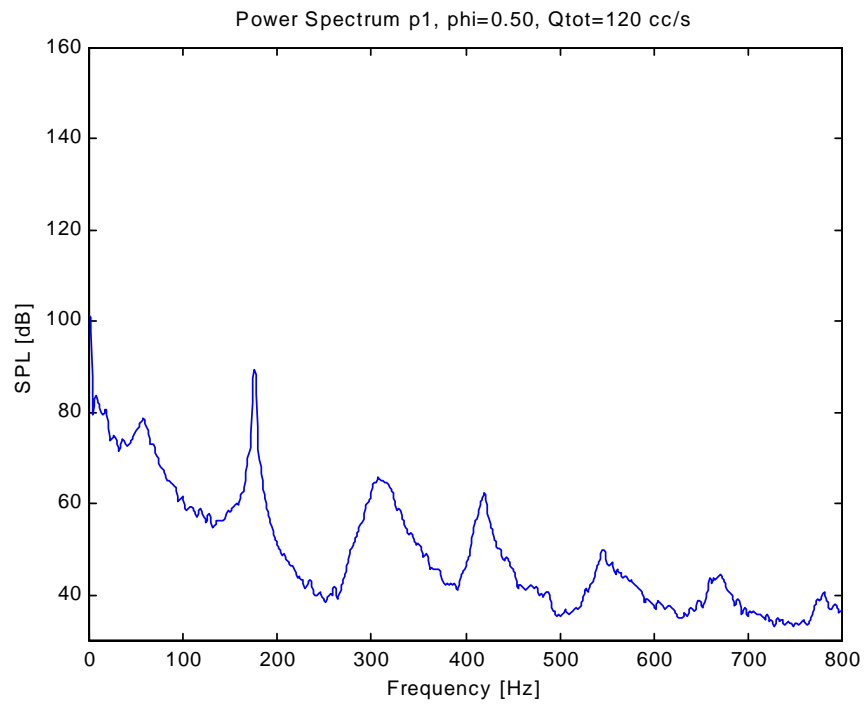


Figure B.7 Pressure power spectrum for  $\phi = 0.50$ ,  $Q_{tot}=120$  cc/s

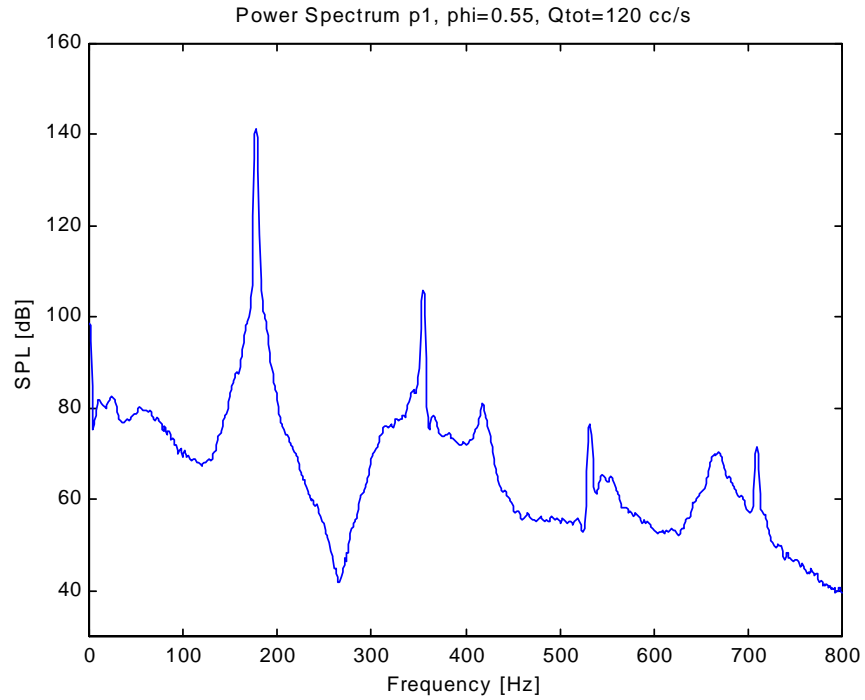


Figure B.8 Pressure power spectrum for  $\phi = 0.55$ ,  $Q_{tot}=120$  cc/s

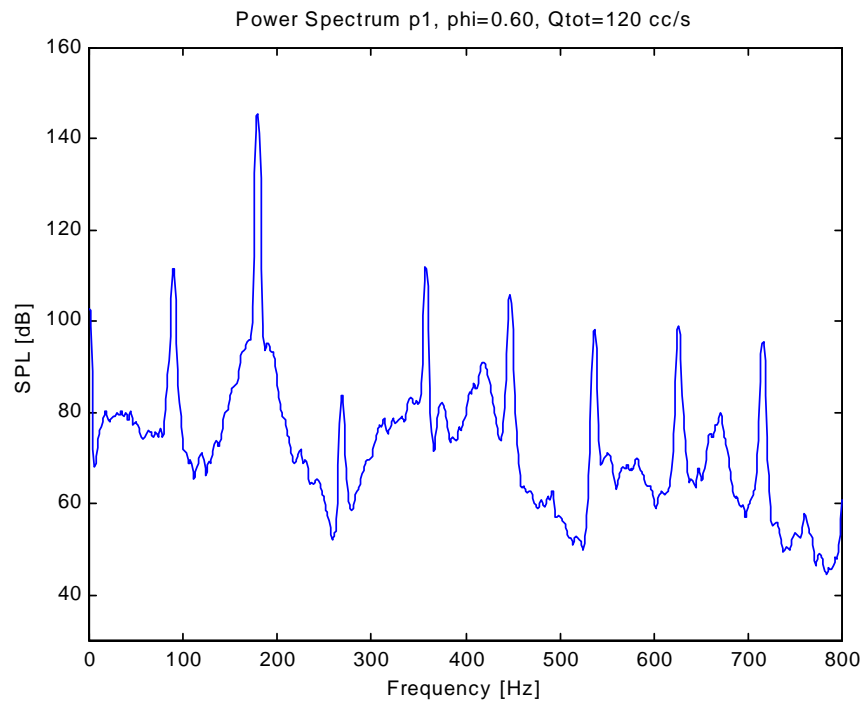


Figure B.9 Pressure power spectrum for  $\phi = 0.60$ ,  $Q_{tot}=120$  cc/s

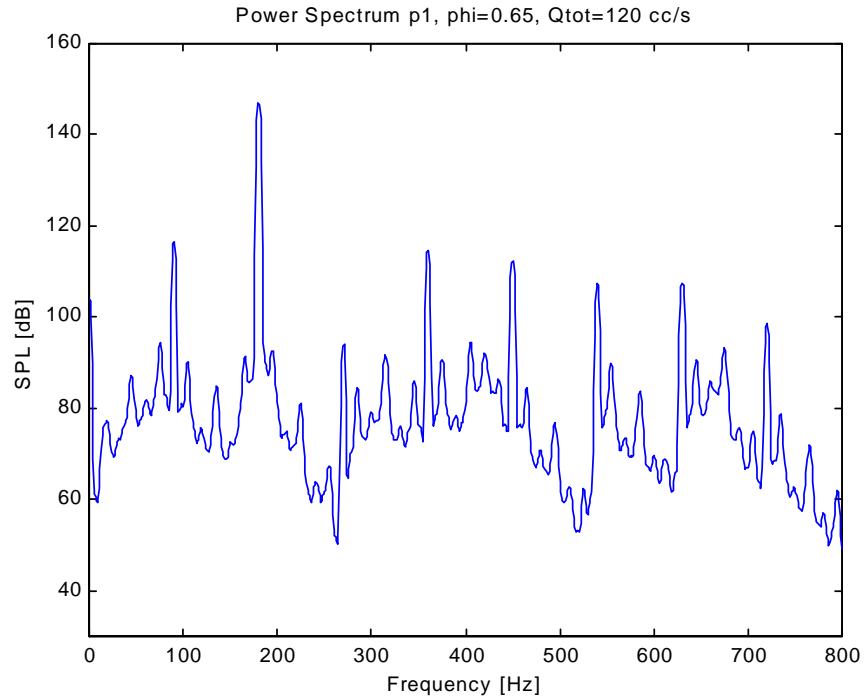


Figure B.10 Pressure power spectrum for  $\phi = 0.65$ ,  $Q_{tot}=120$  cc/s

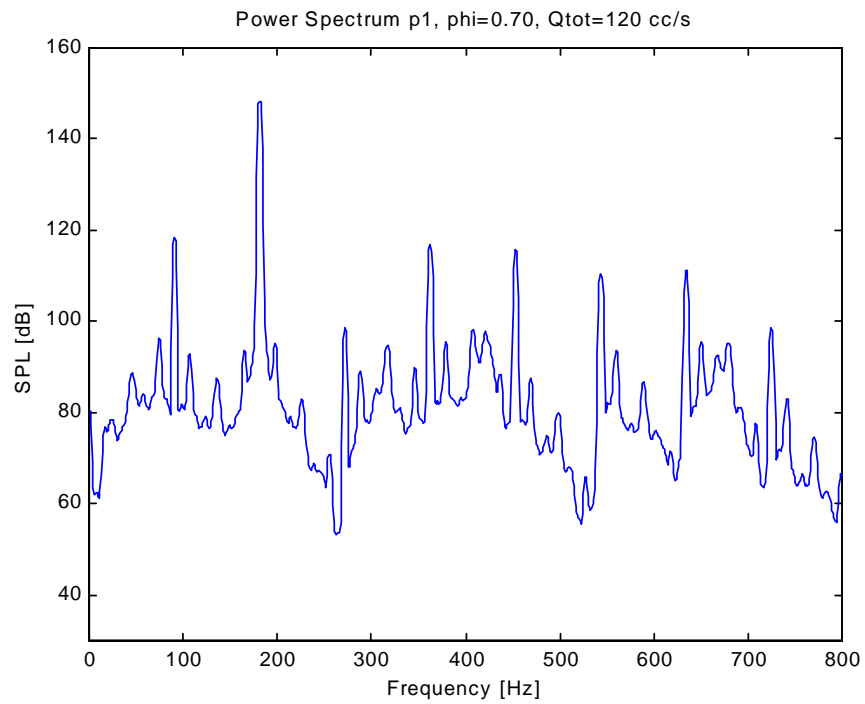


Figure B.11 Pressure power spectrum for  $\phi = 0.70$ ,  $Q_{tot}=120$  cc/s

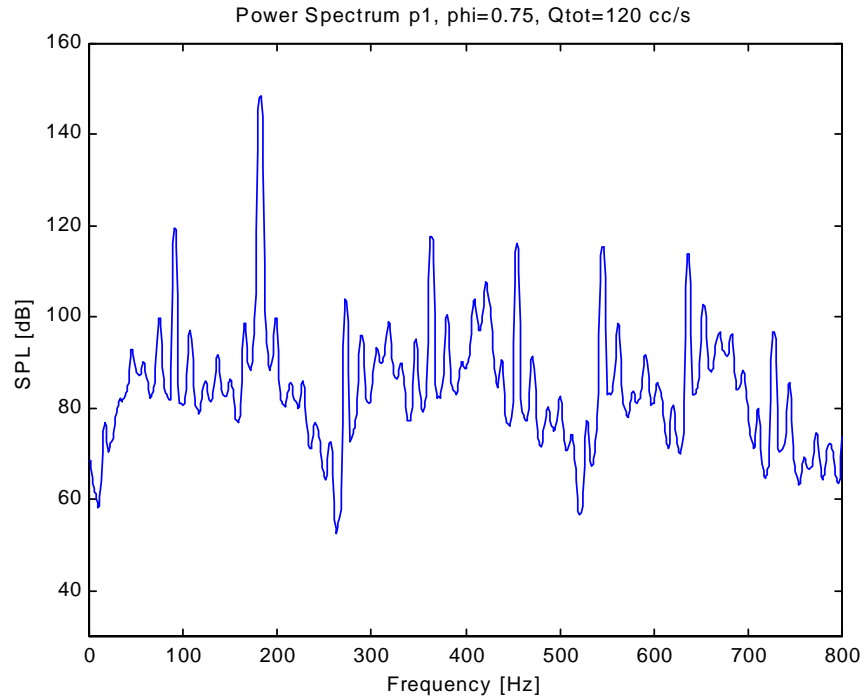


Figure B.12 Pressure power spectrum for  $\phi = 0.75$ ,  $Q_{tot}=120$  cc/s

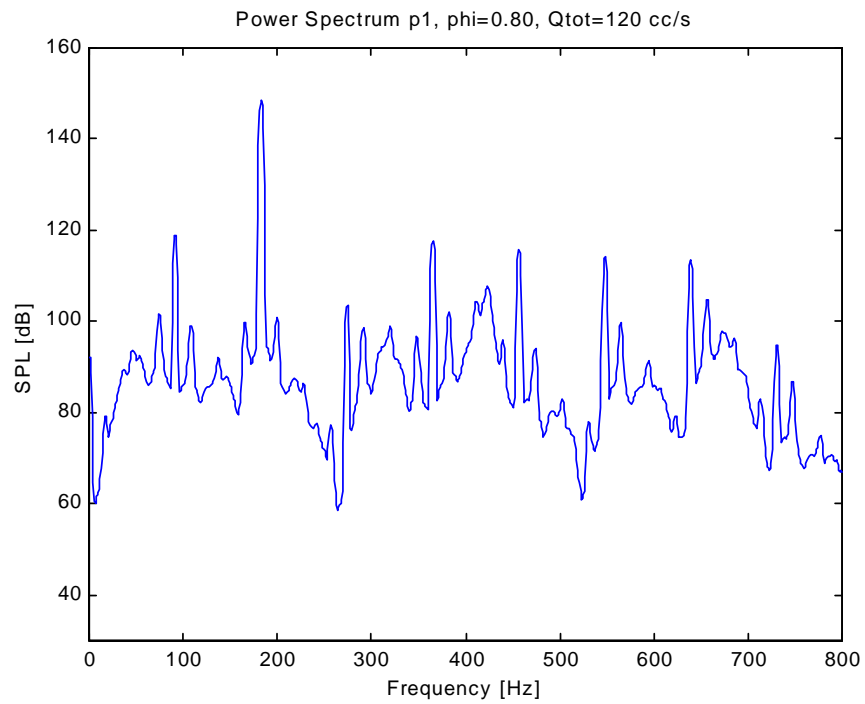


Figure B.13 Pressure power spectrum for  $\phi = 0.80$ ,  $Q_{tot}=120$  cc/s

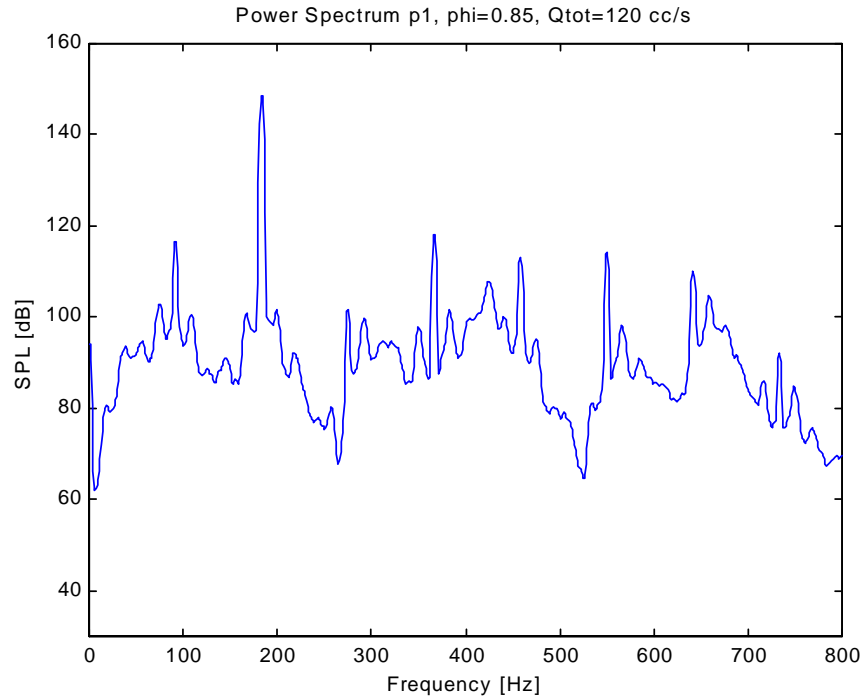


Figure B.14 Pressure power spectrum for  $\phi = 0.85$ ,  $Q_{tot}=120$  cc/s

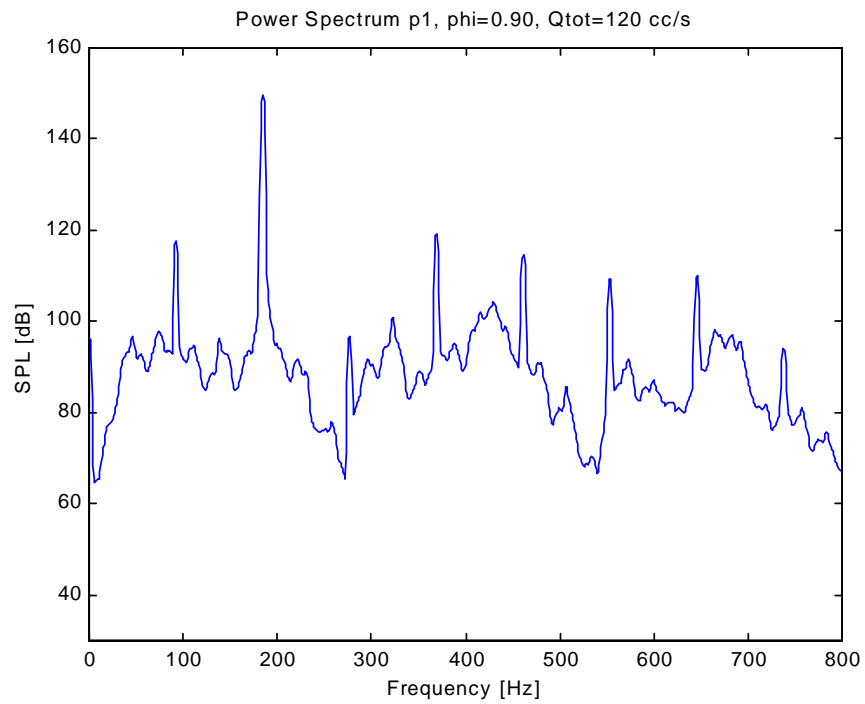


Figure B.15 Pressure power spectrum for  $\phi = 0.90$ ,  $Q_{tot}=120$  cc/s

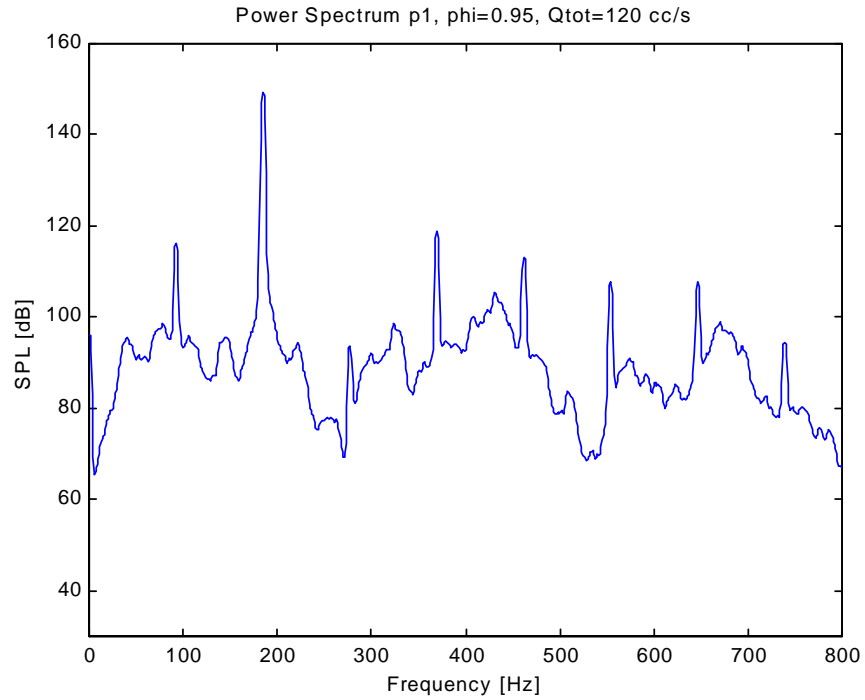


Figure B.16 Pressure power spectrum for  $\phi = 0.95$ ,  $Q_{tot}=120$  cc/s

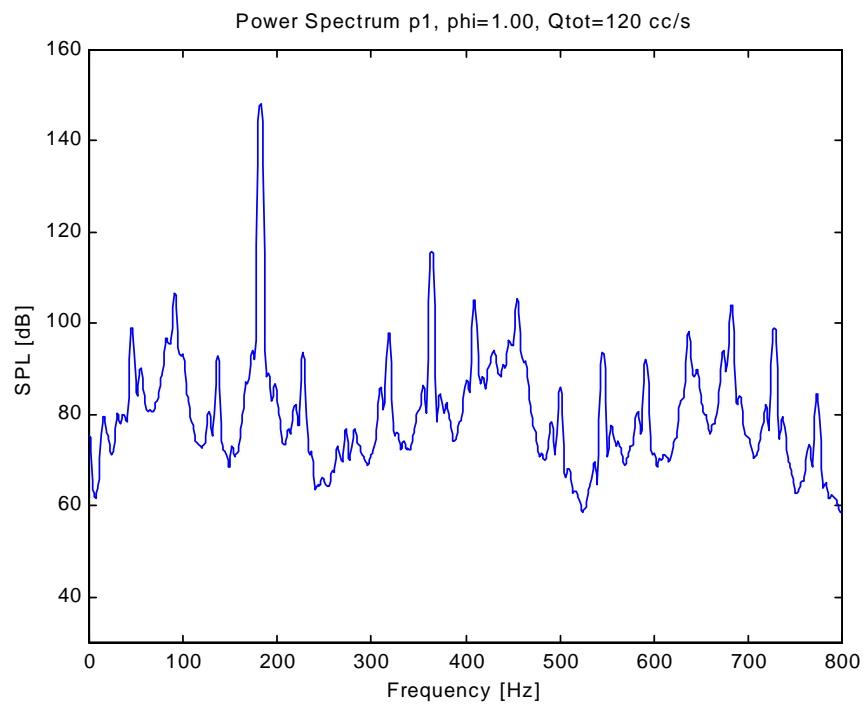


Figure B.17 Pressure power spectrum for  $\phi = 1.00$ ,  $Q_{tot}=120$  cc/s

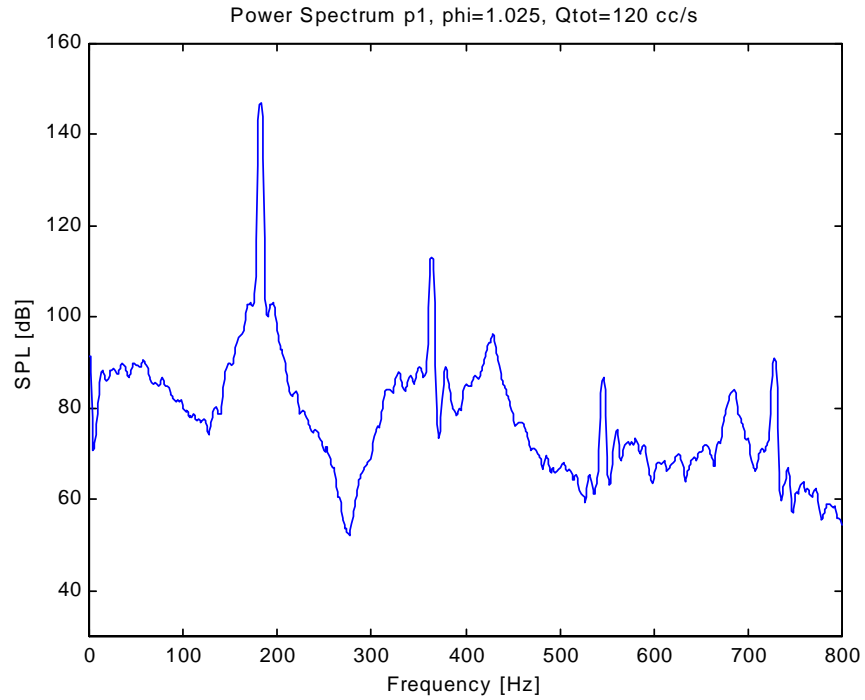


Figure B.18 Pressure power spectrum for  $\phi = 1.025$ ,  $Q_{tot}=120$  cc/s

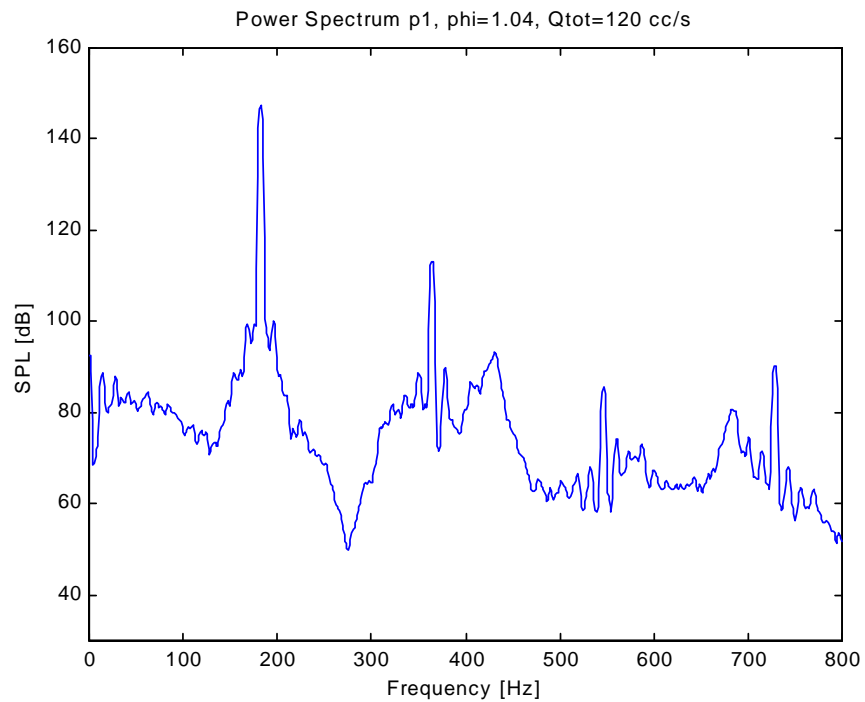


Figure B.19 Pressure power spectrum for  $\phi = 1.04$ ,  $Q_{tot}=120$  cc/s

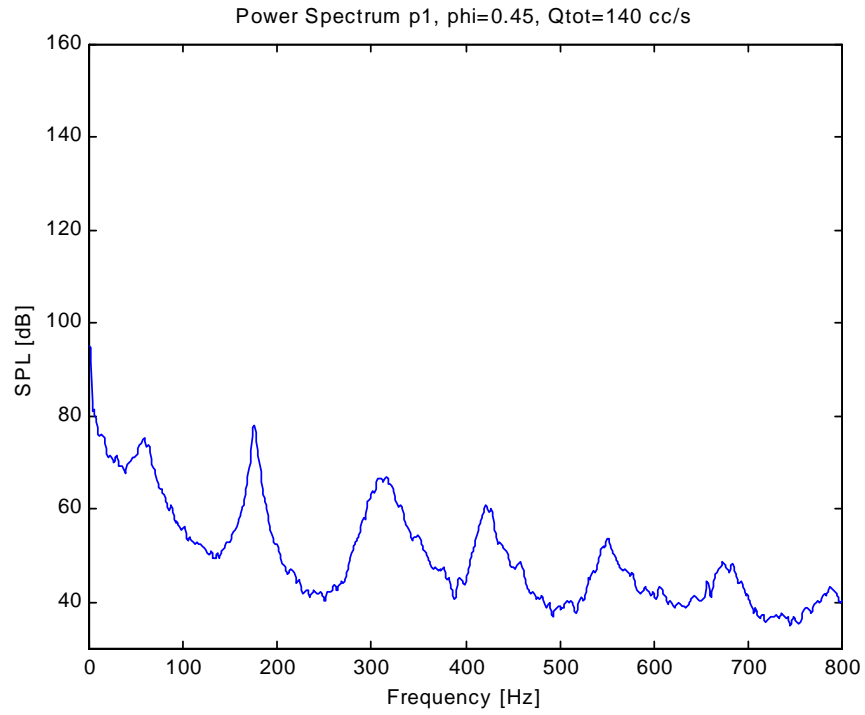


Figure B.20 Pressure power spectrum for  $\phi = 0.45$ ,  $Q_{tot}=140$  cc/s

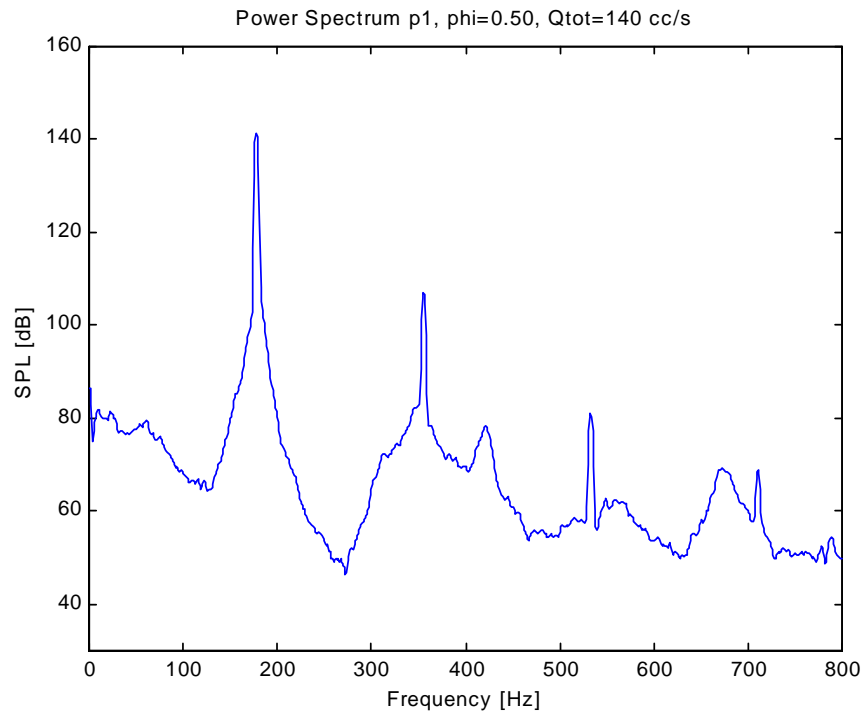


Figure B.21 Pressure power spectrum for  $\phi = 0.50$ ,  $Q_{tot}=140$  cc/s

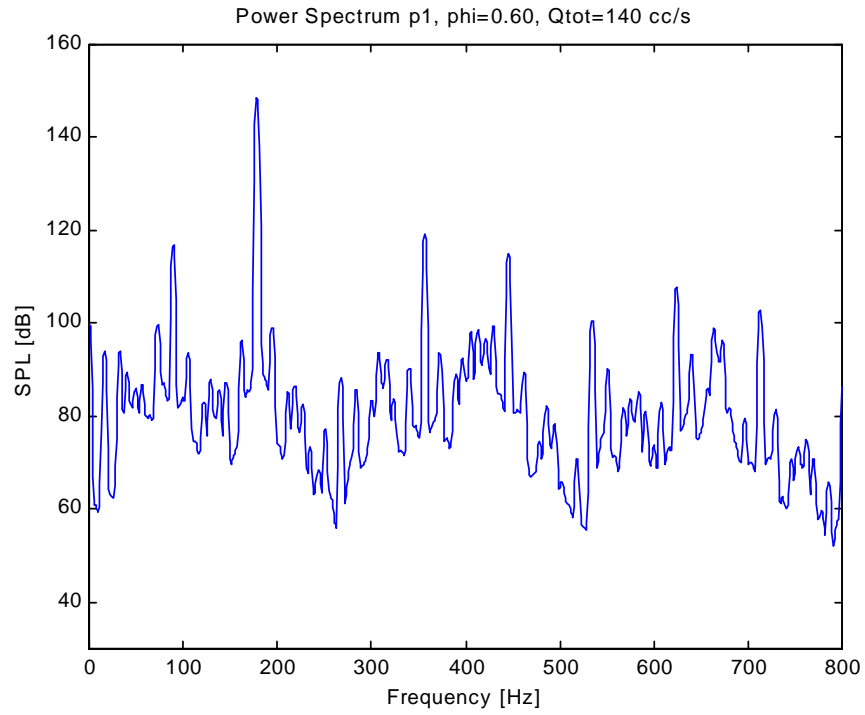


Figure B.22 Pressure power spectrum for  $\phi = 0.60$ ,  $Q_{tot}=140$  cc/s

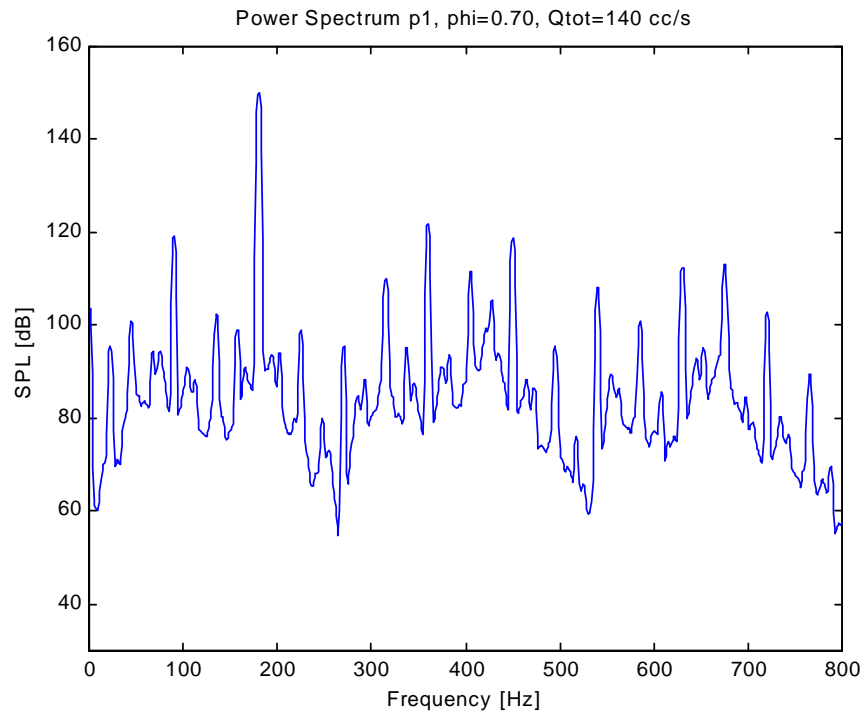


Figure B.23 Pressure power spectrum for  $\phi = 0.70$ ,  $Q_{tot}=140$  cc/s

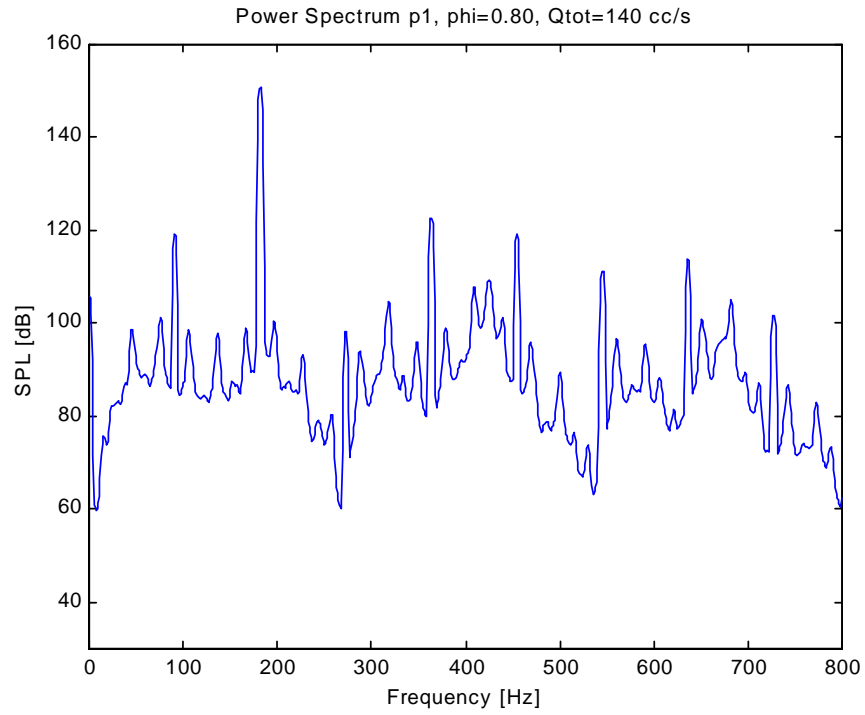


Figure B.24 Pressure power spectrum for  $\phi = 0.80$ ,  $Q_{tot}=140$  cc/s

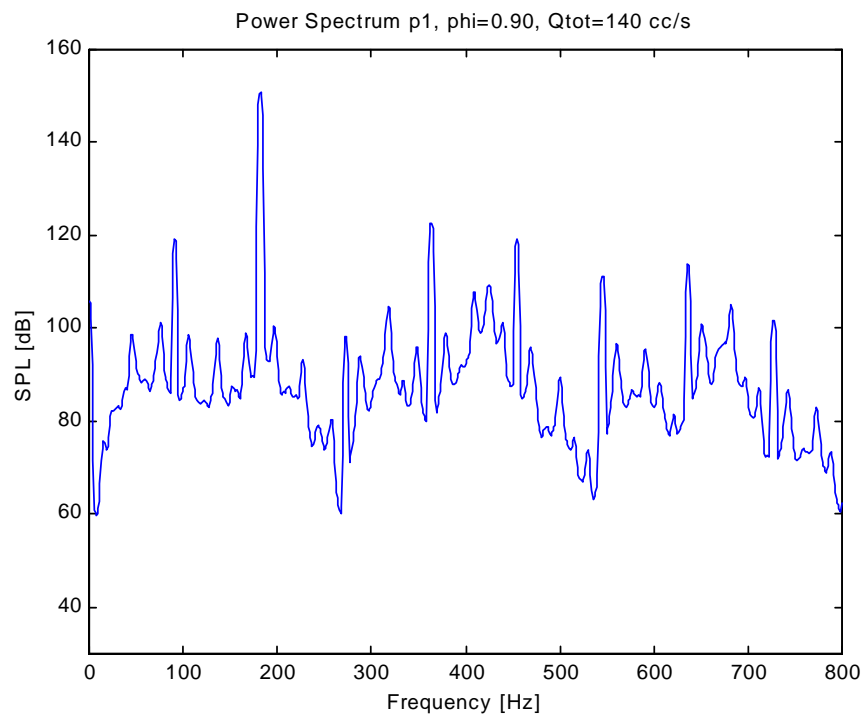


Figure B.25 Pressure power spectrum for  $\phi = 0.90$ ,  $Q_{tot}=140$  cc/s

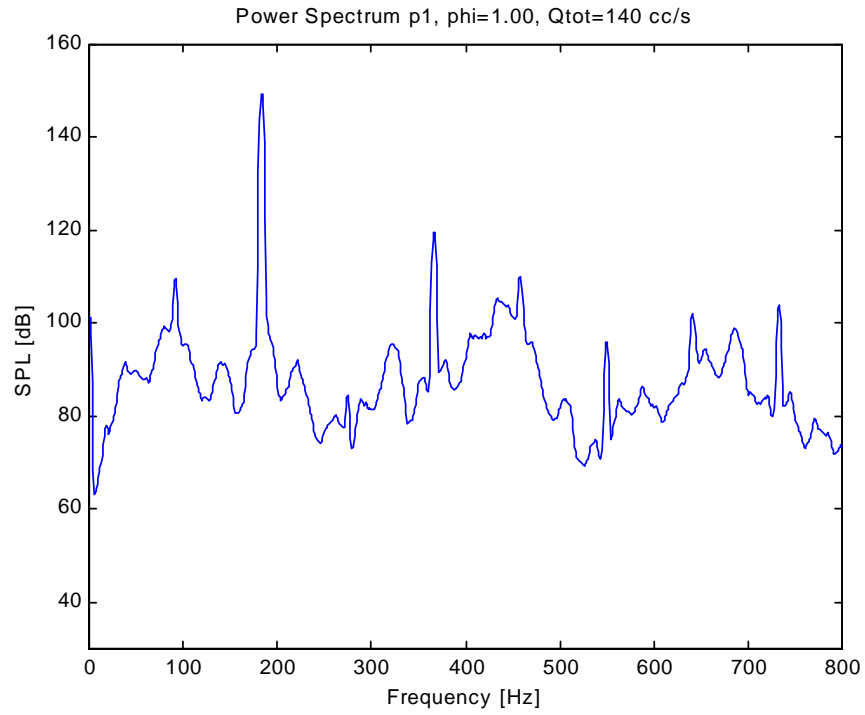


Figure B.26 Pressure power spectrum for  $\phi = 1.00$ ,  $Q_{tot}=140$  cc/s

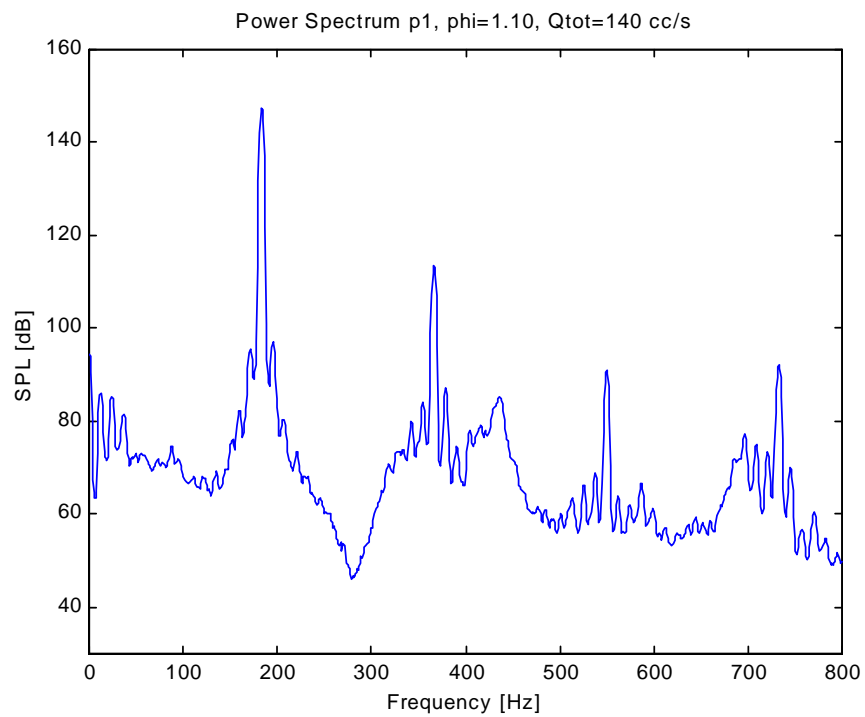


Figure B.27 Pressure power spectrum for  $\phi = 1.10$ ,  $Q_{tot}=140$  cc/s

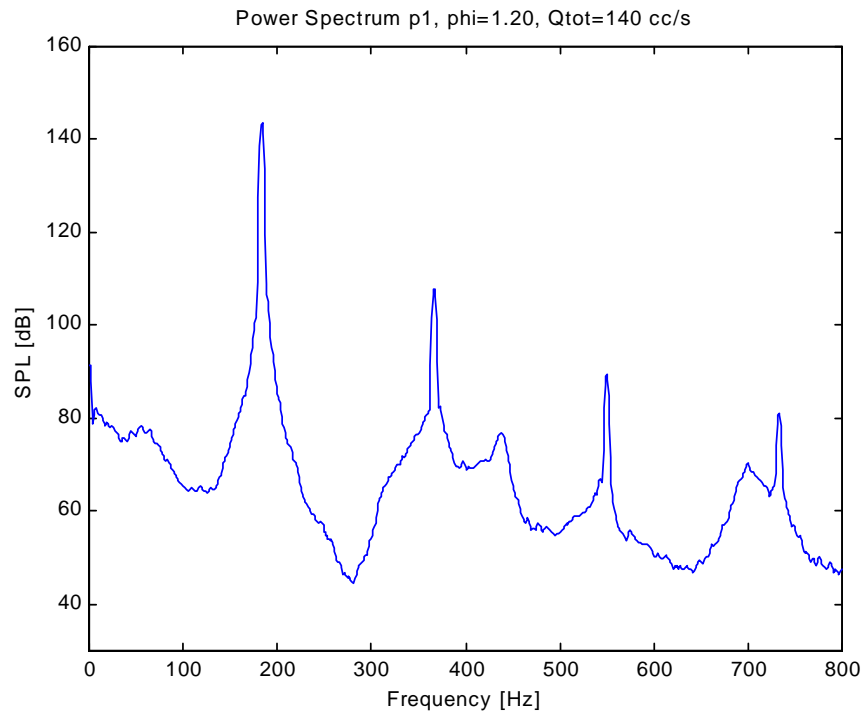


Figure B.28 Pressure power spectrum for  $\phi = 1.20$ ,  $Q_{tot}=140$  cc/s

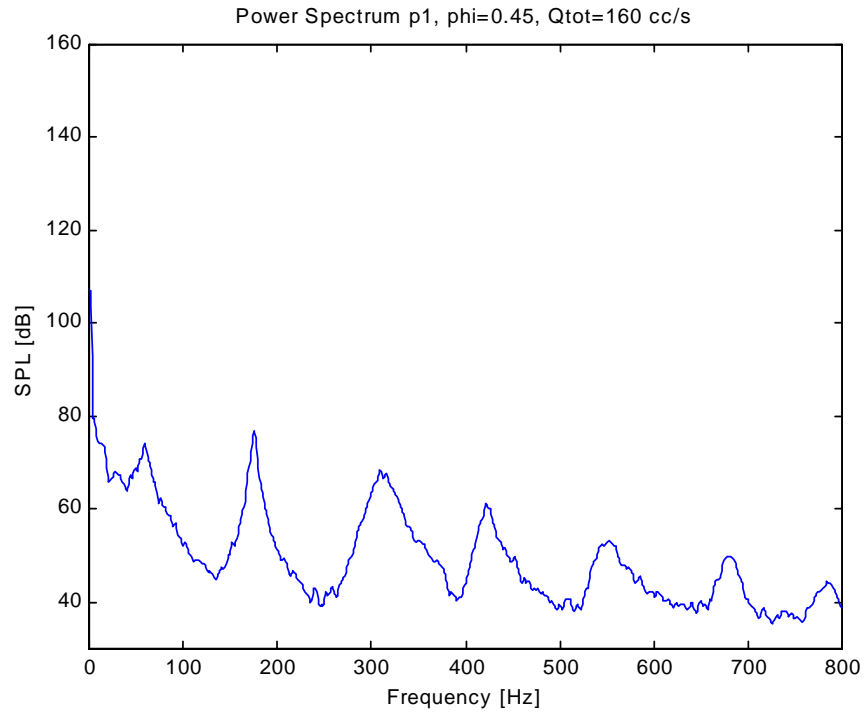


Figure B.29 Pressure power spectrum for  $\phi = 0.45$ ,  $Q_{tot}=160$  cc/s

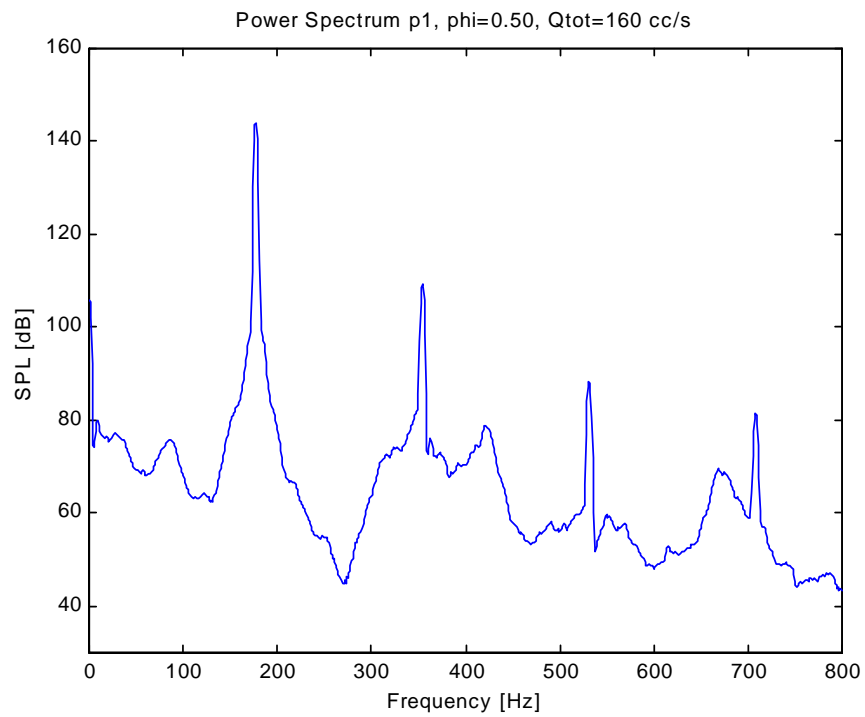


Figure B.30 Pressure power spectrum for  $\phi = 0.50$ ,  $Q_{tot}=160$  cc/s

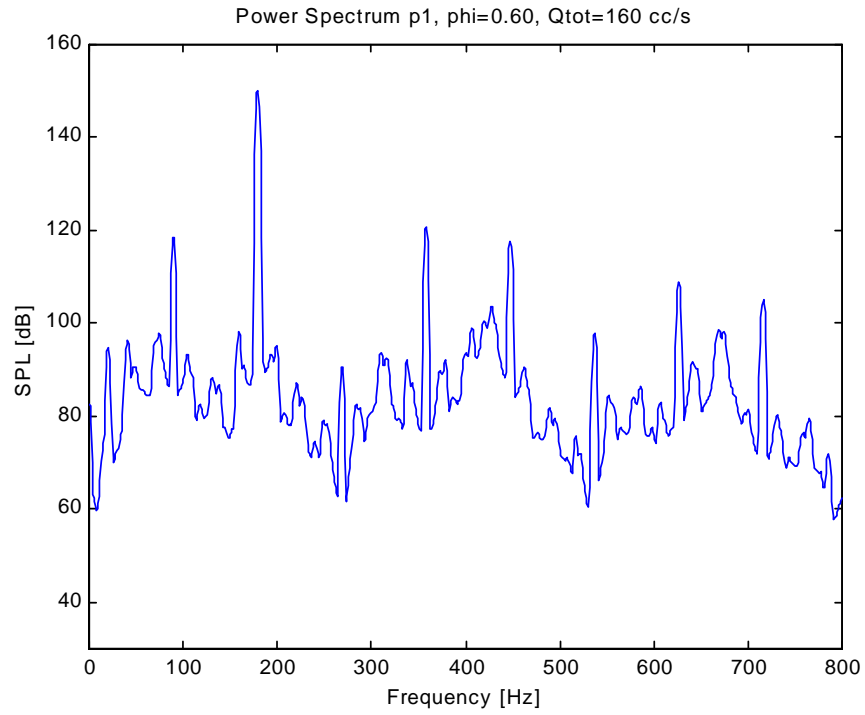


Figure B.31 Pressure power spectrum for  $\phi = 0.60$ ,  $Q_{tot}=160$  cc/s

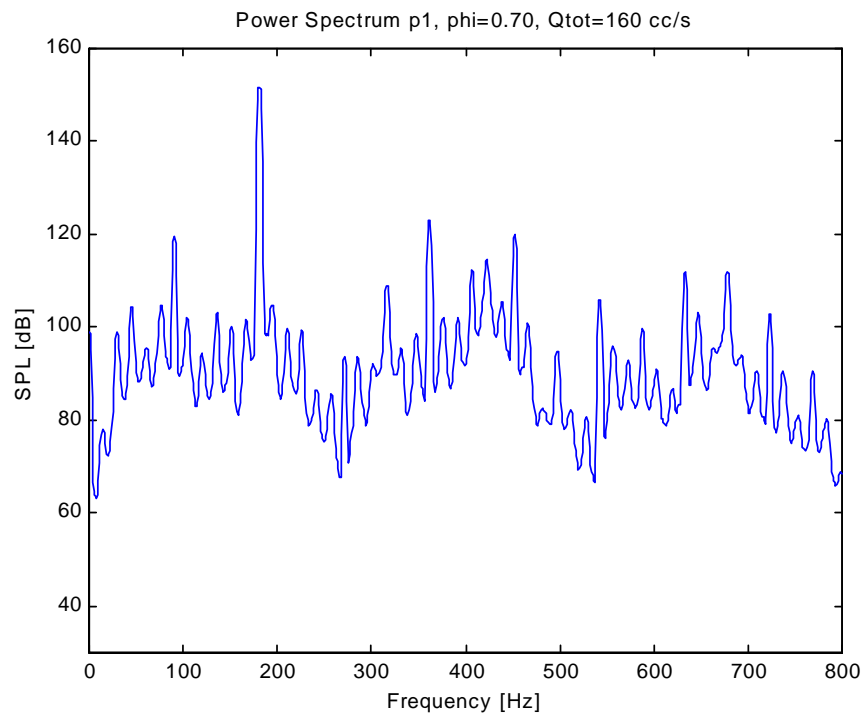


Figure B.32 Pressure power spectrum for  $\phi = 0.70$ ,  $Q_{tot}=160$  cc/s

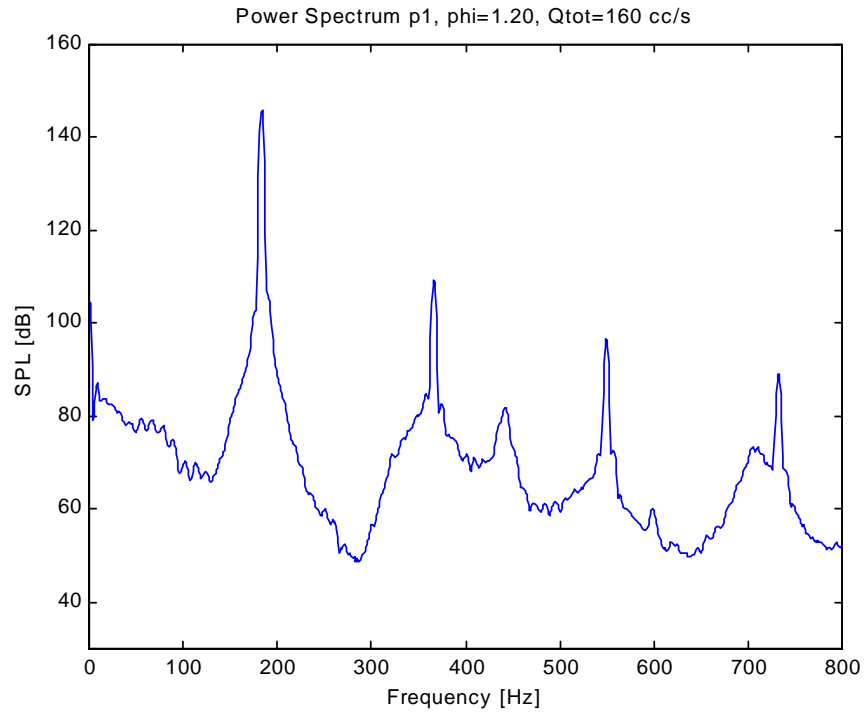


Figure B.33 Pressure power spectrum for  $\phi = 1.20$ ,  $Q_{tot}=160$  cc/s

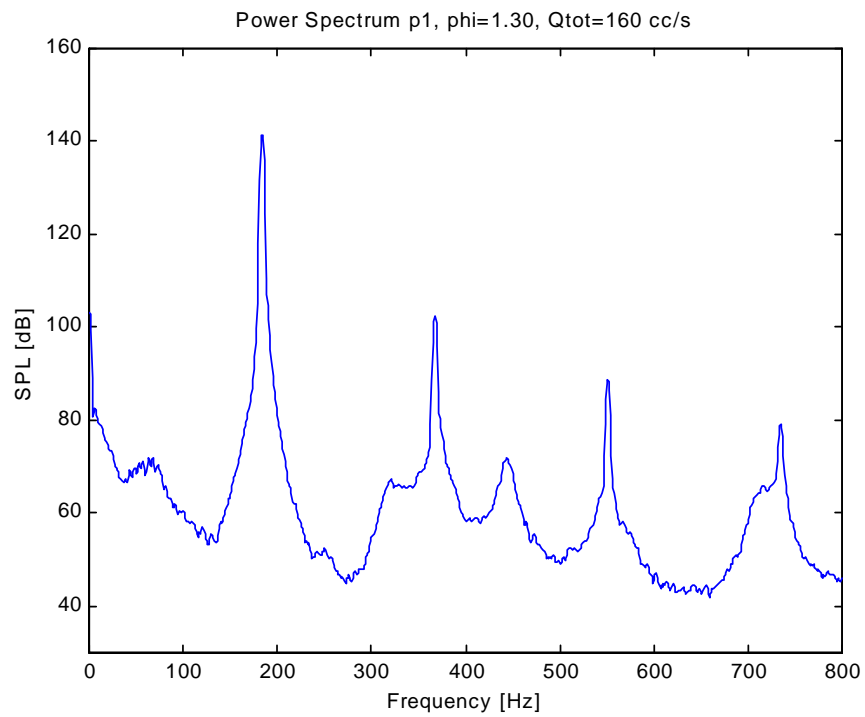


Figure B.34 Pressure power spectrum for  $\phi = 1.30$ ,  $Q_{tot}=160$  cc/s

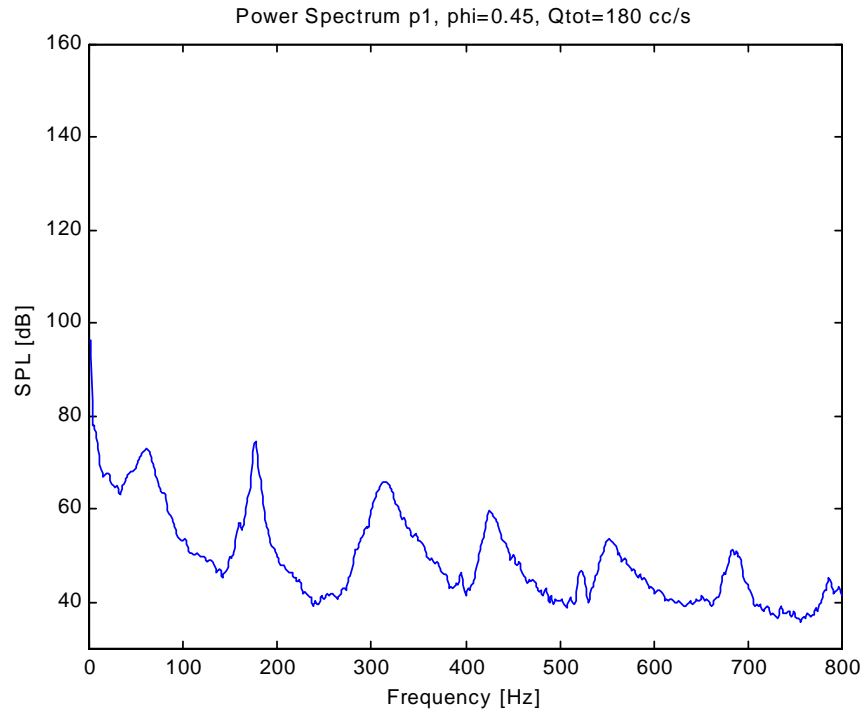


Figure B.35 Pressure power spectrum for  $\phi = 0.45$ ,  $Q_{tot} = 180$  cc/s

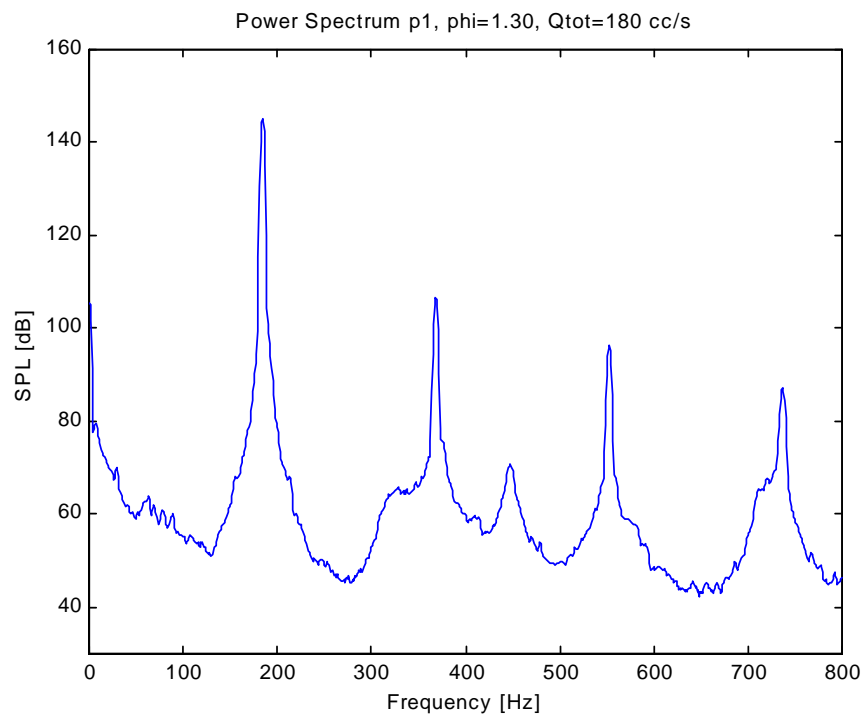


Figure B.36 Pressure power spectrum for  $\phi = 1.30$ ,  $Q_{tot} = 180$  cc/s

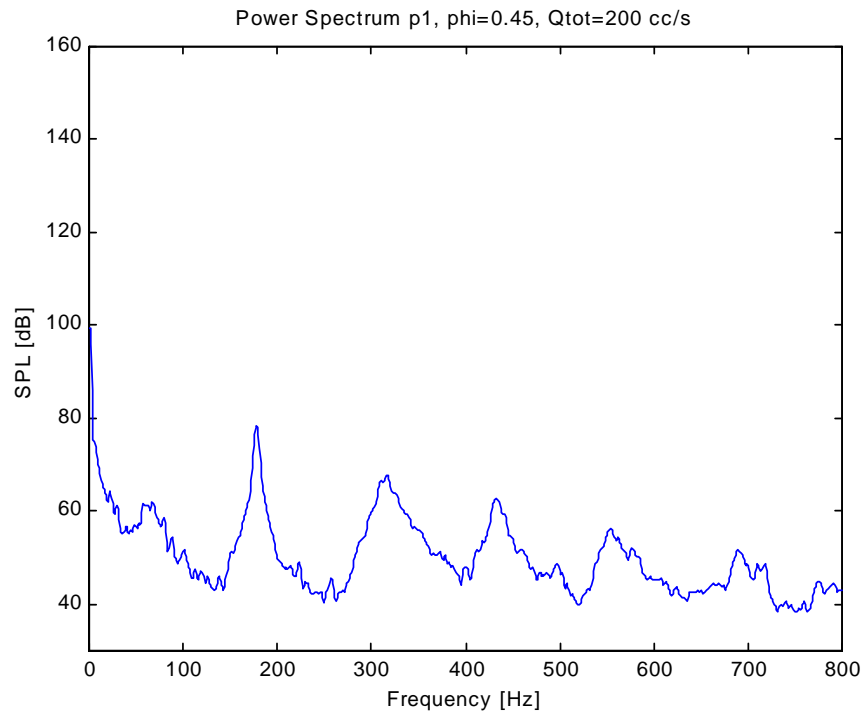


Figure B.37 Pressure power spectrum for  $\phi = 0.45$ ,  $Q_{tot}=200$  cc/s

## **Appendix C    OH\* Power Spectra for Constant Equivalence Ratio**

In Appendix C, power spectra of the OH\* measurements from the extensive mapping experiments will be presented. The equivalence ratio was held constant with varying flow rate for each data series. First the 0.50-equivalence ratio series will be presented, followed by  $\phi = 0.60, 0.80$  and  $1.00$  respectively. All OH\* voltage levels have a reference voltage of 1 Vrms.

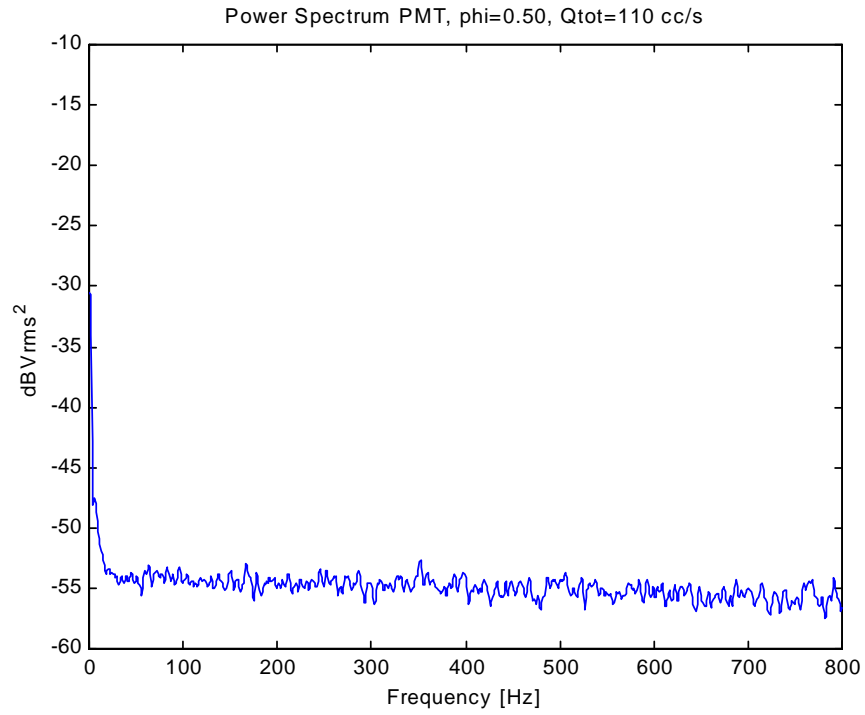


Figure C.1  $OH^*$  power spectrum for  $\phi = 0.50$ ,  $Q_{tot}=110$  cc/s

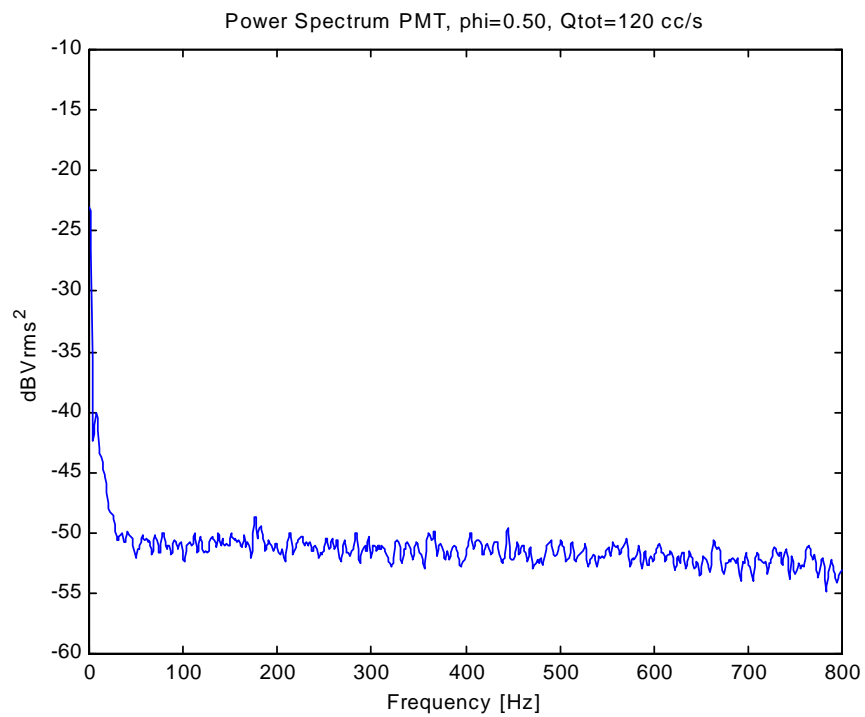


Figure C.2  $OH^*$  power spectrum for  $\phi = 0.50$ ,  $Q_{tot}=120$  cc/s

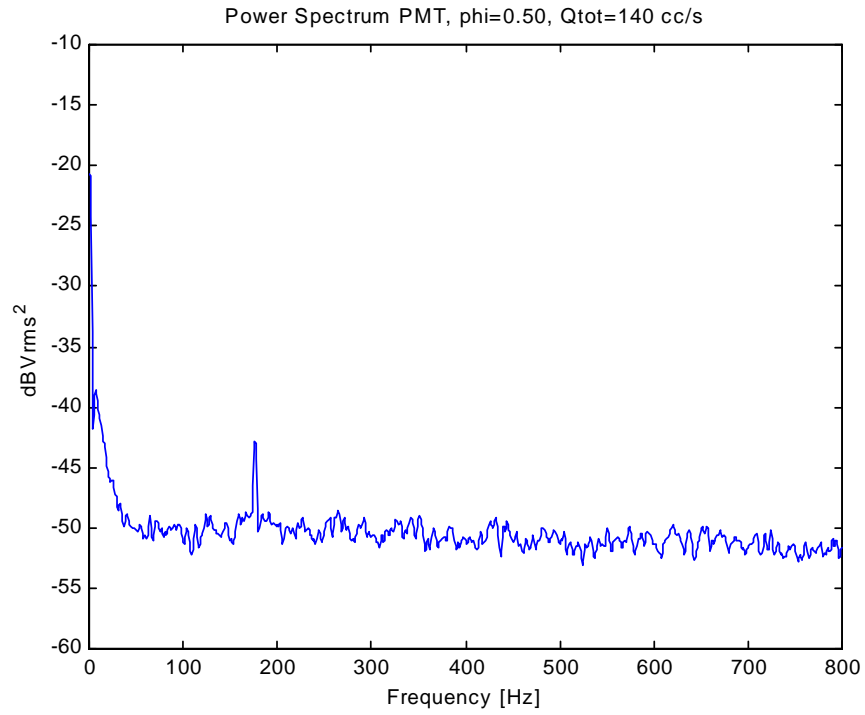


Figure C.3  $OH^*$  power spectrum for  $\phi = 0.50$ ,  $Q_{tot}=140$  cc/s

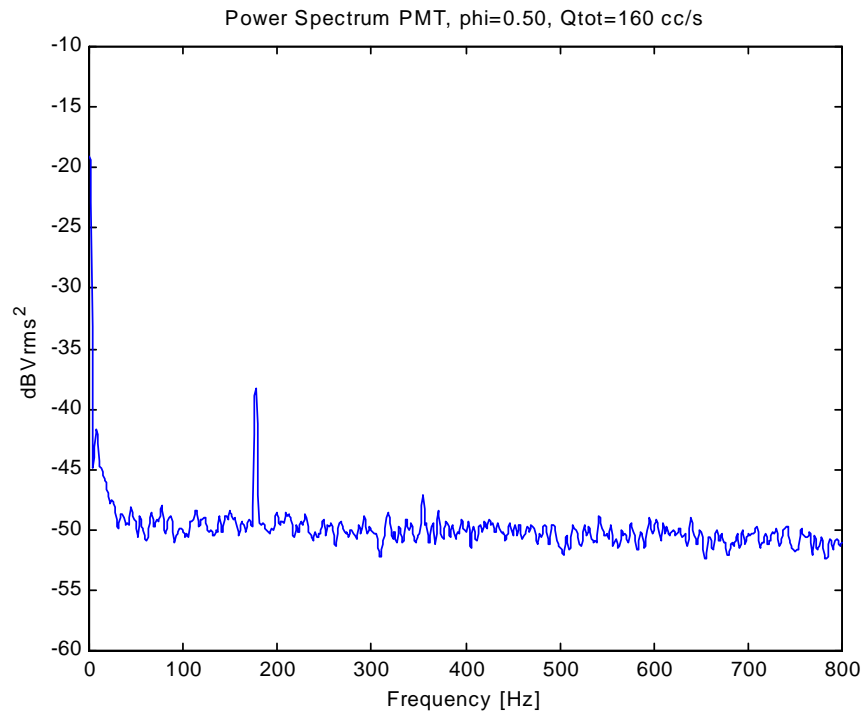


Figure C.4  $OH^*$  power spectrum for  $\phi = 0.50$ ,  $Q_{tot}=160$  cc/s

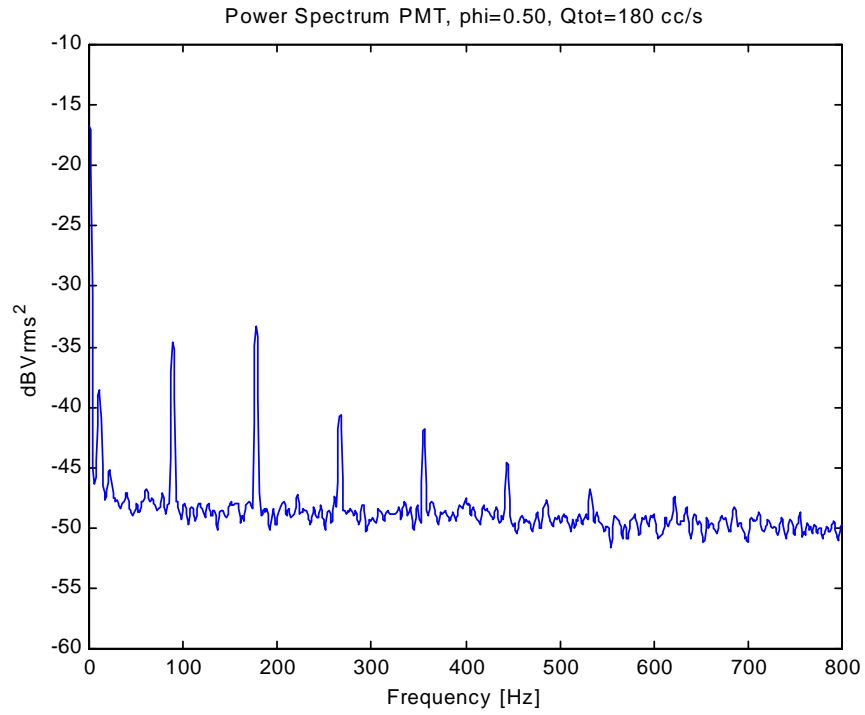


Figure C.5  $OH^*$  power spectrum for  $\phi = 0.50$ ,  $Q_{tot}=180$  cc/s

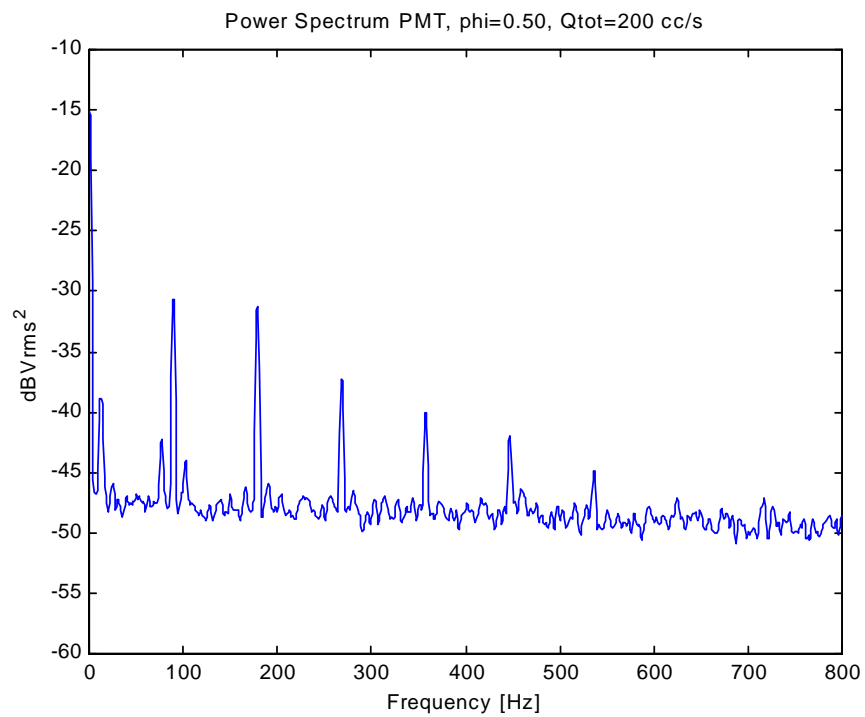


Figure C.6  $OH^*$  power spectrum for  $\phi = 0.50$ ,  $Q_{tot}=200$  cc/s

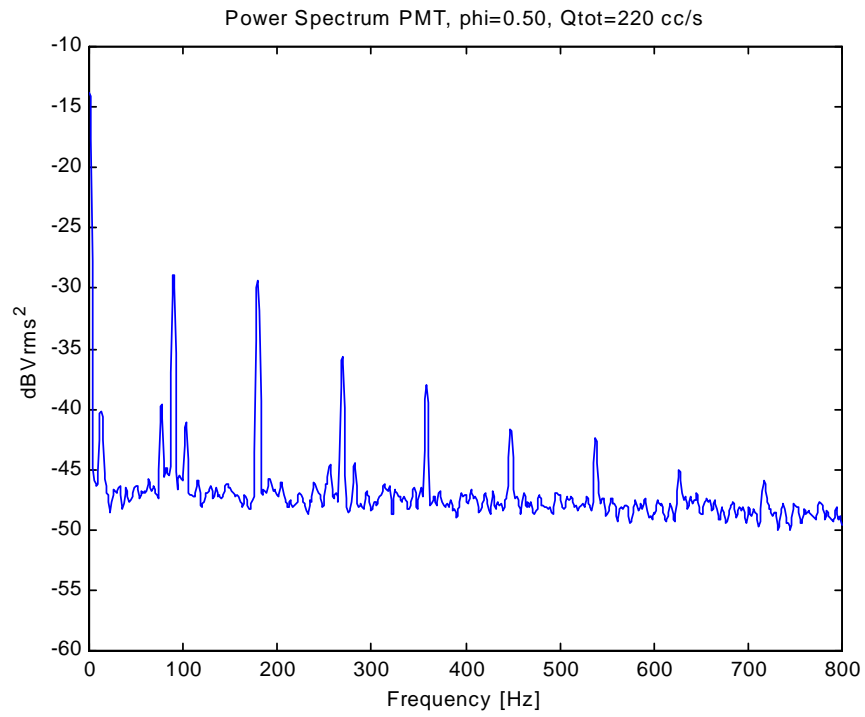


Figure C.7  $OH^*$  power spectrum for  $\phi = 0.50$ ,  $Q_{tot}=220$  cc/s

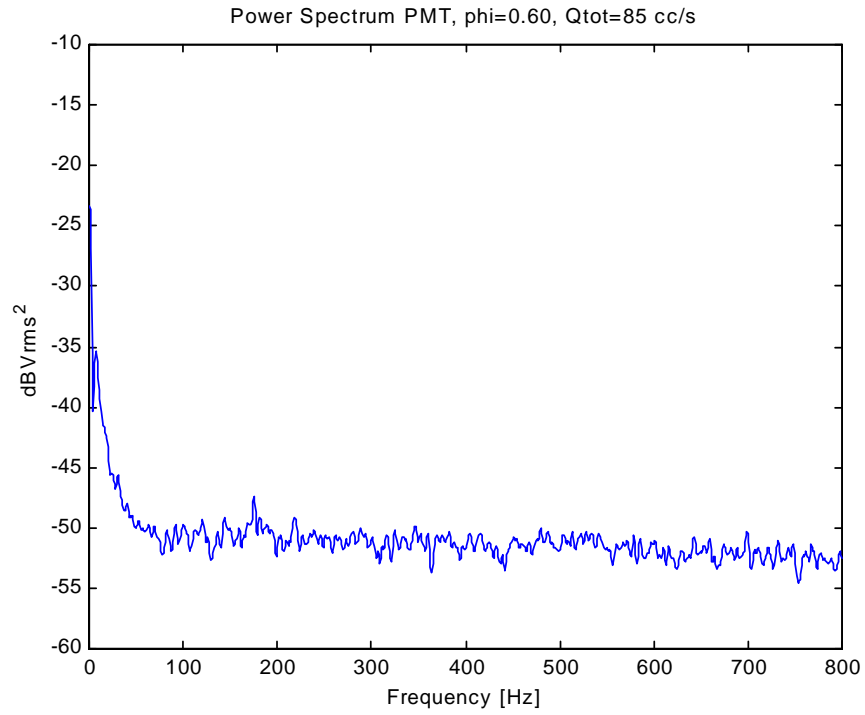


Figure C.8  $OH^*$  power spectrum for  $\phi = 0.60$ ,  $Q_{tot}=85$  cc/s

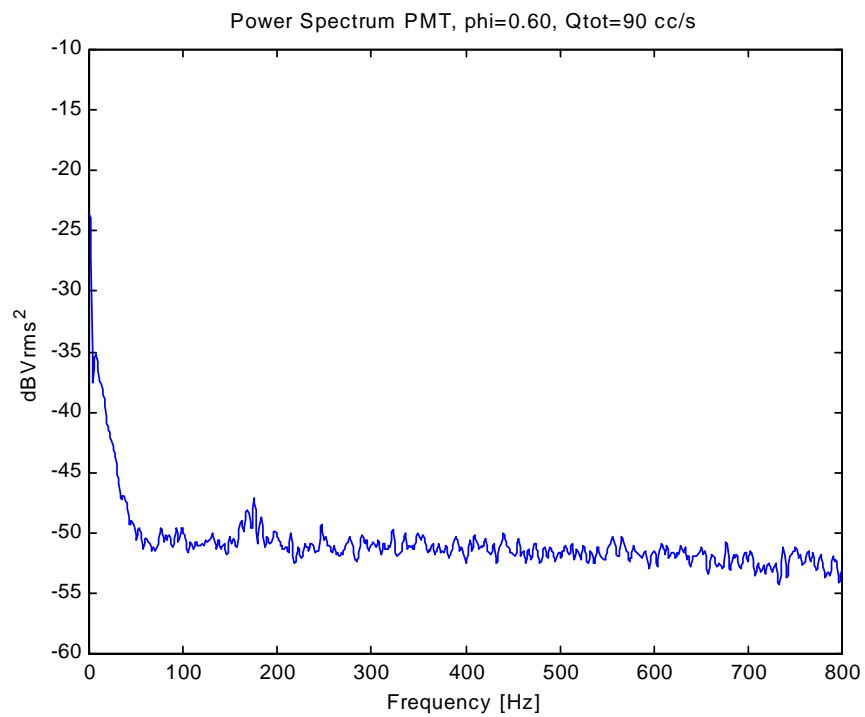


Figure C.9  $OH^*$  power spectrum for  $\phi = 0.60$ ,  $Q_{tot}=90$  cc/s

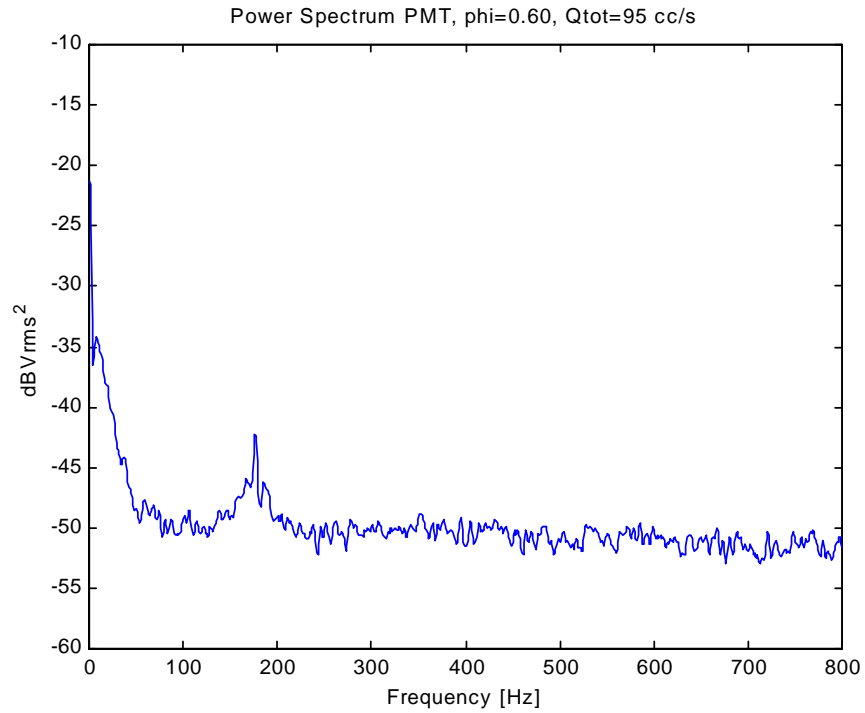


Figure C.10  $OH^*$  power spectrum for  $\phi = 0.60$ ,  $Q_{tot}=95$  cc/s

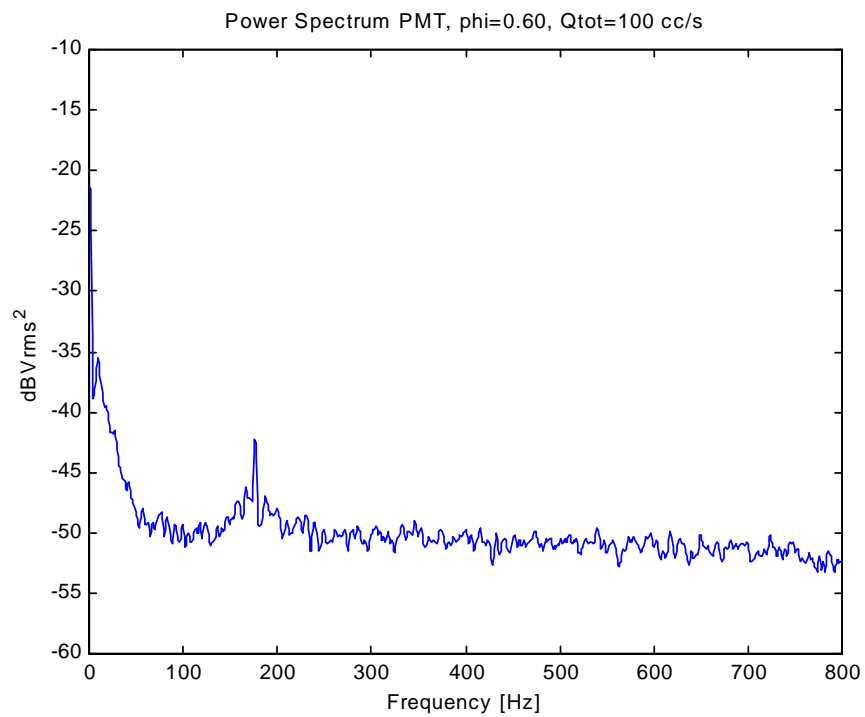


Figure C.11  $OH^*$  power spectrum for  $\phi = 0.60$ ,  $Q_{tot}=100$  cc/s

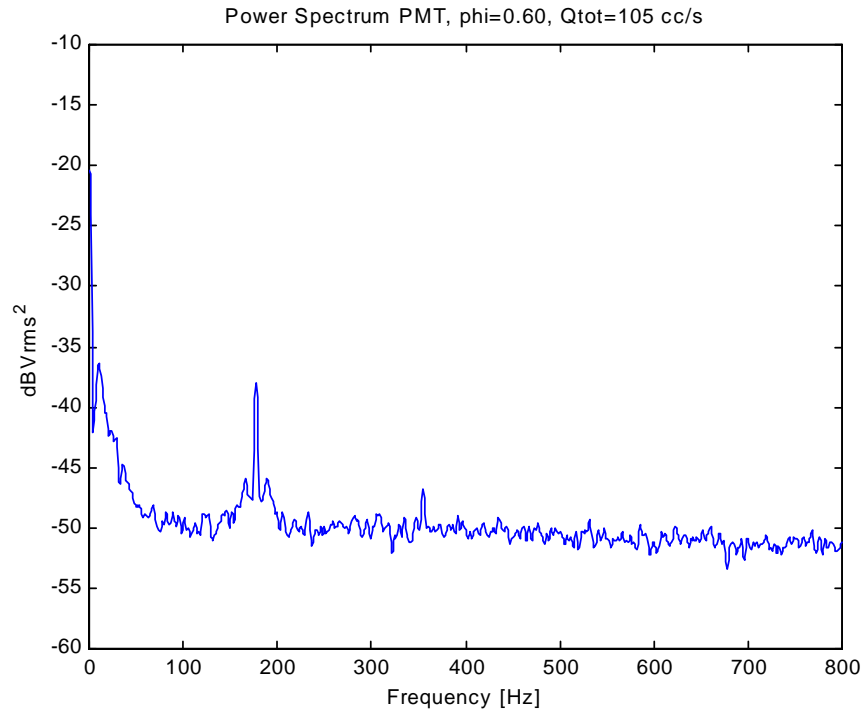


Figure C.12  $OH^*$  power spectrum for  $\phi = 0.60$ ,  $Q_{tot}=105$  cc/s

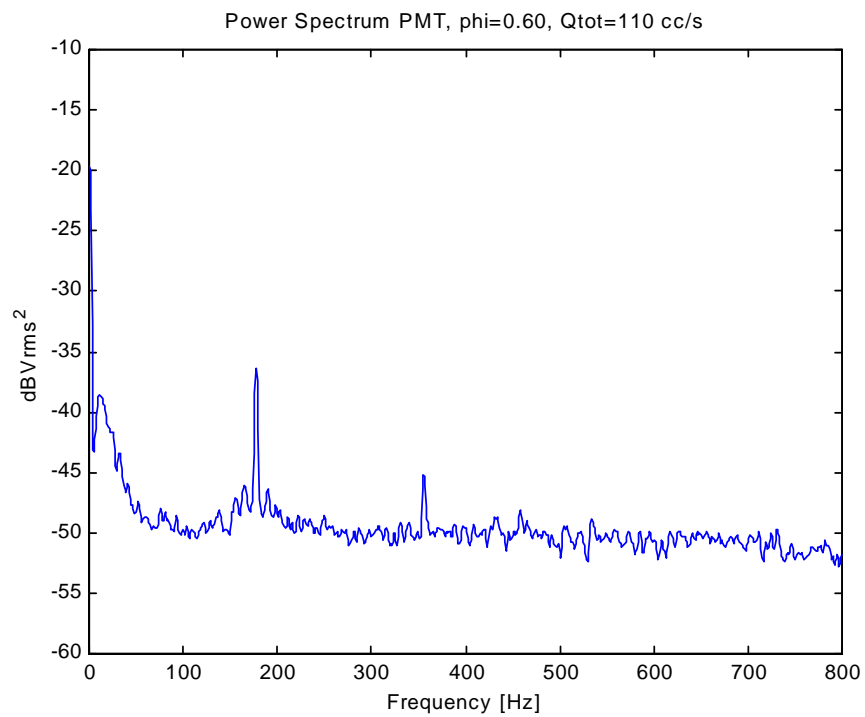


Figure C.13  $OH^*$  power spectrum for  $\phi = 0.60$ ,  $Q_{tot}=110$  cc/s

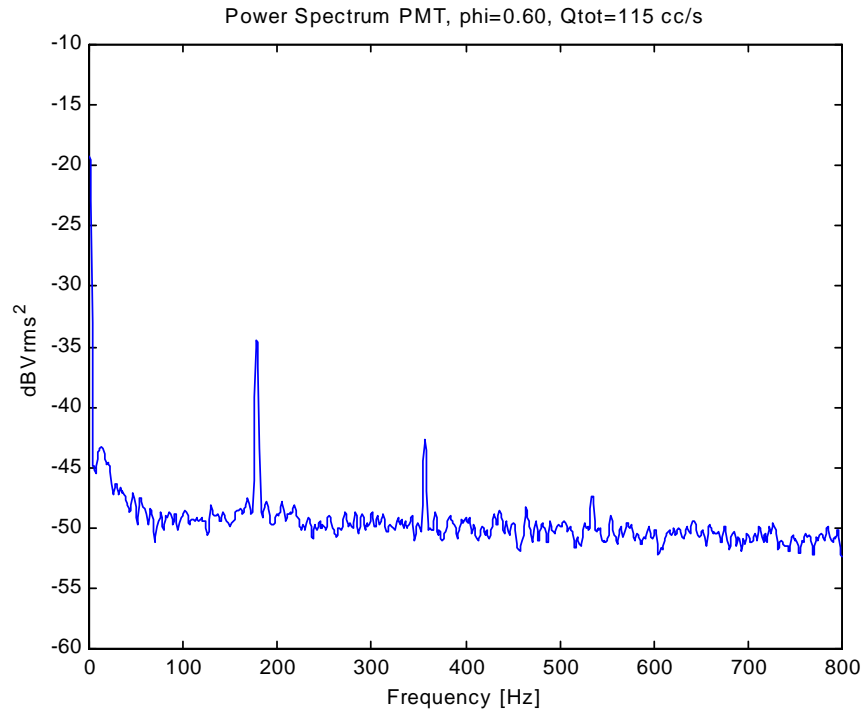


Figure C.14  $OH^*$  power spectrum for  $\phi = 0.60$ ,  $Q_{tot}=115$  cc/s

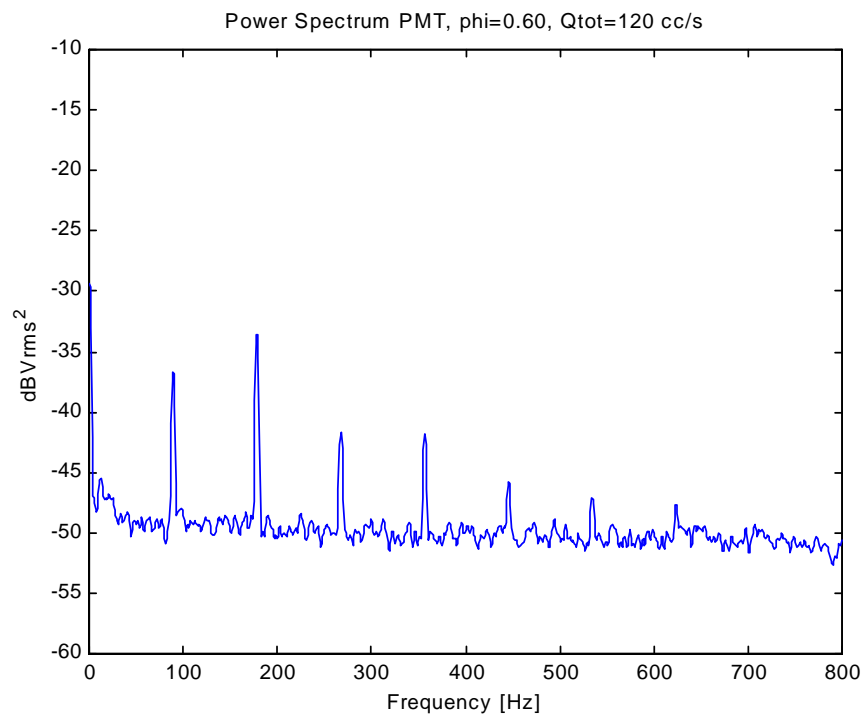


Figure C.15  $OH^*$  power spectrum for  $\phi = 0.60$ ,  $Q_{tot}=120$  cc/s

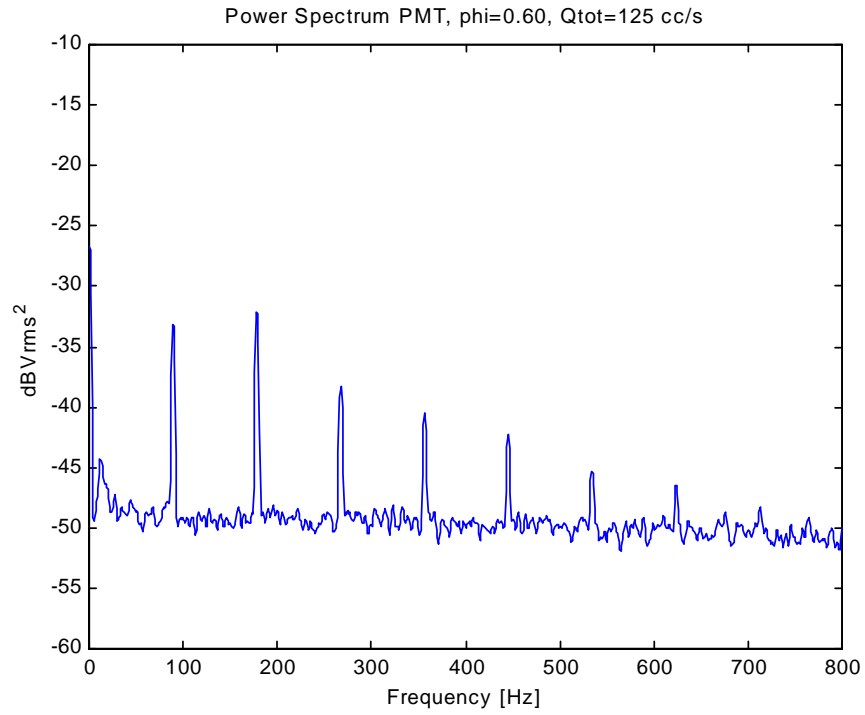


Figure C.16  $OH^*$  power spectrum for  $\phi = 0.60$ ,  $Q_{tot}=125$  cc/s

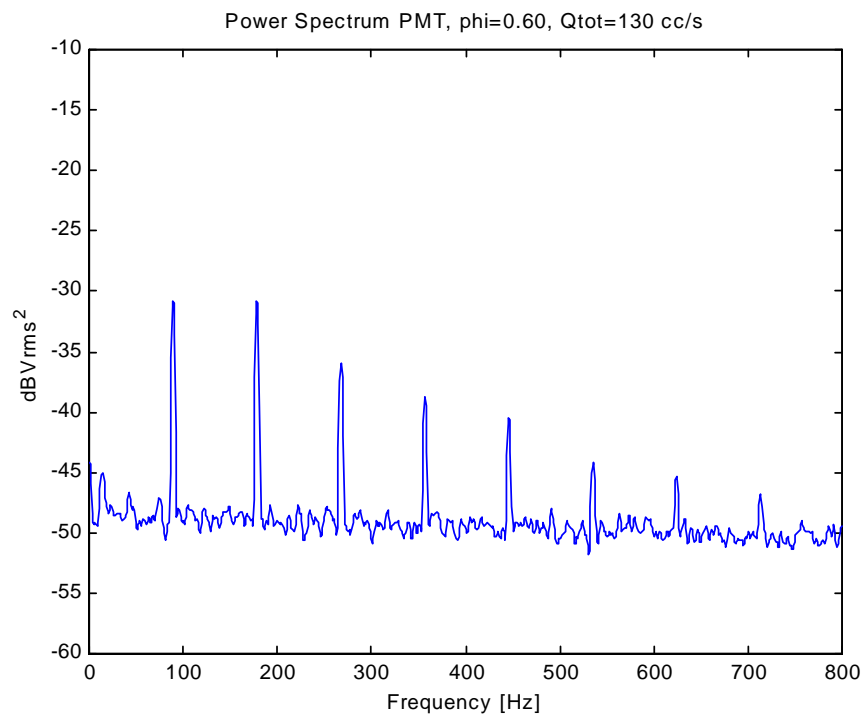


Figure C.17  $OH^*$  power spectrum for  $\phi = 0.60$ ,  $Q_{tot}=130$  cc/s

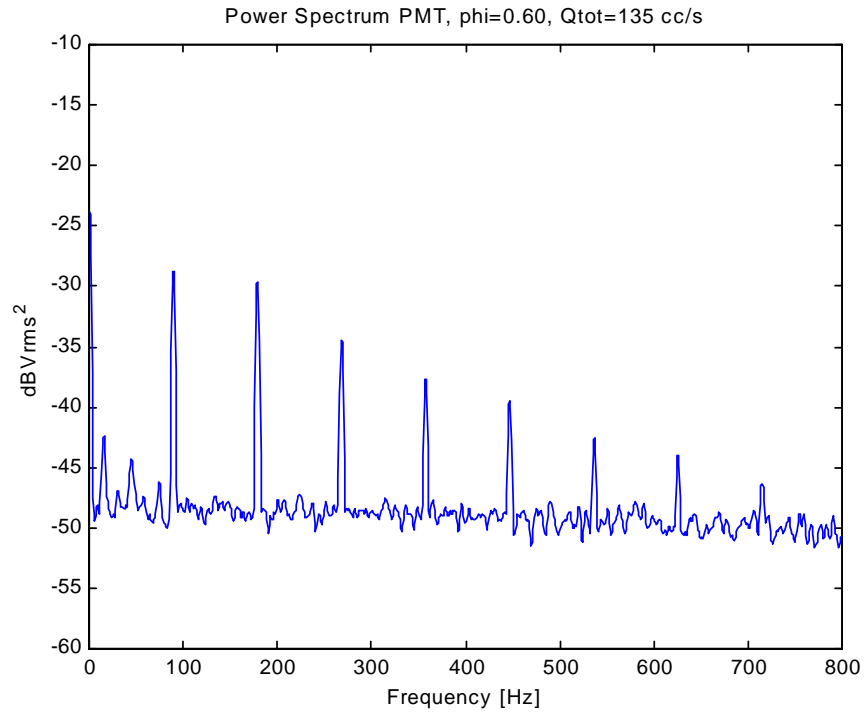


Figure C.18  $OH^*$  power spectrum for  $\phi = 0.60$ ,  $Q_{tot}=135$  cc/s

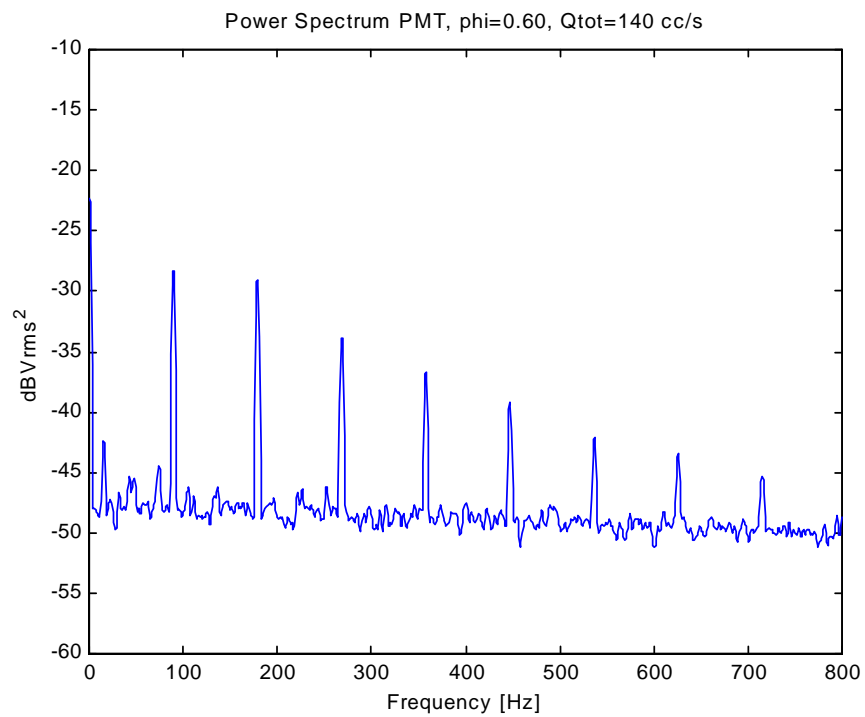


Figure C.19  $OH^*$  power spectrum for  $\phi = 0.60$ ,  $Q_{tot}=140$  cc/s

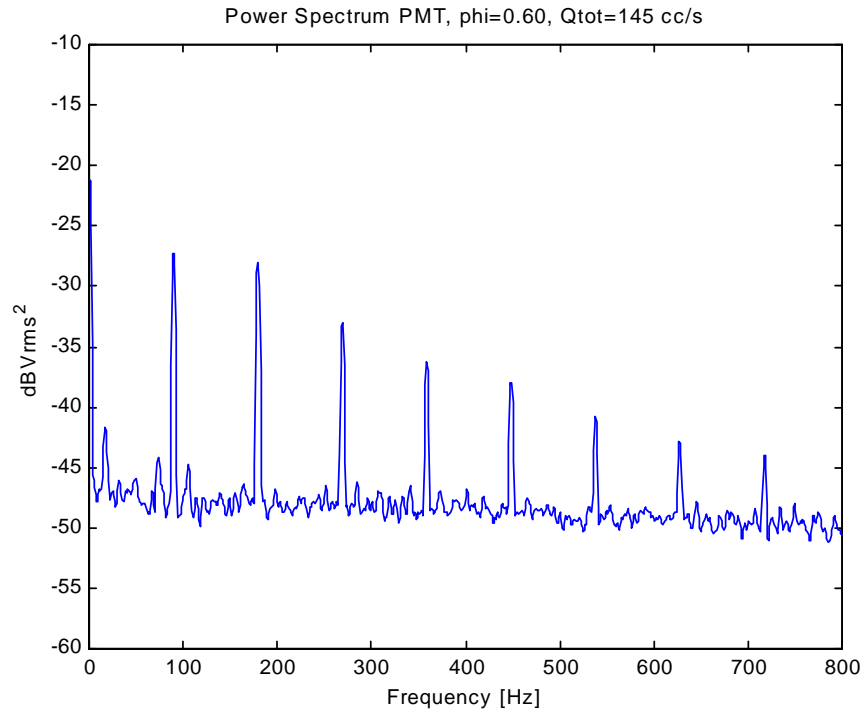


Figure C.20  $OH^*$  power spectrum for  $\phi = 0.60$ ,  $Q_{tot}=145$  cc/s

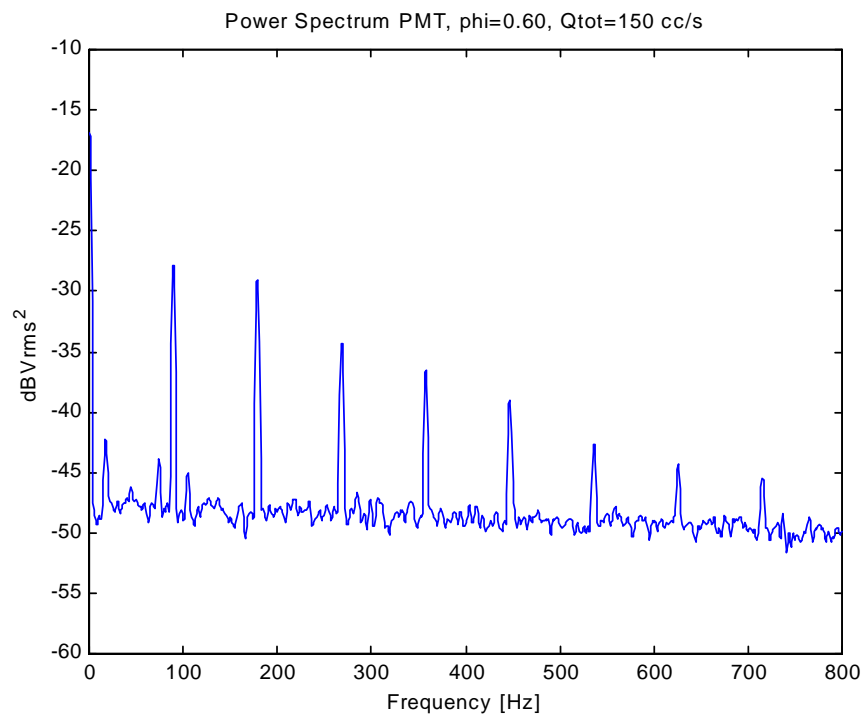


Figure C.21  $OH^*$  power spectrum for  $\phi = 0.60$ ,  $Q_{tot}=150$  cc/s

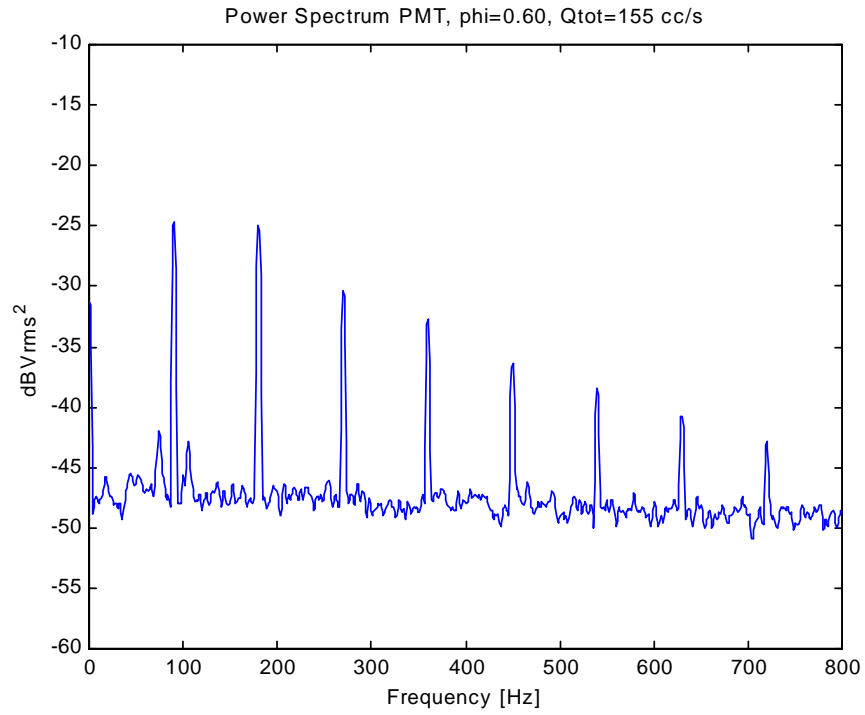


Figure C.22  $OH^*$  power spectrum for  $\phi = 0.60$ ,  $Q_{tot}=155$  cc/s

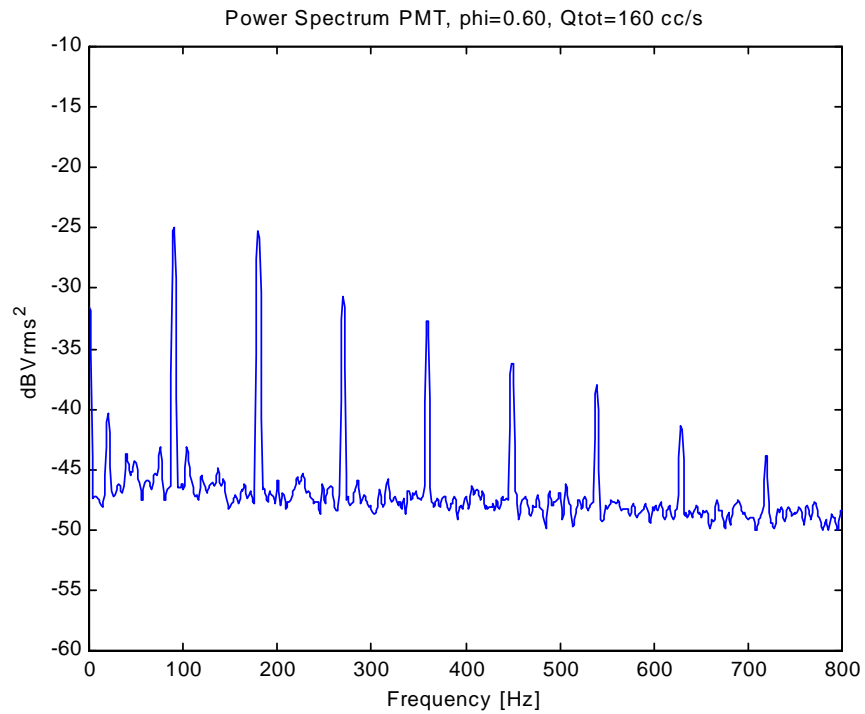


Figure C.23  $OH^*$  power spectrum for  $\phi = 0.60$ ,  $Q_{tot}=160$  cc/s

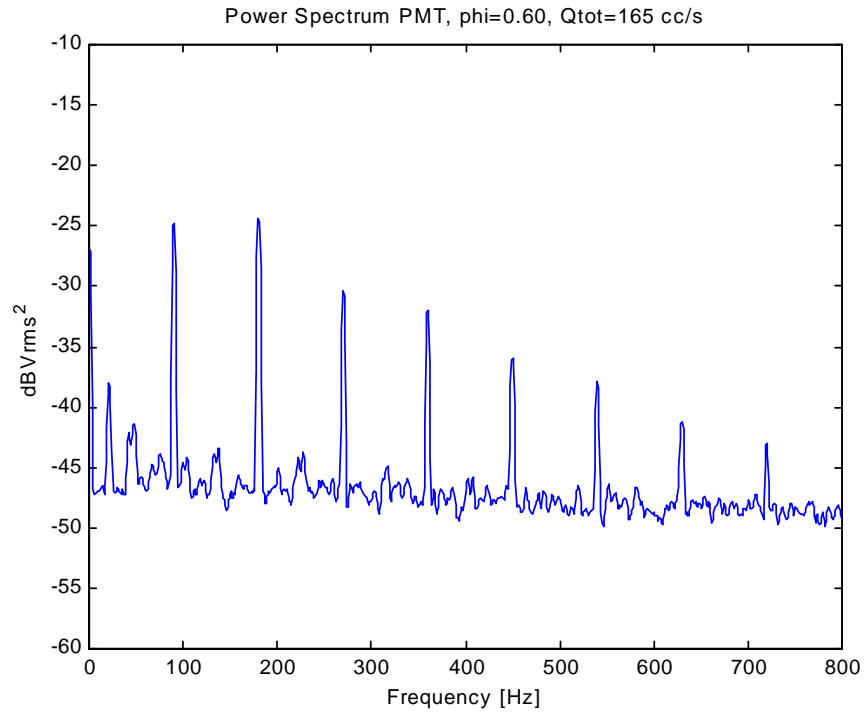


Figure C.24  $OH^*$  power spectrum for  $\phi = 0.60$ ,  $Q_{tot}=165$  cc/s

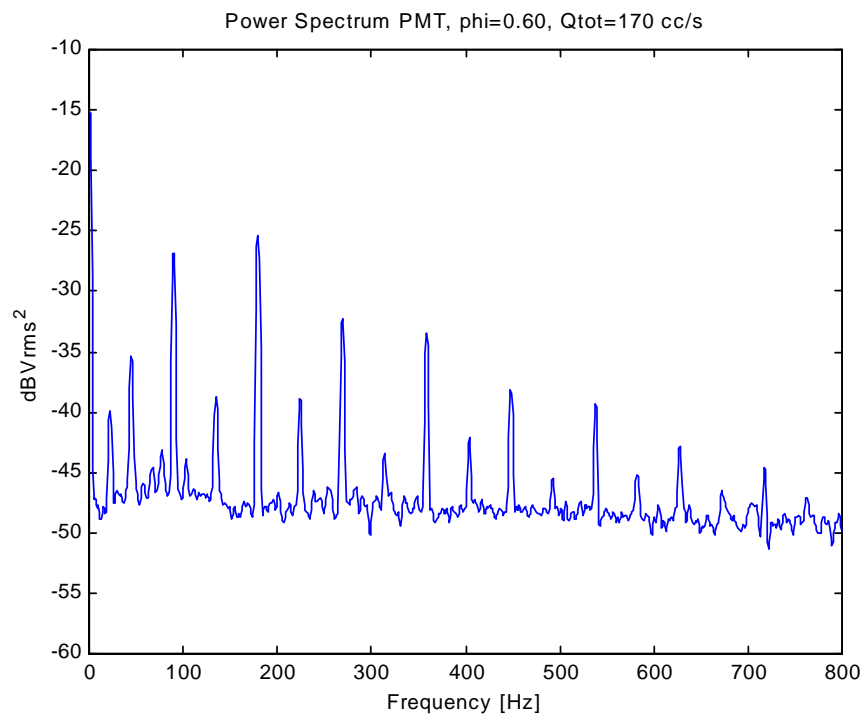


Figure C.25  $OH^*$  power spectrum for  $\phi = 0.60$ ,  $Q_{tot}=170$  cc/s

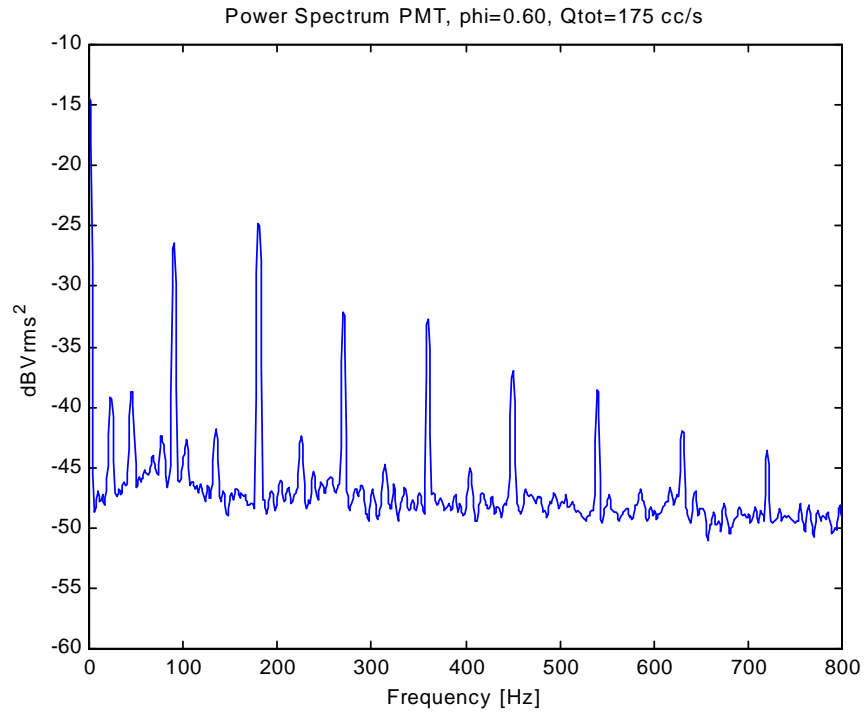


Figure C.26  $OH^*$  power spectrum for  $\phi = 0.60$ ,  $Q_{tot}=175$  cc/s

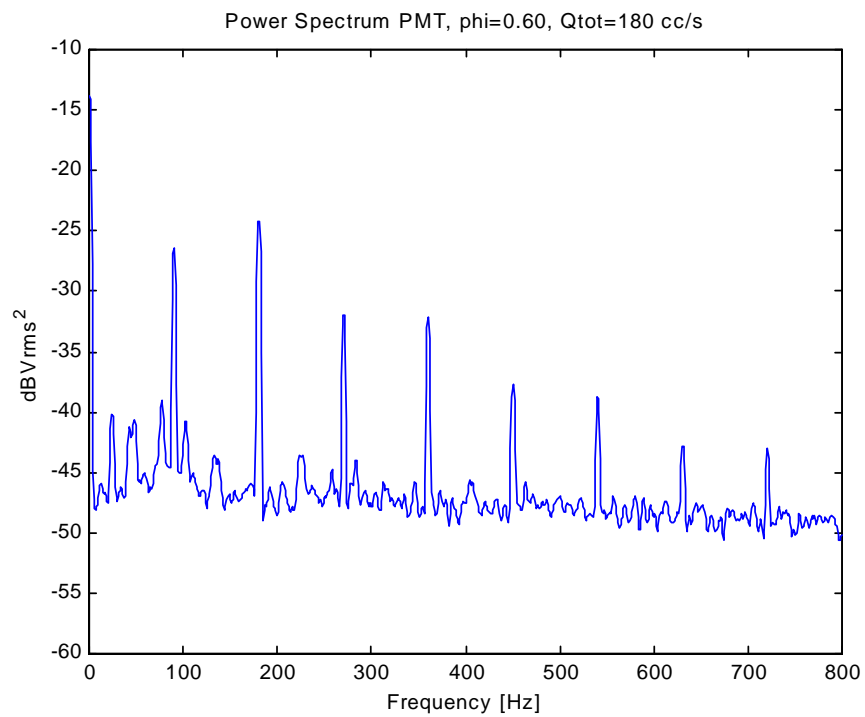


Figure C.27  $OH^*$  power spectrum for  $\phi = 0.60$ ,  $Q_{tot}=180$  cc/s

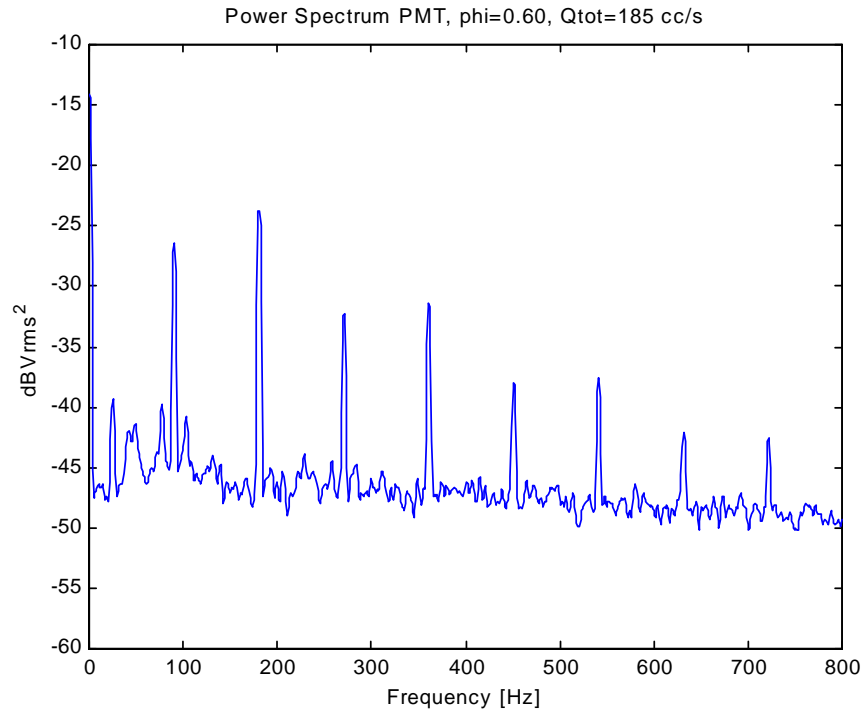


Figure C.28  $OH^*$  power spectrum for  $\phi = 0.60$ ,  $Q_{tot}=185$  cc/s

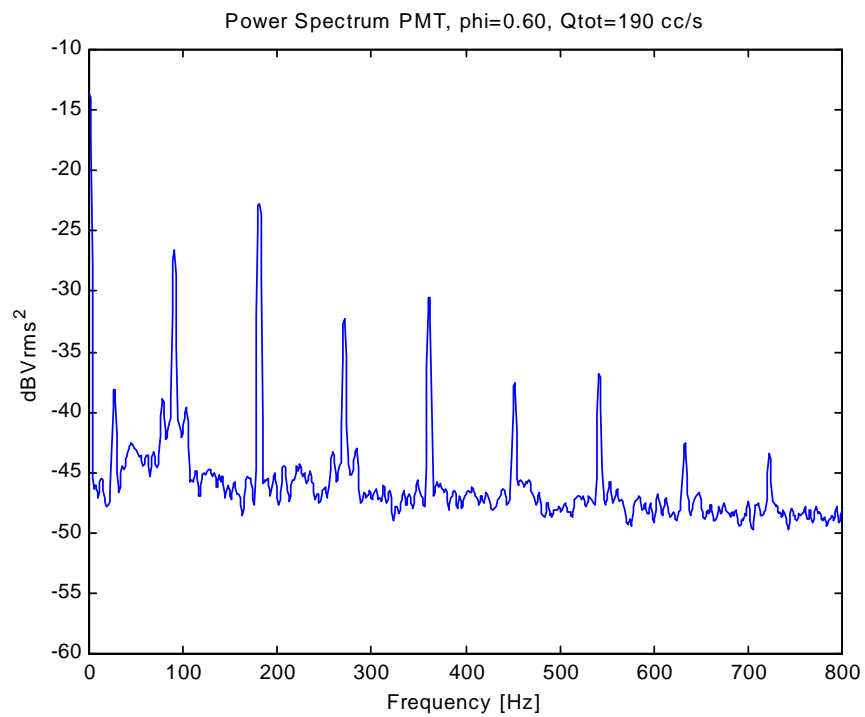


Figure C.29  $OH^*$  power spectrum for  $\phi = 0.60$ ,  $Q_{tot}=190$  cc/s

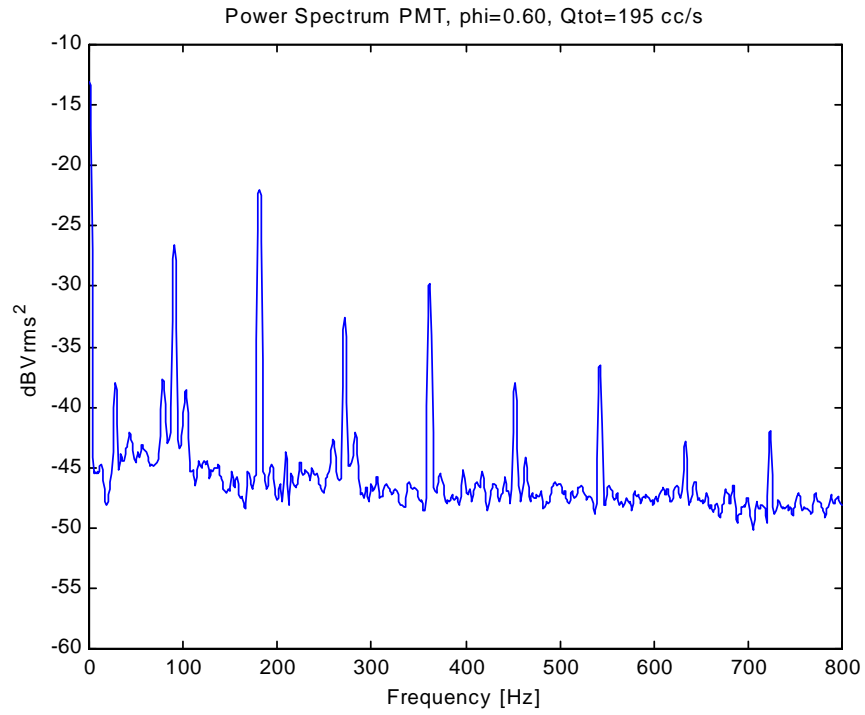


Figure C.30  $OH^*$  power spectrum for  $\phi = 0.60$ ,  $Q_{tot}=195$  cc/s

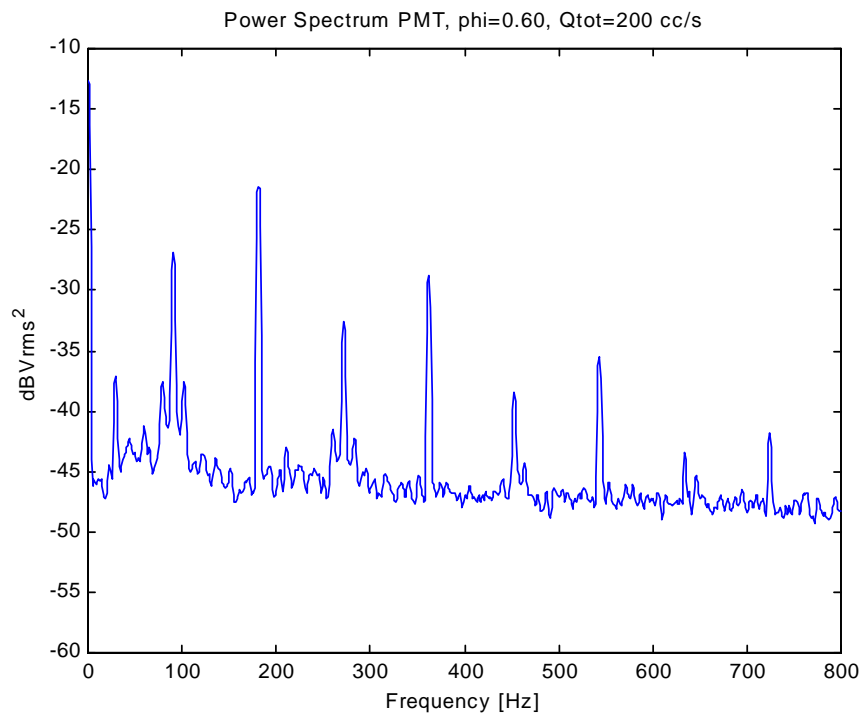


Figure C.31  $OH^*$  power spectrum for  $\phi = 0.60$ ,  $Q_{tot}=200$  cc/s

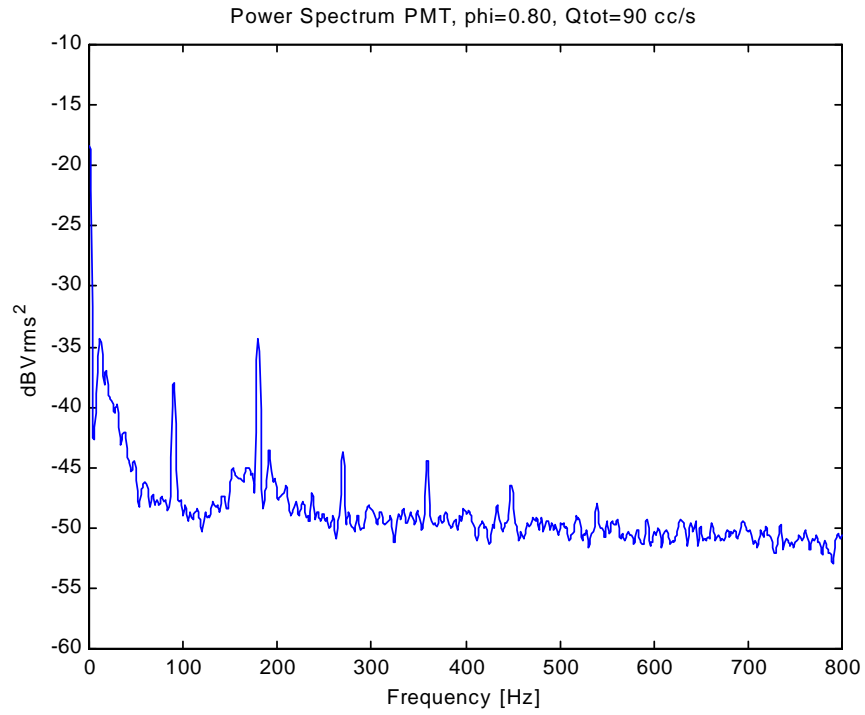


Figure C.32  $OH^*$  power spectrum for  $\phi = 0.80$ ,  $Q_{tot}=90$  cc/s

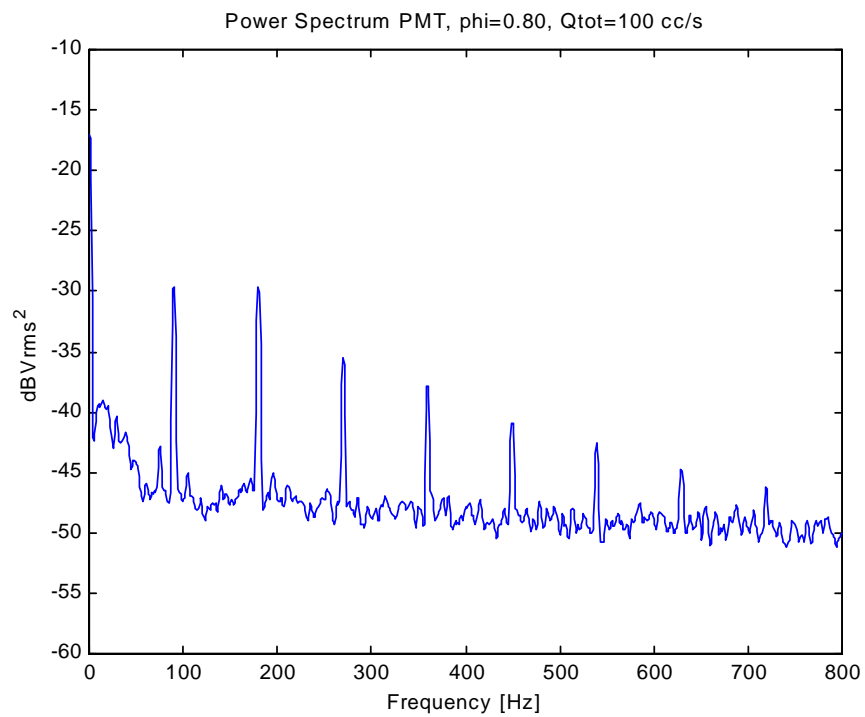


Figure C.33  $OH^*$  power spectrum for  $\phi = 0.80$ ,  $Q_{tot}=100$  cc/s

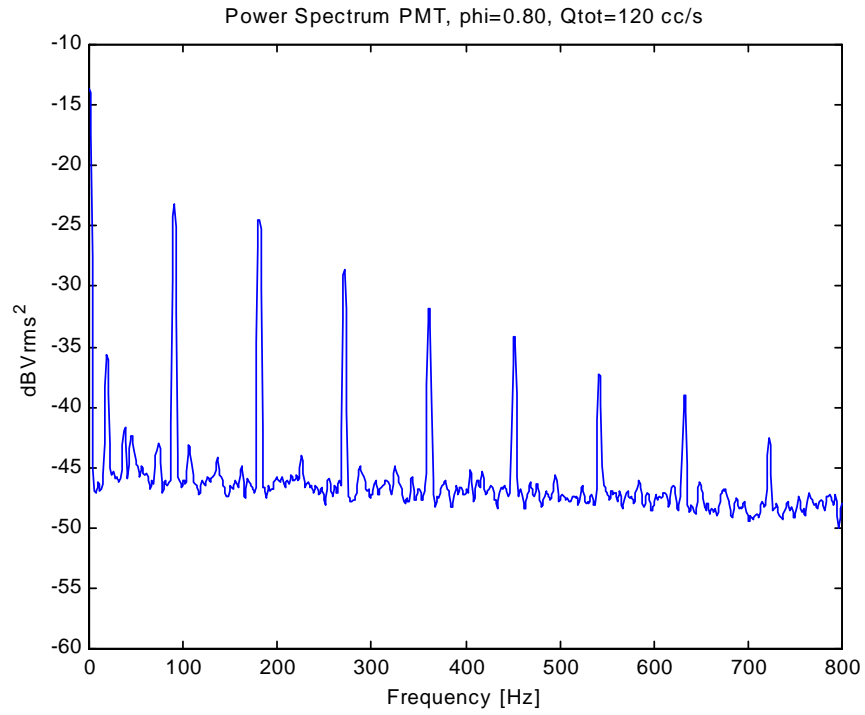


Figure C.34  $OH^*$  power spectrum for  $\phi = 0.80$ ,  $Q_{tot}=120$  cc/s

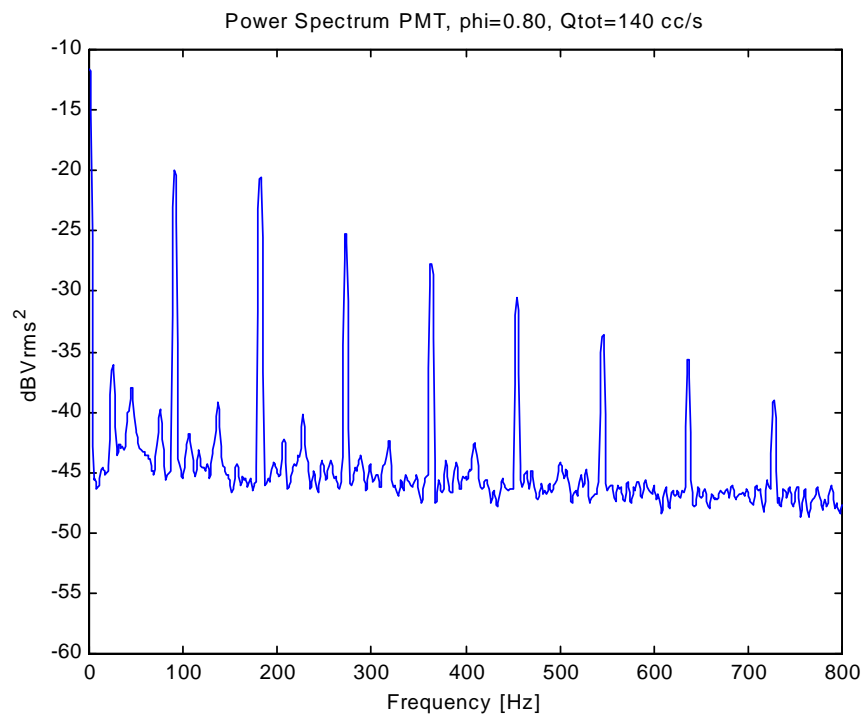


Figure C.35  $OH^*$  power spectrum for  $\phi = 0.80$ ,  $Q_{tot}=140$  cc/s

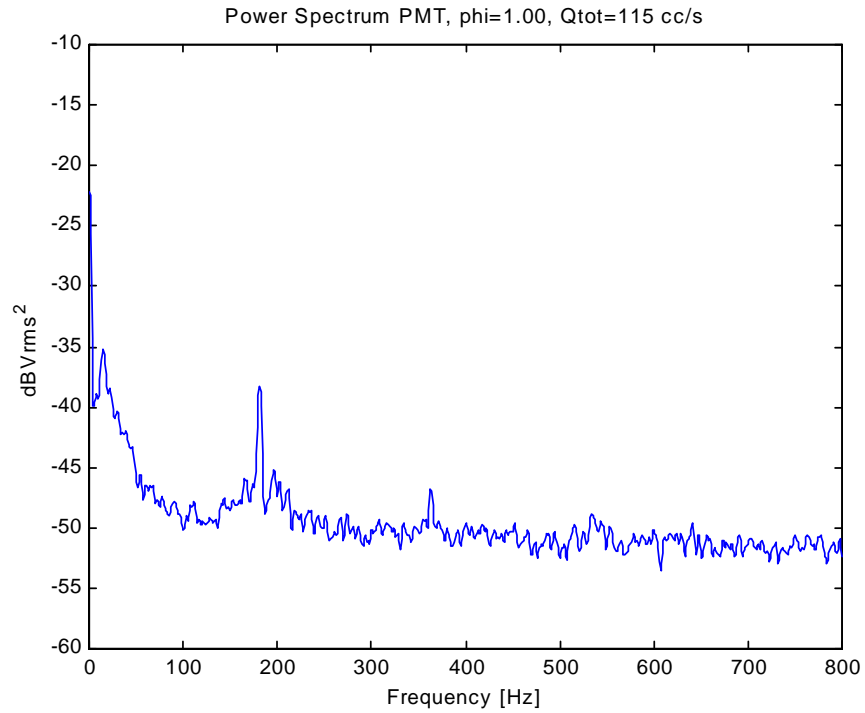


Figure C.36  $OH^*$  power spectrum for  $\phi = 1.00$ ,  $Q_{tot} = 115$  cc/s

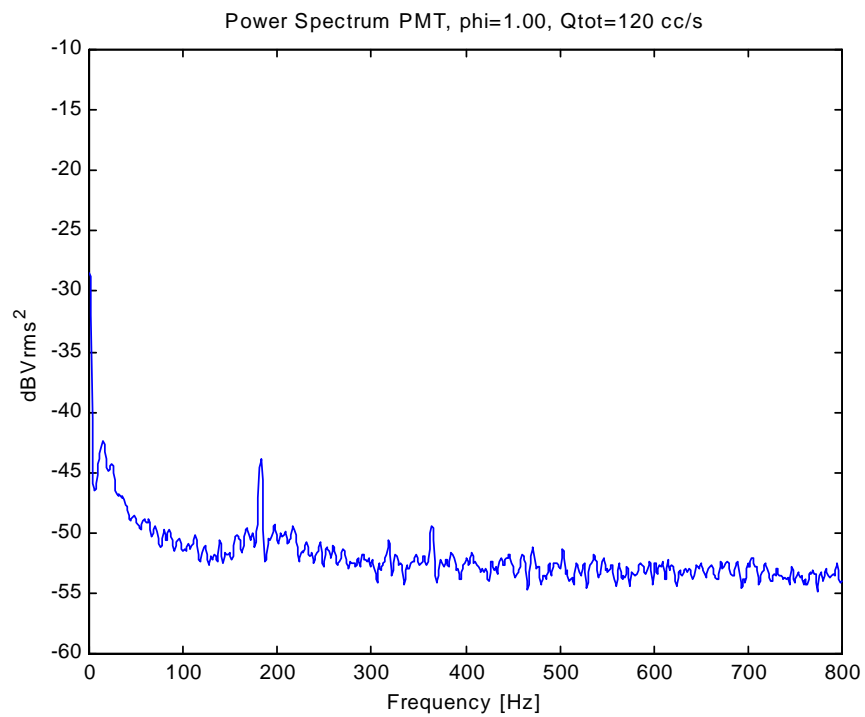


Figure C.37  $OH^*$  power spectrum for  $\phi = 1.00$ ,  $Q_{tot} = 120$  cc/s

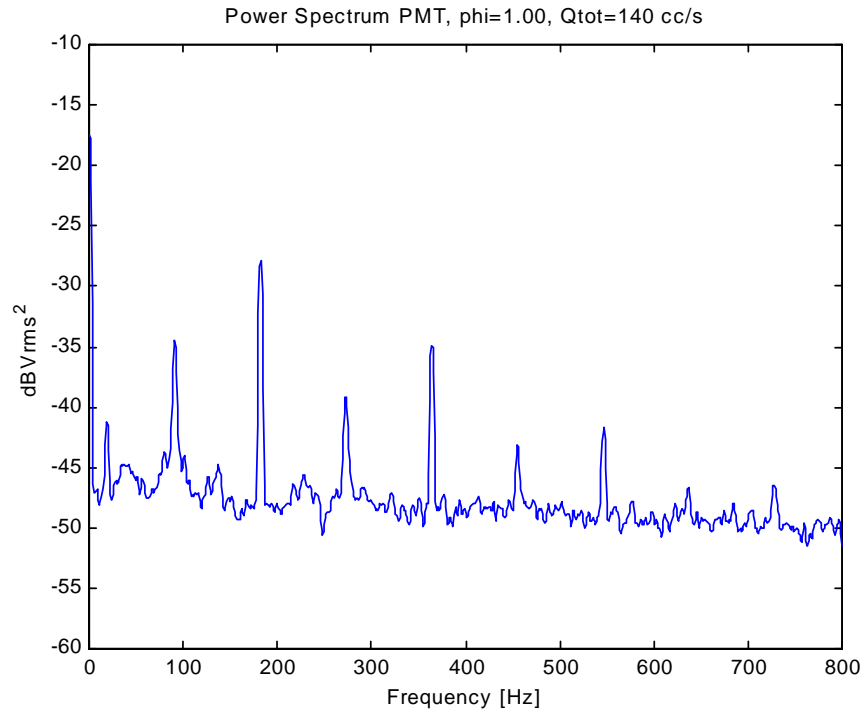


Figure C.38  $OH^*$  power spectrum for  $\phi = 1.00$ ,  $Q_{tot}=140$  cc/s

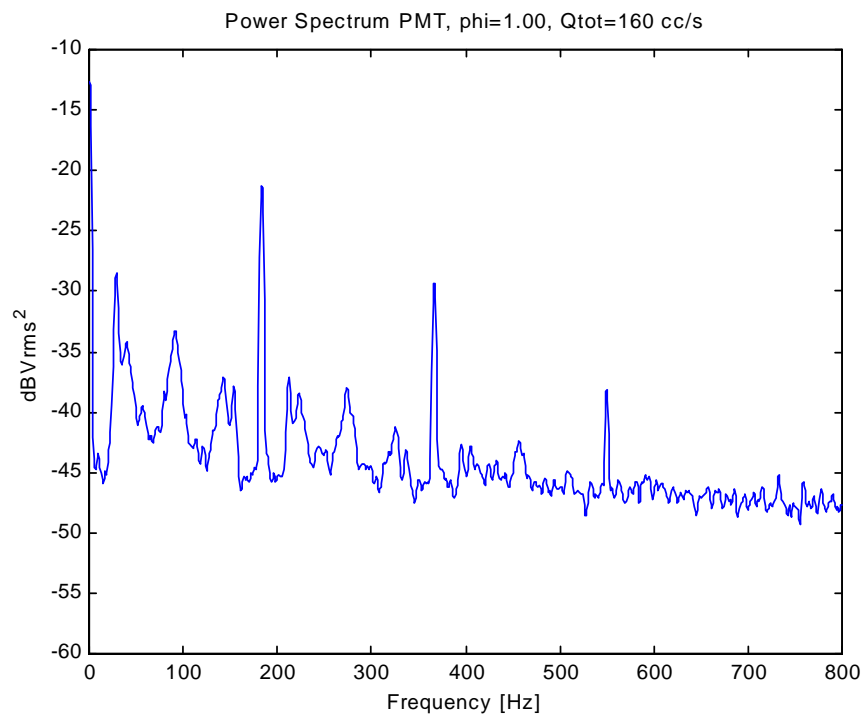


Figure C.39  $OH^*$  power spectrum for  $\phi = 1.00$ ,  $Q_{tot}=160$  cc/s

## **Appendix D    OH\* Power Spectra for Constant Flow Rate**

In Appendix D, power spectra of the OH\* measurements from the extensive mapping experiments will be presented. The flow rate was held constant with varying equivalence ratio for each data series. First the 100 cc/s flow rate series will be presented, followed by Q = 120, 140, 160, 180, and 200 cc/s series. All OH\* voltage levels have a reference voltage of 1 Vrms.

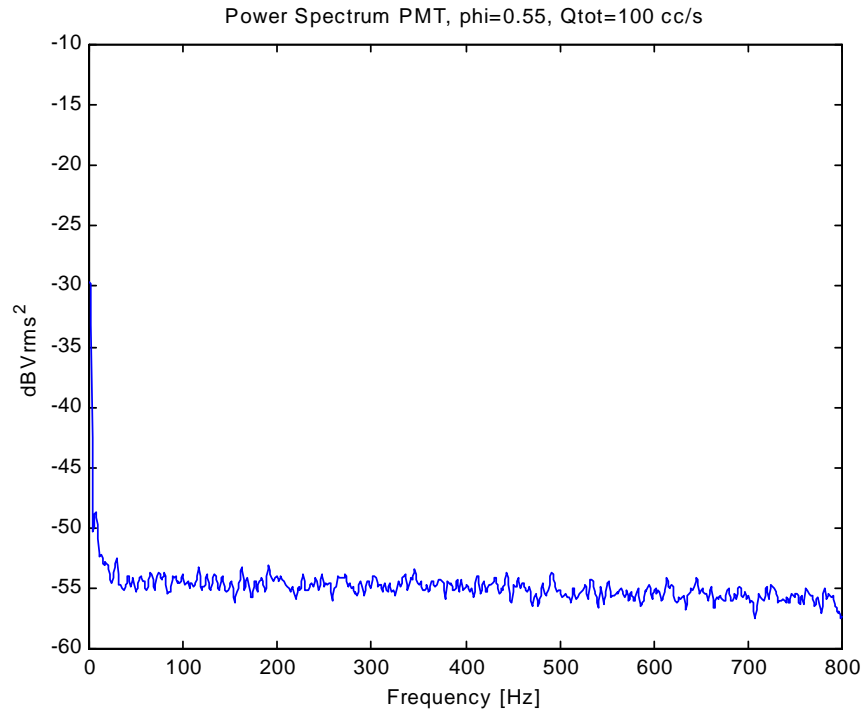


Figure D.1  $OH^*$  power spectrum for  $\phi = 0.55$ ,  $Q_{tot}=100$  cc/s

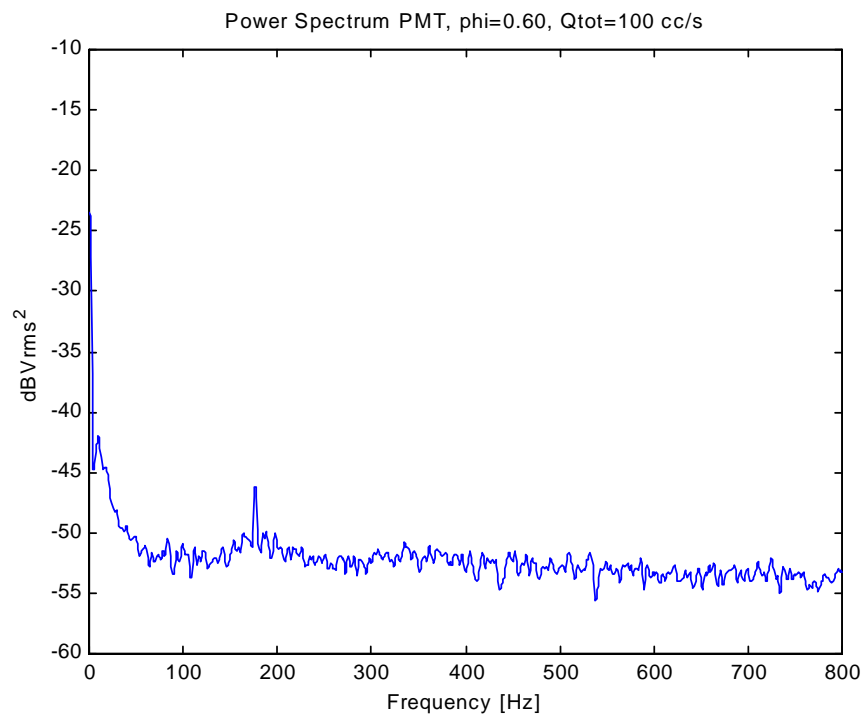


Figure D.2  $OH^*$  power spectrum for  $\phi = 0.60$ ,  $Q_{tot}=100$  cc/s

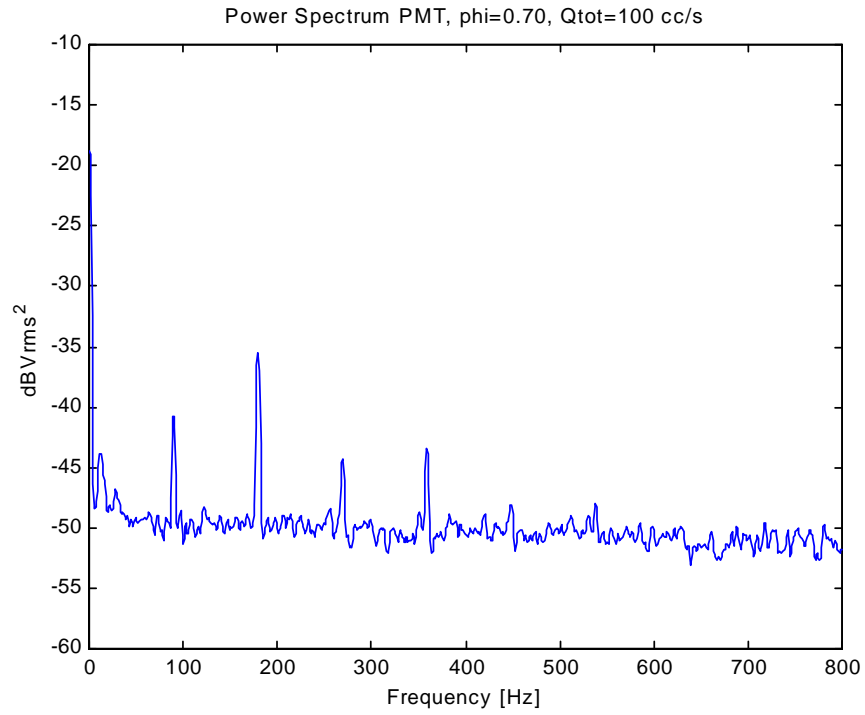


Figure D.3  $OH^*$  power spectrum for  $\phi = 0.70$ ,  $Q_{tot}=100$  cc/s

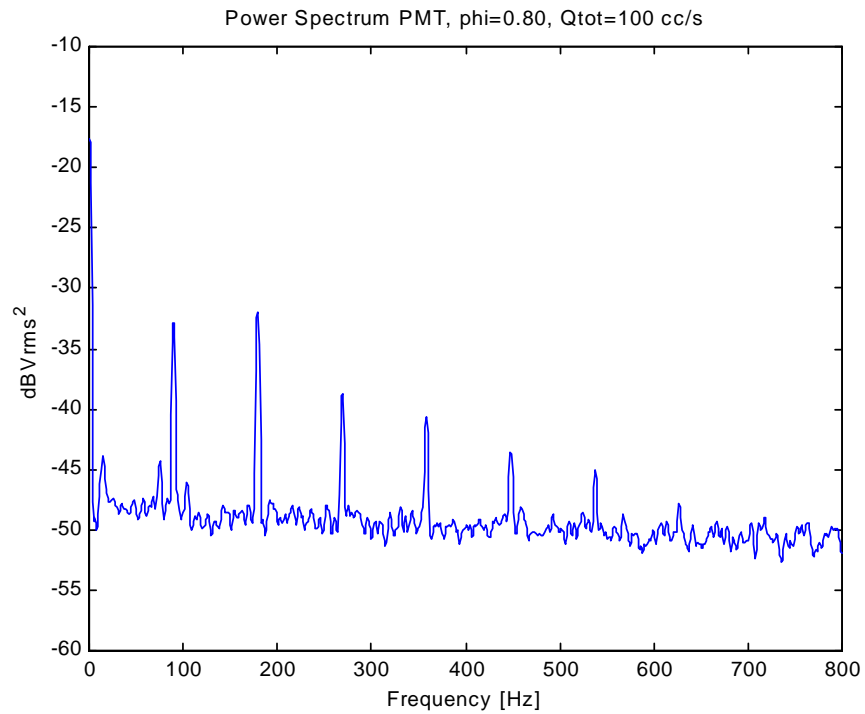


Figure D.4  $OH^*$  power spectrum for  $\phi = 0.80$ ,  $Q_{tot}=100$  cc/s

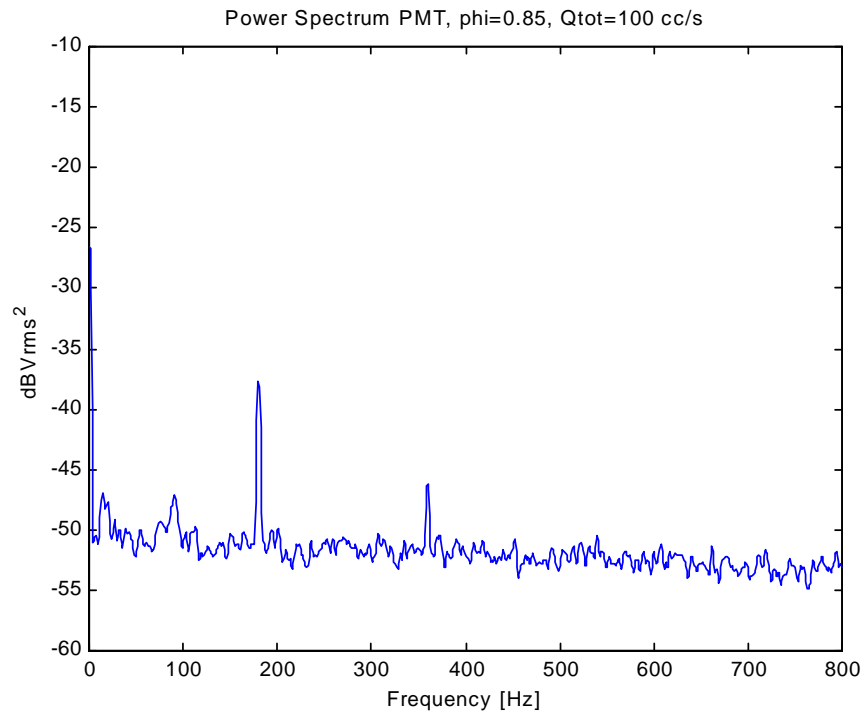


Figure D.5  $OH^*$  power spectrum for  $\phi = 0.85$ ,  $Q_{tot}=100$  cc/s

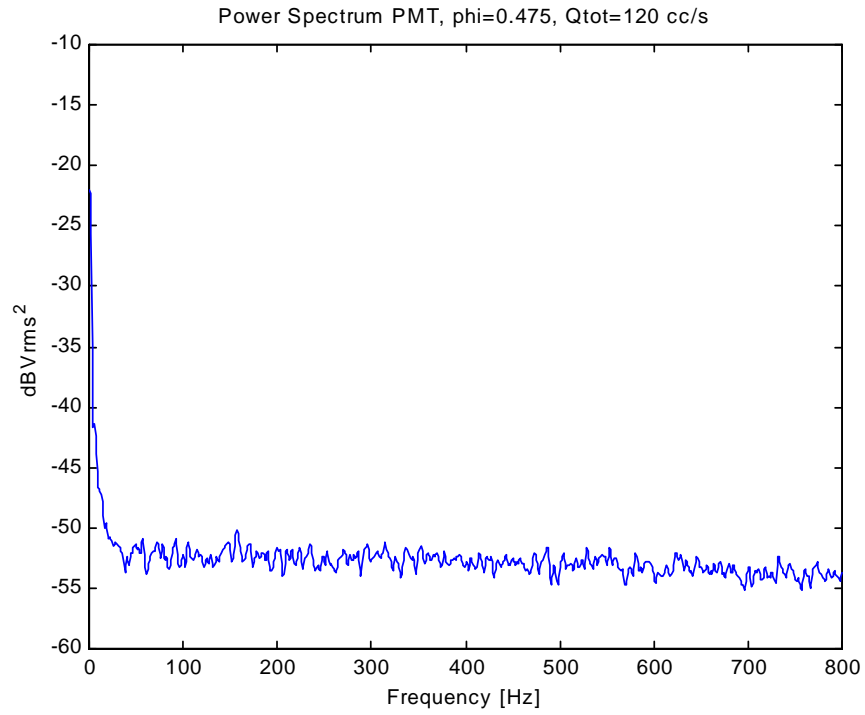


Figure D.6  $OH^*$  power spectrum for  $\phi = 0.475$ ,  $Q_{tot}=120$  cc/s

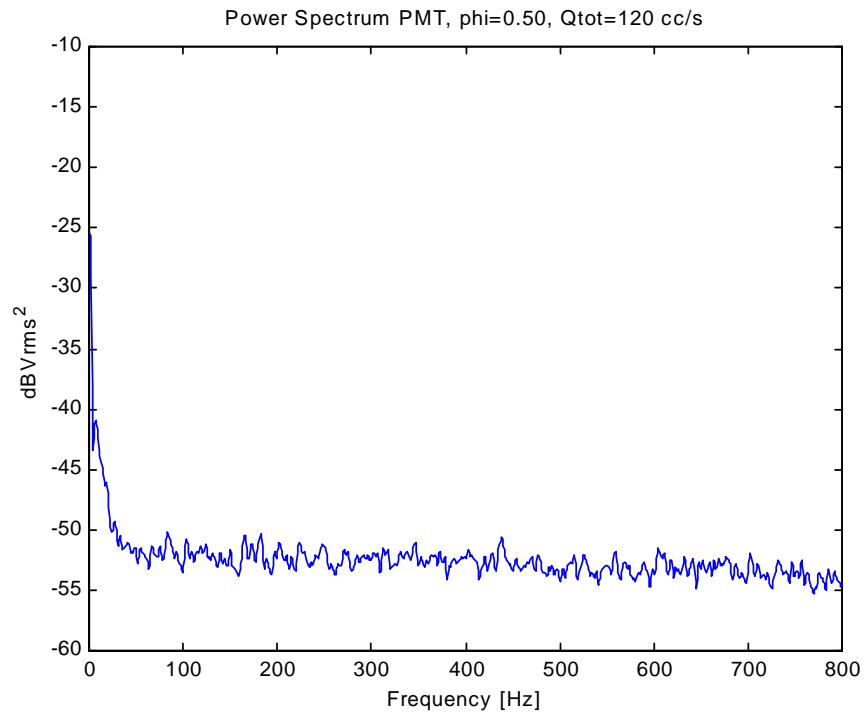


Figure D.7  $OH^*$  power spectrum for  $\phi = 0.50$ ,  $Q_{tot}=120$  cc/s

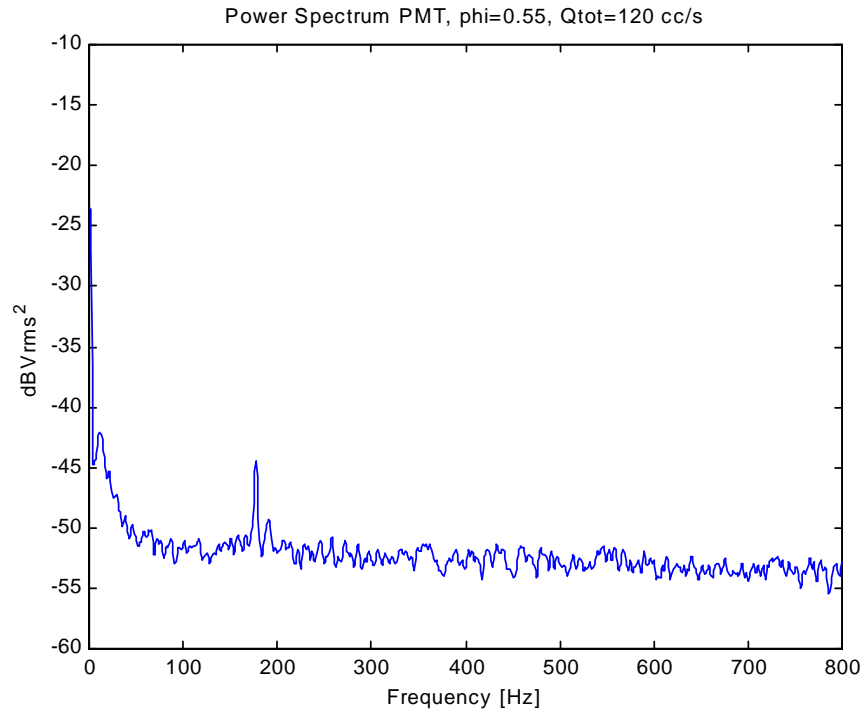


Figure D.8  $OH^*$  power spectrum for  $\phi = 0.55$ ,  $Q_{tot}=120$  cc/s

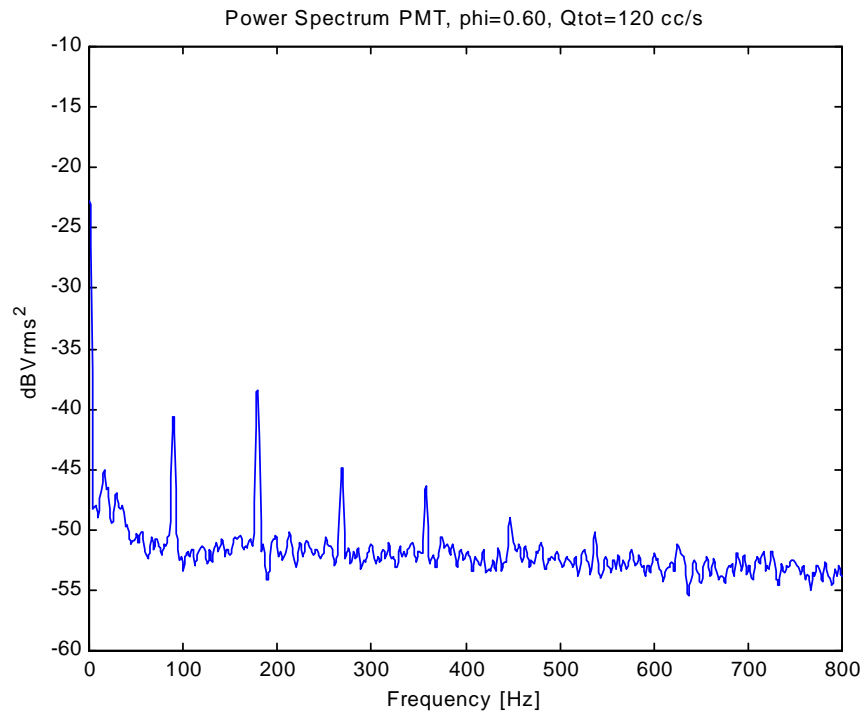


Figure D.9  $OH^*$  power spectrum for  $\phi = 0.60$ ,  $Q_{tot}=120$  cc/s

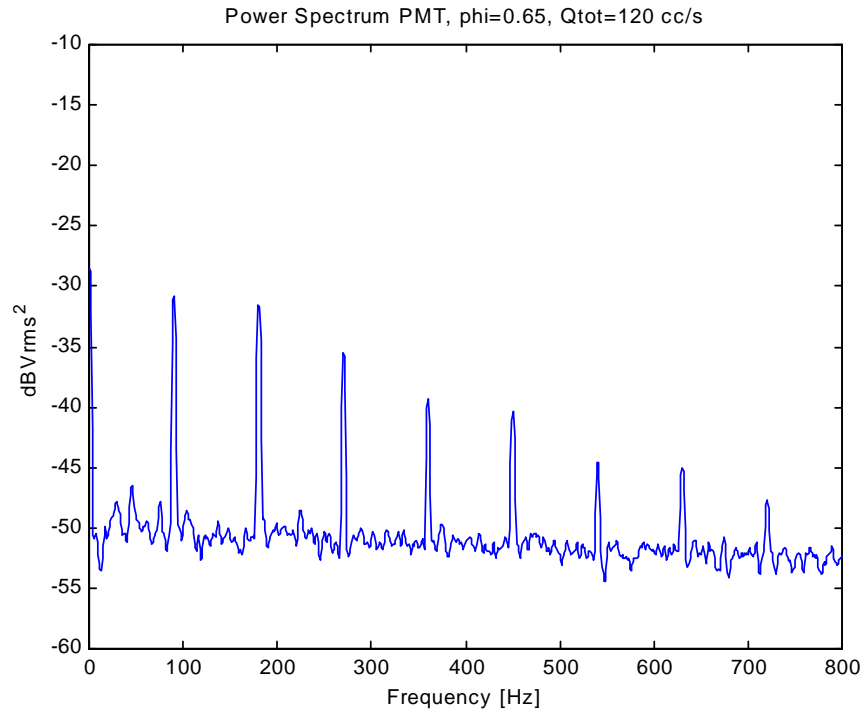


Figure D.10  $OH^*$  power spectrum for  $\phi = 0.65$ ,  $Q_{tot}=120$  cc/s

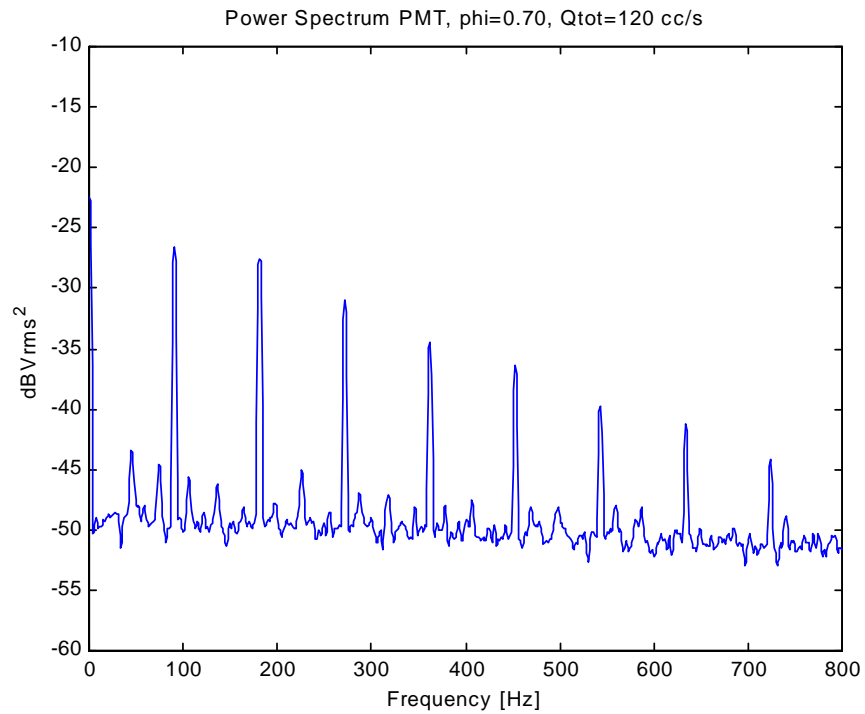


Figure D.11  $OH^*$  power spectrum for  $\phi = 0.70$ ,  $Q_{tot}=120$  cc/s

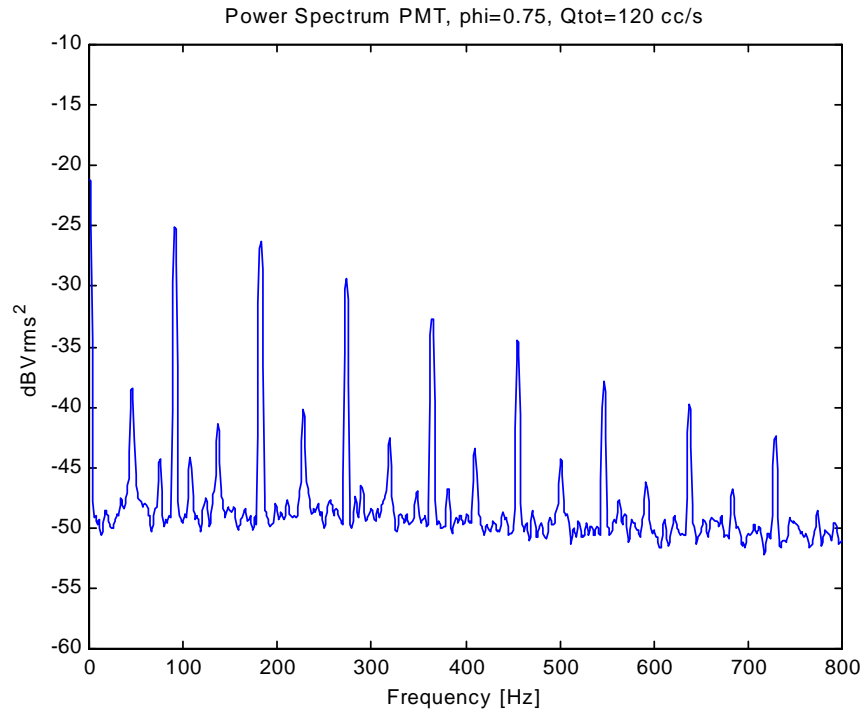


Figure D.12  $OH^*$  power spectrum for  $\phi = 0.75$ ,  $Q_{tot}=120$  cc/s

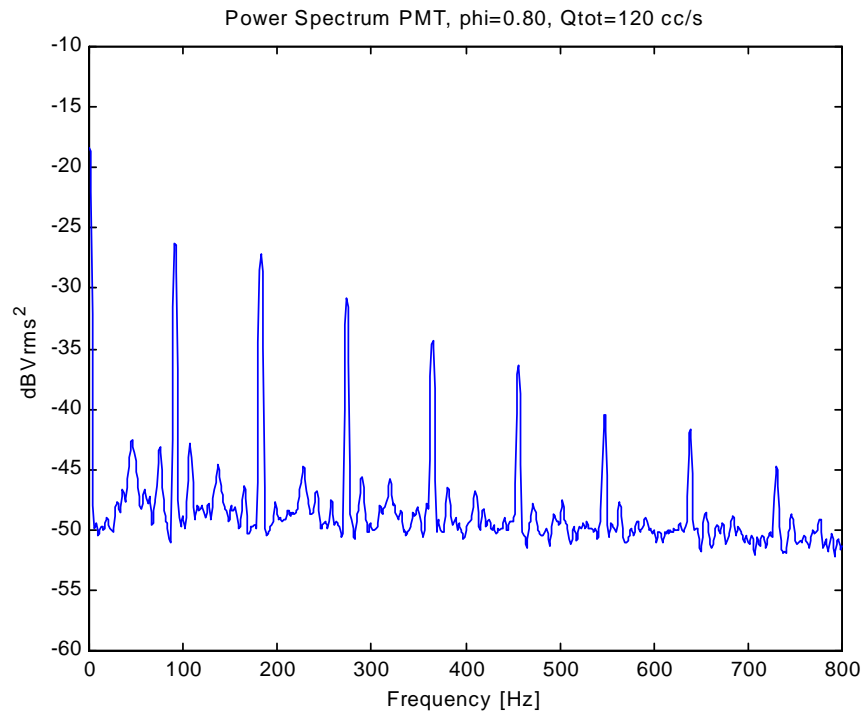


Figure D.13  $OH^*$  power spectrum for  $\phi = 0.80$ ,  $Q_{tot}=120$  cc/s

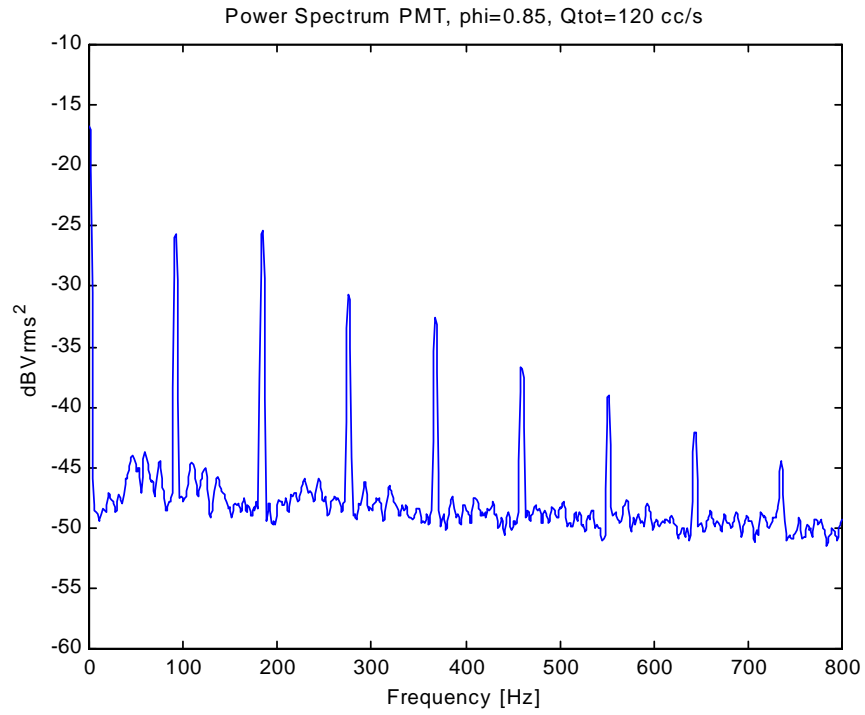


Figure D.14  $OH^*$  power spectrum for  $\phi = 0.85$ ,  $Q_{tot}=120$  cc/s

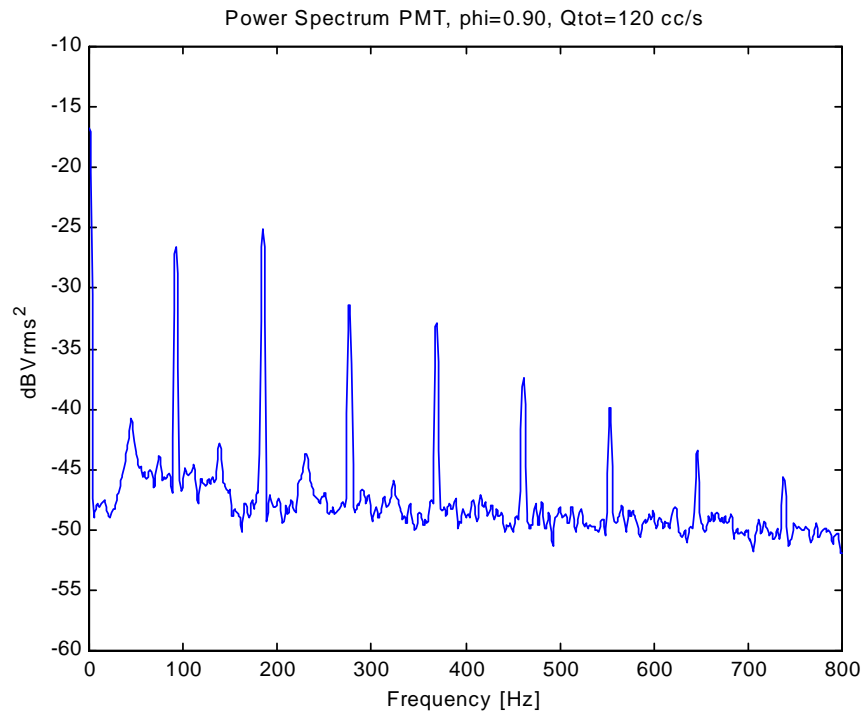


Figure D.15  $OH^*$  power spectrum for  $\phi = 0.90$ ,  $Q_{tot}=120$  cc/s

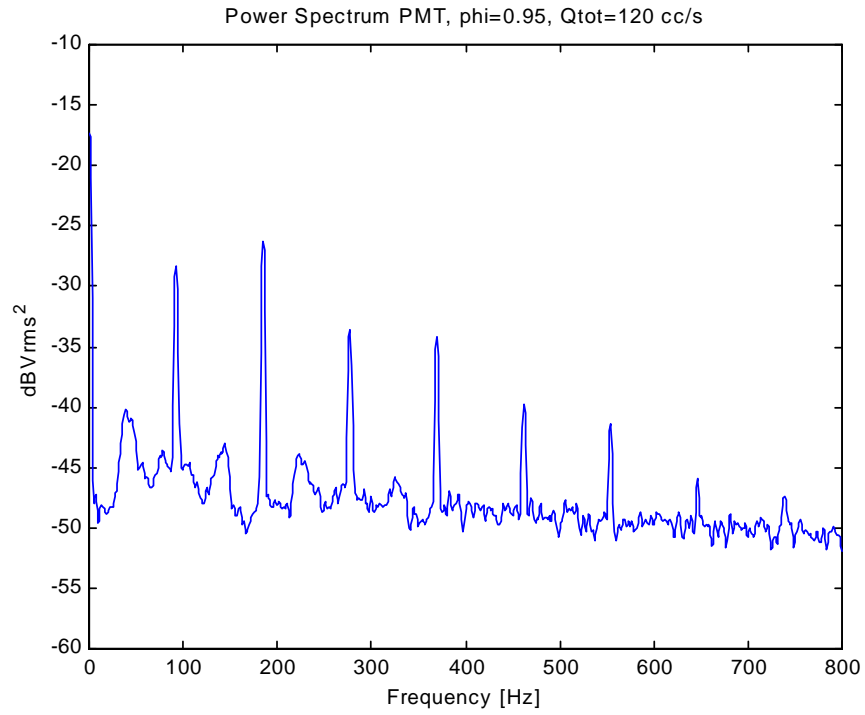


Figure D.16  $OH^*$  power spectrum for  $\phi = 0.95$ ,  $Q_{tot}=120$  cc/s

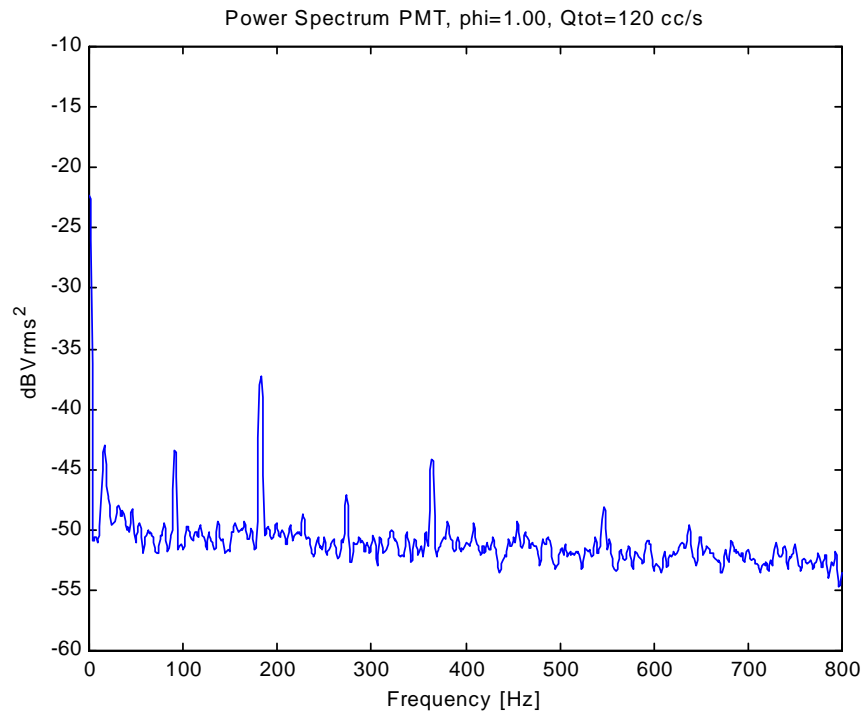


Figure D.17  $OH^*$  power spectrum for  $\phi = 1.00$ ,  $Q_{tot}=120$  cc/s

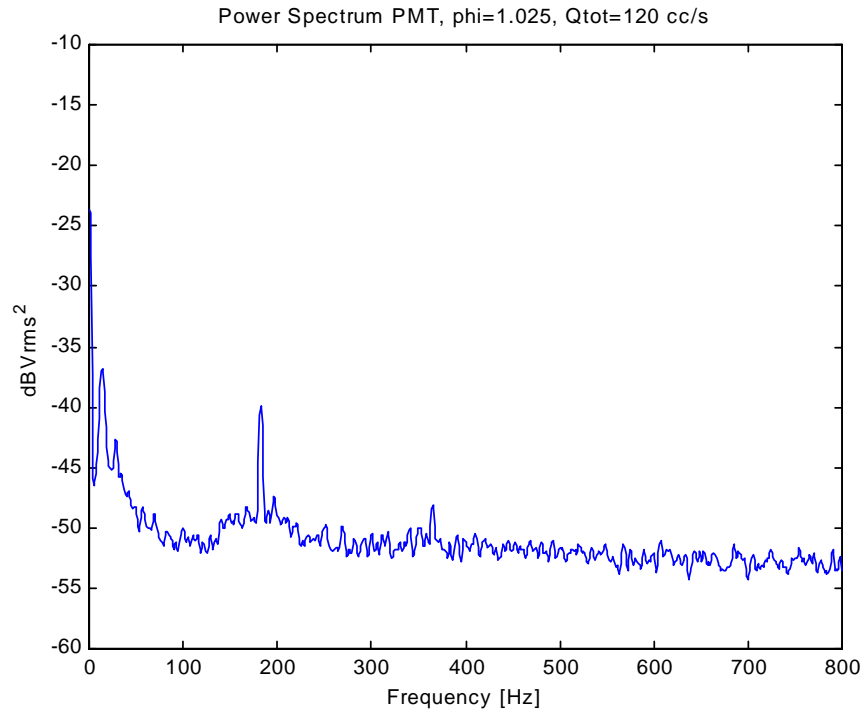


Figure D.18  $OH^*$  power spectrum for  $\phi = 1.025$ ,  $Q_{tot}=120$  cc/s

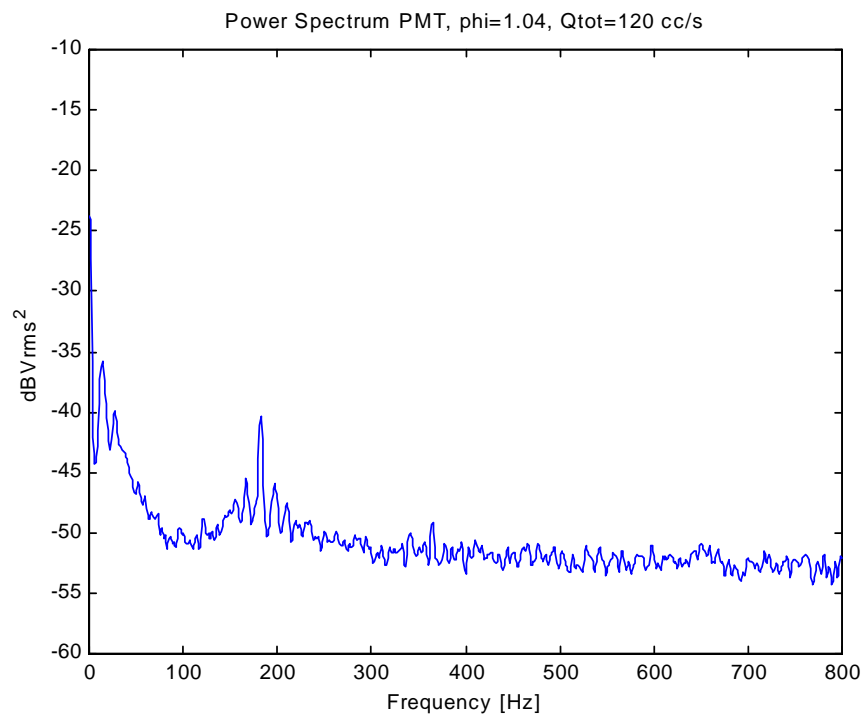


Figure D.19  $OH^*$  power spectrum for  $\phi = 1.04$ ,  $Q_{tot}=120$  cc/s

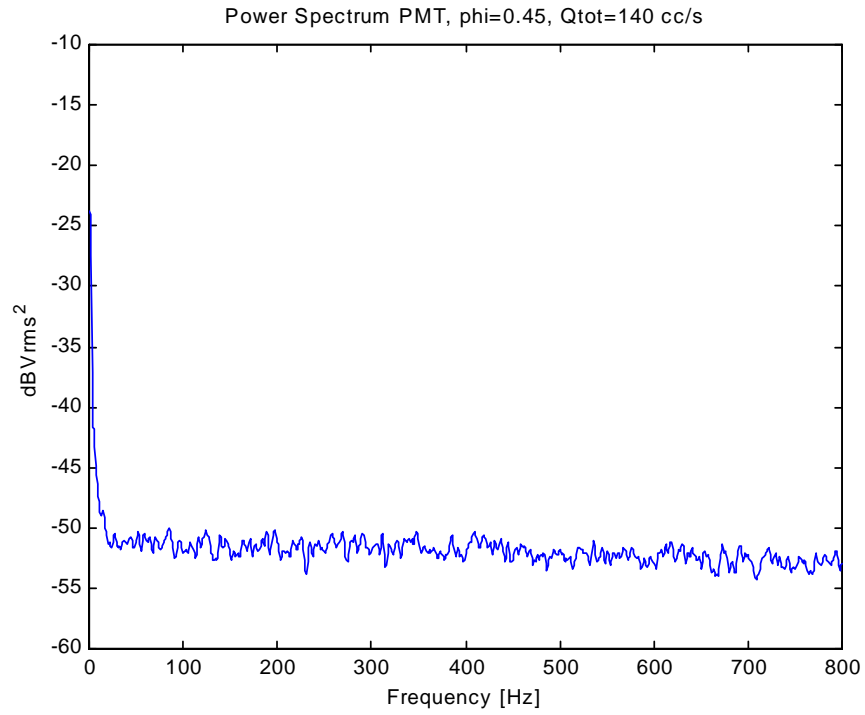


Figure D.20  $OH^*$  power spectrum for  $\phi = 0.45$ ,  $Q_{tot}=140$  cc/s

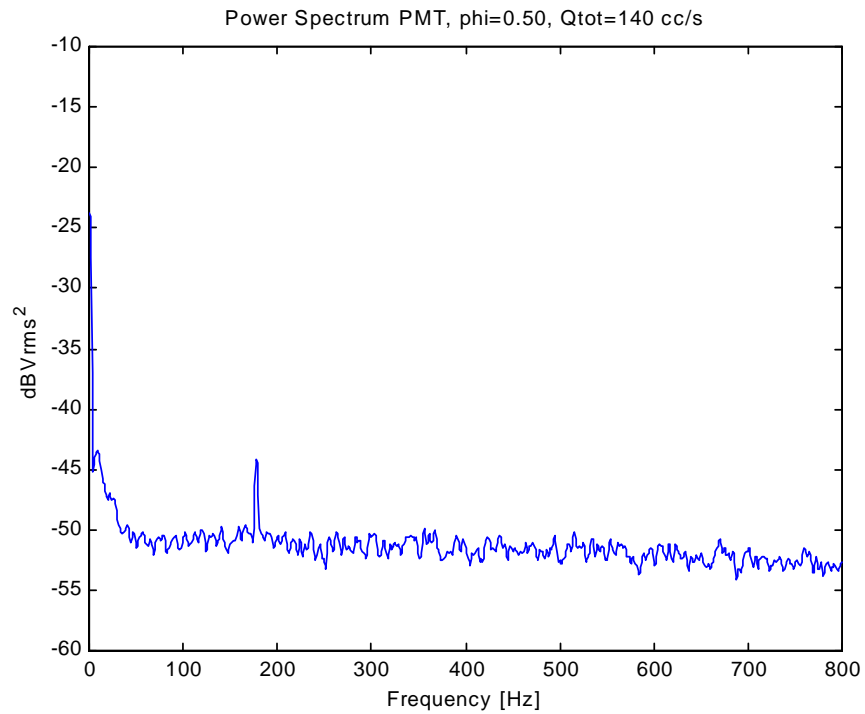


Figure D.21  $OH^*$  power spectrum for  $\phi = 0.50$ ,  $Q_{tot}=140$  cc/s

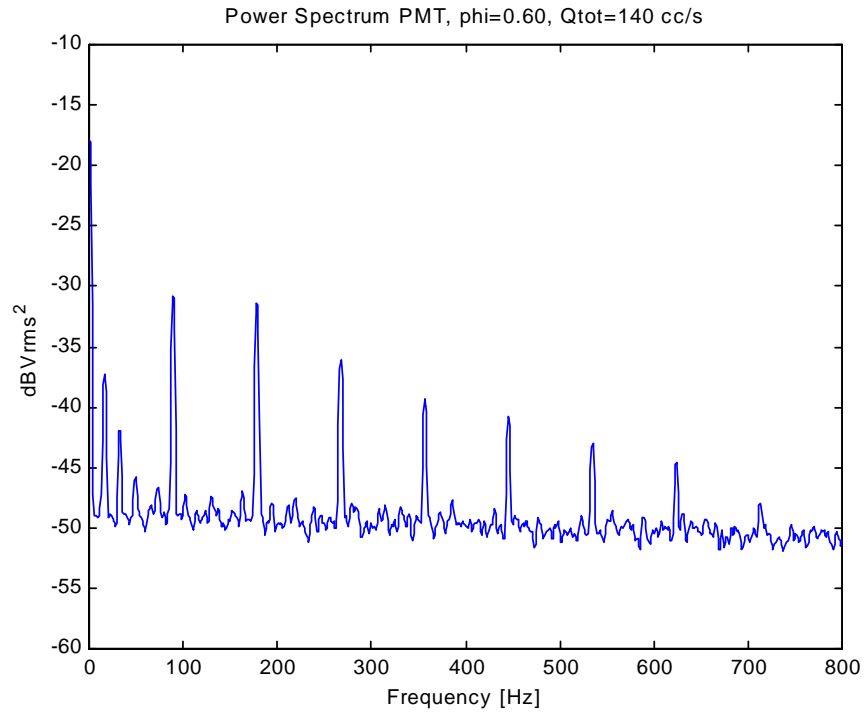


Figure D.22  $OH^*$  power spectrum for  $\phi = 0.60$ ,  $Q_{tot}=140$  cc/s

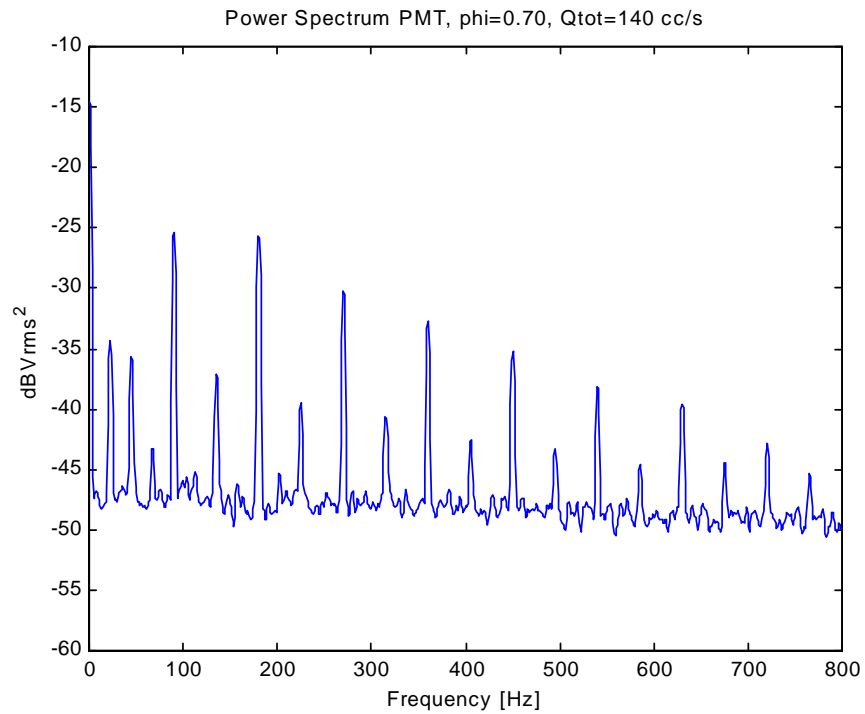


Figure D.23  $OH^*$  power spectrum for  $\phi = 0.70$ ,  $Q_{tot}=140$  cc/s

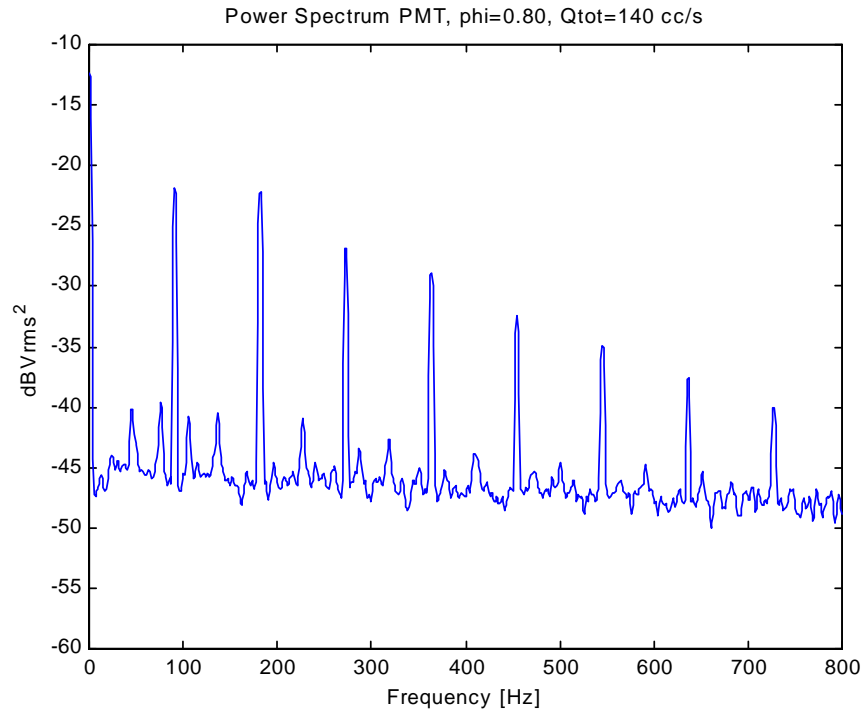


Figure D.24  $OH^*$  power spectrum for  $\phi = 0.80$ ,  $Q_{tot}=140$  cc/s

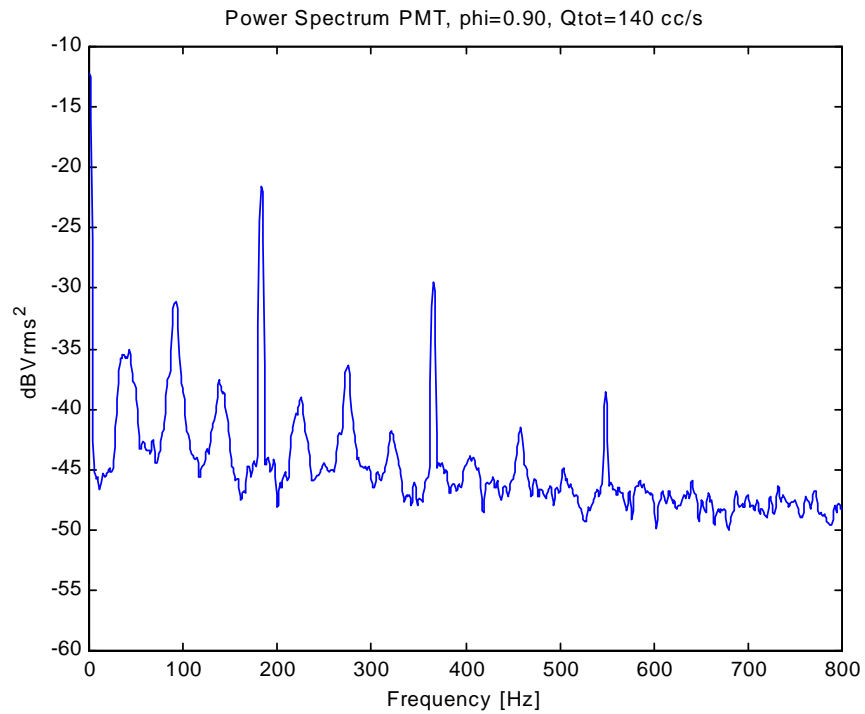


Figure D.25  $OH^*$  power spectrum for  $\phi = 0.90$ ,  $Q_{tot}=140$  cc/s

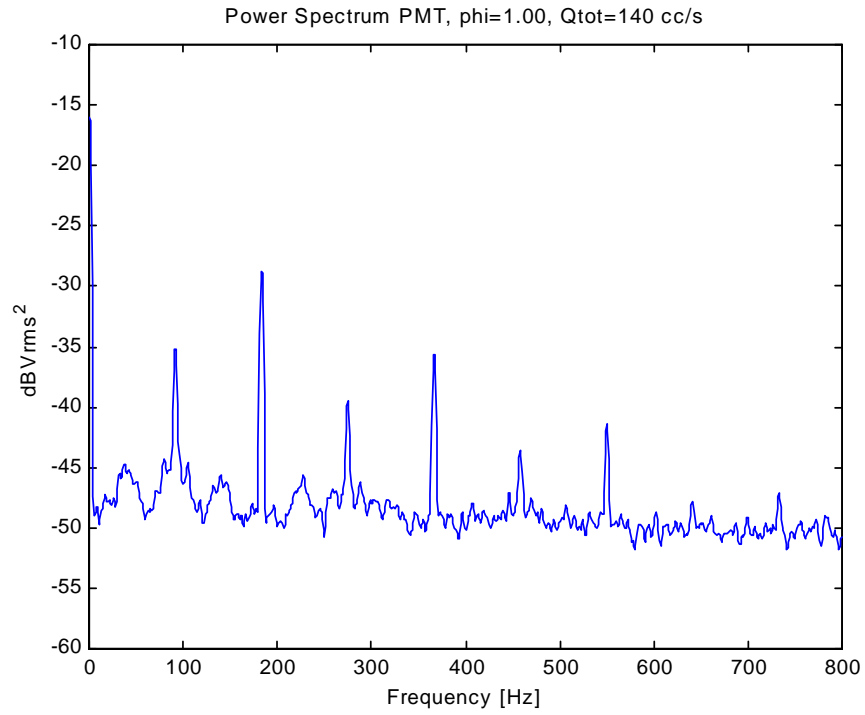


Figure D.26  $OH^*$  power spectrum for  $\phi = 1.00$ ,  $Q_{tot}=140$  cc/s

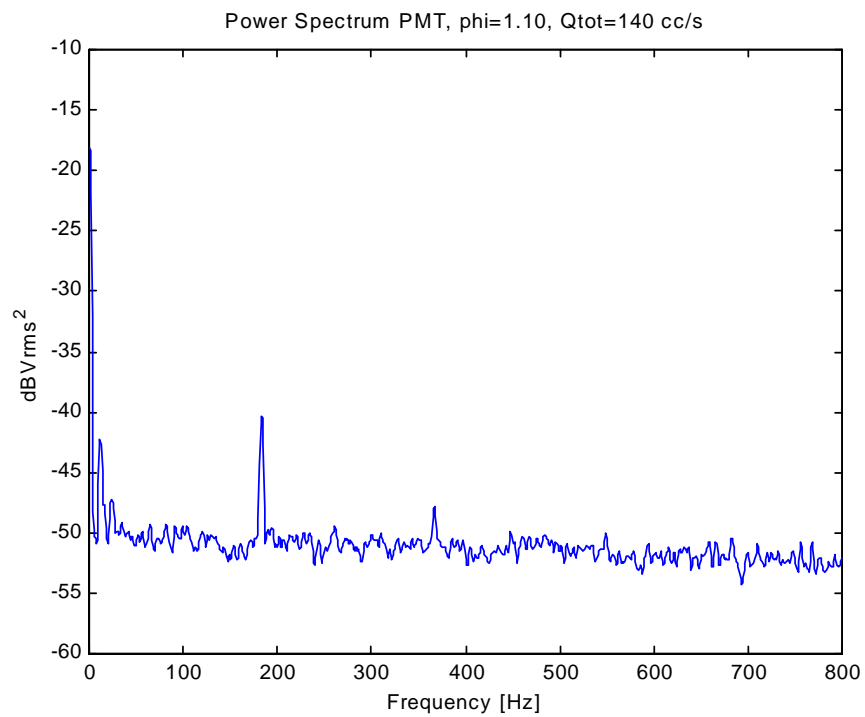


Figure D.27  $OH^*$  power spectrum for  $\phi = 1.10$ ,  $Q_{tot}=140$  cc/s

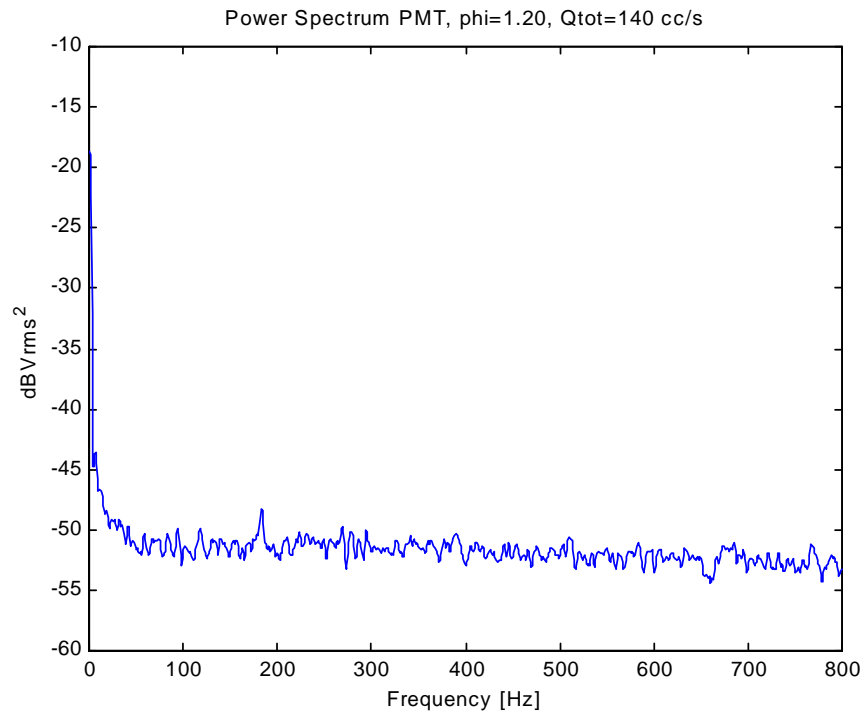


Figure D.28  $OH^*$  power spectrum for  $\phi = 1.20$ ,  $Q_{tot}=140$  cc/s

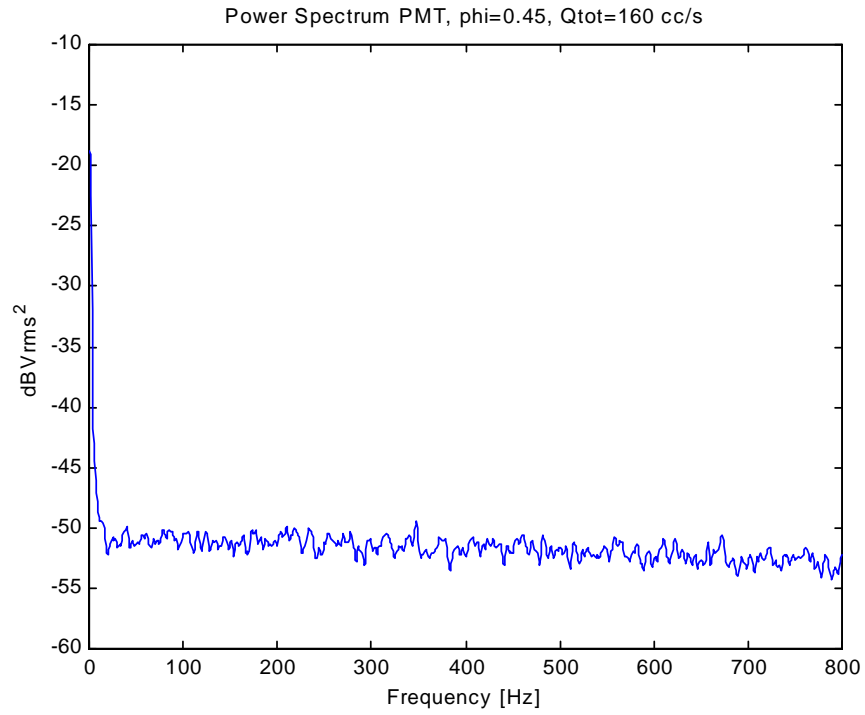


Figure D.29  $OH^*$  power spectrum for  $\phi = 0.45$ ,  $Q_{tot}=160$  cc/s

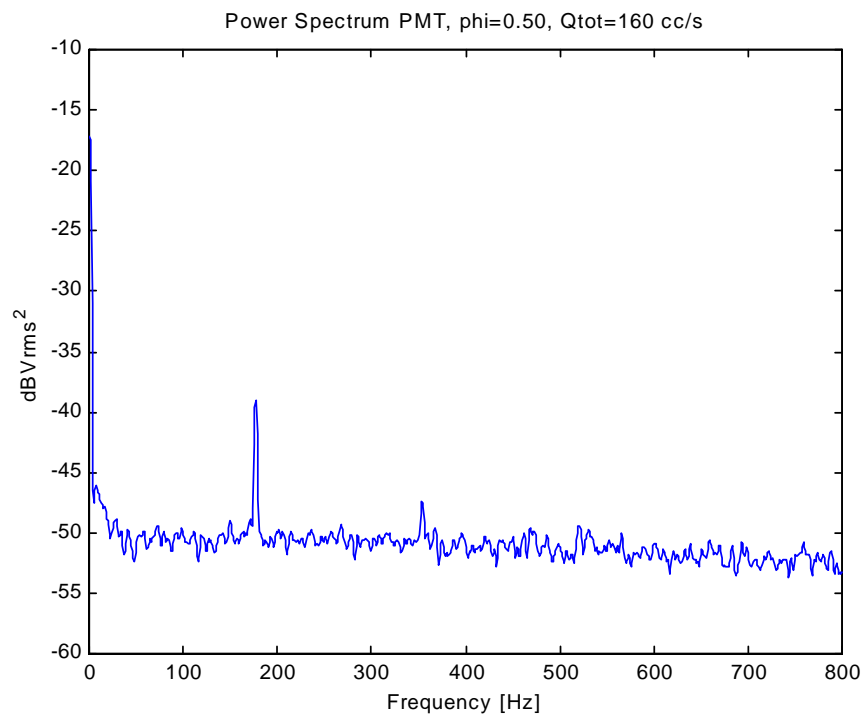


Figure D.30  $OH^*$  power spectrum for  $\phi = 0.50$ ,  $Q_{tot}=160$  cc/s

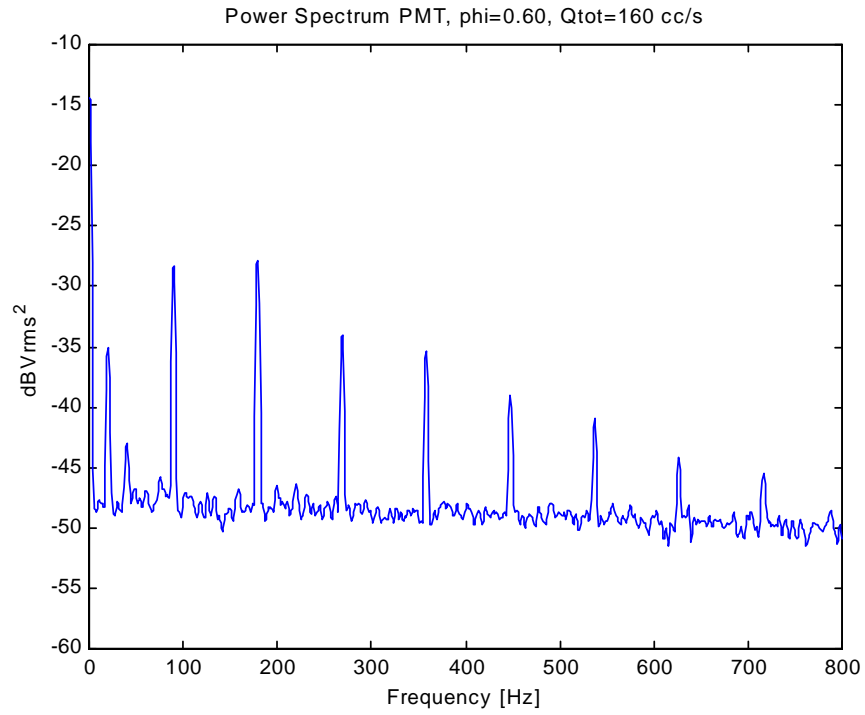


Figure D.31  $OH^*$  power spectrum for  $\phi = 0.60$ ,  $Q_{tot}=160$  cc/s

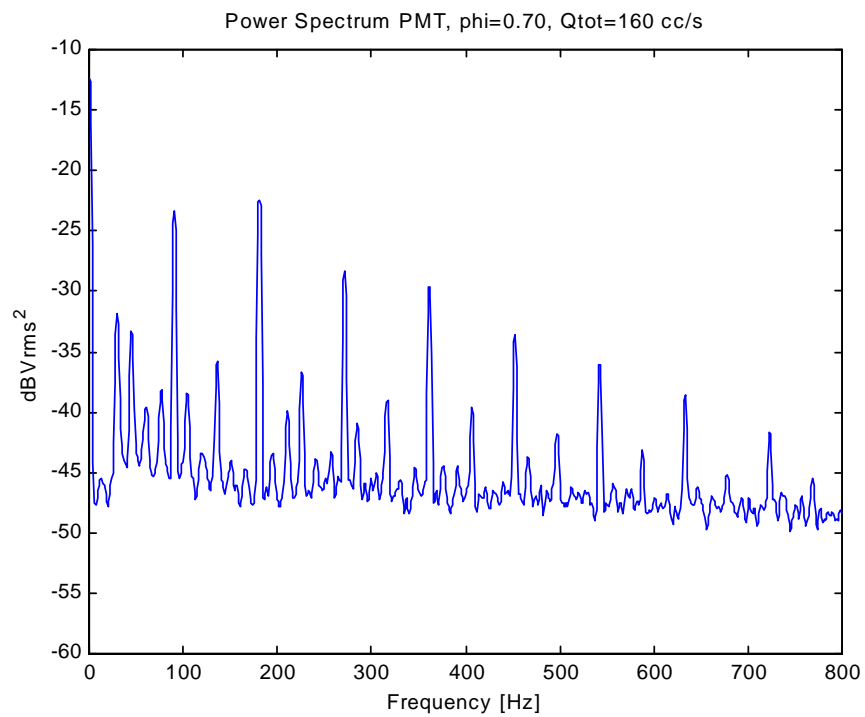


Figure D.32  $OH^*$  power spectrum for  $\phi = 0.70$ ,  $Q_{tot}=160$  cc/s

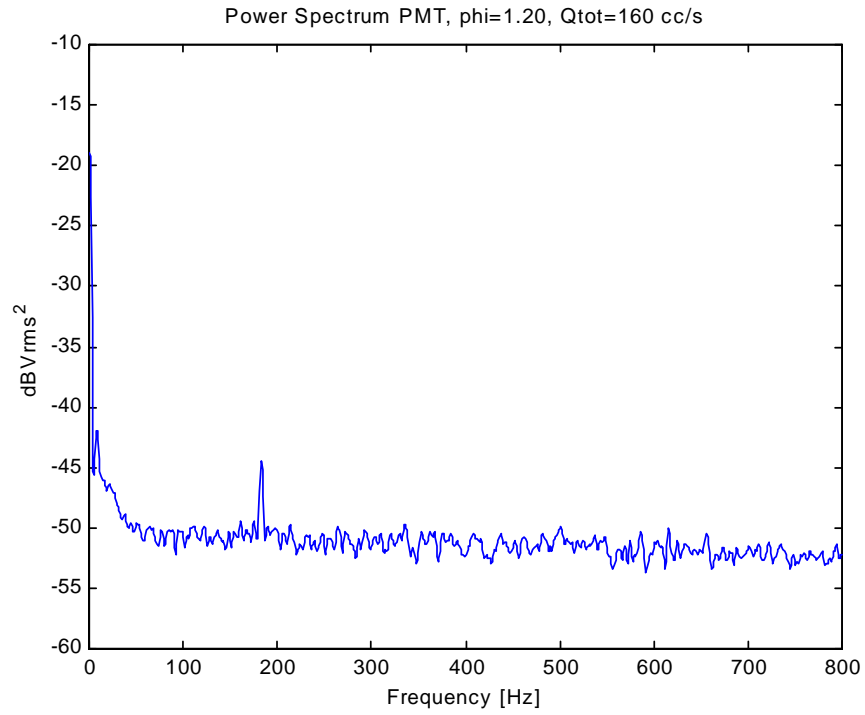


Figure D.33  $OH^*$  power spectrum for  $\phi = 1.20$ ,  $Q_{tot}=160$  cc/s

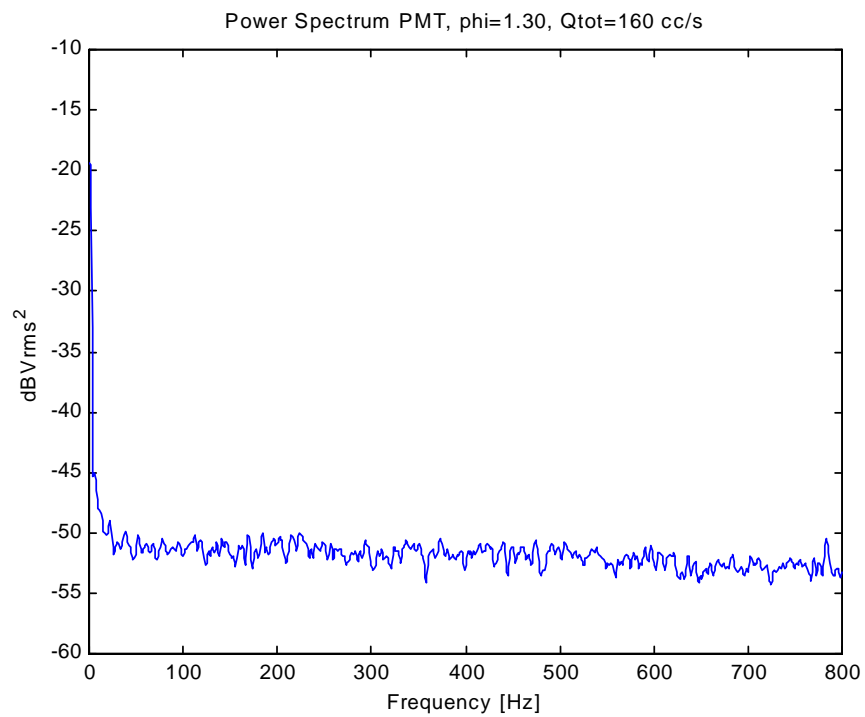


Figure D.34  $OH^*$  power spectrum for  $\phi = 1.30$ ,  $Q_{tot}=160$  cc/s

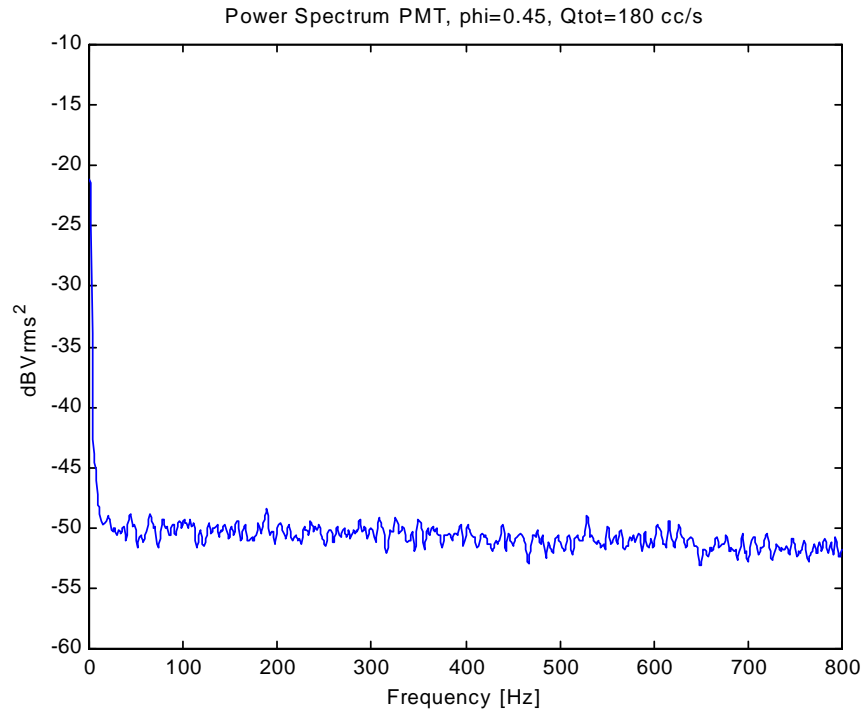


Figure D.35  $OH^*$  power spectrum for  $\phi = 0.45$ ,  $Q_{tot}=180$  cc/s

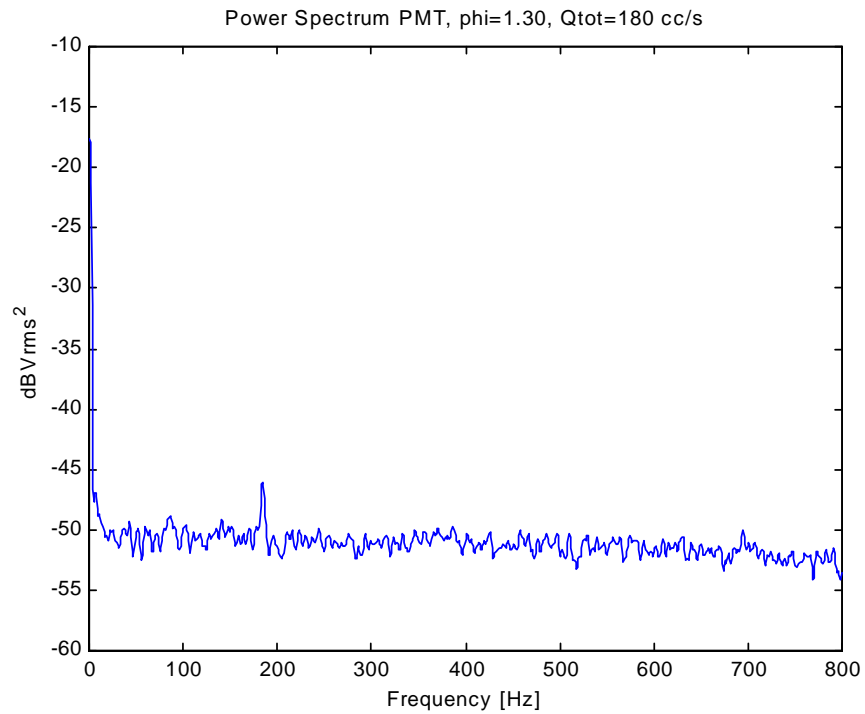


Figure D.36  $OH^*$  power spectrum for  $\phi = 1.30$ ,  $Q_{tot}=180$  cc/s

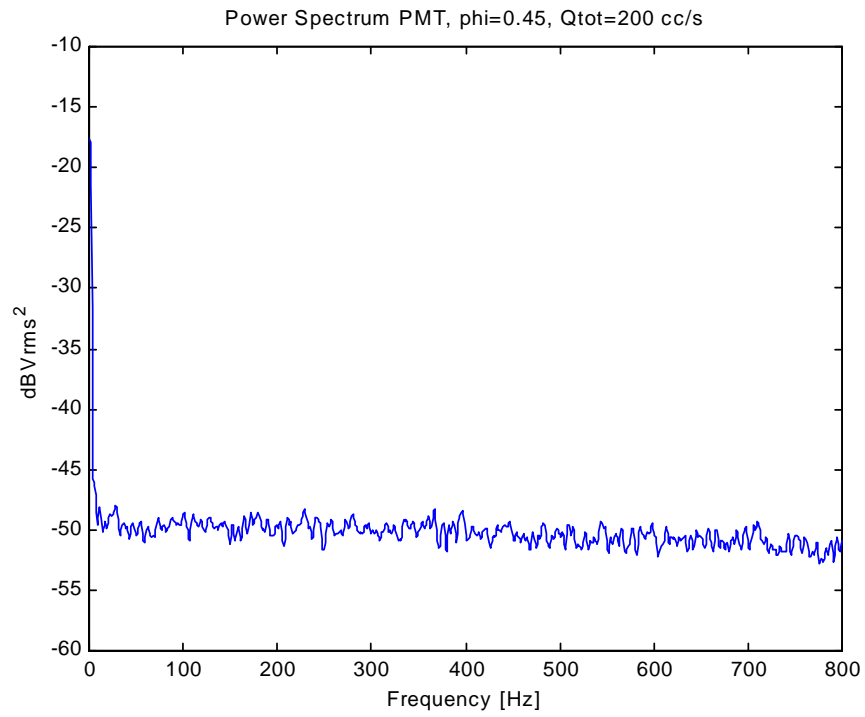


Figure D.37  $OH^*$  power spectrum for  $\phi = 0.45$ ,  $Q_{tot}=200$  cc/s

## **Appendix E     Axial Temperature Distribution for Constant Equivalence Ratio**

In Appendix E, axial temperature distributions of the extensive mapping experiments will be presented. The axial distance is measured from the closed bottom end of the combustor. The equivalence ratio was held constant with varying flow rate for each data series. First the 0.50-equivalence ratio series will be presented, followed by  $\phi = 0.60$ , 0.80 and 1.00 respectively.

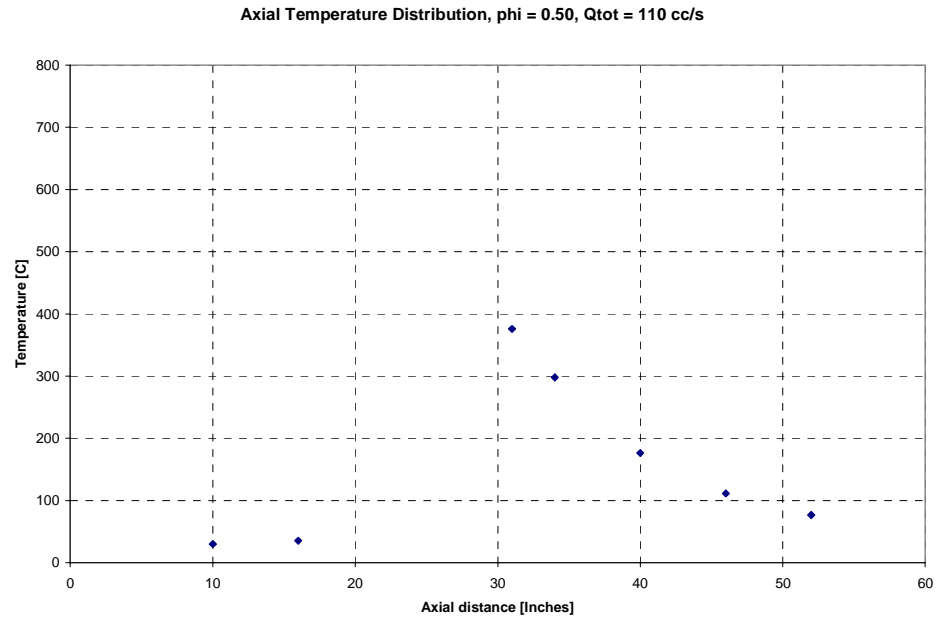


Figure E.1 Axial temperature distribution for  $\phi = 0.50$ ,  $Q_{tot} = 110$  cc/s

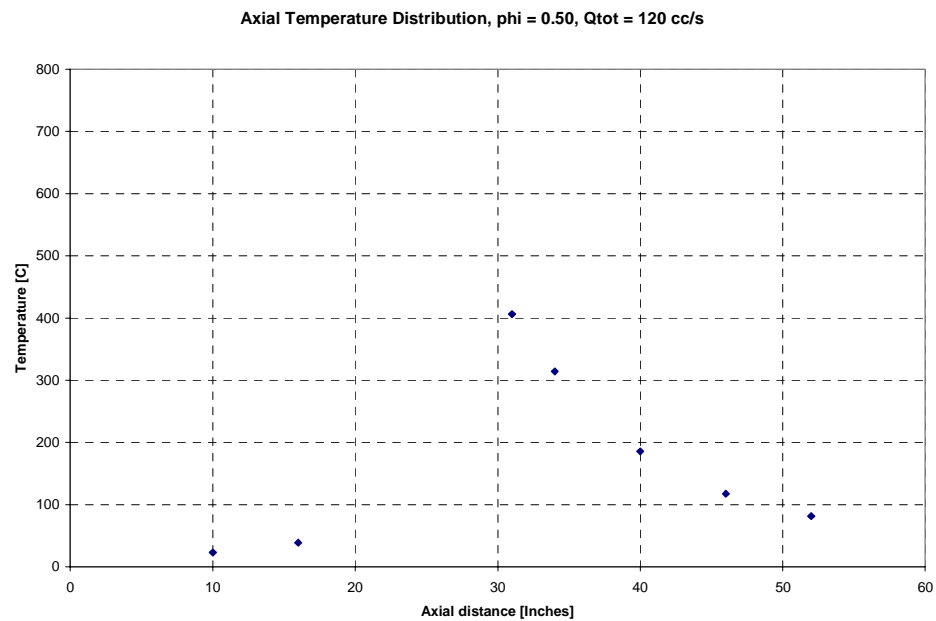


Figure E.2 Axial temperature distribution for  $\phi = 0.50$ ,  $Q_{tot} = 120$  cc/s

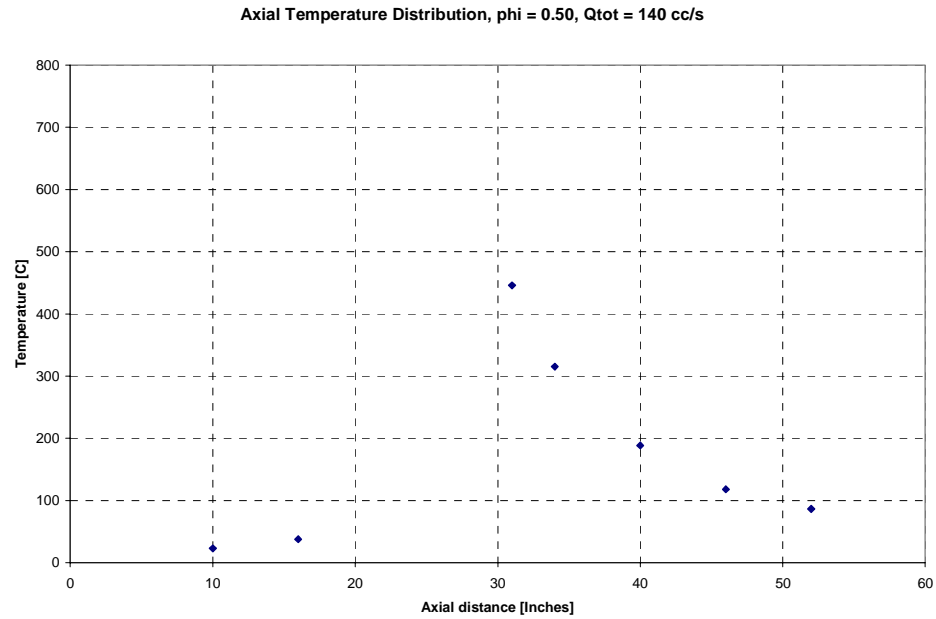


Figure E.3 Axial temperature distribution for  $\phi = 0.50$ ,  $Q_{tot} = 140$  cc/s

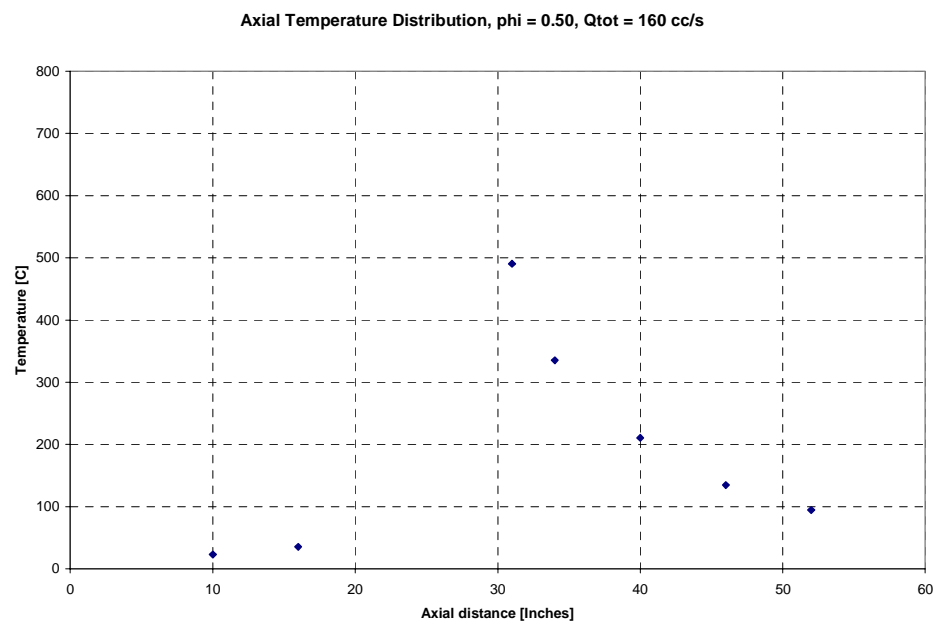


Figure E.4 Axial temperature distribution for  $\phi = 0.50$ ,  $Q_{tot} = 160$  cc/s

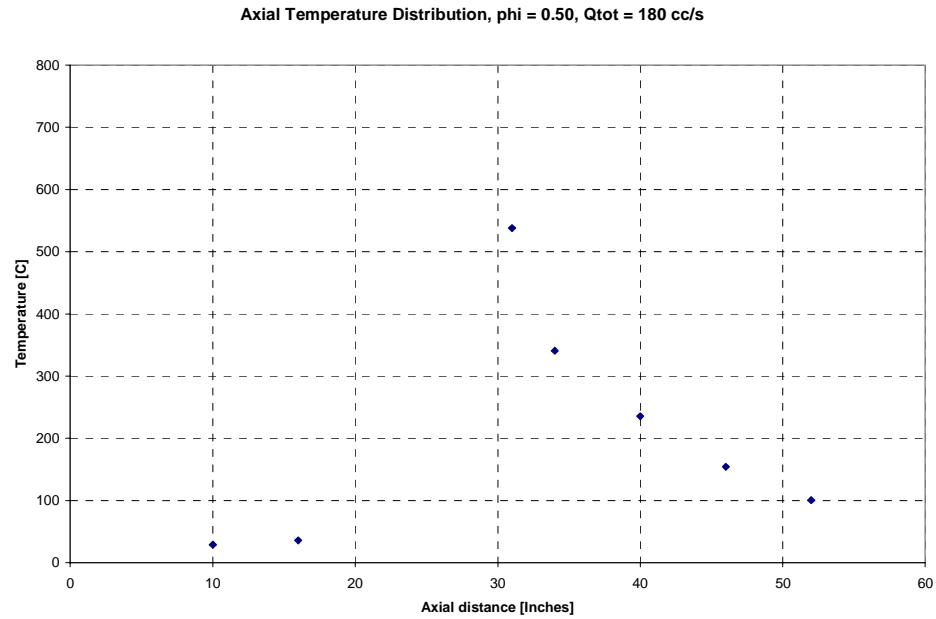


Figure E.5 Axial temperature distribution for  $\phi = 0.50$ ,  $Q_{tot} = 180$  cc/s

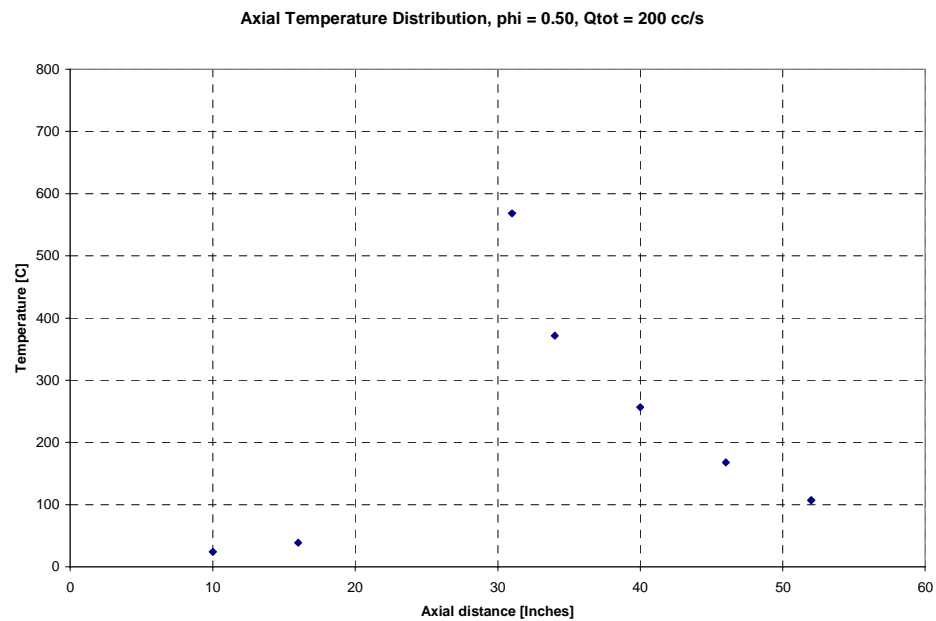


Figure E.6 Axial temperature distribution for  $\phi = 0.50$ ,  $Q_{tot} = 200$  cc/s

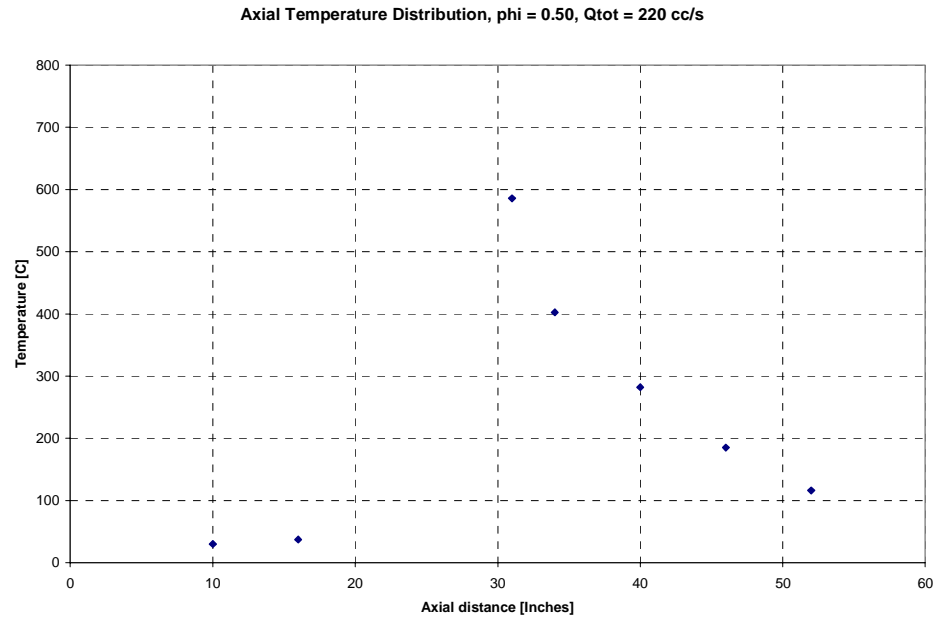


Figure E.7 Axial temperature distribution for  $\phi = 0.50$ ,  $Q_{tot} = 220$  cc/s

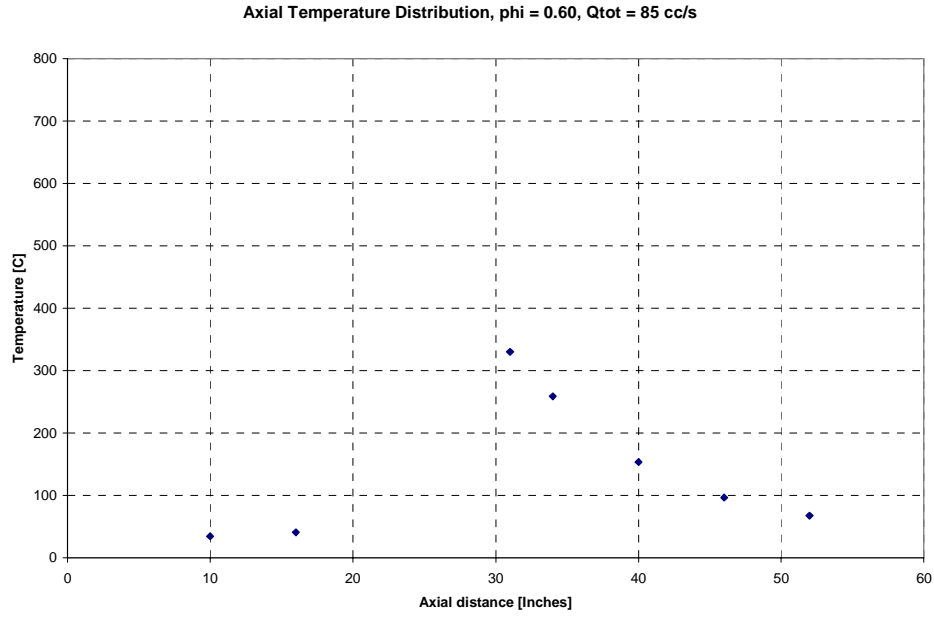


Figure E.8 Axial temperature distribution for  $\phi = 0.60$ ,  $Q_{tot}=85$  cc/s

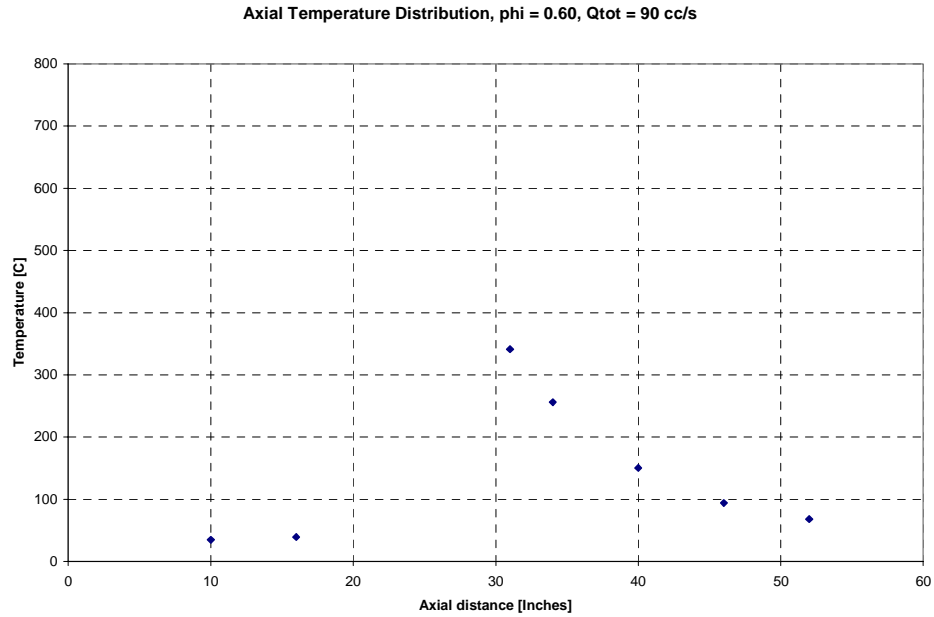


Figure E.9 Axial temperature distribution for  $\phi = 0.60$ ,  $Q_{tot}=90$  cc/s

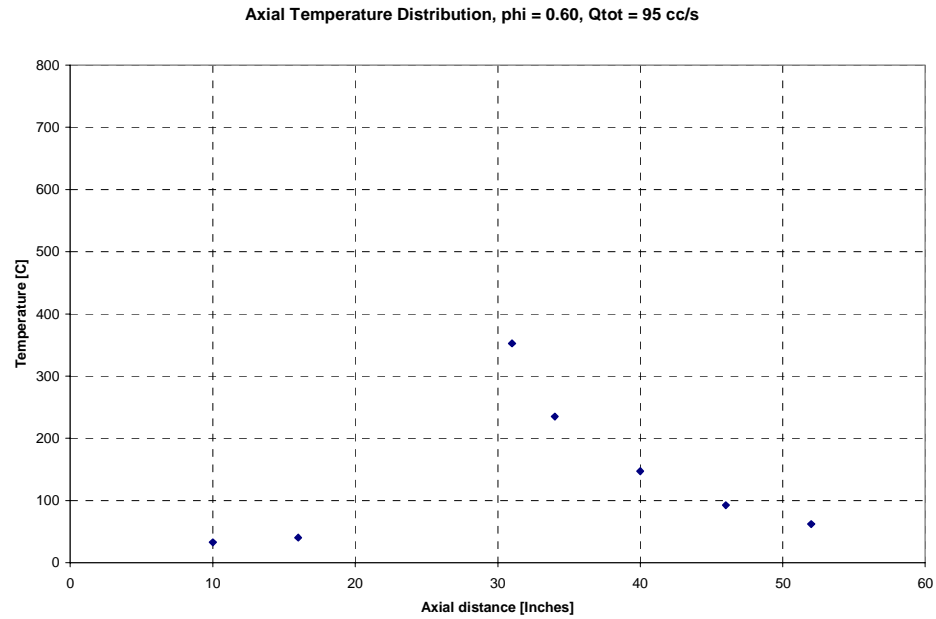


Figure E.10 Axial temperature distribution for  $\phi = 0.60$ ,  $Q_{tot} = 95$  cc/s

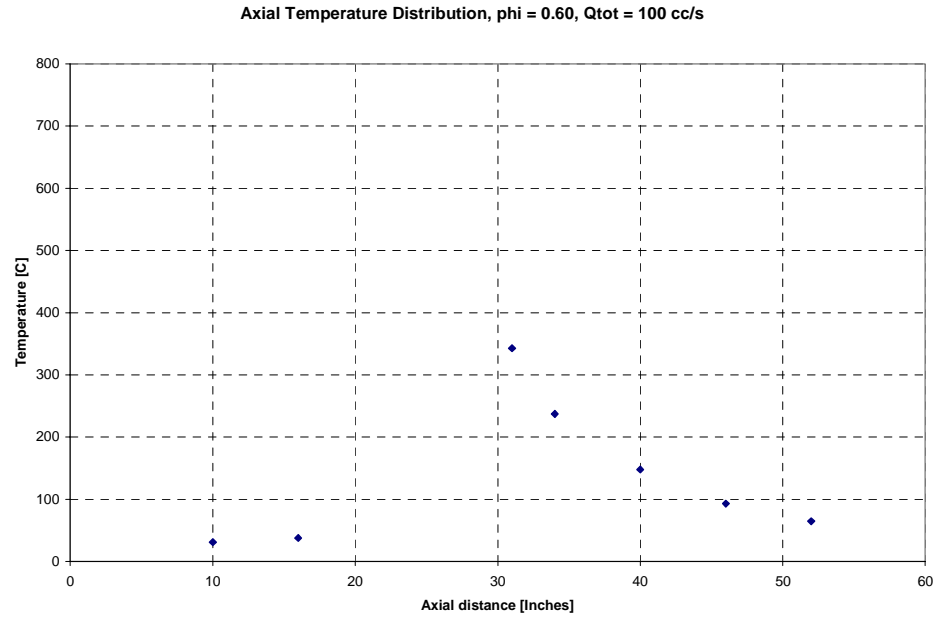


Figure E.11 Axial temperature distribution for  $\phi = 0.60$ ,  $Q_{tot} = 100$  cc/s

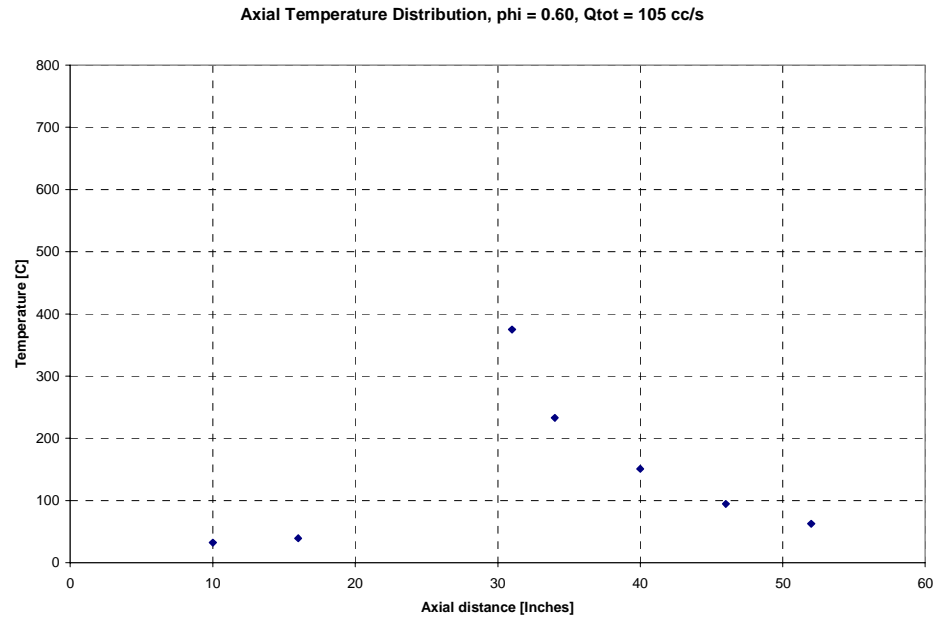


Figure E.12 Axial temperature distribution for  $\phi = 0.60$ ,  $Q_{tot} = 105$  cc/s

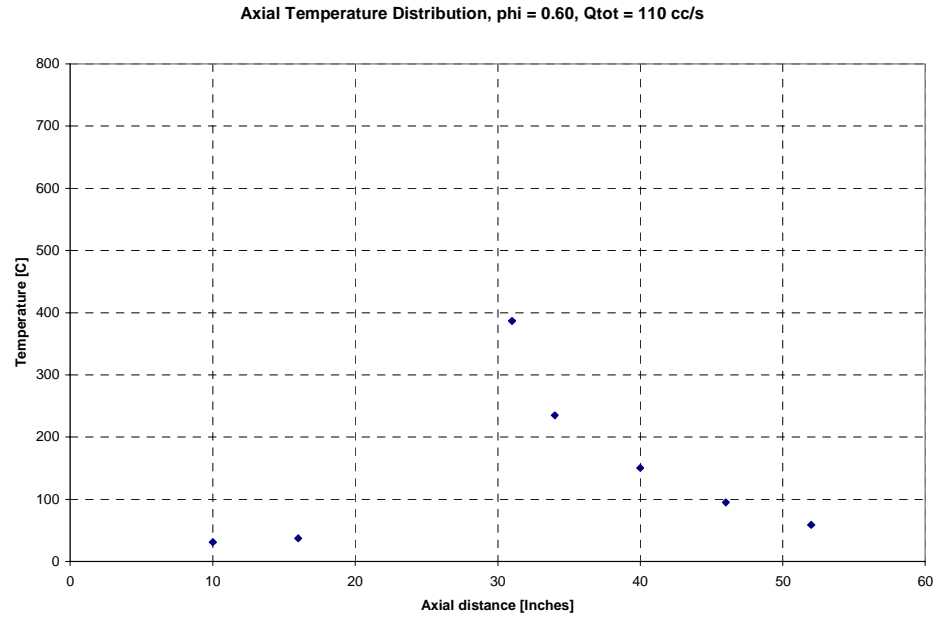


Figure E.13 Axial temperature distribution for  $\phi = 0.60$ ,  $Q_{tot} = 110$  cc/s

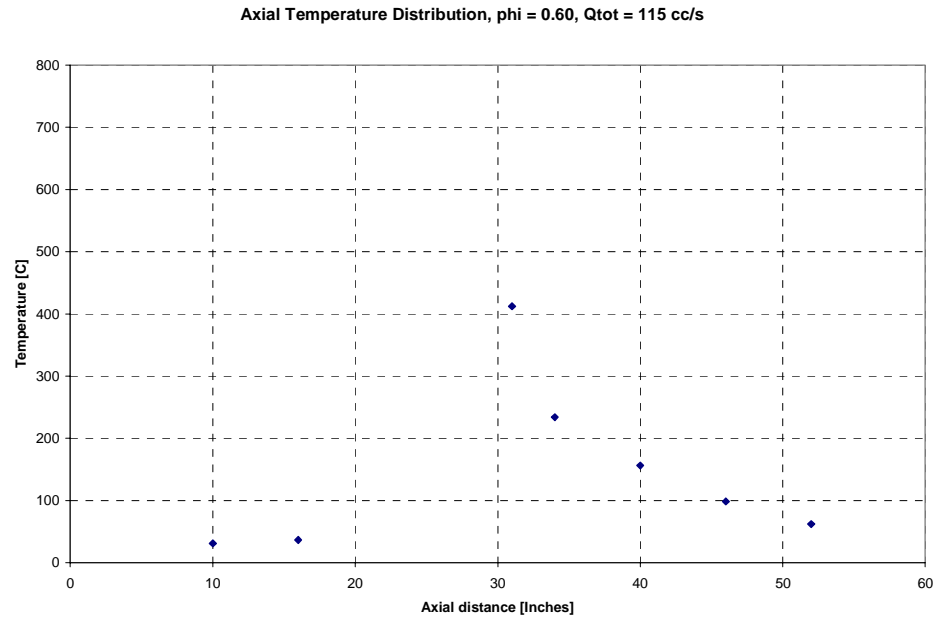


Figure E.14 Axial temperature distribution for  $\phi = 0.60$ ,  $Q_{tot} = 115$  cc/s

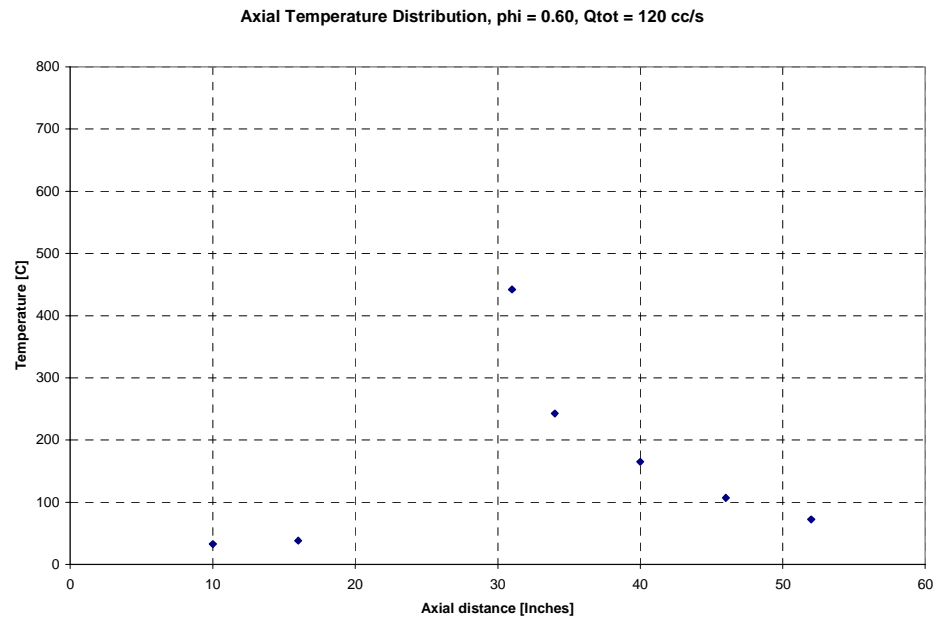


Figure E.15 Axial temperature distribution for  $\phi = 0.60$ ,  $Q_{tot} = 120$  cc/s

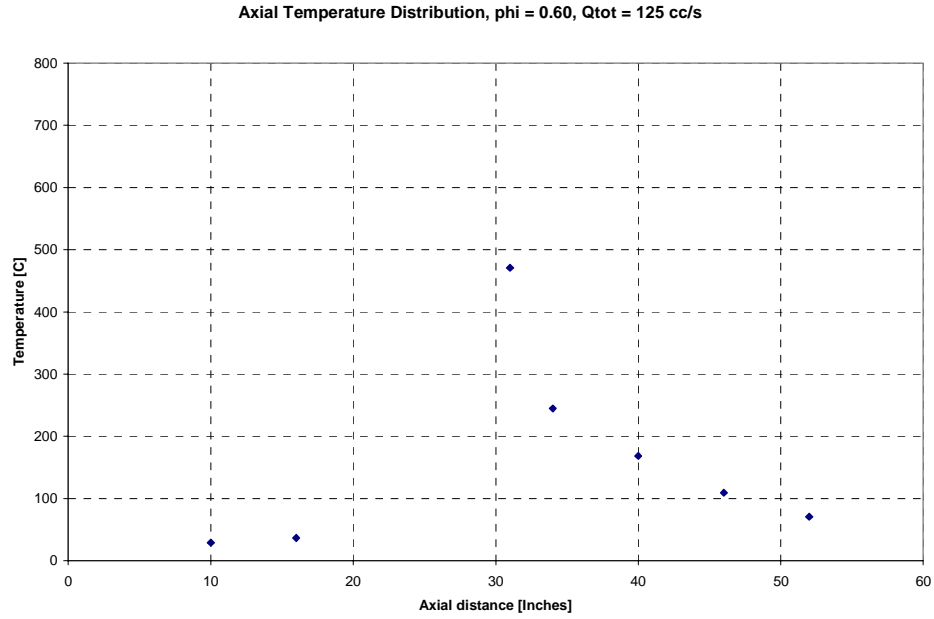


Figure E.16 Axial temperature distribution for  $\phi = 0.60$ ,  $Q_{tot}=125$  cc/s

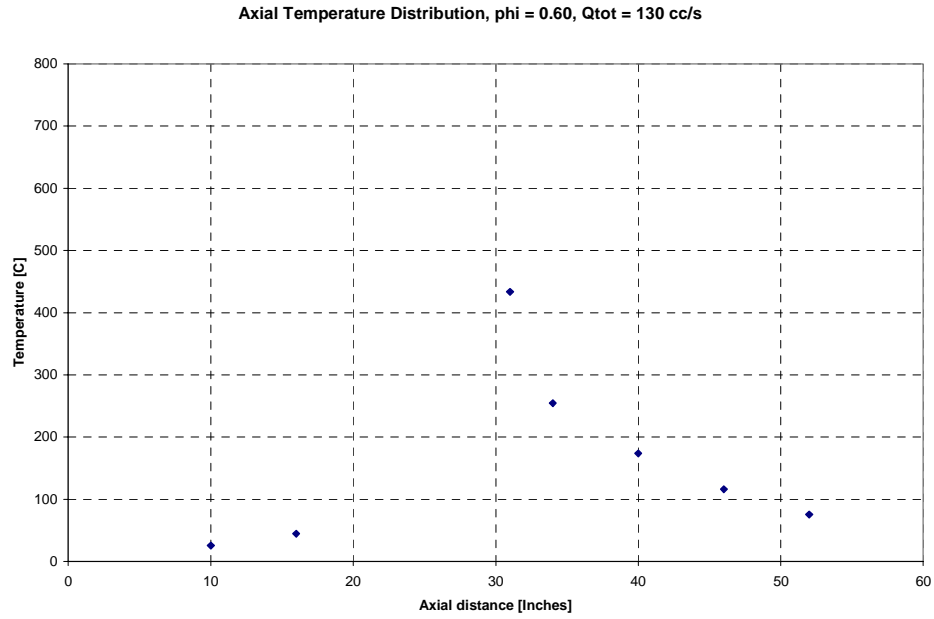


Figure E.17 Axial temperature distribution for  $\phi = 0.60$ ,  $Q_{tot}=130$  cc/s

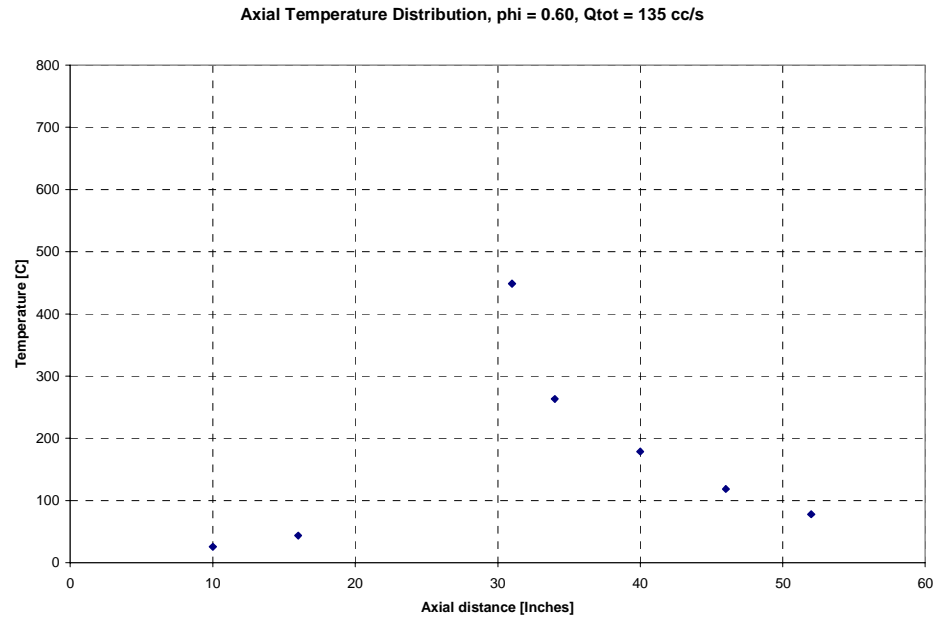


Figure E.18 Axial temperature distribution for  $\phi = 0.60$ ,  $Q_{tot} = 135$  cc/s

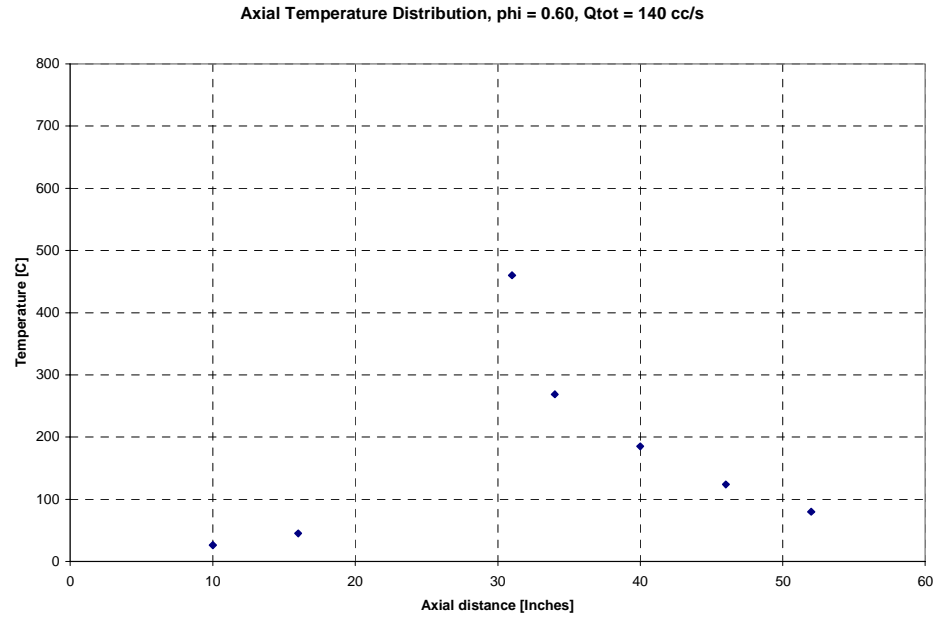


Figure E.19 Axial temperature distribution for  $\phi = 0.60$ ,  $Q_{tot} = 140$  cc/s

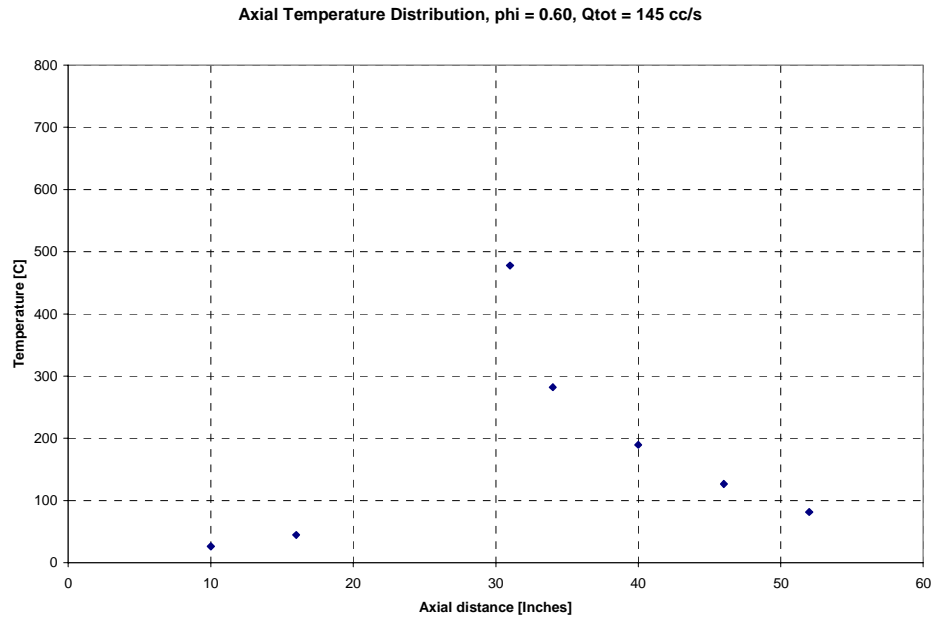


Figure E.20 Axial temperature distribution for  $\phi = 0.60$ ,  $Q_{tot} = 145$  cc/s

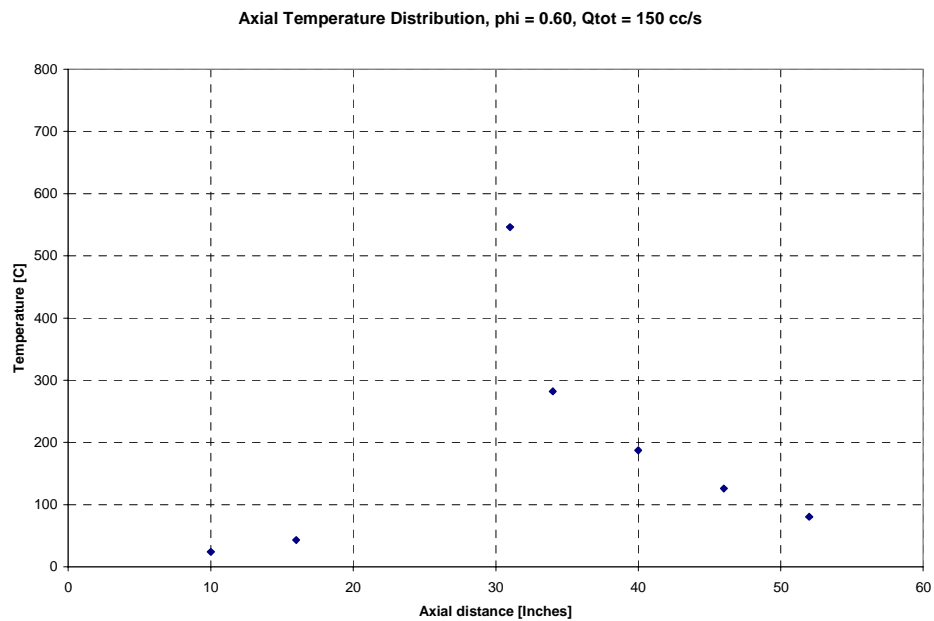


Figure E.21 Axial temperature distribution for  $\phi = 0.60$ ,  $Q_{tot} = 150$  cc/s

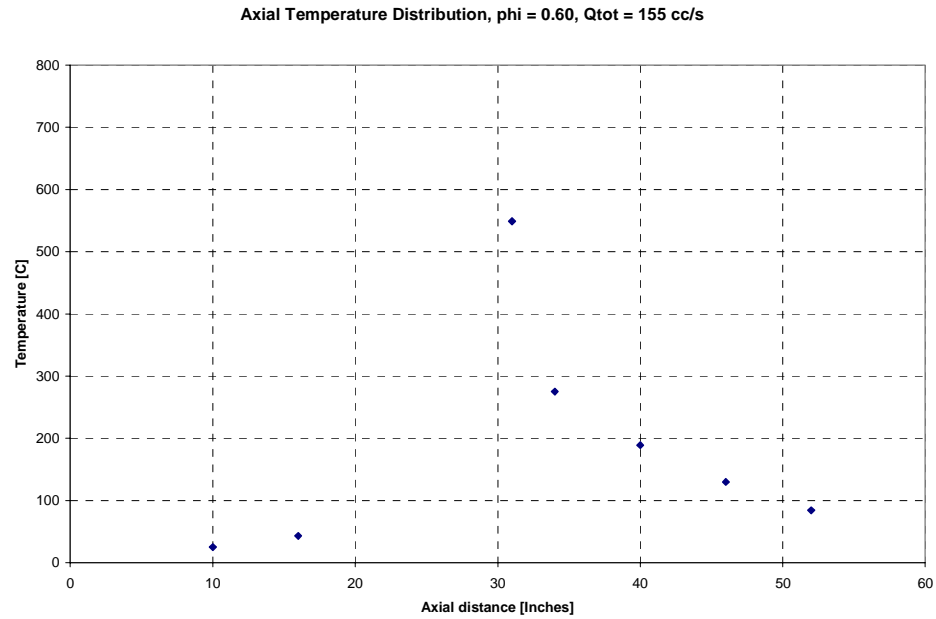


Figure E.22 Axial temperature distribution for  $\phi = 0.60$ ,  $Q_{tot} = 155$  cc/s

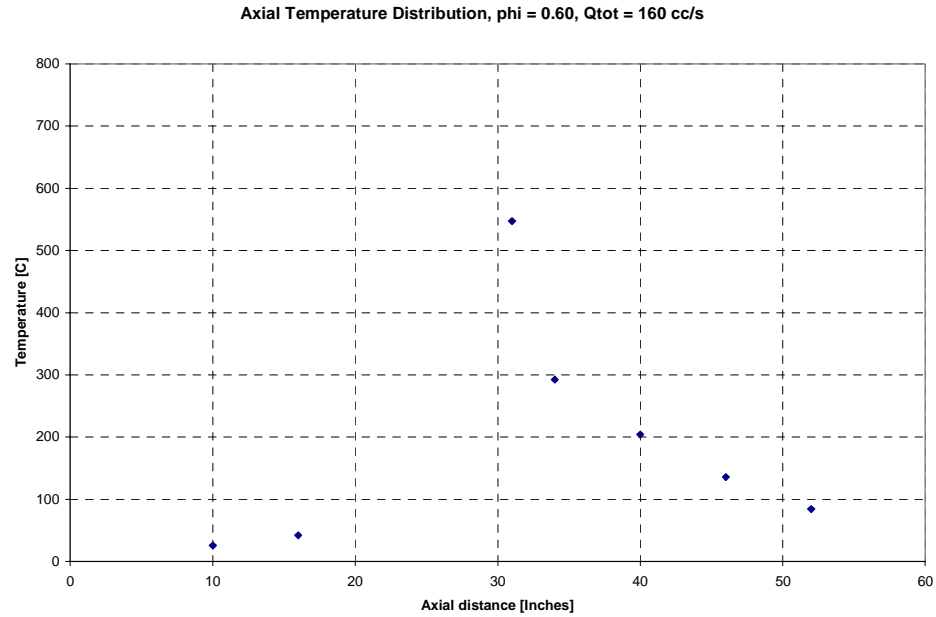


Figure E.23 Axial temperature distribution for  $\phi = 0.60$ ,  $Q_{tot} = 160$  cc/s

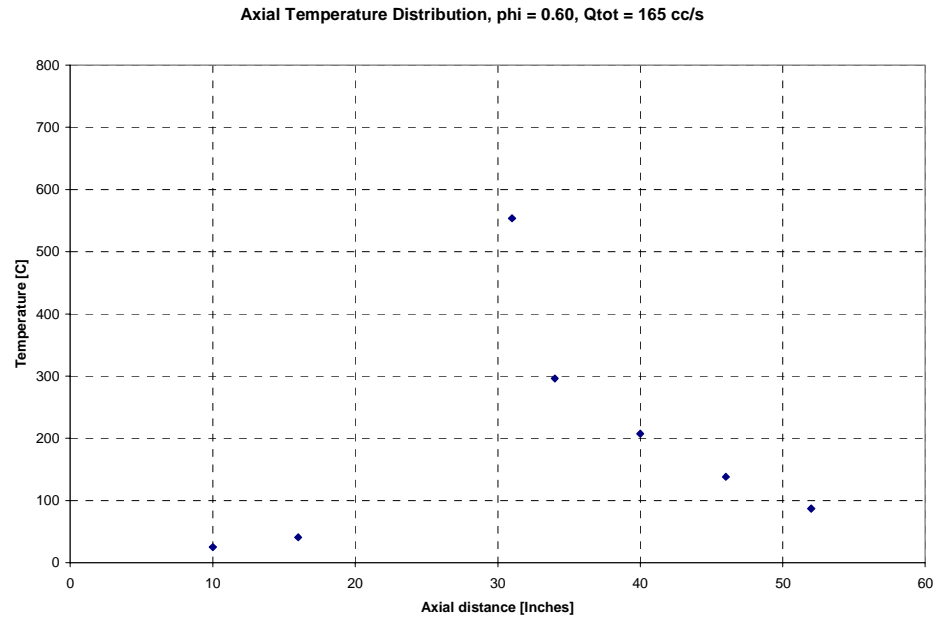


Figure E.24 Axial temperature distribution for  $\phi = 0.60$ ,  $Q_{tot} = 165$  cc/s

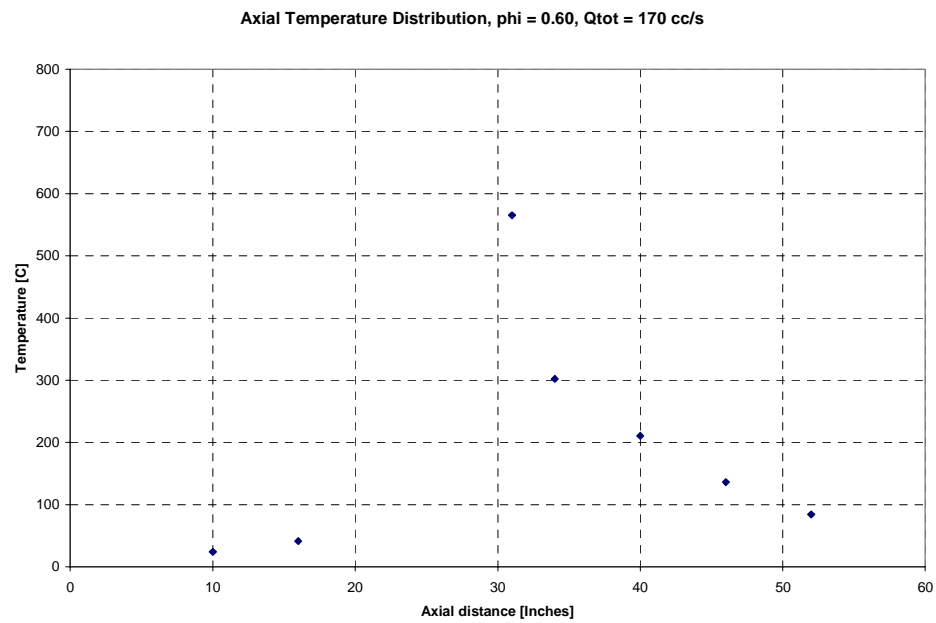


Figure E.25 Axial temperature distribution for  $\phi = 0.60$ ,  $Q_{tot} = 170$  cc/s

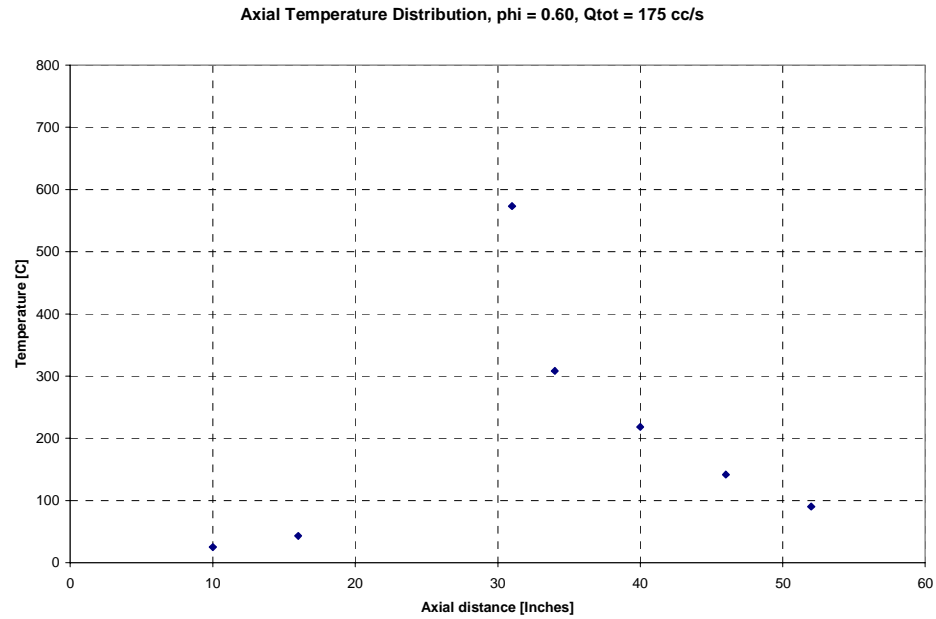


Figure E.26 Axial temperature distribution for  $\phi = 0.60$ ,  $Q_{tot} = 175$  cc/s

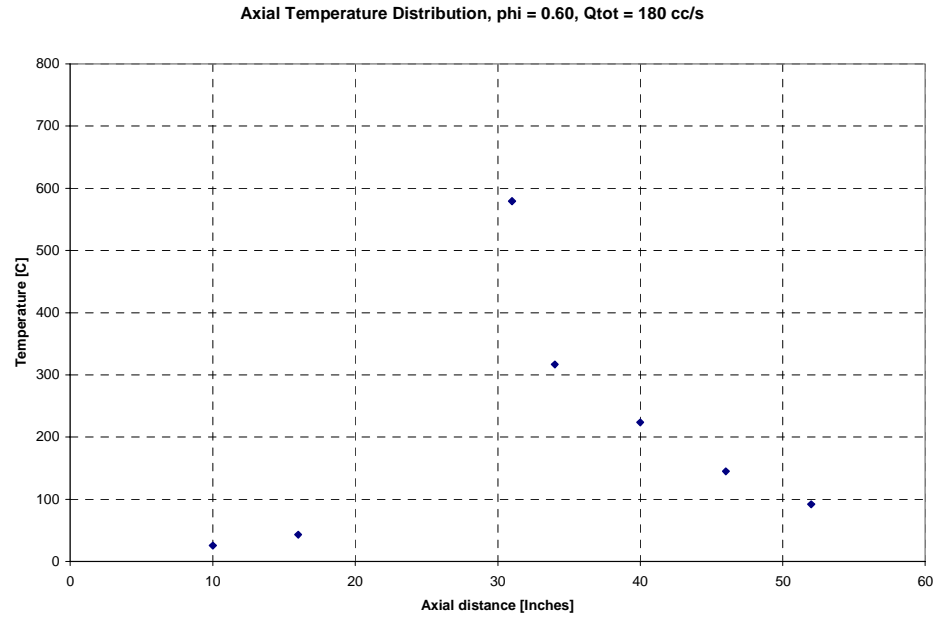


Figure E.27 Axial temperature distribution for  $\phi = 0.60$ ,  $Q_{tot} = 180$  cc/s

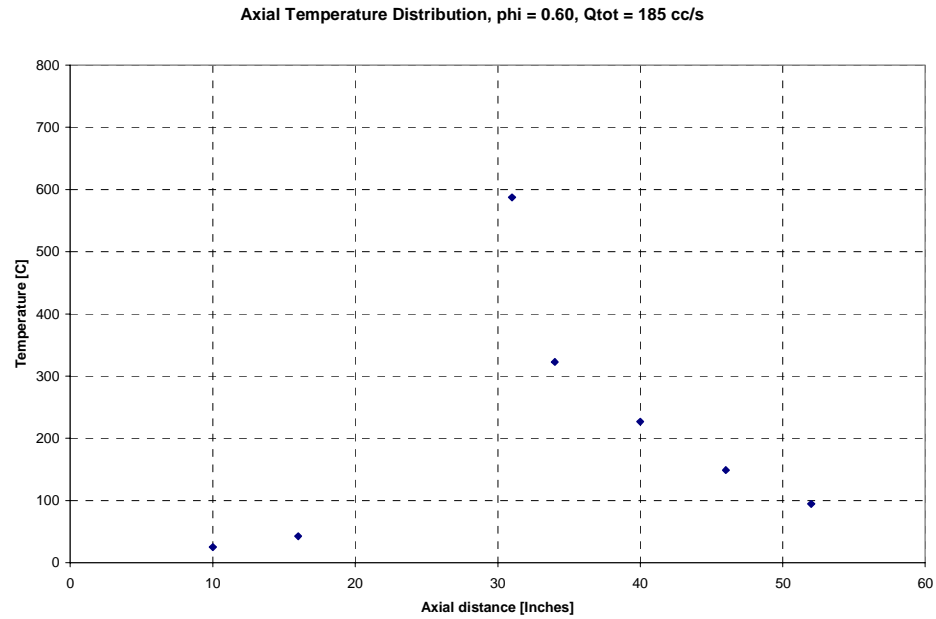


Figure E.28 Axial temperature distribution for  $\phi = 0.60$ ,  $Q_{tot} = 185$  cc/s

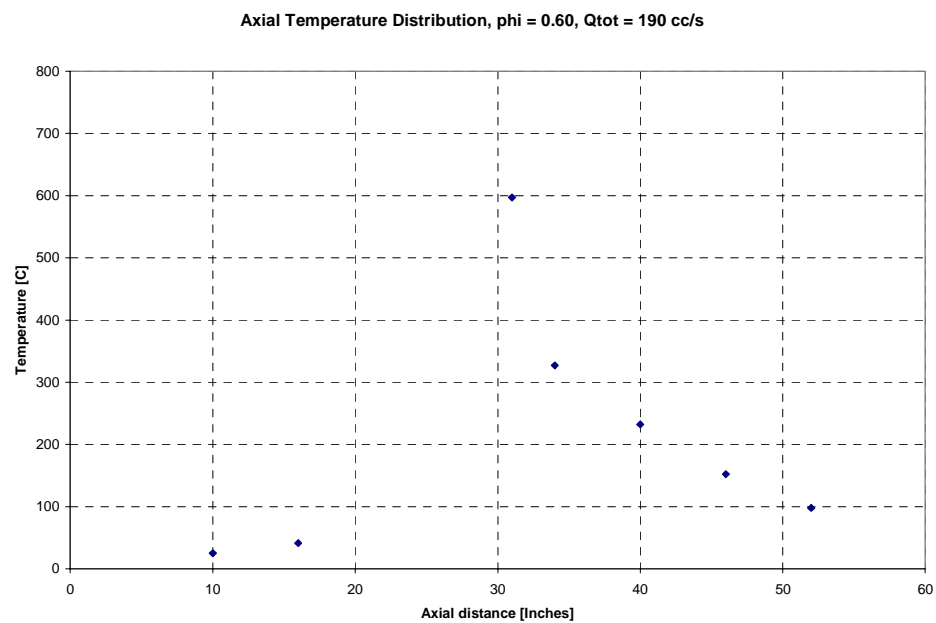


Figure E.29 Axial temperature distribution for  $\phi = 0.60$ ,  $Q_{tot} = 190$  cc/s

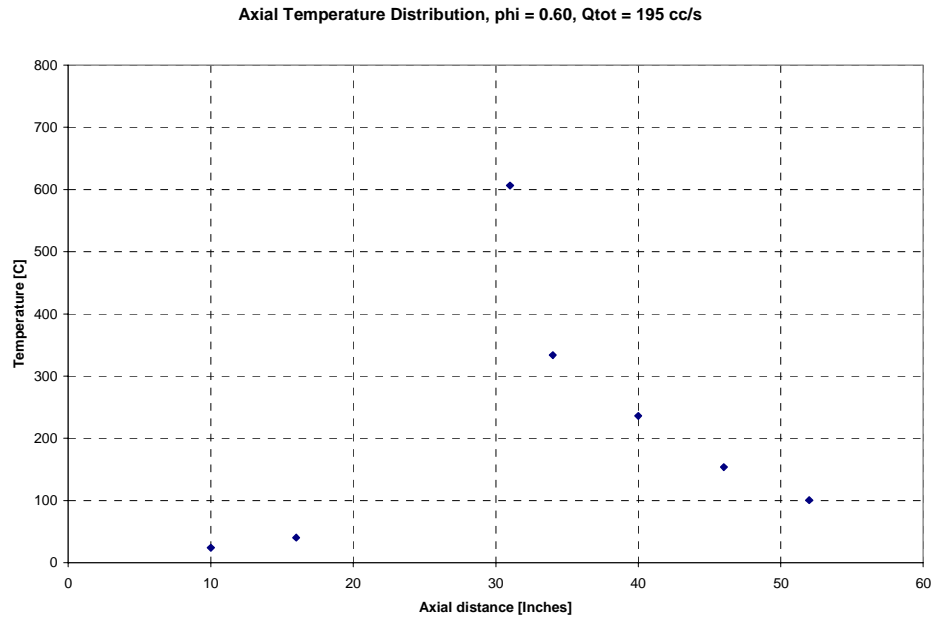


Figure E.30 Axial temperature distribution for  $\phi = 0.60$ ,  $Q_{tot} = 195$  cc/s

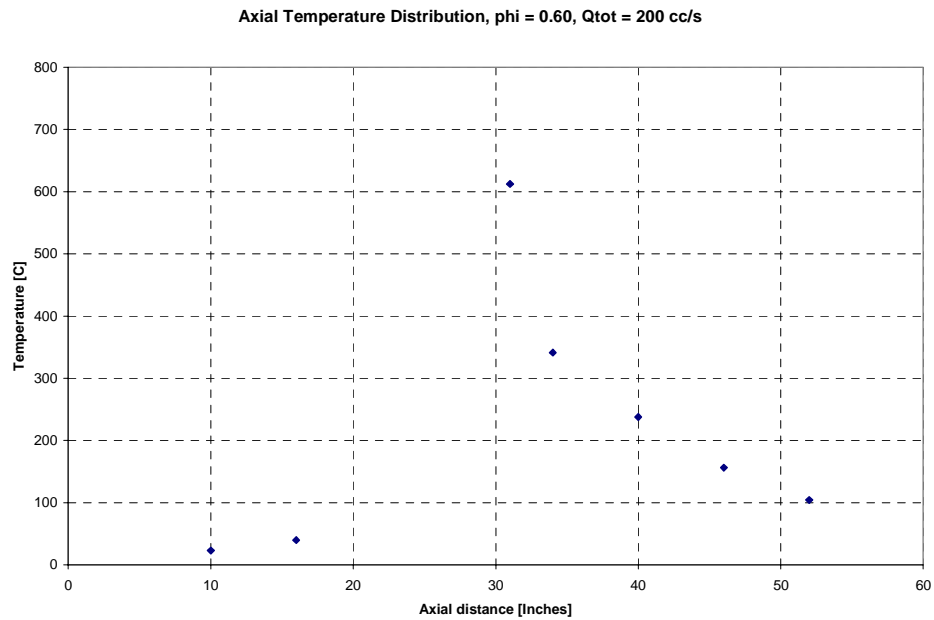


Figure E.31 Axial temperature distribution for  $\phi = 0.60$ ,  $Q_{tot} = 200$  cc/s

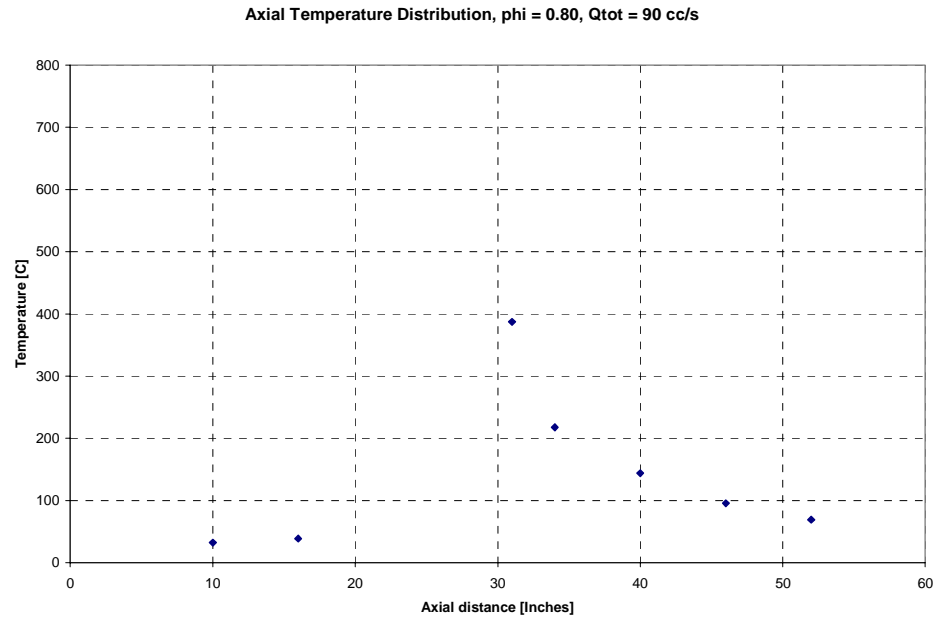


Figure E.32 Axial temperature distribution for  $\phi = 0.80$ ,  $Q_{tot} = 90$  cc/s

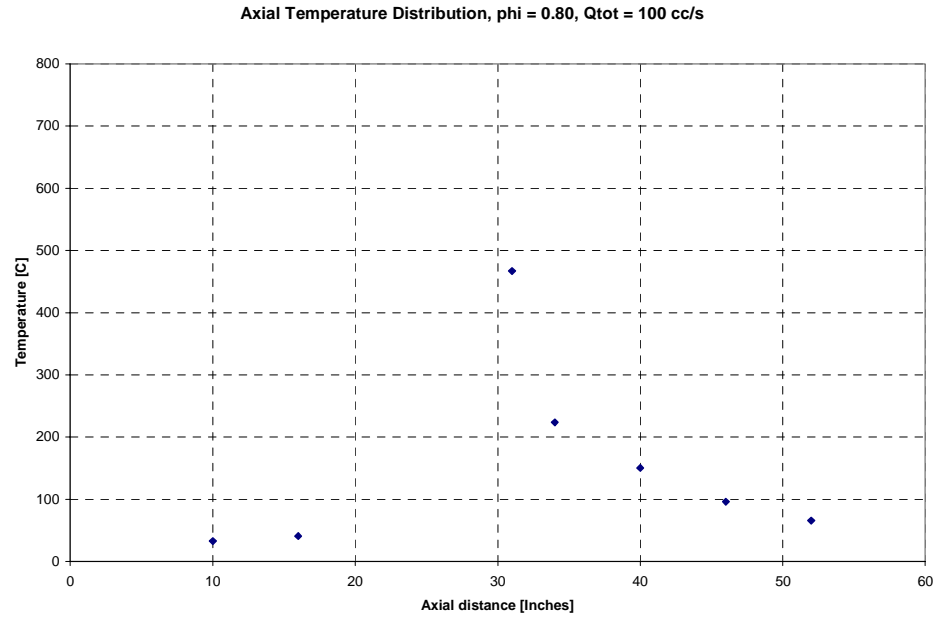


Figure E.33 Axial temperature distribution for  $\phi = 0.80$ ,  $Q_{tot} = 100$  cc/s

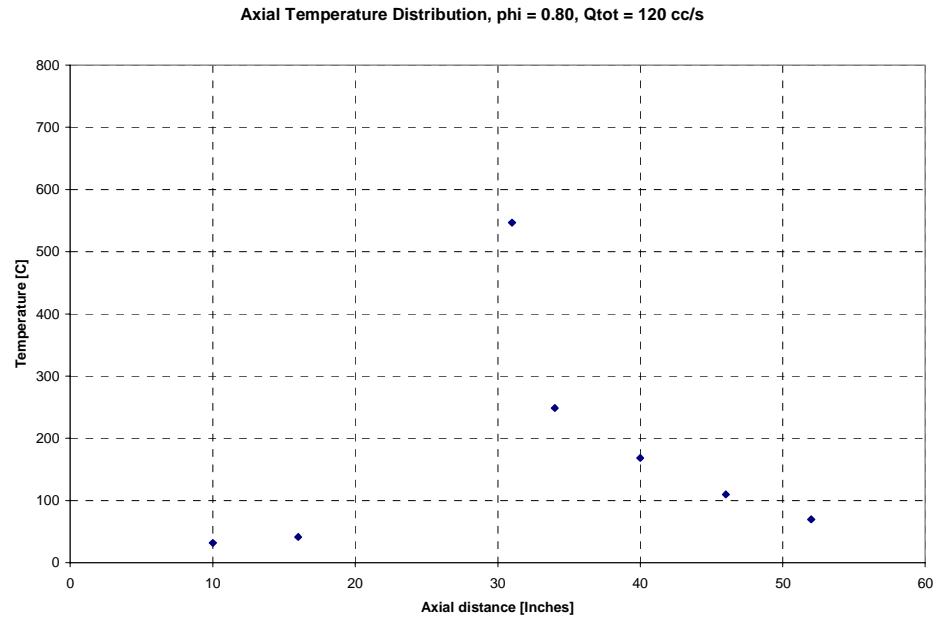


Figure E.34 Axial temperature distribution for  $\phi = 0.80$ ,  $Q_{tot} = 120$  cc/s

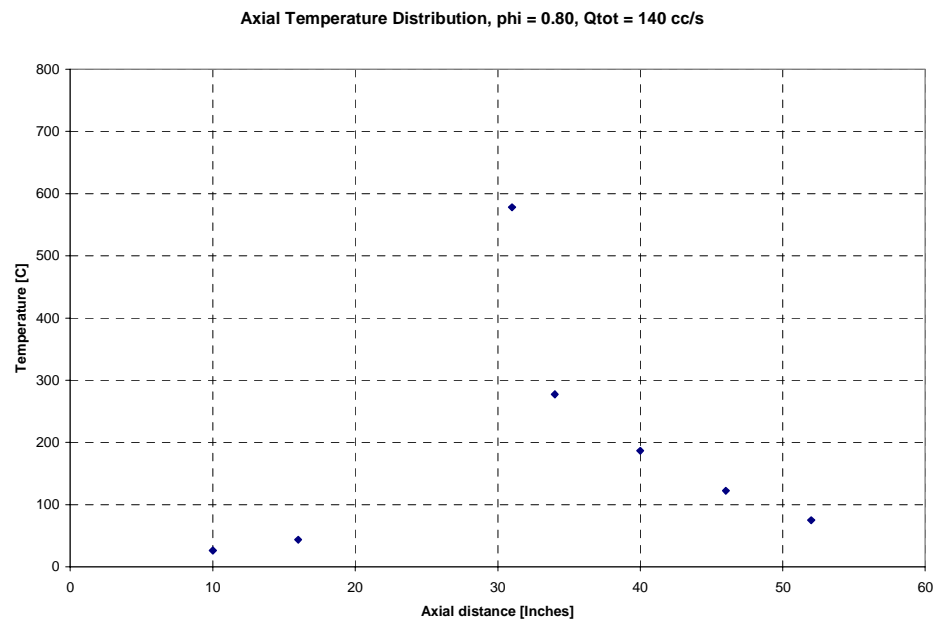


Figure E.35 Axial temperature distribution for  $\phi = 0.80$ ,  $Q_{tot} = 140$  cc/s

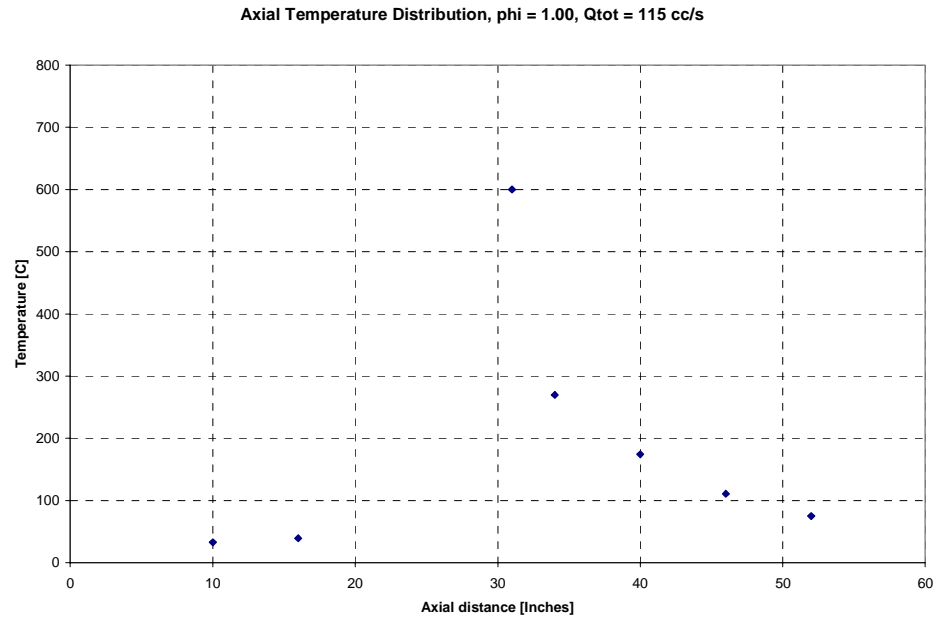


Figure E.36 Axial temperature distribution for  $\phi = 1.00$ ,  $Q_{tot} = 115$  cc/s

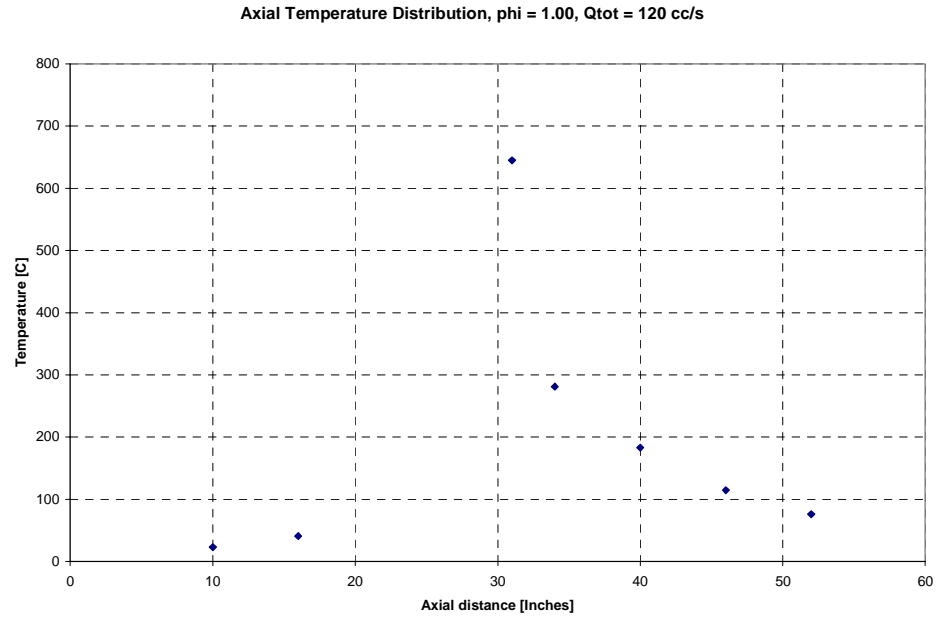


Figure E.37 Axial temperature distribution for  $\phi = 1.00$ ,  $Q_{tot} = 120$  cc/s

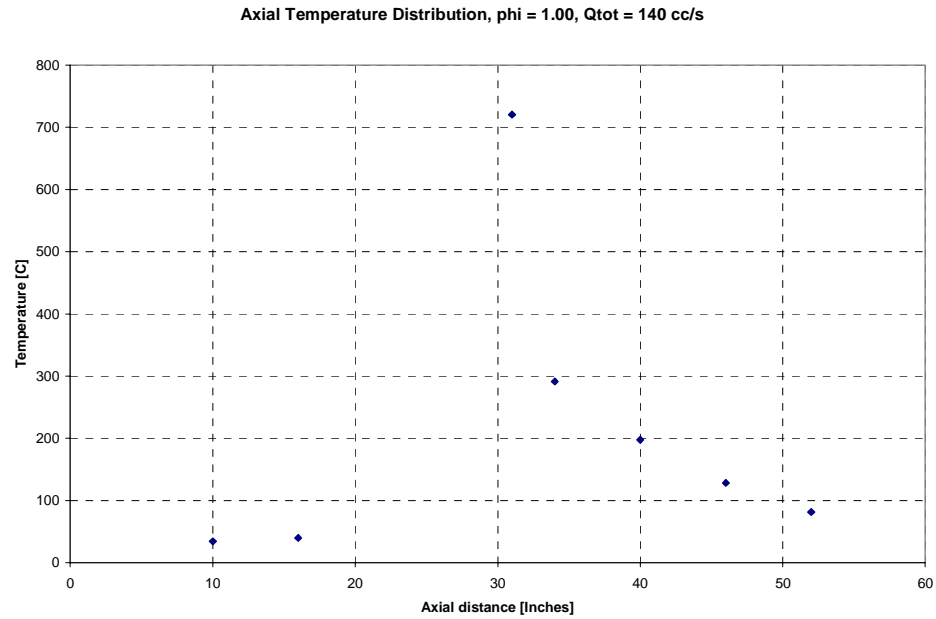


Figure E.38 Axial temperature distribution for  $\phi = 1.00$ ,  $Q_{tot} = 140$  cc/s

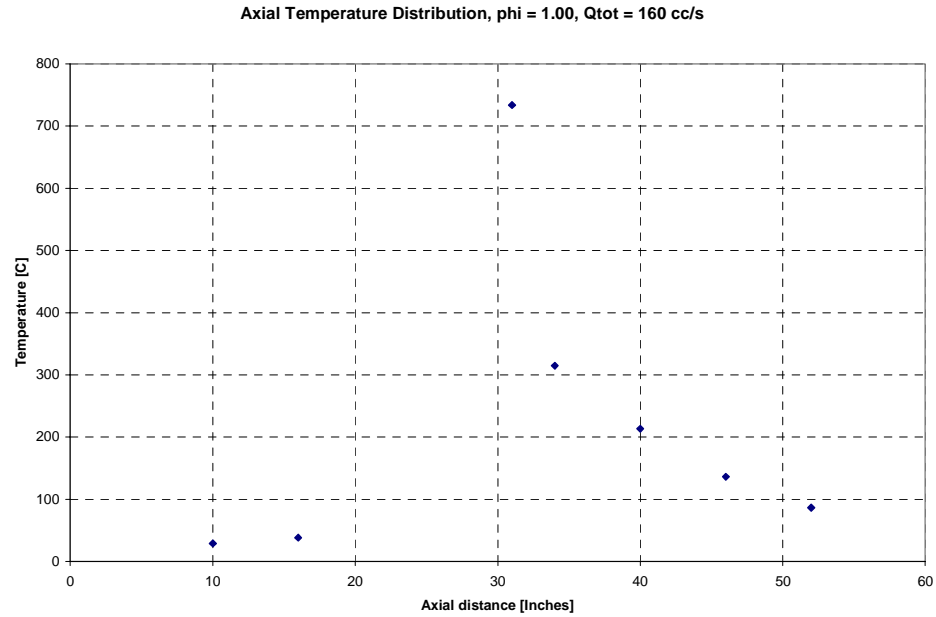


Figure E.39 Axial temperature distribution for  $\phi = 1.00$ ,  $Q_{tot} = 160$  cc/s

## **Appendix F      Axial Temperature Distribution for Constant Flow Rate**

In Appendix F, axial temperature distributions of the extensive mapping experiments will be presented. The axial distance is measured from the closed bottom end of the combustor. The flow rate was held constant with varying equivalence ratio for each data series. First the 100 cc/s flow rate series will be presented, followed by  $Q = 120, 140, 160, 180,$  and 200 cc/s series.

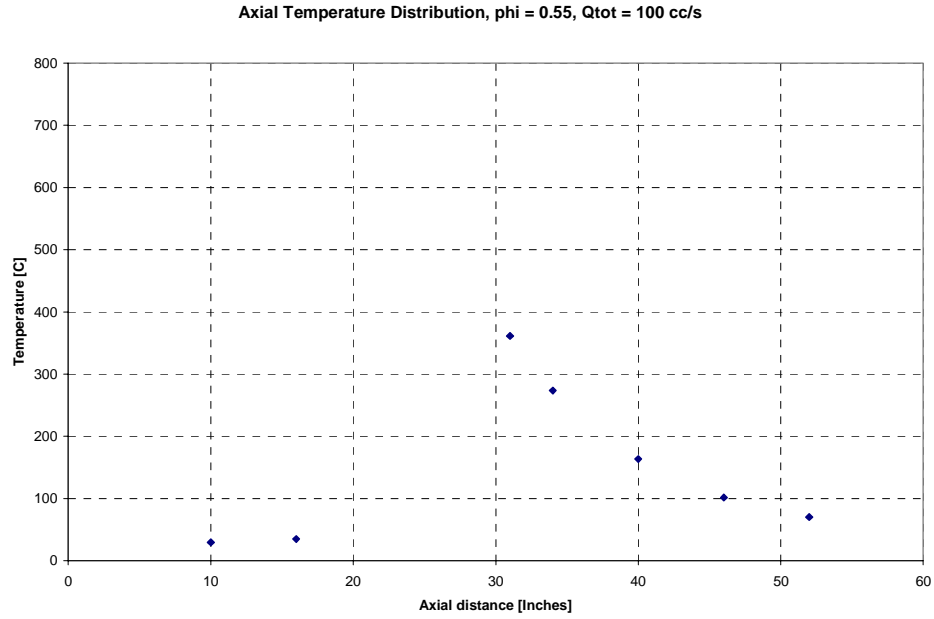


Figure F.1 Axial temperature distribution for  $\phi = 0.55$ ,  $Q_{tot} = 100$  cc/s

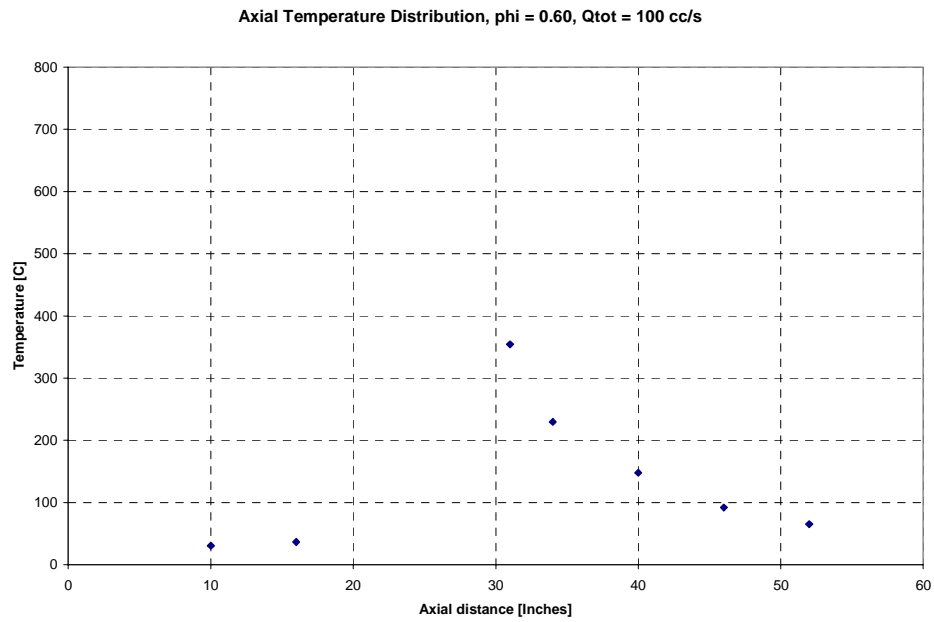


Figure F.2 Axial temperature distribution for  $\phi = 0.60$ ,  $Q_{tot} = 100$  cc/s

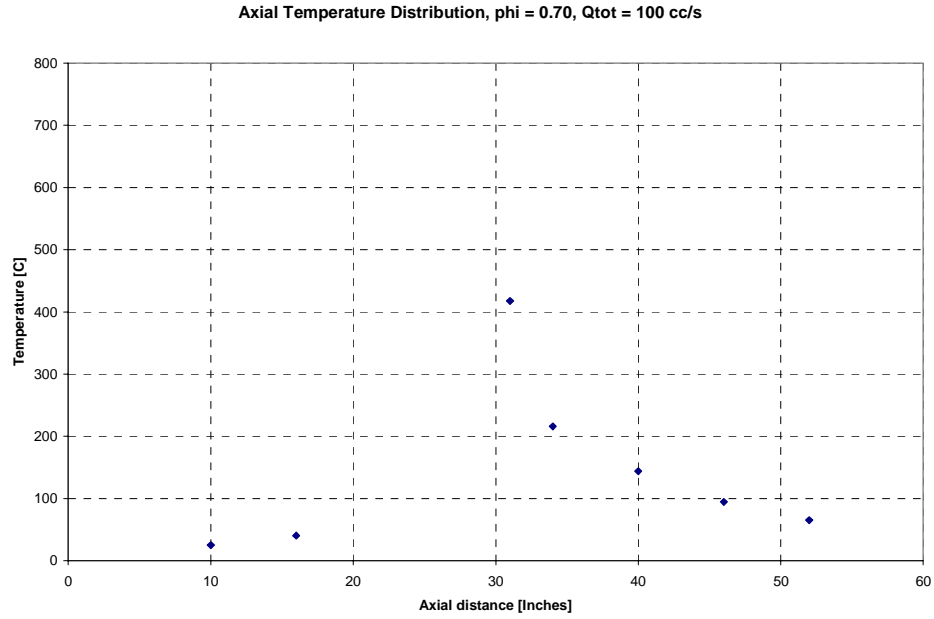


Figure F.3 Axial temperature distribution for  $\phi = 0.70$ ,  $Q_{tot} = 100$  cc/s

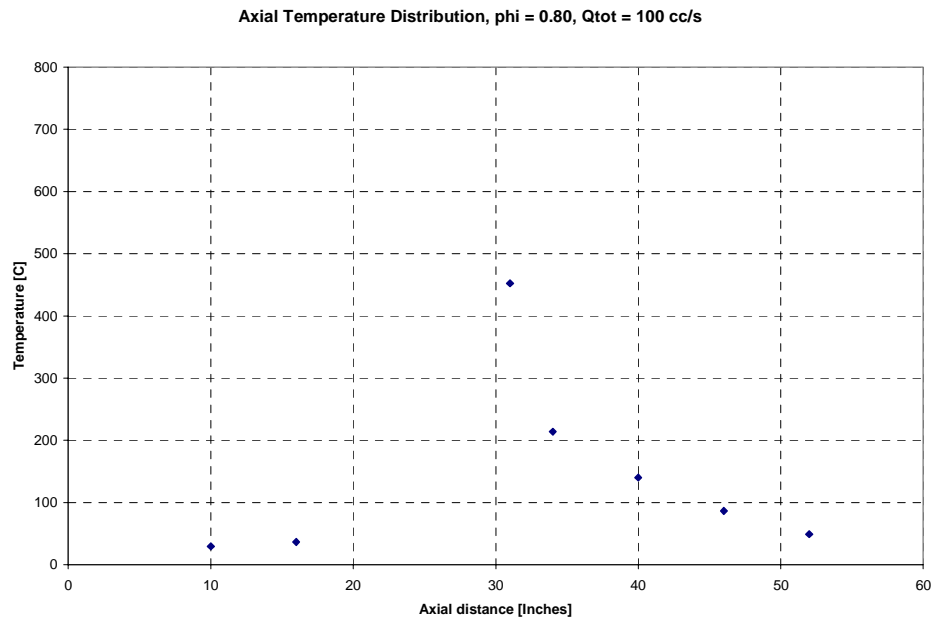


Figure F.4 Axial temperature distribution for  $\phi = 0.80$ ,  $Q_{tot} = 100$  cc/s

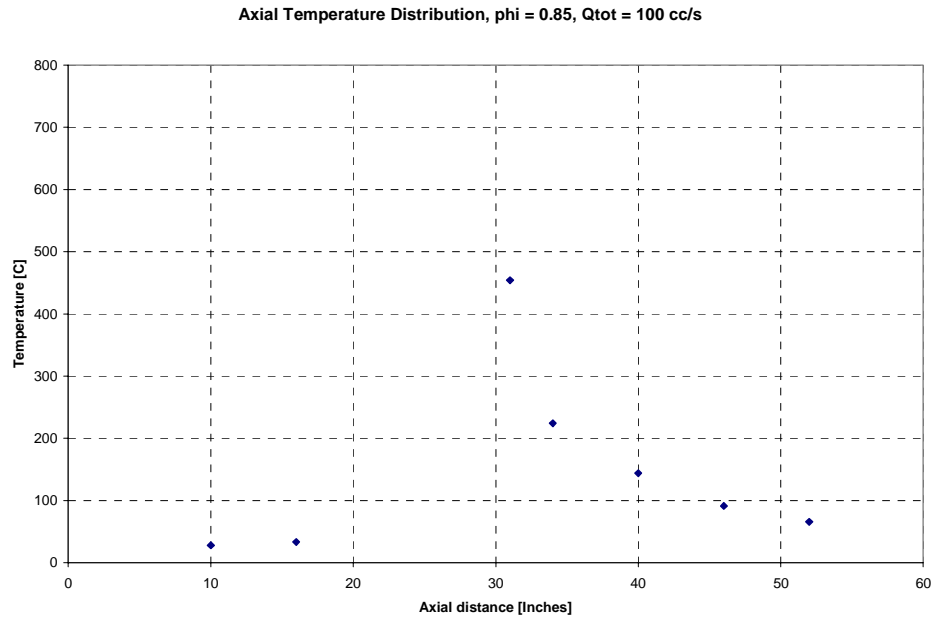


Figure F.5 Axial temperature distribution for  $\phi = 0.85$ ,  $Q_{tot} = 100$  cc/s

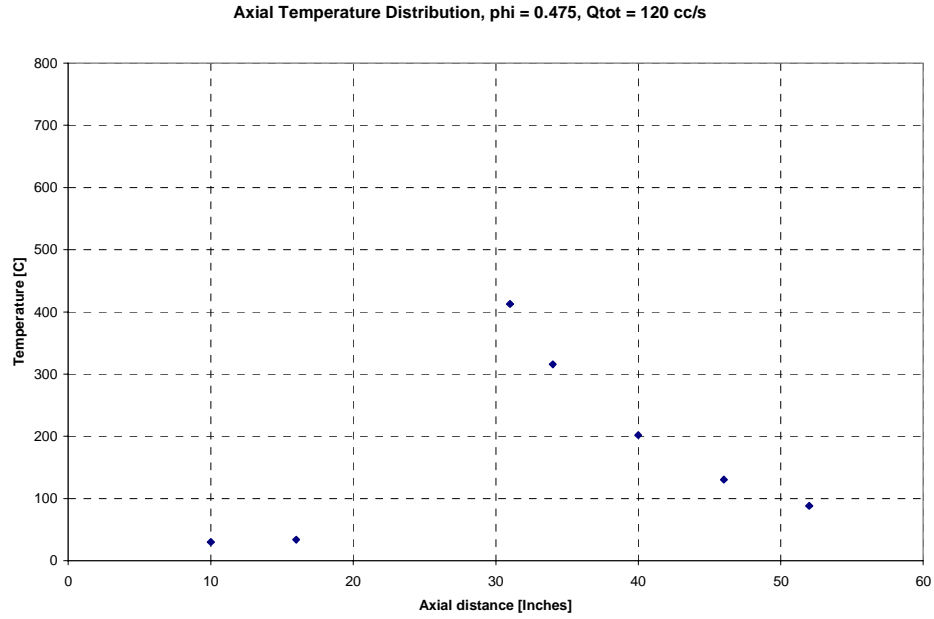


Figure F.6 Axial temperature distribution for  $\phi = 0.475$ ,  $Q_{tot} = 120$  cc/s

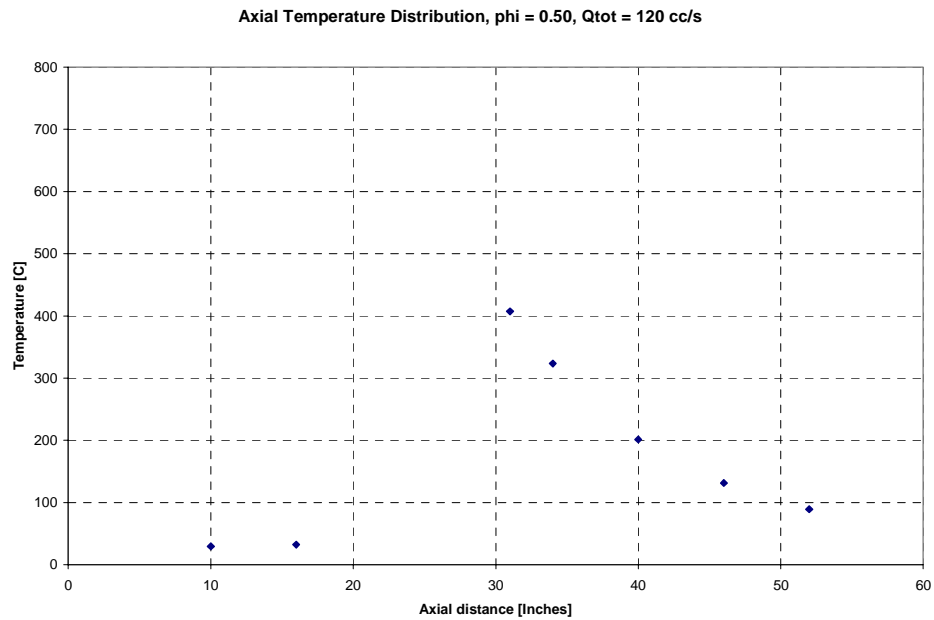


Figure F.7 Axial temperature distribution for  $\phi = 0.50$ ,  $Q_{tot} = 120$  cc/s

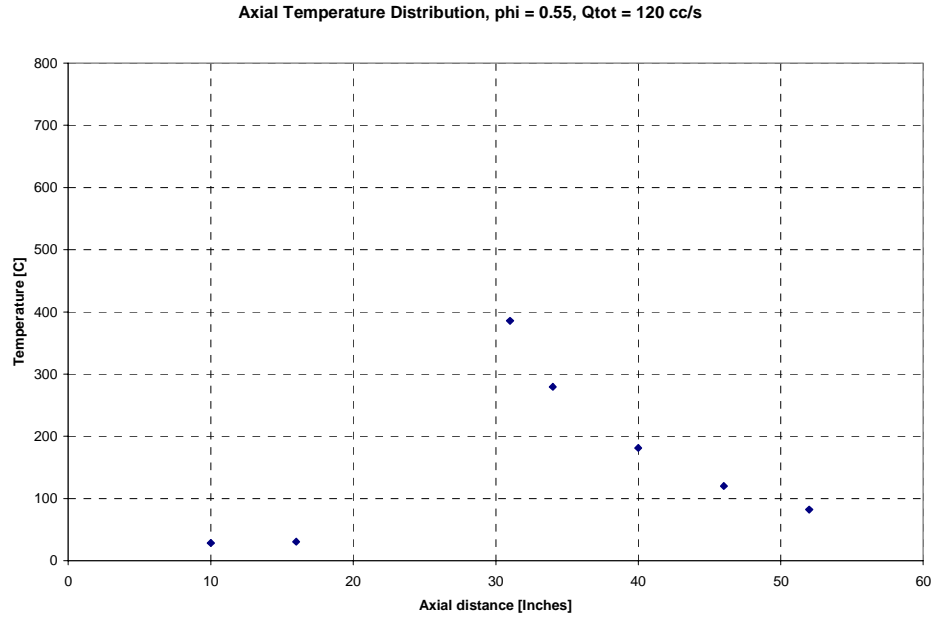


Figure F.8 Axial temperature distribution for  $\phi = 0.55$ ,  $Q_{tot} = 120$  cc/s

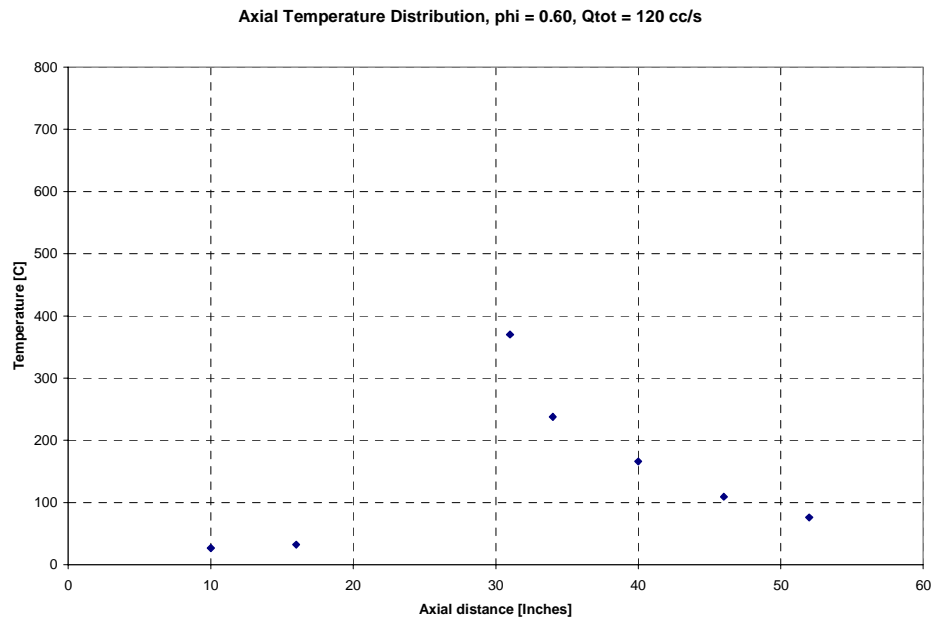


Figure F.9 Axial temperature distribution for  $\phi = 0.60$ ,  $Q_{tot} = 120$  cc/s

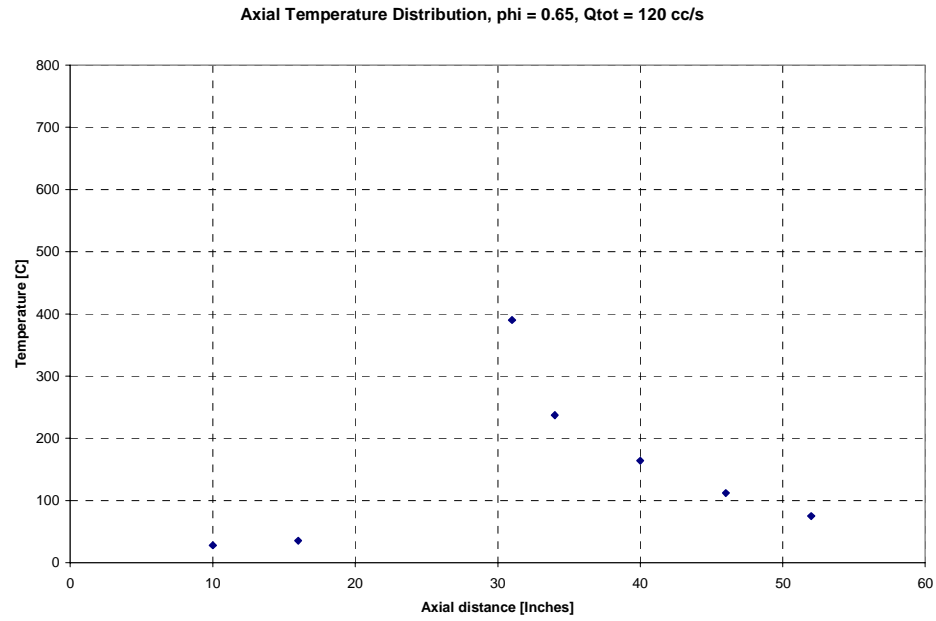


Figure F.10 Axial temperature distribution for  $\phi = 0.65$ ,  $Q_{tot} = 120$  cc/s

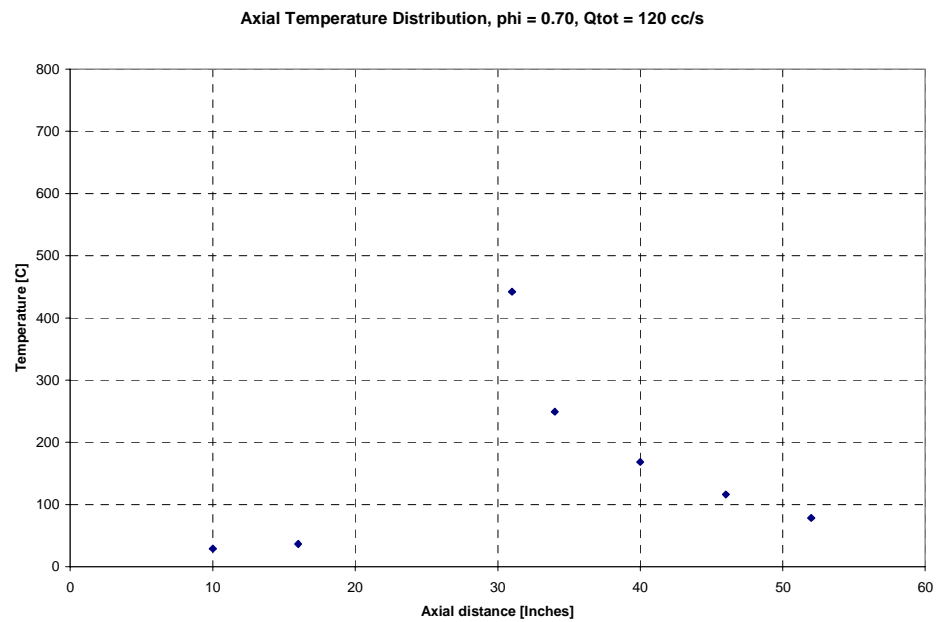


Figure F.11 Axial temperature distribution for  $\phi = 0.70$ ,  $Q_{tot} = 120$  cc/s

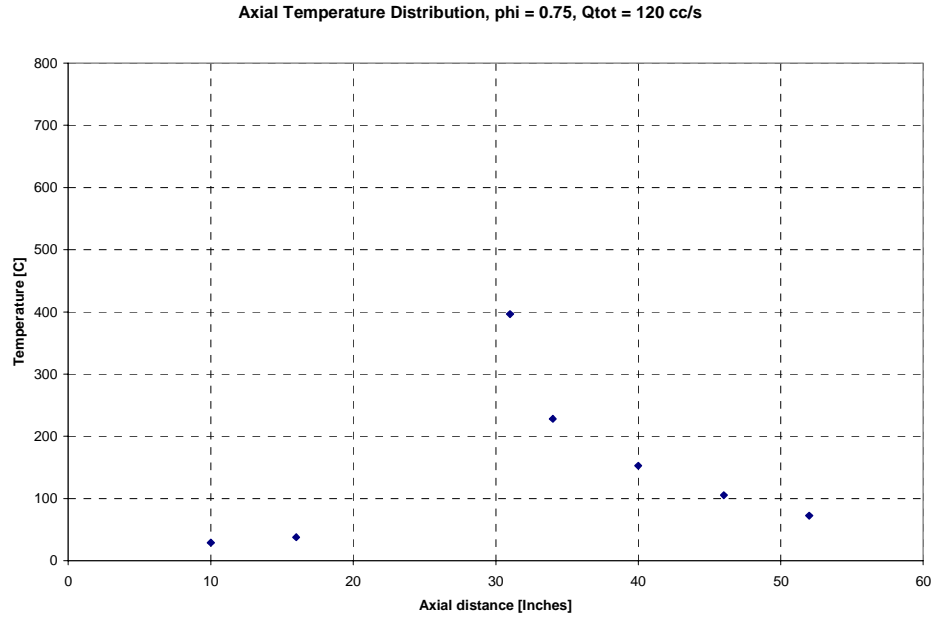


Figure F.12 Axial temperature distribution for  $\phi = 0.75$ ,  $Q_{tot} = 120$  cc/s

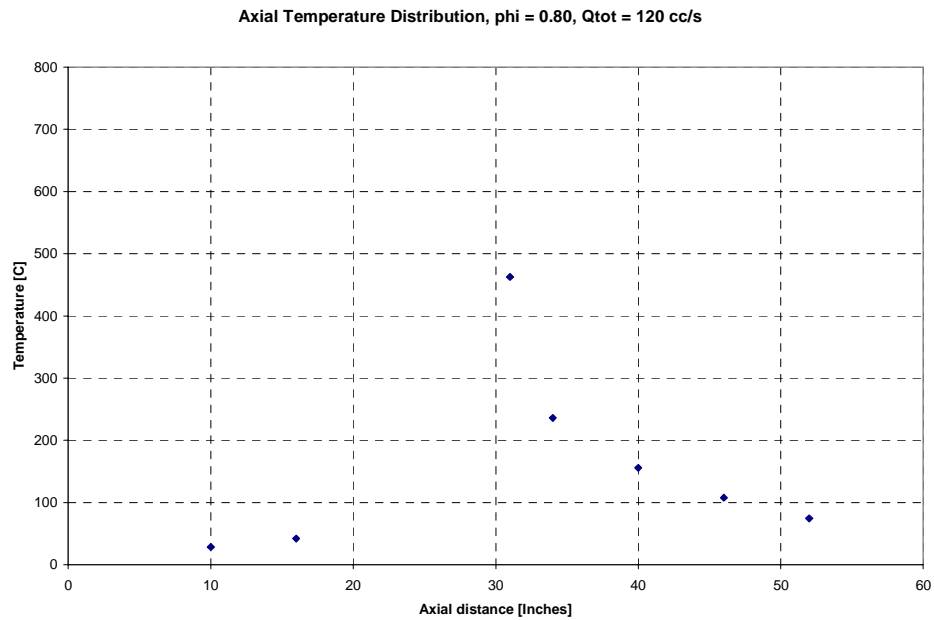


Figure F.13 Axial temperature distribution for  $\phi = 0.80$ ,  $Q_{tot} = 120$  cc/s

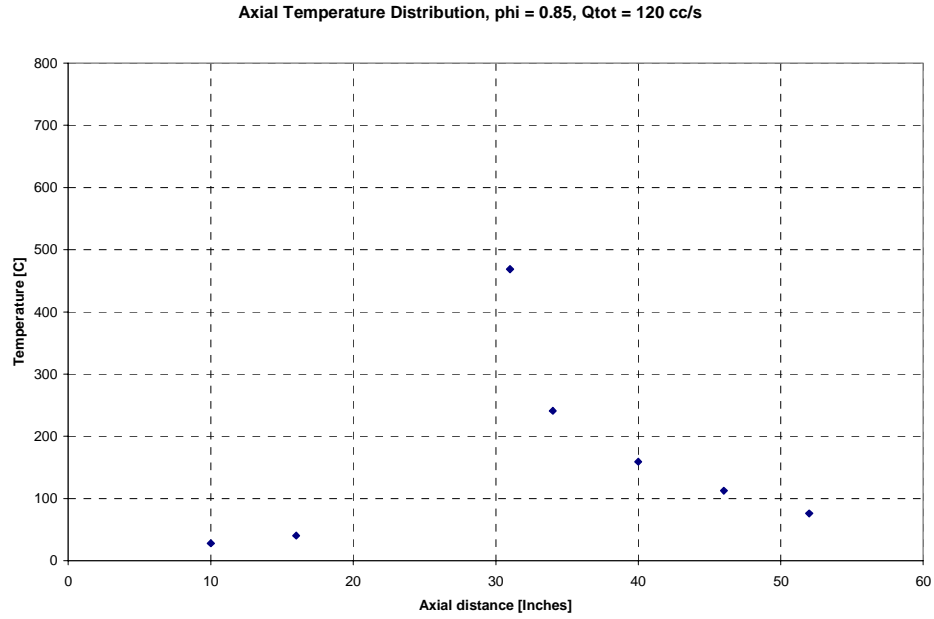


Figure F.14 Axial temperature distribution for  $\phi = 0.85$ ,  $Q_{tot} = 120$  cc/s

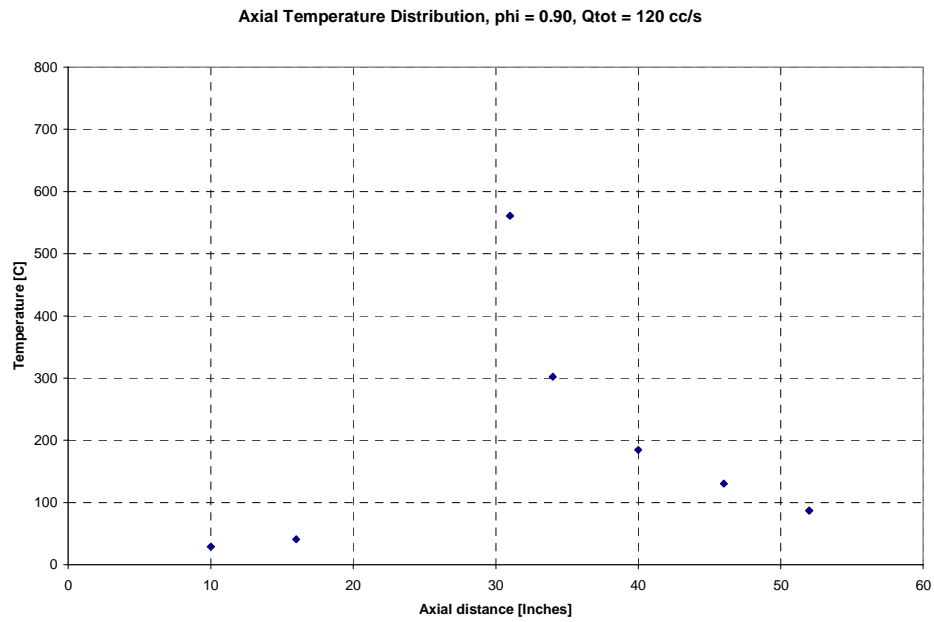


Figure F.15 Axial temperature distribution for  $\phi = 0.90$ ,  $Q_{tot} = 120$  cc/s

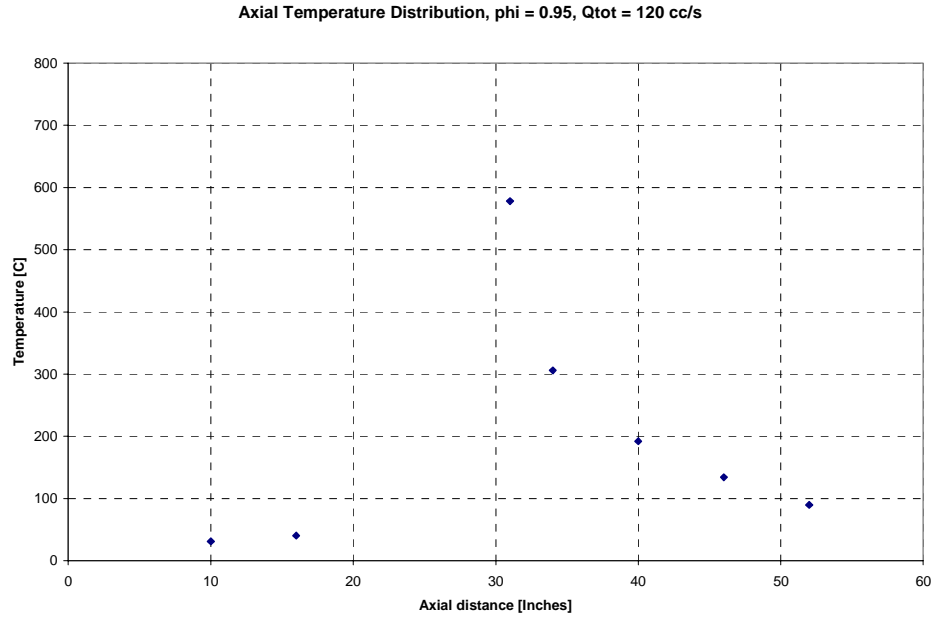


Figure F.16 Axial temperature distribution for  $\phi = 0.95$ ,  $Q_{tot} = 120$  cc/s

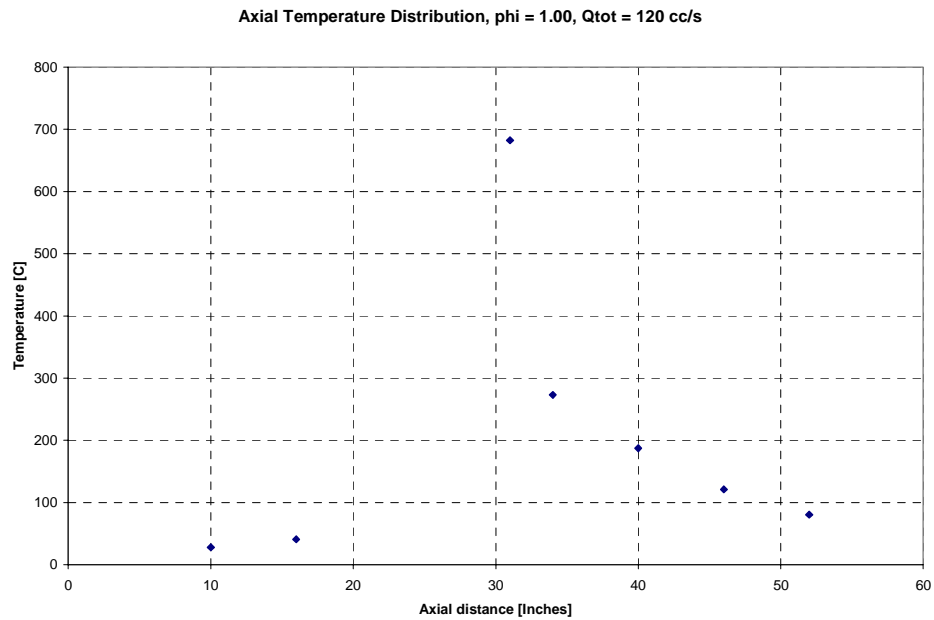


Figure F.17 Axial temperature distribution for  $\phi = 1.00$ ,  $Q_{tot} = 120$  cc/s

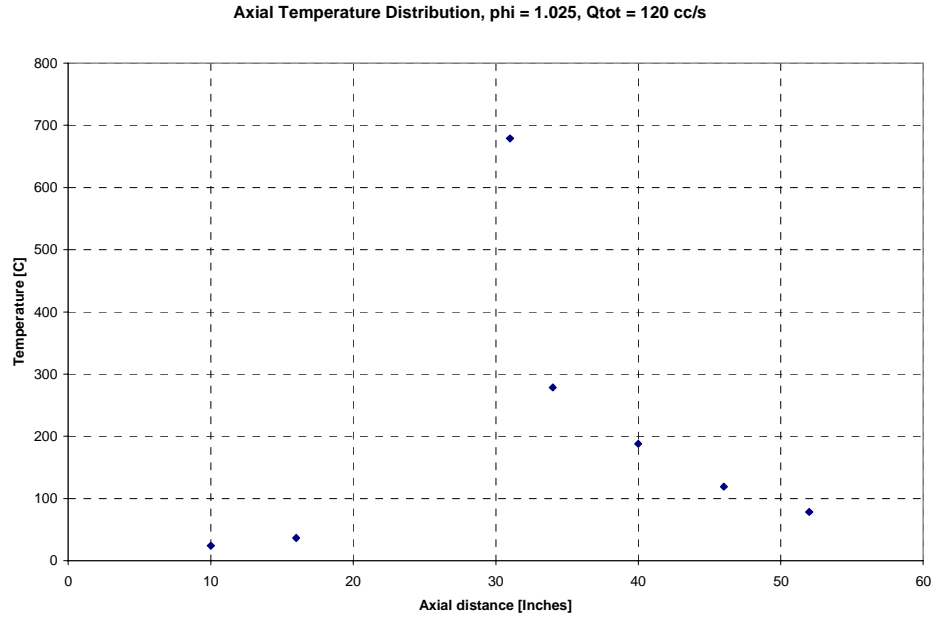


Figure F.18 Axial temperature distribution for  $\phi = 1.025$ ,  $Q_{tot} = 120$  cc/s

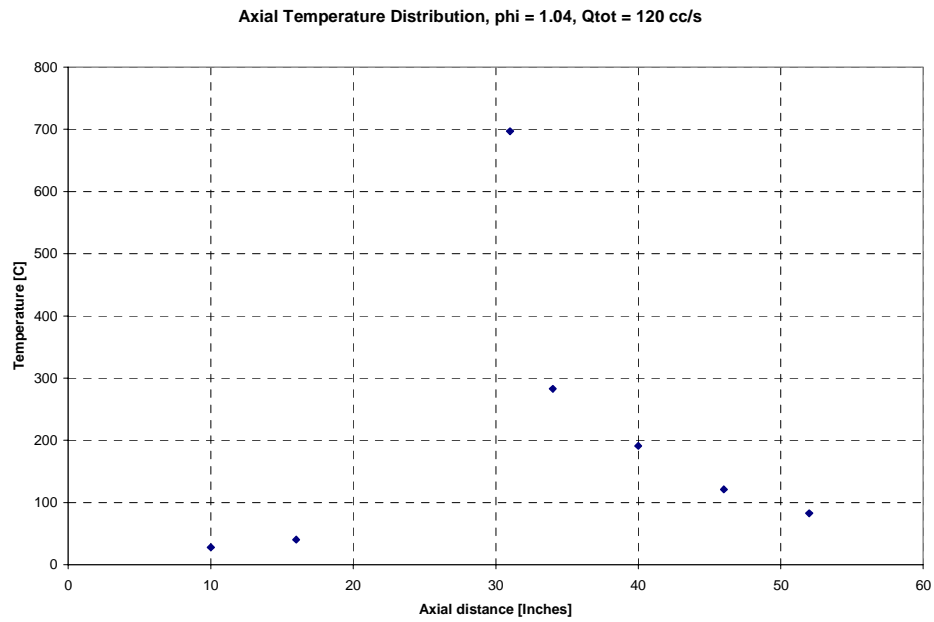


Figure F.19 Axial temperature distribution for  $\phi = 1.04$ ,  $Q_{tot} = 120$  cc/s

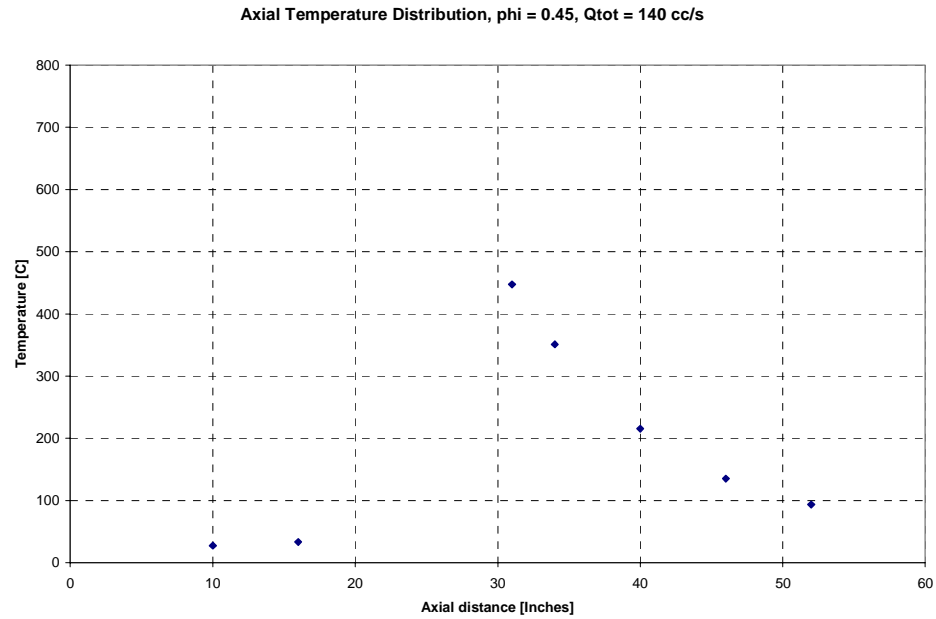


Figure F.20 Axial temperature distribution for  $\phi = 0.45$ ,  $Q_{tot} = 140$  cc/s

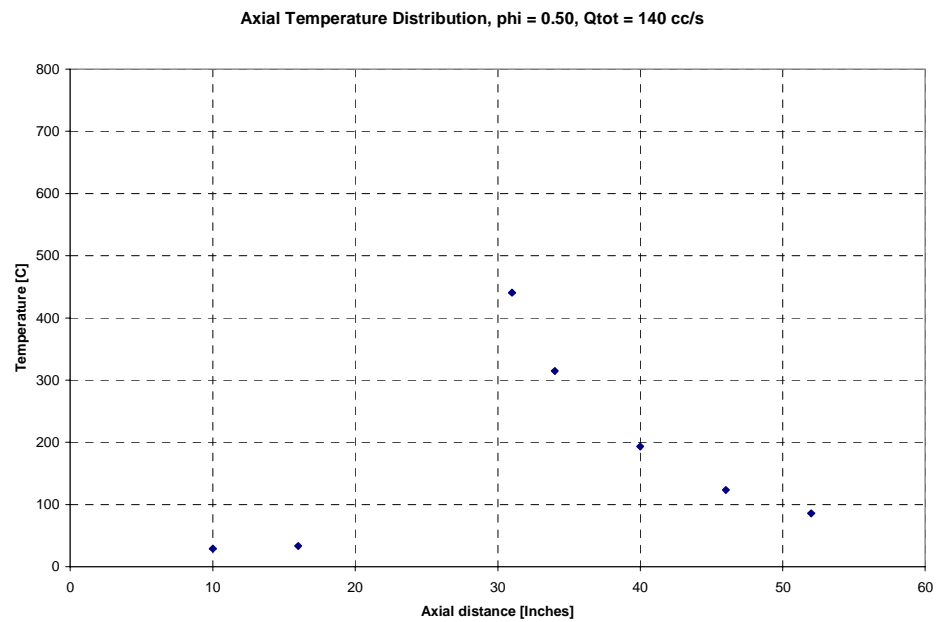


Figure F.21 Axial temperature distribution for  $\phi = 0.50$ ,  $Q_{tot} = 140$  cc/s

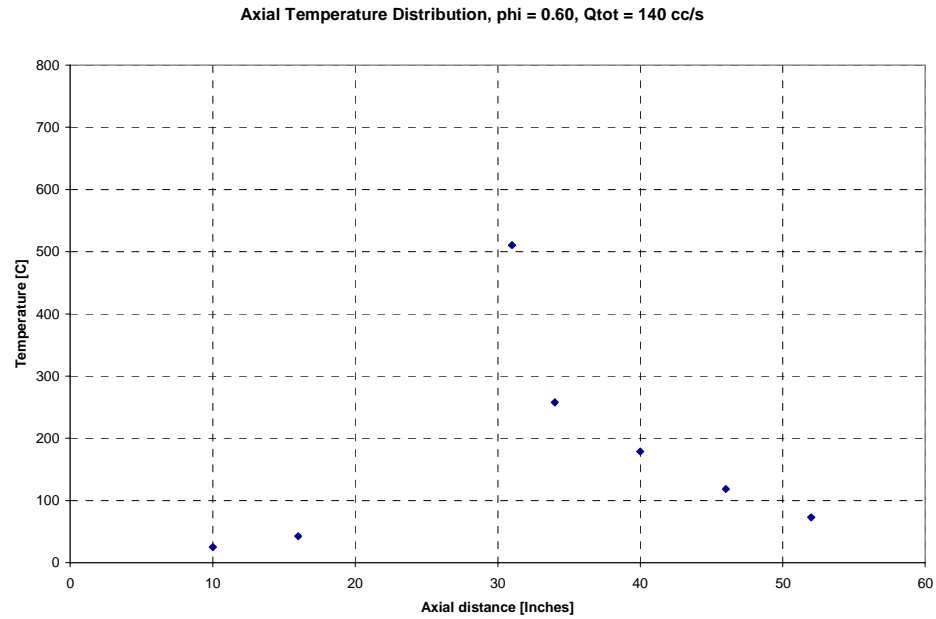


Figure F.22 Axial temperature distribution for  $\phi = 0.60$ ,  $Q_{tot} = 140$  cc/s

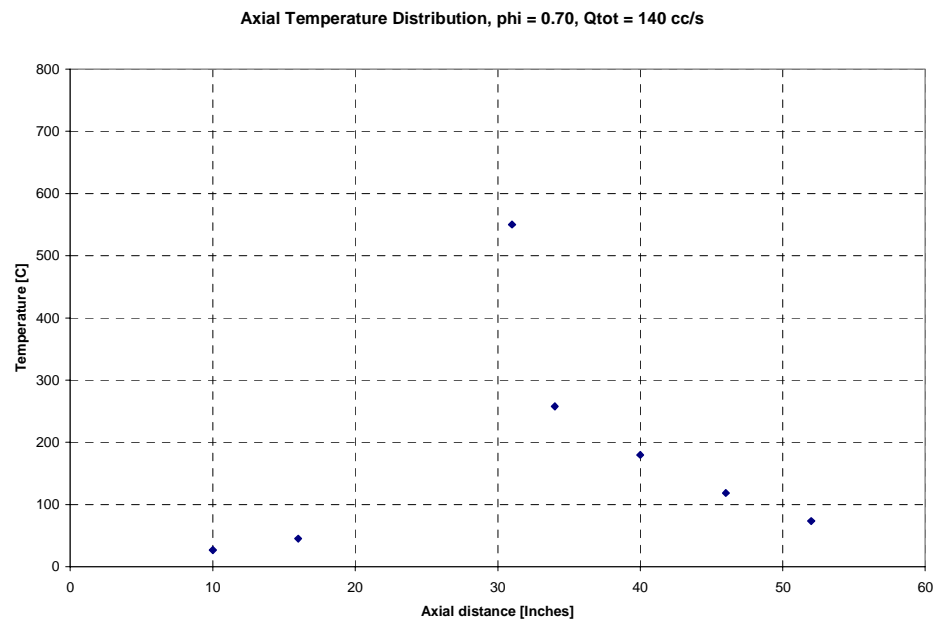


Figure F.23 Axial temperature distribution for  $\phi = 0.70$ ,  $Q_{tot} = 140$  cc/s

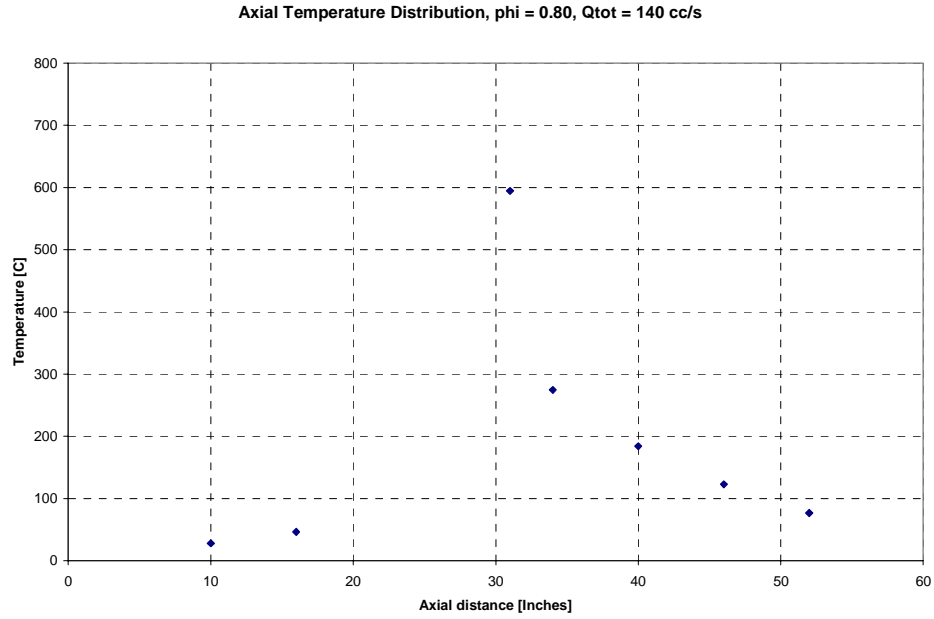


Figure F.24 Axial temperature distribution for  $\phi = 0.80$ ,  $Q_{tot} = 140$  cc/s

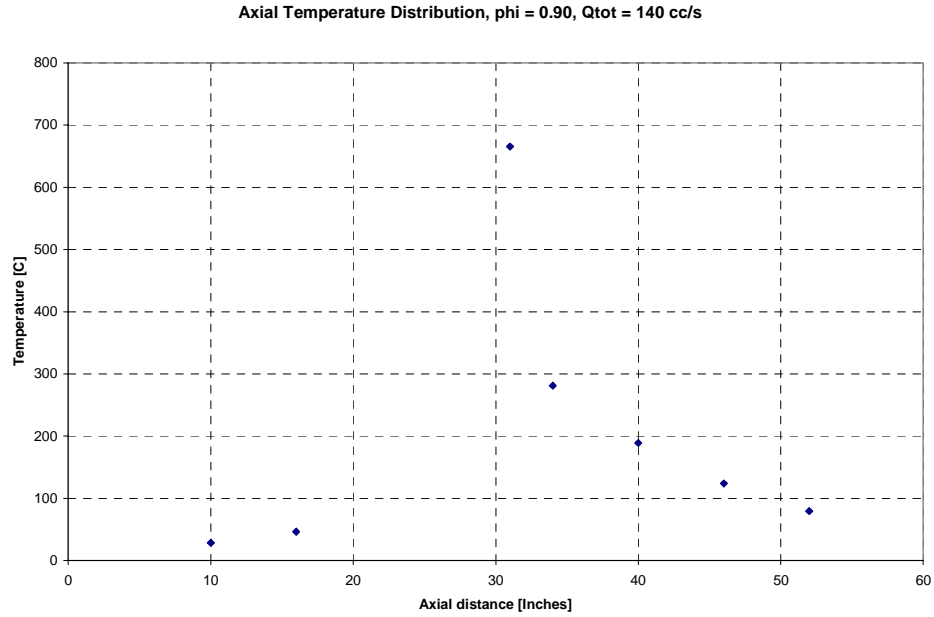


Figure F.25 Axial temperature distribution for  $\phi = 0.90$ ,  $Q_{tot} = 140$  cc/s

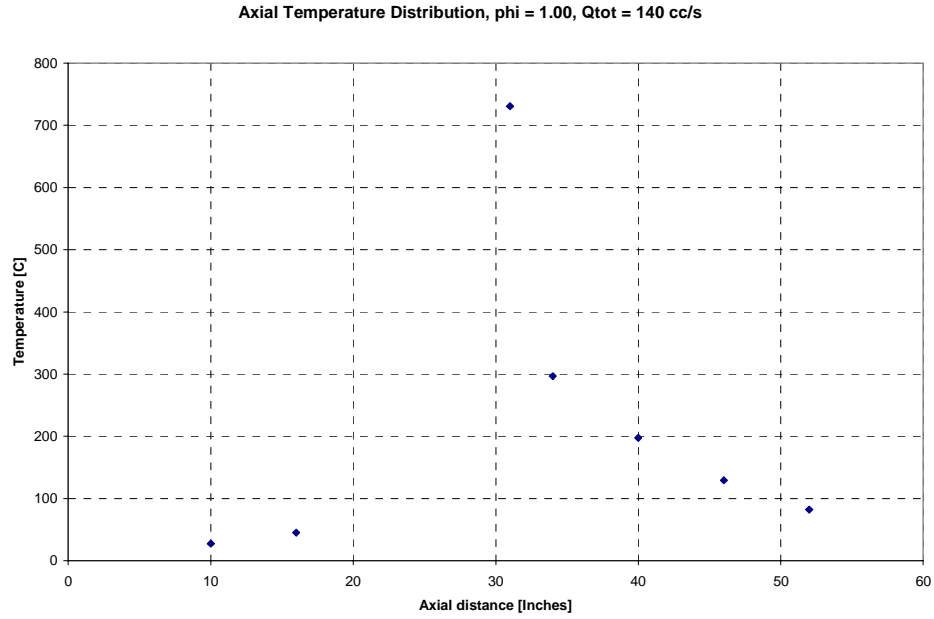


Figure F.26 Axial temperature distribution for  $\phi = 1.00$ ,  $Q_{tot} = 140$  cc/s

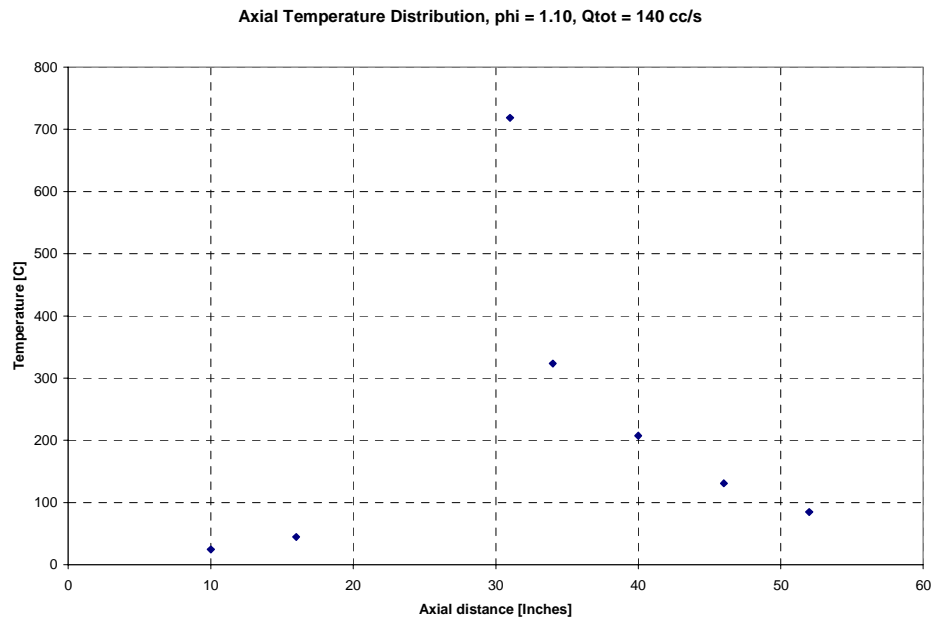


Figure F.27 Axial temperature distribution for  $\phi = 1.10$ ,  $Q_{tot} = 140$  cc/s

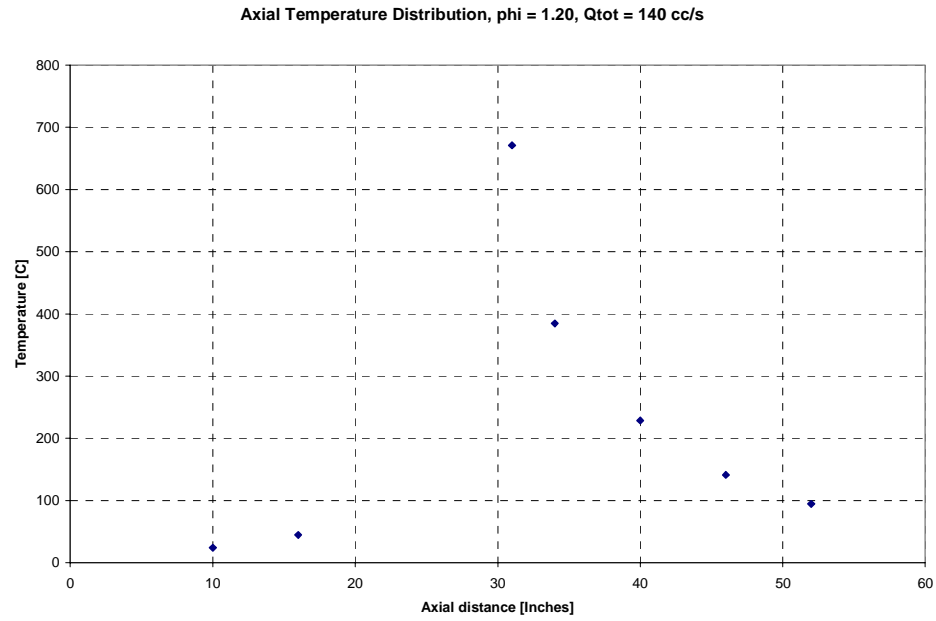


Figure F.28 Axial temperature distribution for  $\phi = 1.20$ ,  $Q_{tot} = 140$  cc/s

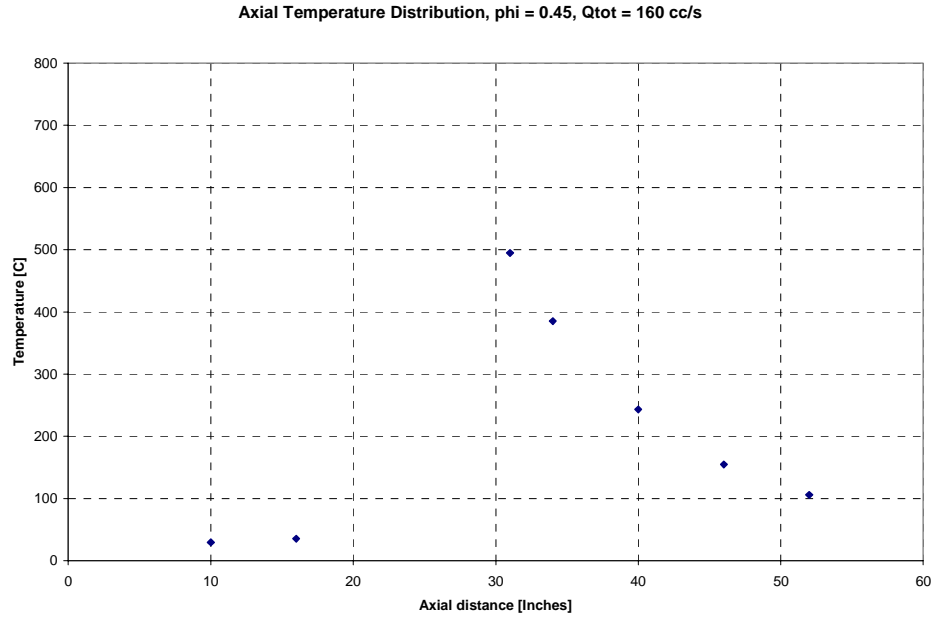


Figure F.29 Axial temperature distribution for  $\phi = 0.45$ ,  $Q_{tot} = 160$  cc/s

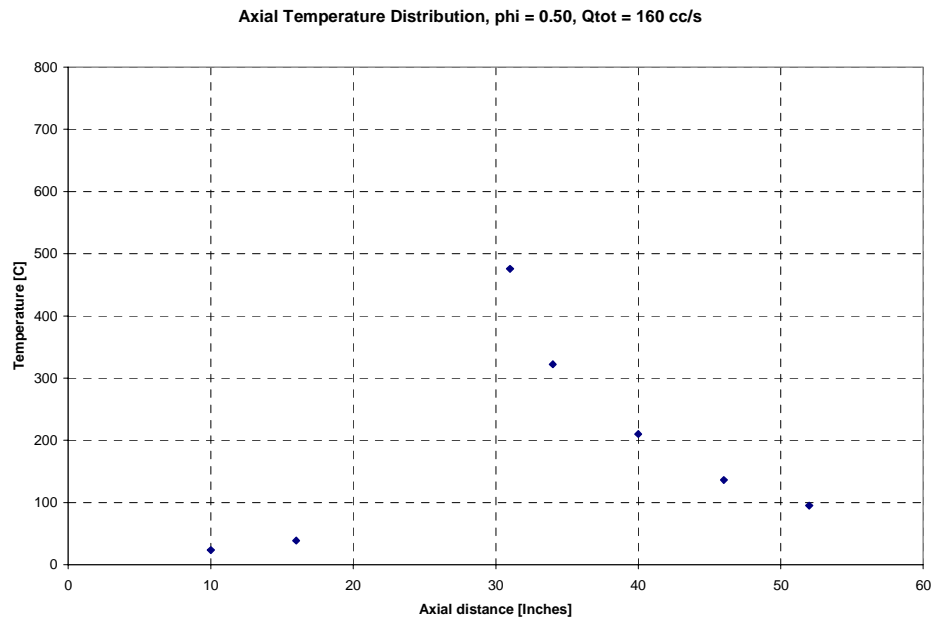


Figure F.30 Axial temperature distribution for  $\phi = 0.50$ ,  $Q_{tot} = 160$  cc/s

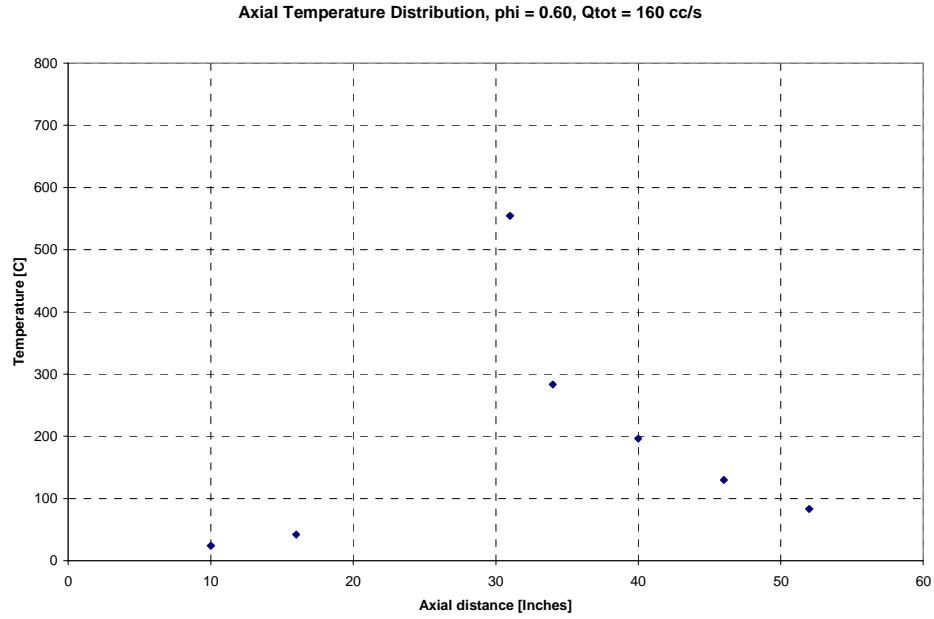


Figure F.31 Axial temperature distribution for  $\phi = 0.60$ ,  $Q_{tot} = 160$  cc/s

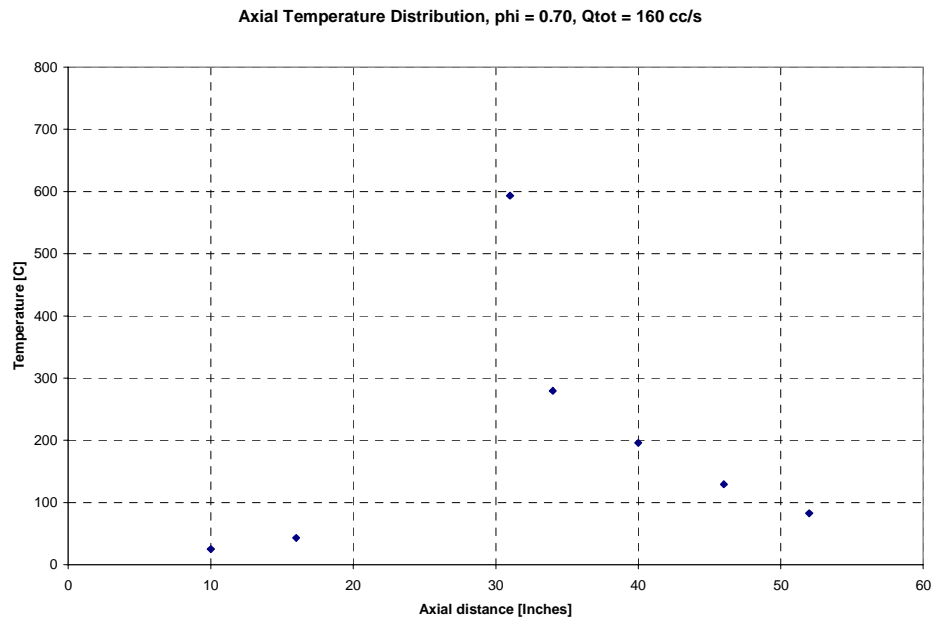


Figure F.32 Axial temperature distribution for  $\phi = 0.70$ ,  $Q_{tot} = 160$  cc/s

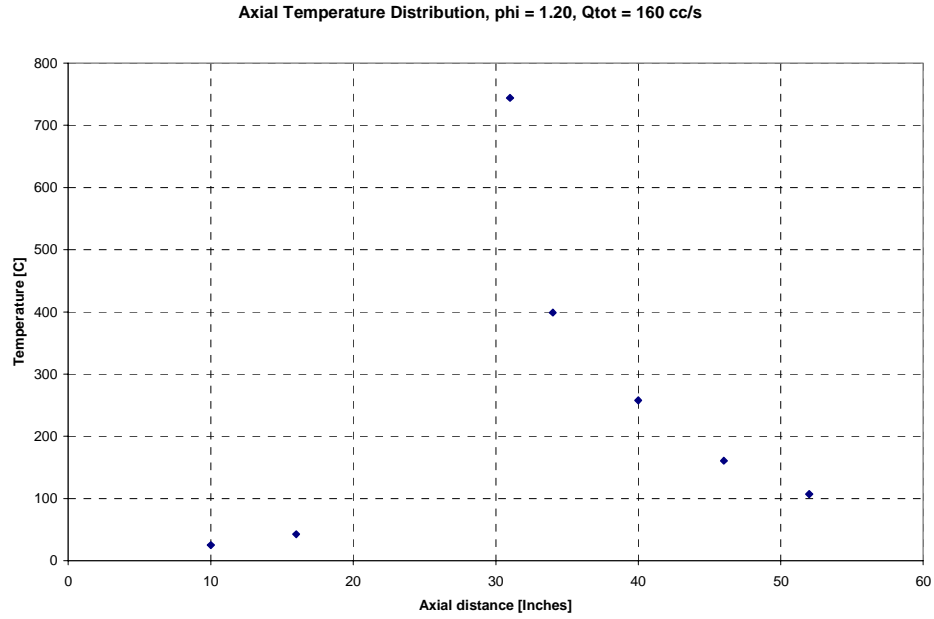


Figure F.33 Axial temperature distribution for  $\phi = 1.20$ ,  $Q_{tot} = 160$  cc/s

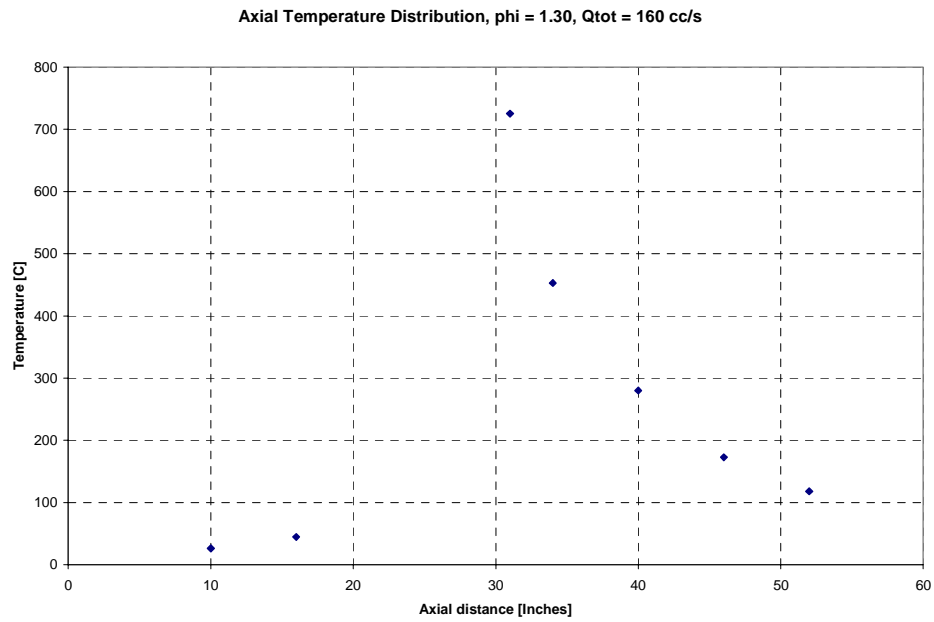


Figure F.34 Axial temperature distribution for  $\phi = 1.30$ ,  $Q_{tot} = 160$  cc/s

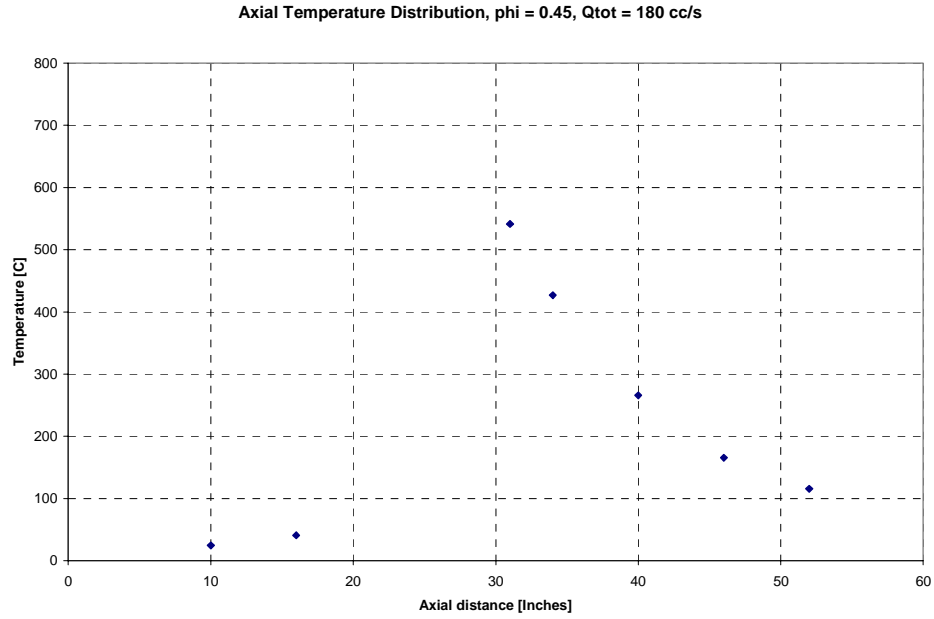


Figure F.35 Axial temperature distribution for  $\phi = 0.45$ ,  $Q_{tot} = 180$  cc/s

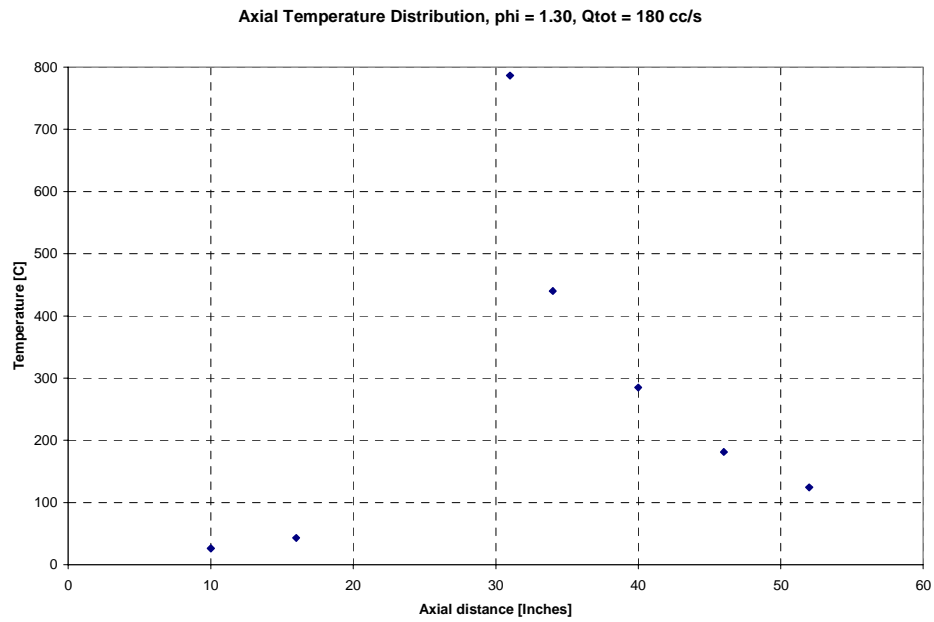


Figure F.36 Axial temperature distribution for  $\phi = 1.30$ ,  $Q_{tot} = 180$  cc/s

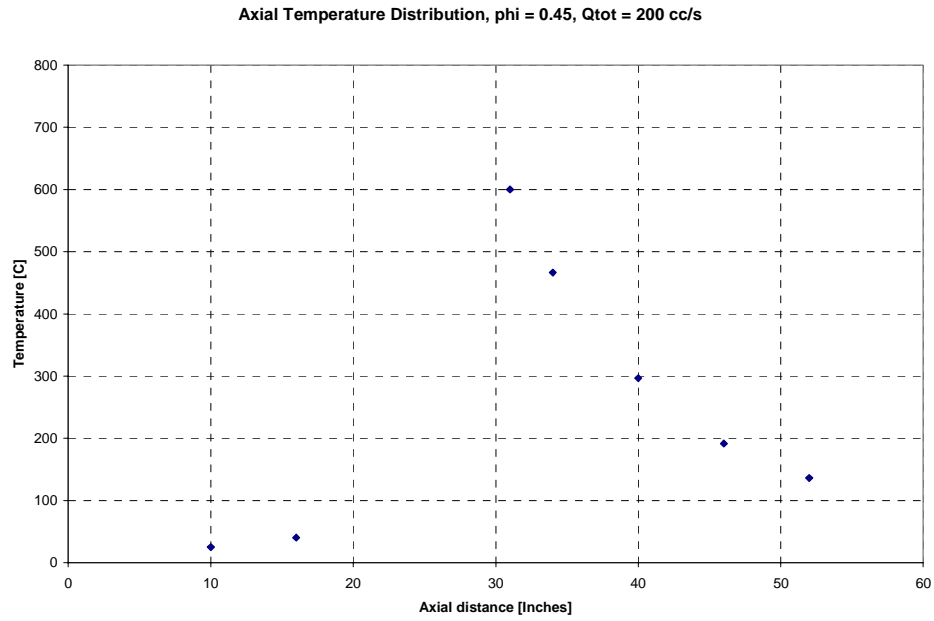


Figure F.37 Axial temperature distribution for  $\phi = 0.45$ ,  $Q_{tot} = 200$  cc/s

## **Vita**

Lars Nord was born in October 18, 1972 and grew up in Soderhamn, Sweden. He graduated from Polhemsskolan, Gavle, 1992, where he went to high school studying Mechanical Engineering. A year later, he started his university studies at the department of Mechanical Engineering at Lulea University of Technology in Sweden. After finishing the class work in four years, he spent 5 months at ABB STAL working on a project involving pressure pulsations in gas turbine combustion chambers to complete his degree. After the degree he received a scholarship at the department of Mechanical Engineering at Virginia Tech and started his graduate studies there in January of 1998. The research at Virginia Tech was in the field of thermoacoustics; a path already started at ABB STAL. The class work was finished in May of 1999, when he began working at ABB Power Generation, Inc., in Richmond, VA, in the field of gas turbine performance, emissions, and pulsations.